TiO_2 Modifications and Their Environmental Photocatalytic Performance: An EPR Investigation

Sofia Salli

Department of Chemistry

Cardiff University

2024

To and for my family, with all my love

Προς και για την οικογένεια μου,

με όλη μου την αγάπη

Acknowledgments

My thanks must go to the following:

To Dr Emma Richards, my supervisor, for her guidance through my PhD years. I would also like to thank Dr Erik Cerrato, my PostDoc and friend, who even though stayed a short time we spent hours (including those long Saturdays) exploring this world and for many helpful discussions and constant willingness to help.

I would also like to thank people within the EPR group during my time for the constant support and laughter, especially Rebekah Taylor and Giuseppina Magri as friendships formed even during our COVID restrictions times and Dr Tom Stonelake, who joined the group later but quickly became a wonderful company to discuss with.

To the friends I made outside my university hours, that were spent in a pool. A specially thank you to my good friend Laura, for helping me deal and persevere with a lot of the downs during this PhD, even if that meant a toss in the pool sometimes.

And finally, my love and gratitude go to my family, my everything. To my sister, Eleni, you are so smart, and you always help me laugh no matter how I feel. Watching you keep going has helped me to do the same even on the hardest days. To my mum, who has supported me, encouraged me and helped me in every way possible through my life within and outside of my studies. Mum I couldn’t have done this without you.

Abstract

This thesis investigates the generation and behaviour of paramagnetic states in various titanium dioxide (TiO_2) materials using electron paramagnetic resonance (EPR) spectroscopy. The study focuses on the synthesis of novel co-doped materials, their characterisation and exposure to oxygen under different wavelengths irradiation, highlighting the sensitivity and non-invasive nature of EPR in detecting these states. Additionally, the capabilities of the catalysts were studied via introduction of organic substrates mixtures and formation monitoring of the different radical species. This thesis studies the differences in activity for the various polymorphs of the co-doped TiO_2. Thus, allowing for the further development of TiO_2 catalysts to be achieved, by improving the efficiency of the materials.

It was demonstrated that the photocatalytic activity of the TiO_2 materials was influenced by the phase and the variety of lattice modifications. This was achieved via the incorporation of aliovalent dopant atoms via sol-gel synthesis and different calcination methods. The metal dopants selected were tungsten and tantalum, as they are reasonably inexpensive and abundant compared to platinum group metals, while nitrogen was chosen as the non-metal dopant. Doping aimed to modify the optical properties and surface chemistry of TiO_2, as it has been demonstrated to introduce energy levels within the band gap of the semiconductor and thus later the charge carriers production. These modifications allow for the catalysis to take place under solar visible light over the current limited UV light, as it only makes up 4% of solar energy.

Through this work, it was demonstrated that the polymorphic activity from the different calcinations, the influence of dopants on the band structure and the photocatalytic activity allows for a more targeted design of co-doped TiO_2. Though some materials underperformed compared to commercial P25 under UV light, their true potential may lie in visible light-driven processes, such as volatile organic compounds decomposition and glycerol transformation. The insights gained from this thesis provide new directions for designing efficient photocatalysts, with significant implications for industrial applications.

Table of Contents

Chapter 1. General Properties of Titanium dioxide (TiO_2)

1.1 Introduction

Titanium dioxide (TiO_2) specifically is a widely used metal oxide in photocatalytic applications due to its unique structural, electronic, and surface properties. Optimizing these properties through a variety of modifications, such as doping, can significantly enhance performance of TiO_2 in applications such as environmental purification, solar energy conversion, and hydrogen production. (1) One of the major challenges in utilizing TiO_2 for photocatalytic applications is its limited absorption of visible light. The photonic efficiency is limited due to the band gap excitation being in the UV region of light (3–3.3 eV), thus, only 4% of solar irradiation occurs in this region. (2) As a result, modifications to improve the visible light photo—response are being explored, such doping with either metal elements (W, Ta, etc.) or non—metal elements (N, S, etc.).This chapter will delve into the structural, geometrical, and electronic optimization of co-doped TiO_2, highlighting its significance and applications.

Metals are well-known for their high melting points, high densities, and low ionization potentials, making them excellent heat and electricity conductors. A significant portion of the metals in the periodic table are transition metals, characterized by their loosely bound ‘d’ orbital valence electrons. These electrons contribute to the metals' inherent properties, such as high electrical conductivity and a wide range of oxidation states. (3) The diverse oxidation states of transition metals make them highly desirable for catalytic applications, as they enable the formation of a variety of compounds. For instance, titanium can form multiple compounds, including Ti, TiO_2, and $FeTiO_3$.

Metal oxides, a specific and universal category of materials, are formed by the combination of metals with oxygen in the oxide ion (O^{2-}) form. In these materials, the metal cation is often stabilized in its highest oxidation state. Metal oxide surfaces play a crucial role in numerous applications, such as thin film gas sensors, varistor devices, and coatings. (4) Therefore, a deeper understanding of these materials is essential for enhancing device performance, prompting extensive investigation into their surface properties.

The structure of a transition metal oxide significantly influences its chemical properties, as structure is directly related to surface energy. (5) Changes in the material's structure can either benefit or impair its applications. An important parameter is the difference between the surface and bulk position of an ion. When a surface is created, it reconstructs to minimize the Gibbs free energy (ΔG), leading to the most stable surface. The stability is determined by the level of coordination and the polarity. The level of coordination measures the number of bonds that need to be broken to form a surface; fewer broken bonds result in a more stable surface and a reduction in Gibbs free energy. (6)

In surface science TiO_2 has become one of the most commonly studied metal oxide materials. TiO_2 has been shown to be used with ease in many experimental techniques, thus, making the process of identifying new phenomena on its surface much easier and increasing its popularity in the scientific community. Hence, TiO_2 is now recognised as the model system for characterizing the surface science of metal oxides. (7)

It is of great interest to further study the reactions that occur on the polycrystalline (anatase and rutile) varieties of TiO_2, as it is commonly the powdered form of the material that is employed in industrial applications, and this therefore provides a more realistic view of the processes that occur over the semiconductor catalyst. It is important to understand that it is very difficult to gain any site-specific information from the polycrystalline samples; in order to understand site-specific, it is necessary to study single crystals. Therefore, in this study, several reactions will be performed on two morphs of the powdered samples of TiO_2 in order to gain information on reaction mechanisms and surface stability of radicals.

1.2 TiO_2: Structure, and applications

Titanium exhibits typical transition metal properties, forming a range of coordination and addition compounds with non-metals, including halides, chalcogenides, hydrides, sulphides and oxides. Titanium dioxide is the most common form of naturally occurring oxides, existing in the three forms, anatase, rutile and brookite. (8) In comparison to anatase and rutile, brookite rarely occurs and displays no photocatalytic properties or commercial uses and therefore will not be discussed further. (9)

Pure titanium dioxide is a colourless, crystalline solid and is stable over the stoichiometric range $TiO_{2.003}$ to $TiO_{1.988}$- $TiO_{<2}$ is stable, non-volatile and insoluble in most solvents with its highest solubility in H_2SO_4 and HF. (8) It is amphoteric but contains more acidic properties then basic. Generally, TiO_2 is prepared primarily via two main processes known as the Sulphate Process and the Chloride Process. (10,11)

1.2.1 Structure of TiO_2

The different structures of anatase and rutile TiO_2 produce observed variations in activities, with anatase as the most active during catalytic processes followed by rutile and then brookite. This hierarchy is primarily due to differences in their crystal structures, surface properties, and charge carrier dynamics. For example, anatase TiO_2 consistently shows the highest photocatalytic activity for volatile organic compounds (VOC) degradation due to its favourable surface properties and efficient charge carrier dynamics. Rutile, while less active than anatase, still contributes significantly towards the VOC degradation, due to its thermal stability and broader light absorption range. (12) Within the unit cell of anatase and rutile, the titanium atom is surrounded by six oxygen atoms in a distorted octahedron, each Ti is surrounded by 3 adjacent Ti atoms, Figure 1.1. In the anatase structure, the octahedra are connected with their edges, whereas in rutile the neighbouring octahedra share one corner along the [1 1 0] directions and the axes of neighbouring octahedral pairs alternate by 90^{o}. This small variation results in a more closed packed structure compared to anatase, therefore resulting in different properties such as higher refractive index and greater chemical stability, Table 1.1.

While rutile melts at 2098 K (1825^{o}C), anatase does not have a melting point, instead anatase irreversibly converts to rutile before melting in a process known as rutilisation and occurs between 973-1473 K (700°-1200°C). The transition temperature is dependent on the sample history, crystallite size and the presence of impurities. (13) Thus, rutilisation will be used throughout this thesis to produce materials of the two different polymorphs.

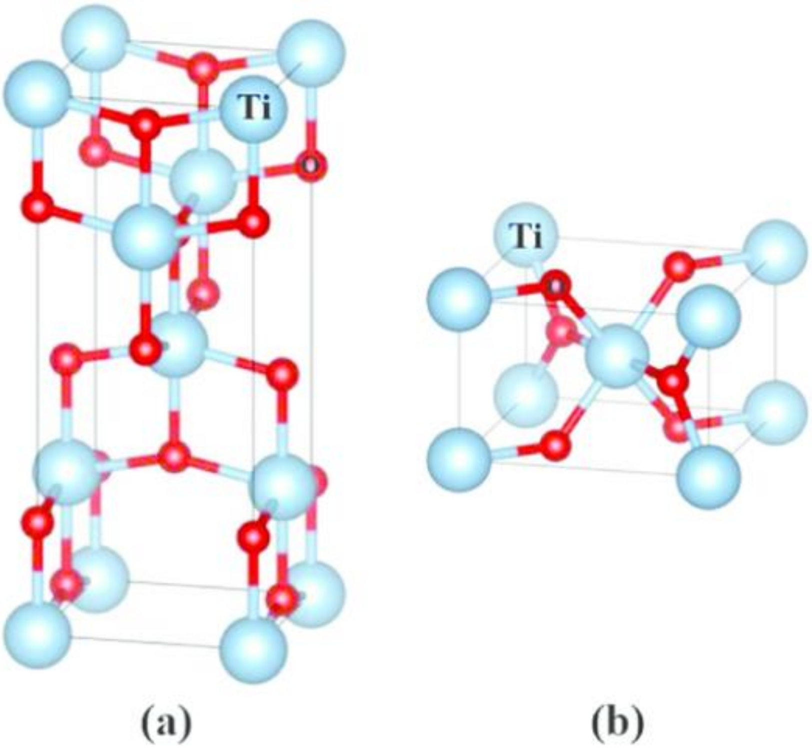

Figure 1.1: Crystal structure of anatase (a) and rutile (b) TiO_2. (14)

Most commercial titania powder catalysts with high photocatalytic efficiency are a mixture of rutile and anatase, e.g., Degussa P25, contains approximately 80% anatase and 20% rutile. There is evidence that anatase has a higher photocatalytic activity than rutile for several reactions such as photo-oxidation despite having a lower refractive index. (15) Anatase and rutile show inherent differences in particle size, and this causes some of the observed differences in chemical properties. The surface energy of a crystal facet is an important factor determining the stability and reactivity of the material, as higher surface energies generally lead to increased reactivity and lower thermodynamic stability. Anatase typically exhibits lower surface energies compared to rutile, which accounts for its greater thermodynamic stability at the nanoscale, particularly in applications where manipulating the surface energy is crucial for enhanced performance. The different surface energies result in varying particle sizes and shapes for anatase and rutile. Due to its lower surface energy, anatase tends to form smaller particles and is often synthesized in nanometre sizes. The typical particle size of anatase ranges from 10 to 50 nm. Rutile, with higher surface energy, tends to form larger particles. The particle size of rutile is usually in the range of 50 to 200 nm, but it can also grow to larger sizes under certain conditions. (16)

It is evident that photoactivity is highly dependent on both the chemical and physical properties of the sample. Although the band gap of anatase and rutile is only slightly different, Table 1.1, the difference does have an effect of the photo-efficiencies. This difference in photo-efficiency indicates that they vary as a function of both band gap and crystal structure. (17, 18)

Table 1.1: Properties of anatase and rutile TiO_2 polymorphs.

Property	Anatase (A)	Rutile (R)
Crystal Structure	Tetragonal	Tetragonal
Crystal Symmetry	D_{4a}	D_{4h}
Crystal Size/nm	130-150	160-250
Unit Cell Parameters/ AA		
a	3.784	4.594
b	3.784	4.594
c	9.514	2.959
Formula unit / cell (Z)	4	2
Band Gap/ eV	3.23	3.02
Melting point / K	N/A	2128
Refractive Index/ ms^{-1}	2.55	2.7
Density/ gcm^{-3}	3.90	4.23
Hardness / Mohs scale	5.5-6	6-7.5
Dielectric constant	14 - 110	86.00
ΔH_f / kJmol^{-1}	-933.00	-944.70
Electrical resistivity / ohm cm	10^{13} - 10^{18}	10^{13} - 10^{18}

1.2.2 Applications of TiO_2

Optical coatings, white pigments for paints and cosmetics, photocatalysis, and ceramics are among the most popular uses of TiO_2. Because the rutile and anatase forms have high refractive indices (2.71 and 2.55, respectively), just a tiny amount of material is needed to produce an opaque white covering, making it an effective opacifier. (19)

The photochemical characteristics of TiO_2 have drawn a lot of attention in recent years. The work of Fujishima and Honda on the photolysis of water over TiO_2 electrodes without an external bias originally shed light on this field of interest. (20) Since then, dye-sensitized nanocrystalline solar cells (DSNCs), the first of which was created by O'Regan and Grätzel, have employed TiO_2 to convert sunlight into power. (21)

Some of the major applications of TiO_2 are listed in Table 1.2, along with a brief description of the physical and chemical properties that make TiO_2 suitable for these applications. (22)

Table 1.2: Applications of TiO_2 based on its physical and chemical properties.

Category	Property	Applications	Morph	Ref
Pigment	Bright white colour, with the highest opacity of any commercial product	Paints, food packaging, cosmetics, paper	R	(23)
Self-sterilising	The photocatalytic activity of titania results in thin coatings of the material exhibiting self-cleaning and disinfecting properties under exposure to UV radiation	Medical devices, food preparation surfaces, air conditioning filters, sanitaryware surfaces	A	(24)
Cancer therapy	Anti-tumour activity	Endoscopic-like instruments	R and A	(25)
Superhydrophilicity	Adsorbed OH groups lower the contact angle for water	Anti-fogging mirrors, self-cleaning windows	A	(24)
Water purifier	Photocatalyst under ambient conditions	Detoxify drinking water, decontaminate industrial wastewater	A	(24)
Gas sensors	Electrical resistivity changes in presence of adsorbed gases	Monitoring exhaust fumes	A	(26)
Air cleaning/ purifier	Photocatalyst under ambient conditions	Indoors room air cleaner, outdoor air purifier for concrete highways, roadways, footpaths, tunnel, sound-proof and building walls.	A	(24)
Solar cells	Adsorbed dye molecules extend UV absorption into solar spectrum	Dye-sensitised nanocrystalline solar cells	A	(27)

1.3 Understanding the surface of the TiO_2 polymorphs

The surface reactivity of TiO_2 is highly dependent on its crystallographic facets. In the study of surface science that targets metal oxides, titanium dioxide is the most investigated single crystalline system, with over 30,000 TiO_2 publications. TiO_2 has a wide range of uses, and significant research has been conducted on this material. The goal is that a better understanding of its fundamental processes will lead to improved performance and enhanced environmental friendliness. On metal oxide surfaces in particular, geometric defects or non-stoichiometries directly influence the electronic structure and, as a result, there is a strong correlation between the structure and the reactivity. (7) The surface properties of TiO_2, such as surface area, porosity, and surface energy, play a crucial role in its catalytic performance. (28) Techniques such as BET (Brunauer-Emmett-Teller) analysis and SEM (Scanning Electron Microscopy) are used to characterise the surface morphology and specific surface area of TiO_2 materials.

1.3.1 Surface Structure of Anatase

Characterising the surface facets of TiO_2 anatase is essential for optimizing its photocatalytic performance. By understanding and controlling the exposure of specific facets via doping, it is possible to enhance surface reactivity, improve charge carrier dynamics, tailor catalytic activity, and ensure stability, leading to more efficient and effective photocatalytic processes. (29)

The Wulff construction is a theoretical calculation that determines the equilibrium shape of the anatase crystal. (30) It is depicted in Figure 1.2 and was developed after extensive research to identify the most stable faces of the crystal.

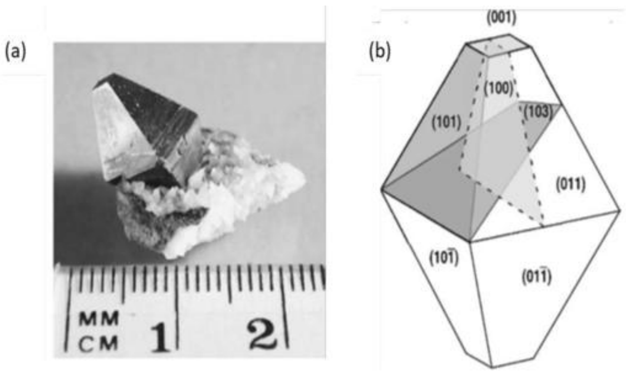

Figure 1.2: (a) Image of crystal of anatase mineral and (b) equilibrium shape of anatase TiO_2 phase according to the Wulff construction. (31)

Different crystal facets exhibit distinct atomic arrangements, electronic structures, and surface energies, all of which influence the photocatalytic activity. Different facets of TiO_2 anatase possess varying surface reactivities. The (001) facet, for example, is more reactive than the (101) facet due to its higher surface energy and unique atomic structure. This higher reactivity enhances the adsorption of reactant molecules, which is a critical step in photocatalysis. The separation and migration of photogenerated charge carriers (electrons and holes) are influenced by the surface properties of different facets. The (101) facet has been found to favour the separation of electrons and holes, reducing recombination and thereby enhancing photocatalytic efficiency. Conversely, the (001) facet can facilitate the trapping of electrons, which might be beneficial in certain redox reactions. (32) Understanding these mechanisms helps in tailoring TiO_2 for specific photocatalytic applications.

The affinity of TiO_2 surfaces for adsorbing water and other reactant molecules varies with different facets. The (001) facet, with its higher surface energy, provides more active sites for the adsorption of water molecules, which are crucial for photocatalytic water splitting. (33) This facet-dependent adsorption significantly impacts the overall photocatalytic activity. Considering that different facets can drive different photocatalytic mechanisms, the example of the (101) facet can demonstrate that this facet is more suitable for oxidation reactions due to its lower surface energy and better charge separation characteristics. (34) Meanwhile, the (001) facet is more active in reduction reactions due to its high energy and reactivity. (35)

Knowledge of facet properties allows for the rational design of TiO_2-based photocatalysts. By selectively exposing certain facets through synthesis methods, such as doping, it is possible to enhance the photocatalytic performance.

1.3.2 Surface Structure of Rutile

The (110) surface of rutile TiO_2 has been demonstrated to have the lowest surface energy, based on surface energy measurements. (36) The Wulff structure in Figure 1.3 displays the findings of their investigation.

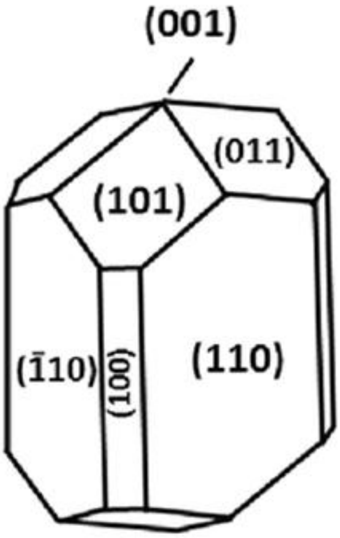

Figure 1.3: Equilibrium shape using Wulff construction for macroscopic crystals of rutile. (37)

Rutile TiO_2 typically exposes several facets, such as (110), (101), and (001), each with distinct atomic configurations and reactivity. For example, the (110) facet is the most thermodynamically stable and commonly exposed facet of rutile TiO_2. It has a relatively lower surface energy compared to other facets, leading to a more stable surface structure, but this stability can sometimes result in lower reactivity for photocatalytic processes. (38)

In contrast, the (001) facet, although less stable, exhibits higher reactivity due to its higher surface energy and under-coordinated atoms, which provide more active sites for photocatalytic reactions. The (101) facet offers a balance between stability and reactivity, making it another important surface for photocatalytic applications. (39)

Different facets of TiO_2 can affect the separation and migration of charge carriers, affecting the photocatalytic efficiency. For instance, the (001) facet has been shown to promote better separation of photogenerated electrons and holes compared to the (110) facet, which tends to have higher recombination rates due to its more stable nature. (40) The adsorption energies and configurations can vary significantly with different facets. The (001) facet, with its higher surface energy and more reactive sites, can adsorb and activate reactants more effectively than the (110) facet, enhancing the overall photocatalytic activity. (41)

Of all the rutile TiO_2 surfaces, the (110) surface is the least dense in dangling bonds and is relatively flat. Two varieties of Ti (5- and 6-fold) and O (2- and 3-fold) ions are present on the surface. Bridging oxygens (Figure 1.4) are the two-fold coordinated O atoms that are in chains along the [001] direction ~2.36 a.u. above the plane of surface Ti atoms. In a (110)-(1x1) surface, the chains of bridging oxygens are separated by approximately 12.21a.u. The coordination of each bridge oxygen to a 6-fold Ti atom is the same as that of Ti atoms in the bulk. Connecting the chains of 6- and 5-fold coordinated Ti atoms are rows of 3-fold coordinated oxygen atoms, which are arranged in the same plane as the Ti atoms. (42)

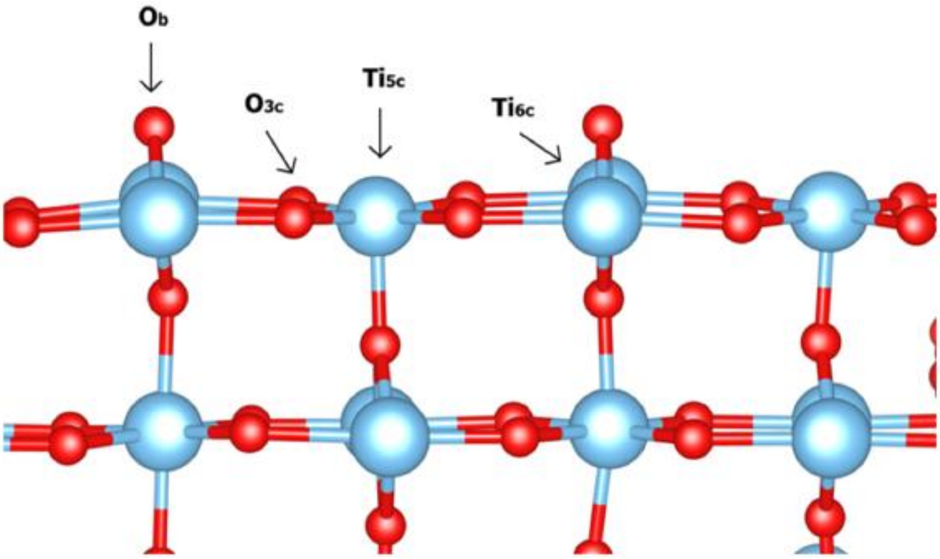

Figure 1.4: Structure of TiO_2 surfaces in the z-direction rutile (110). Where Ob is a bridging oxygen, O_{3c} a three-coordinated surface oxygen, Ti_{5c} a penta-coordinated surface Ti atom, and Ti_{6c} a hexa-coordinated Ti atom. (38)

1.3.3 Defects

1.3.3.1 Bulk Defects

Bulk defects in TiO_2, such as oxygen vacancies or titanium interstitials, can alter the material's band structure, create mid-gap states, and influence charge carrier dynamics. As a result, bulk defects can enhance or hinder photocatalytic efficiency, charge separation, and overall reactivity, making their control and understanding important for optimizing TiO_2 in various applications. TiO_2 has an extraordinarily rich Magneli phase diagram with numerous stable phases expected, indicating easy reduction of TiO_2. (43) Many transition metal oxides have covalent bonding with a high degree of ionic character; thus it is possible to understand the surface chemistry of metal oxides in relation to bulk defects by considering the nature of the bonding.

Reduction of TiO_2 significantly alters its properties, enhancing its performance in a variety of applications, including photocatalysis. (44) By introducing oxygen vacancies and Ti^{3+} sites, the electronic, optical, and catalytic properties of TiO_2 can be tuned to meet the specific requirements of advanced technological applications. TiO_2 can be reduced using a variety of techniques vacuum annealing at high temperatures, reduction with dry hydrogen at temperatures above 200°C and annealing to high temperatures. (45) The observable colour shift of the crystal can be used to gauge the degree of bulk reduction of single crystals of TiO_2. Detailed research by Diebold details the colour changes from a yellow transparent stoichiometric crystal to a dark blue/black substantially reduced crystal; the colour change is a result of the removal of oxygen atoms from the surface of the crystal, forming so-called colour centres. (46) Because the reduction is reversible, the crystal can be thermally annealed in air to return to its initial stoichiometry. These colour changes are shown in Figure 1.5.

In this work the dehydroxylation of the TiO_2 surface was utilised, since the reduction of these materials proved to irreversibly change co-doped materials. Dehydroxylating the TiO_2 surface is a critical process that enhances its functionality across various applications. By removing surface hydroxyl groups, the material's photocatalytic efficiency, electrical properties, catalytic activity, and sensing capabilities can be significantly improved. Understanding and controlling the surface chemistry of TiO_2 through dehydroxylation allows for the tailored design of advanced materials for a wide range of applications.

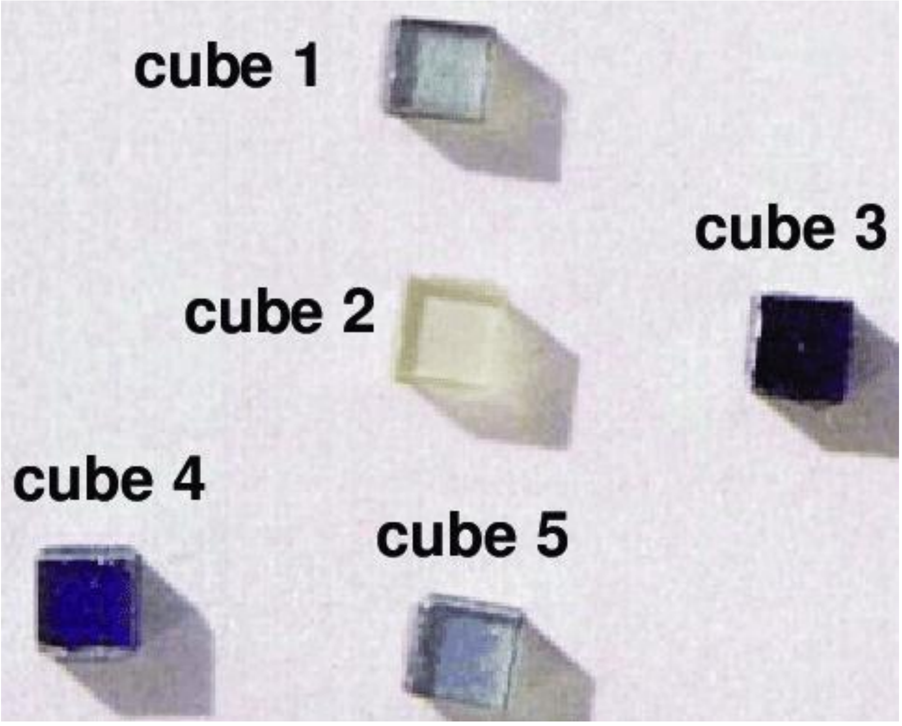

Figure 1.5: Colour changes in TiO_2 (110) crystals due to bulk reductions occurring during annealing. Cube 1: 19 hours at 1273 K; Cube 2: 21 hours 40 minutes at 1450 K (initially similar to Cube 3), Cube 3: then re-oxidised in air at 1450 K; Cube 4: 35 minutes at 1450 K; Cube 5: 1 hour 10 minutes at 1350 K. (46)The degree of oxygen deficit, which is influenced by temperature, gas pressure, and lattice imperfections, determines the type of defects present in TiO_2 crystals. Although it has been demonstrated that Ti interstitials are the predominant defect in the region between $TiO_{1.9996}$ and $TiO_{1.9999}$, the relationship between the type of defect and the degree of oxygen deficit is still unclear. (47)

Reconstructions result from the development of oxygen vacancies, and these will be covered in more detail later. Atoms must diffuse throughout the crystal for reconstruction to occur, and the diffusion mechanisms varied depending on the type of defect. It is widely acknowledged that interstitial Ti atoms diffuse in the direction of the crystallographic c-axis, seen in Figure 1.1, through the open channels. (48) However, the oxygen diffusion case remains unresolved. The most straightforward mechanism to assume for the diffusion of oxygen vacancies would be the displacement of one oxygen atom from the original site as a result of the neighbouring oxygen atom in the bridging row moving into the vacancy; this would ultimately result in diffusion along the (001) direction. Nevertheless, STM research by Schaub et al. indicates that the vacancies disperse perpendicular to the bridging oxygen rows in the (110) direction following the crystal's exposure to O_2. (49)

1.3.3.2 Surface Defects

The characteristics of the surface and any imperfections have a significant impact on how TiO_2 powders and single crystal samples behave. The amount of research done on the TiO_2 (110) surface has allowed for a thorough understanding of the characteristics of these defects and the surface preparations that cause them to arise.

On both the powdered and single crystal samples, the oxygen vacancies produced on the surface as a result of thermal annealing are of particular importance. Defects on the surface of TiO_2 (110) can be seen in STM images as bright spots on dark rows, frequently with a density of less than 7% per surface unit cell. (50) Spectroscopic methods like ultraviolet photoemission spectroscopy and X-ray photoelectron spectroscopy can be used to study defects because they cause changes in the crystal's electrical structure. For example, Ultraviolet Photoelectron Spectroscopy (UPS) investigations showed the formation of a surface state at 0.8eV below the Fermi level after TiO_2 (110) surfaces were annealed to high temperatures. This surface state is eliminated upon oxygen adsorption. This finding implies that the vacuum-annealed surface has oxygen vacancies. (51-53) Chemical evidence on the nature of these surface flaws is provided by their reactivity with adsorbates. The vacuum annealed surface is oxygen deficient, as confirmed by the chemisorption investigation of Lu et al., which showed the preferential extraction of O atoms from the adsorbate molecules (such as D_2O, $13CH_2O$, and 15NO) exclusively on the vacuum annealed surface and not on the completely oxidised surface. (54)

On the surface of TiO_2 (110), surface oxygen defects can be produced in two different ways: by removing an in-plane or bridging oxygen atom. Eliminating a bridge oxygen atom is more advantageous from an energy standpoint since it is coordinated to only two sublayer Ti cations, whereas the in-plane oxygens are coordinated three times. Bridging oxygen vacancies are also indicated to be the more likely defect by the low on-set temperature (~500K) for the formation of the point defects on the surface. Another method for creating vacancies is to spit high energy rare gas ions onto the surface. The removal of oxygen atoms from surface and subsurface areas during the sputtering process causes a two-fold to four-fold shift in symmetry. (55, 56) Finally, UV irradiation can be used to induce surface flaws. (57)

1.4 Mixed Phase TiO_2: Structure and Reactivity

It is evident from available data that mixed phase catalysts have higher photoactivity than pure polymorphs like rutile and anatase, Degussa P25 is a great example of this. The initial theory put forth to explain the increased photoactivity of the mixed phase catalysts, as diagrammatically portrayed in Figure 1.6, postulated the transfer of electrons from the anatase phase into lower energy trapping sites in the rutile phase, thereby increasing the catalytic activity through improved electron-hole separation efficiency. (58)

Hurum et al.'s EPR study of Degussa P25 was conducted in order to understand this phenomenon better. They contended that neither the energy levels of the lattice nor the surface trapping sites of the two phases were considered in the evidence substantiating the above-described notion. For instance, the anatase trapping site was reported to be located 0.8 eV below the anatase conduction band, which puts it below the energy of the rutile conduction band and prevents electrons from moving from anatase to rutile, (59, 60) a more detailed explanation and importance of band theory is given in Chapter 2.

Following their initial study Hurum et al. examined a number of P25 colloidal suspensions made using a modified sonication/centrifugation technique. (59, 60) The EPR results demonstrated that there was a comparable increase in the population of the rutile lattice trapping sites when the aggregates' sizes increased along with their rutile content. This implied a reduced electron transport from the rutile to the anatase phase. The EPR spectra obtained following P25's UV irradiation in the presence of methanol verified the electron transfer from rutile to anatase. Since methanol scavenges holes, it is possible to study the electron transport processes apart from the recombination events. The unusually small rutile particles, 200 nm, in photoactive P25 enable close interaction with the anatase phase, resulting in the formation of catalytic hot spots at the phase interface, Figure 1.6. A direct result of the change in particle size was the transfer of rutile electrons to anatase was observed when the UV irradiation of the sample was stopped. This increased the intensity of the anatase trapping sites concurrent with a reduction in the intensity of the rutile trapping sites. The interface between the two phases in the TiO_2 sample and the size of the particles within each phase are crucial factors in this electron transfer process.

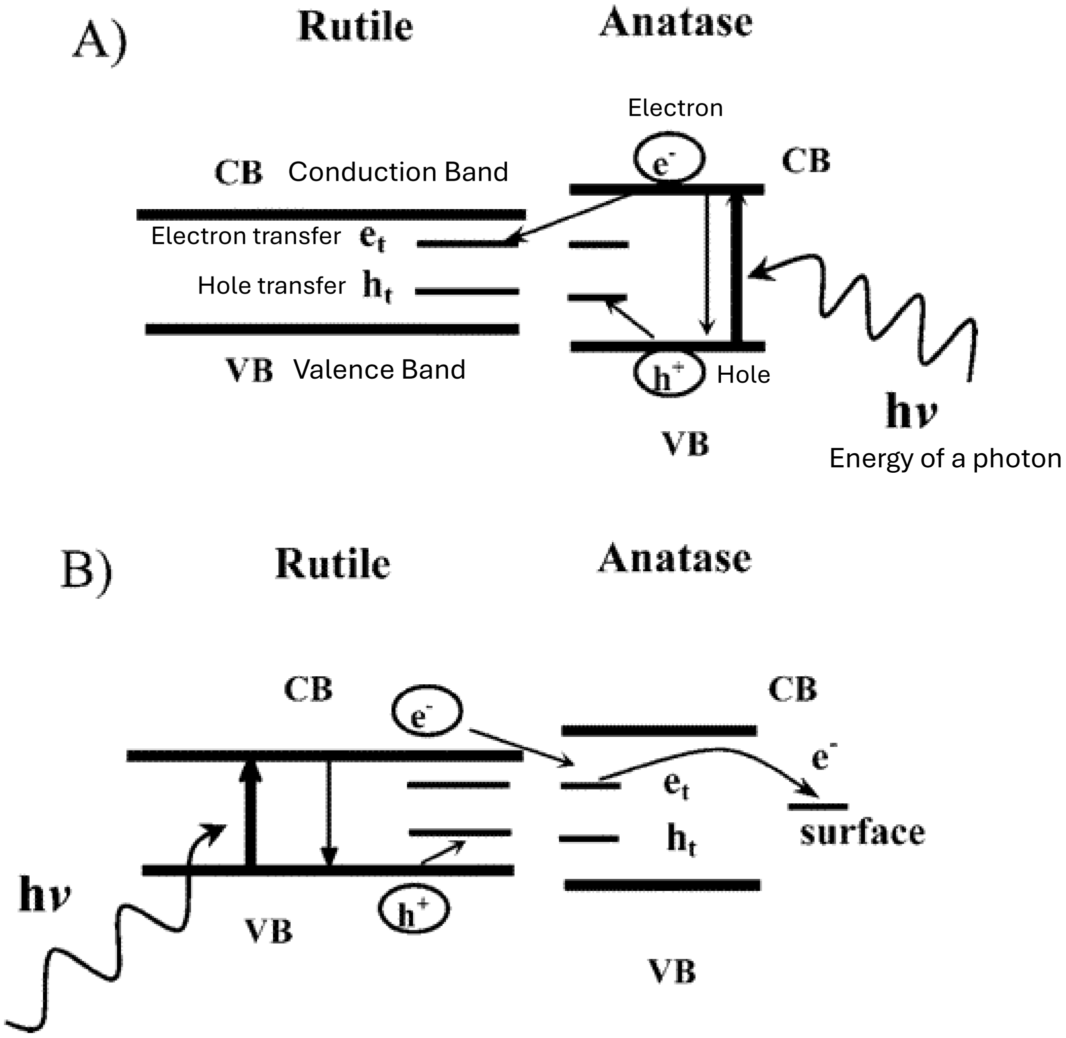

Figure 1.6: (A) P25 older activity model where rutile acts as an electron sink while the charge separation occurs on anatase. (B) Rutile antenna and subsequent charge separation. (55, 60)

1.5 Polycrystalline TiO_2

1.5.1 UV irradiation under an O_2 atmosphere

Hoffmann et al. demonstrated that the hydroxylation state of the sample surface affects the lifetimes of the photogenerated conduction band electrons, which are dependent on the timescale of minutes, through the use of diffuse reflectance infrared spectroscopy to examine TiO_2 samples following band-gap excitation using a high-pressure Xe lamp. (61) This finding by Hoffmann et al. is important because it highlights the critical role that surface hydroxylation plays in controlling the lifetimes of photogenerated conduction band electrons in TiO_2. Longer electron lifetimes can significantly improve photocatalytic performance by increasing the chances of participating in redox reactions before recombination occurs. Understanding how surface chemistry influences electron dynamics allows for better design and optimization of TiO_2-based photocatalysts, improving their efficiency in environmental and energy-related applications.

In order to examine the charge trapping affects that occurred during photoexcitation of an MOCVD-generated anatase sample (with a 350W high-pressure Hg lamp), Berger et al. combined an EPR and IR investigation. The EPR spectra of trapped electrons, Ti^{3+}, and trapped holes, O^-, could be resolved after 20 minutes of UV illumination at 90K. EPR spectroscopy was used to monitor the electron and hole trapping process by measuring the signal strength at constant magnetic field levels. During the first 100 s, both Ti^{3+} and O^- signals intensities rose monotonically. At later time points, the Ti signal stayed relatively constant while the O^- signal kept growing and it took around 500 seconds to achieve steady state. The concentration of Ti^{3+} cations did not exceed 10% of the concentration of O^-, as seen in Figure 1.7, suggesting that the majority of the photogenerated electrons stay in the TiO_2's conduction band. (62)

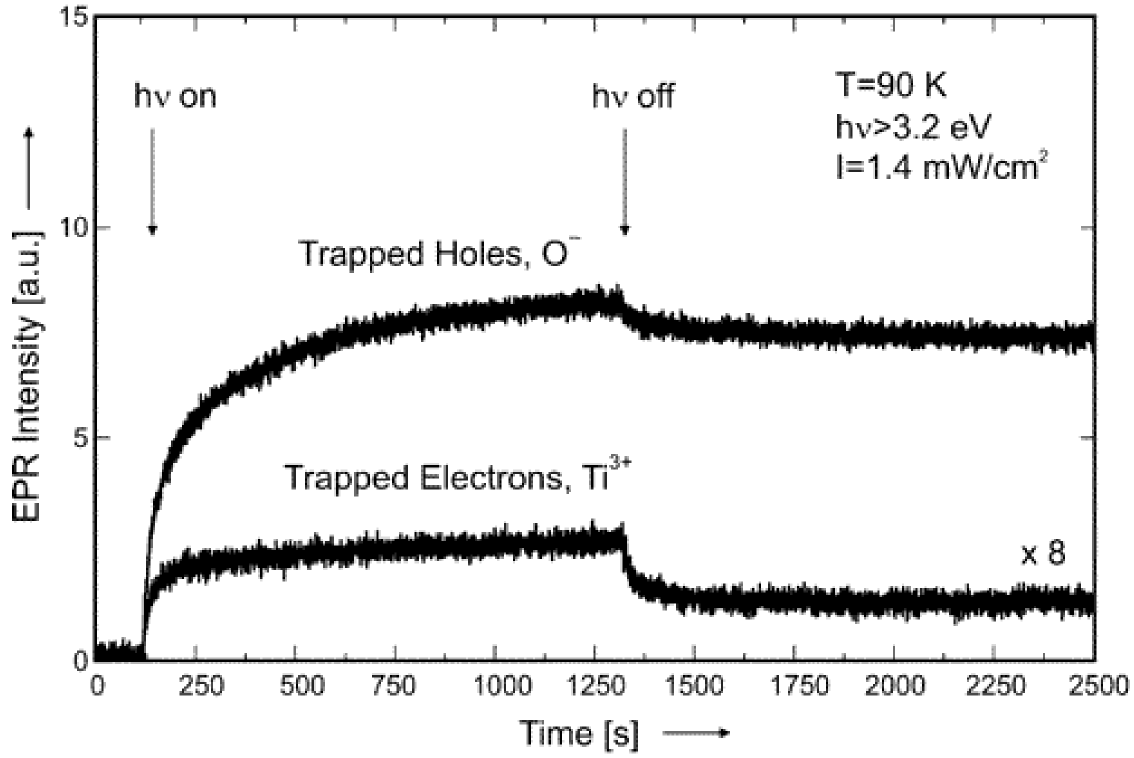

Figure 1.7: Concentration of O^- and Ti^{3+} centres as a function of UV exposure time. (62)

Using EPR spectroscopy, the temperature dependencies of the aforementioned processes were also discovered. Even after cooling the sample to 90K, no Ti^{3+} centres could be resolved upon UV excitation at 140K. The intensity of the O^- signal was significantly lower at 140K, although it was still resolved. Based on these findings, Berger and colleagues deduced that the diffusion of photogenerated electrons trapped from shallow Ti^{3+} sites had an activation value of approximately 0.01 eV. (62)

Interaction with surface adsorbed species can prolong the lifespan of the photogenerated charge carriers. Specifically, it has been reported by a number of groups that photogenerated electrons are trapped as a result of molecular oxygen adsorption. Berger et al.'s research demonstrated that while several oxygen - centred radicals were detected, no Ti sites could be resolved upon oxygen addition to a pre-irradiated anatase sample (or irradiation in the presence of adsorbed oxygen) at 140K. Both surface adsorbed superoxide (O^{2-}) radicals and the O^- signal resulting from trapped holes remained. According to the following description, these radicals are created by the interfacial transfer of electrons from conduction band and localised paramagnetic states to molecular oxygen, equation 1.1 - 1.2 (62)

$Ti^{3+} + O_2 \rightarrow Ti^{4+}....... O^{2-}$ (1.1)

$Ti^{4+} + e^{-} + O_2 \rightarrow Ti^{4+}......O^{2-}$ (1.2)

A thermally reduced anatase sample was exposed to radiation; no additional rise in the concentration of Ti^{3+} was observed, and only minute amounts of O^- trapped hole centres were resolved. It was also proposed that the lack of photoexcited trapped holes in thermally reduced TiO_2 is associated with the thermal treatment-induced shortage of lattice oxygen trapping sites. In comparison to oxygen adsorption on a material that has already been exposed to radiation, the surface concentration of superoxide anions is increased when UV irradiation is applied to the sample when oxygen is present. (62)

A thorough EPR and FTIR investigation on the properties of the species generated during UV irradiation of nanostructured TiO_2 was conducted by Coronado et al. As anticipated, the development of Ti^{3+} centres were seen upon UV irradiation of stoichiometric TiO_2 in static vacuum at 77K. Following the termination of the UV radiation, the samples were subjected to 77K molecular O_2 exposure. A new signal with **g** values of g_1 = 2.024, g_2 = 2.009, and g_3 = 2.003 replaced the Ti^{3+} signal with identical integral on samples prepared by the hydrothermal procedure. This signal was eventually linked to the superoxide radical. After being exposed to oxygen, the thermally treated samples displayed a distinct set of signals. When compared to the UV-irradiated sample, the total signal intensity rose, and it was discovered that the spectra were made up of at least three distinct signals. Based on theoretical calculations, the signal with **g** parameters of g_1 = 2.035, g_2 = 2.009, and g_3 = 2.003 was attributed to $^{\bullet}OOH$ radicals. The UV-irradiated sample also showed a signal with the g parameters of g_1 = 2.028, g_2 = 2.016, and g_3 = 2.002; however, this signal was quenched following the addition of molecular oxygen, leading the authors to attribute it to surface O^- species (i.e. a surface trapped hole). Ultimately, O_3^- radicals were identified as the third signal detected on this sample, with **g** values of g_1 = 2.011, g_2 = 2.007, and g_3 = 2.002. These results are described by the reactions in Equations 1.3 – 1.9 (63):

Charge carrier

production: $TiO_2 + hv \longrightarrow TiO_2\ (h^+ + e^-)$ (1.3)

e- trap: $Ti^{4+} + e^- \longrightarrow Ti^{3+}$ (1.4)

h+ trap: $Ti^{4+}\text{-}O^{2-}\text{-}Ti^{4+}\text{-}OH^- + h^+ \longrightarrow Ti^{4+}\text{-}O^-\text{-}Ti^{4+}\text{-}OH^-$ (1.5)

$Ti^{4+}\text{-}OH^- + h^+ \longrightarrow Ti^{4+}\text{-}OH^\bullet$ (1.6)

$Ti^{4+}\text{-}O^{2-} + h^+ \longrightarrow Ti^{4+}\text{-}O^-$ (1.7)

In presence of oxygen

Ozonide: $Ti^{4+}\text{-}O^- + O_2 \longrightarrow Ti^{4+}\text{-}O_3^-$ (1.8)

Superoxide: $Ti^{3+} + O_2 \longrightarrow Ti^{4+}\text{-}O_2^-$ (1.9)

Using sample treatment conditions, the dependency on signal form was able to be detected. The signal originating from Ti^{3+} cations in the amorphous samples studied showed a very broad shape in the spectrum, suggesting a highly heterogeneous environment. Substantially sharper Ti^{3+} signals were obtained from the highly crystalline hydrothermal samples, suggesting a much more regular environment of axially deformed octahedral distortion. The stabilisation of photogenerated radicals was promoted by an increase in the surface-bulk ratio, while e^-/h^+ recombination could be exacerbated by the low crystallinity of TiO_2 samples with small particle sizes. Consequently, a critical particle size was determined for optimal photocatalytic performance based on these two conflicting tendencies. (63) It can be concluded that the crystallinity and particle size of TiO_2 samples have a significant impact on their photocatalytic performance. Amorphous TiO_2 samples with low crystallinity and small particle sizes exhibit broad Ti^{3+} signals, indicating a highly heterogeneous environment, which can promote electron-hole recombination and reduce efficiency. In contrast, highly crystalline TiO_2 samples show sharper Ti^{3+} signals, suggesting a more ordered structure that stabilizes photogenerated radicals. (62, 63)

1.5.2 UV irradiation under an organic atmosphere

For the breakdown of waste materials in both aqueous and gaseous media, the photocatalytic oxidation of organic molecules is of great environmental significance. As Figure 1.8 illustrates, volatile organic compounds (VOCs) are generated as waste products in a variety of industrial processes. Since several of these VOCs are recognised to pose health risks their clean-up is very crucial. Considering the effective method of treating wastewaters, semiconductors have been shown to be utilised, as semiconductor photocatalysis through flat-bed reactors has been employed, which uses the photocatalyst constantly and regeneratively.

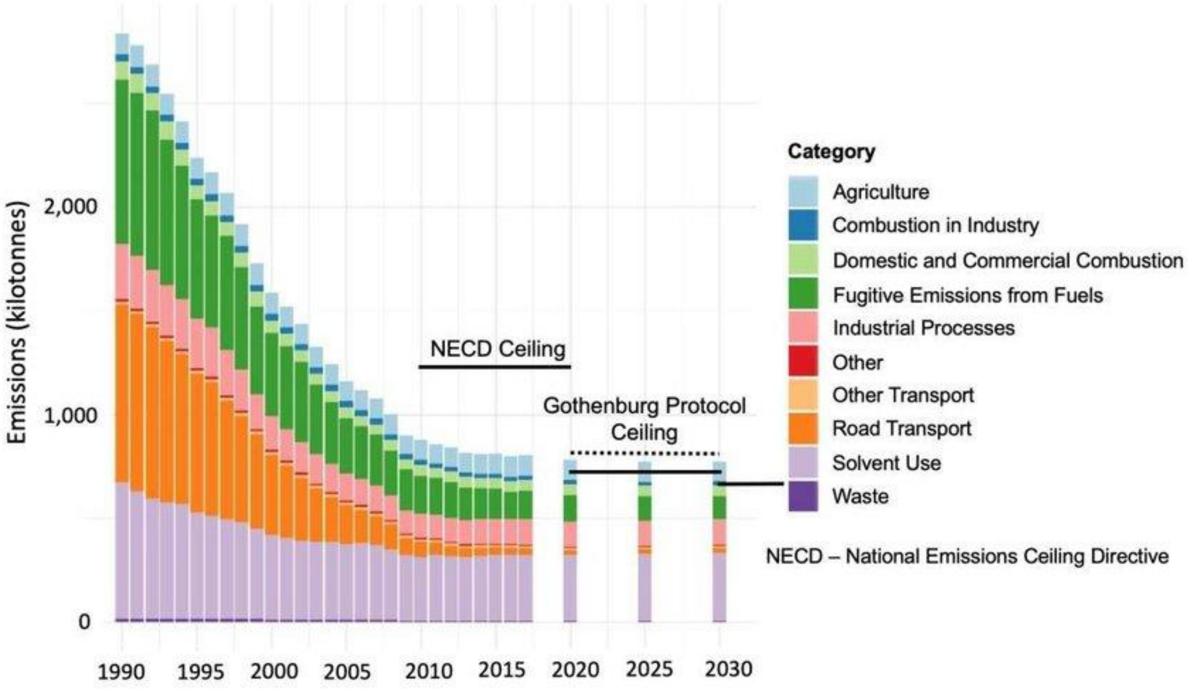

Figure 1.8: Emissions of Volatile Organic Compounds from Anthropogenic Sources in the United Kingdom from 1990 to 2017, with estimates for 2020 and 2030. During that time frame, the National Emissions Ceiling Directive ceiling is represented by the solid black marker lines. With the exception of emissions from agriculture (light blue bar), all industries included in the series are subject to the 2020–2029 cap. The revised Gothenburg Protol's 2020–2029 ceiling, which applies to all industries including agriculture, is shown by the dotted lines. (64)

As was previously indicated, the characteristics of the powders have a major impact on the species that are generated when TiO_2 particles are exposed to UV radiation. A connection between the surface characteristics of several TiO_2 catalysts and their relative activity towards the photodegradation of toluene were investigated following UV irradiation in the presence of oxygen. (65, 66) The EPR spectra of the TiO_2 catalysts only revealed a progressive weakening of the signal due to subsurface O^- ions $[Ti^{4+} - (O^-) - Ti^{4+} - OH^-]$ and an increase in the signal due to surface O^- ions $[Ti^{4+} - (O^{2-}) - Ti^{4+} - O^-]$ as the particle size increased. While the two catalysts only partially oxidised to benzaldehyde, the most promising catalyst (labelled P6 by the authors) performed the best overall in the photooxidation of toluene to CO_2 and H_2O. This, according to one theory, was caused by the photogenerated electrons and holes exhibiting more separation and reactivity at P6's surface than on the bigger catalysts, which produced charge carriers. The increasing intensity of the superoxide radical at the surface, which is created when an oxygen molecule absorbs a photogenerated electron, was shown to correspond with the greater separation. It was suggested that the various structural sites (such as planar, edge, and corner) that are present could account for the varying photoactivities of the various catalysts. For instance, there was a greater percentage of edge and corner sites on the P6 catalyst that could trap the charge carriers produced by photosynthesis. This study suggested a relationship between the type of surface sites and the catalyst's relative photoactivity, but it also urged more research to be done to determine the function of the paramagnetic species under discussion in photocatalytic oxidation. (67)

Due to the combined effects of photochemical oxidation in the gas phase and photocatalytic oxidation on TiO_2, it was evident that the use of TiO_2 under 254 + 185 nm light irradiation considerably boosted the photodegradation of toluene relative to UV alone. With UV light irradiation, maximum conversion and mineralization were achieved. Furthermore, even at high beginning toluene concentrations, significant conversions were attained. The UV light also prevented catalyst deactivation. Reactive oxygen species effectively broke down the less reactive carbon deposits on the TiO_2 catalyst, preventing catalyst deactivation, according to regeneration studies conducted using the deactivated catalyst under various conditions. (66, 67)

The methylene blue method has been the most widely used technique for assessing the photocatalytic activity of TiO_2-based photocatalysts. (68) However, because this chemical may absorb light in the visible spectrum, various doubts over its dependability have surfaced in recent years. Dimethyl sulfoxide (DMSO) will be employed as the photocatalytic test substance in this work. This solvent interacts with the radical $^{\bullet}OH$ because it is a hydroxyl scavenging agent. The degradation of this chemical by Degussa P25 and Hombikat UV100, two distinct catalysts, has been demonstrated. Two of the intermediates generated during the reaction, methansulfonate ($CH_3SO_3^-$) and sulphate (SO_4^{2-}), have been recognised, and the total organic carbon is measured in order to study the reaction. TiO_2 Degussa P25 generally performs better in terms of total organic carbon removal, photonic efficiency, and the formation of two intermediates (methansulfonate and sulphate). Despite the fact that Hombikat UV100 has a specific surface area that is six times greater than that of the other photocatalyst, Degussa P25 may have greater photoactivity due to the type of aggregates that form in aqueous solution and the slower pace at which electron/hole pairs recombine. (69) The comparison aims to show that the performance of photocatalysts is influenced by a combination of factors including surface area, aggregate formation, and the dynamics of electron-hole pairs, not just surface area or specific surface area.

The photo-oxidation of glycerol in aqueous suspensions containing TiO_2 samples in the anatase, rutile, or anatase–rutile polymorphic phases were additionally studied as reaction of interest, because it serves as a representative model reaction to study the degradation of organic compounds using photocatalysis. Formic acid, carbon dioxide, glyceraldehyde, and 1,3-dihydroxyacetone have been proven as the glycerol oxidation products and found in the aqueous phase. One potential method for producing value-added compounds from glycerol is through the photocatalytic process. Glycerol's transformation kinetics and mechanism are investigated in relation to a number of operational factors (catalyst type, pH, substrate concentration, and catalyst surface fluorination). When Degussa P25 is used, the photo-transformation rate deviates from Langmuir-Hinshelwood behaviour by exhibiting a sudden maximum at low glycerol content. A kinetic model including substrate-mediated carrier recombination (back reaction) and invoking two reactive sites on P25 TiO_2 provides a qualitative explanation for these findings.

Glyceraldehyde and 1,3-dihydroxyacetone build up in the irradiation solutions at comparatively high substrate concentrations. The most significant effect on P25 is shown by fluorinating the catalyst surface, which suppresses the maximum photo-transformation rate seen on pristine P25 and decreases the glycerol disappearance rate at low substrate concentrations while increasing it five-fold at high concentrations. Fluorides obstruct P25's potent adsorbing active sites, which are in charge of the enzyme's high activity at low substrate concentration and its decline at high substrate concentration as a result of a corresponding rise in back reactions. Fluorinated catalysts increase the formation of glyceraldehyde and 1,3-dihydroxyacetone. Thus, the outcomes highlight P25's unique characteristics and show how important back responses are to photocatalysis. (70) The process's selectivity is significantly impacted by the adjustment of the catalyst's surface characteristics.

1.6 Photocatalysis

TiO_2 for environmental cleanup has been the subject of multiple patents as a result of this development through heterogeneous photocatalysis. (71) Fujishima and Honda discovery that TiO_2 could be used to photo-catalytically split water (Equation 1.10) (72):

$$H_2O + TiO_2 + UV \rightarrow 1/2H_2 + O_2 \tag{1.10}$$

In the process of photocatalysis, the interaction of light with a semiconductor material is fundamental to generating reactive species. If the energy of incident light on a semiconductor exceeds the bandgap, an electron-hole pair is created. If the energy of incident light on a semiconductor exceeds the bandgap, an electron-hole pair is created. The electron is promoted from the occupied valence band into the unoccupied (or partially occupied) conduction band. This produces a hole, also known as an electronic vacancy, in the valence band (Chapter 2). (73)

The bandgap size is related to the photocatalytic activity of TiO_2. With a bandgap of 3.2 eV for anatase and 3.0 eV for rutile, these polymorphs are susceptible to photocatalytic excitation of light with a wavelength of less than 388 nm. In a semiconductor, the electron/hole pair lifetime is long enough (nanosecond regime) for the charge carriers created to migrate to the surface, where they engage in interfacial electron transfer with surface adsorbed species. (73) In Figure 1.9, a surface adsorbed electron donor can be oxidised by transferring an electron to a surface photogenerated hole (route b), and a surface adsorbed electron acceptor can be reduced by absorbing an electron from the surface (route a). The following equations (1.11 and 1.12) describes the anion and cation radicals produced by these processes (Equations 1.11 and 1.12):

$$e^- + A \rightarrow A^{\bullet -} \tag{1.11}$$

$$h^+ + D \rightarrow D^{\bullet +} \tag{1.12}$$

The band edge of the valence and conduction bands of the material and the redox potentials of the adsorbate species determine the rate of charge transfer from photogenerated charge carriers to surface adsorbed species. As an alternative, electron and hole recombination may take place in the semiconductor's bulk (route c) or at its surface (route d).

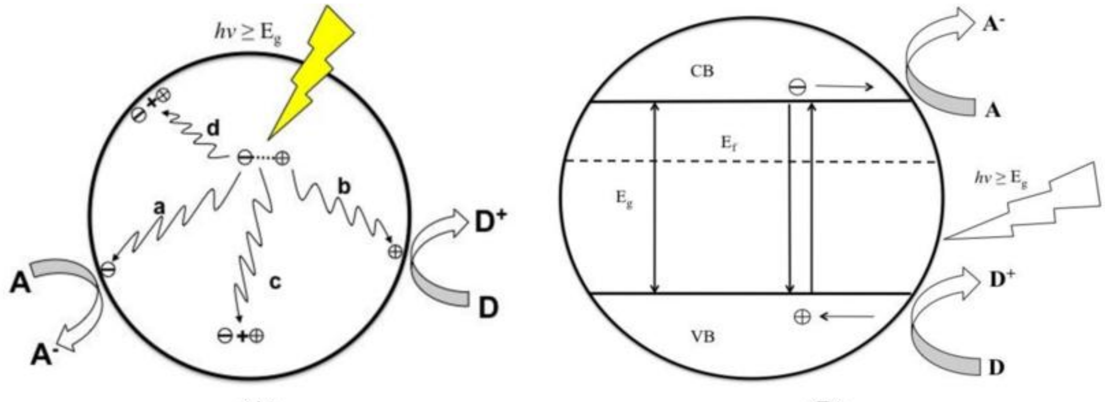

(A) (B)

Figure 1.9: Schematic representation of photoexcitation in a semiconductor, followed by de-excitation events (including recombination and surface reaction). (74)

Any molecule with a reduction potential less negative than the conduction band edge is susceptible to photoinduced reduction. Similarly, since interfacial electron transfer is permitted under these circumstances, photoinduced oxidation will happen to any molecule having an oxidation potential less positive than the semiconductor valence band edge.

The photogenerated charge carriers must stay spatially separated in the photoexcited solid until their interaction with surface adsorbates again in order to be photochemically productive. Charge carrier recombination causes photon energy to be dissipated into heat if there is not enough space between the charge carriers. That is why researching charge carrier production and recombination is crucial to creating effective photocatalysts. It is accepted that in TiO_2, positive holes in the valence band are trapped at oxygen anion sites in the lattice, while conduction band electrons are trapped at particular Ti^{4+} states inside the TiO_2 lattice to create Ti^{3+}. The overall process can be described in Equation 1.13 – 1.15:

$$TiO_2 + hv \rightarrow e^{-}_{CB} + h^{+}_{VB} \quad (1.13)$$

$$e^{-}_{CB} + Ti^{4+} \rightarrow Ti^{3+} \quad (1.14)$$

$$h^{+}_{VB} + O^{2-} \rightarrow O^{-} \quad (1.15)$$

The charge trap must be pre-associated with the photocatalyst surface prior to the start of irradiation because the rate of carrier trapping needs to be quicker than diffusion. (75)

The photo-efficiency of a semiconductor is negatively impacted by electron and hole recombination at the bulk or surface of the semiconductor. The semiconductor can be altered in several ways, such as by applying charge traps, to lessen the chance of recombination. Since it has been demonstrated that even small amounts of bulk dopants can significantly affect the electrical characteristics of these materials, therefore the insertion of metal dopants into the crystal lattice has drawn a lot of attention in recent years. TiO_2, a metal oxide semiconductor, has the rutile structures that makes it highly amenable to the incorporation of metal dopants. (76) The efficiency of a metal dopant is determined by its roles as a recombination centre or a mediator of charge transfer. Understanding the atomic-scale structure of the dopants is essential to comprehending the enhanced activity of metal oxides following the addition of metal ion dopants.

The lack of literature in the field of a tantalum co-doped TiO_2, presented a gap in the research that this work will try to investigate and present the results.

In naturally occurring polycrystalline semiconductors like TiO_2, surface and bulk irregularities have different energies than the bulk solid's valence and conduction bands. (77) By prolonging the lifetime of the charge carriers and lowering the rate of recombination, these states have the ability to function as charge traps.

After the material is exposed to radiation, charge carriers and usually oxygen vacancies are produced, which leads to superhydrophilicity. These oxygen vacancies, water can attach itself to the material's surface and produce hydroxyl radicals ($^{\bullet}OH$). These radicals then break down pollutants that have been adsorbed to the surface (Equation 1.16, X = pollutant). (78)

$$^{\bullet}OH + X \rightarrow CO_2 + H_2O \qquad (1.16)$$

Continuous irradiation improves the contact angle for adsorbed water, which approaches θ = 0°, indicating that the water disperses uniformly throughout the substance, allowing it to remove the deteriorated pollution, Figure 1.10.

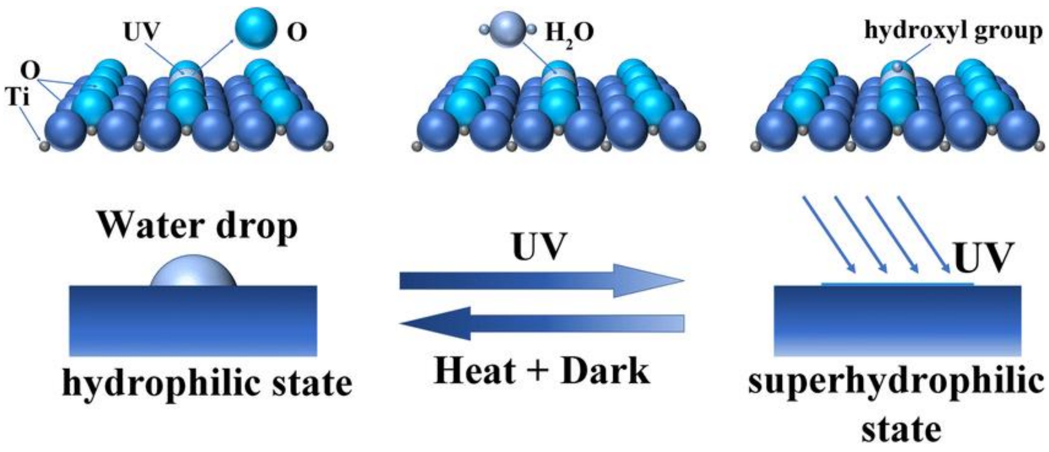

Figure 1.10: Description of TiO_2 superhydrophilicity. (79)

As mentioned in section 1.2.2 TiO_2 can be employed in a wide range of renewable energy applications, including the Gratzel cell, Figure 1.11. (80)

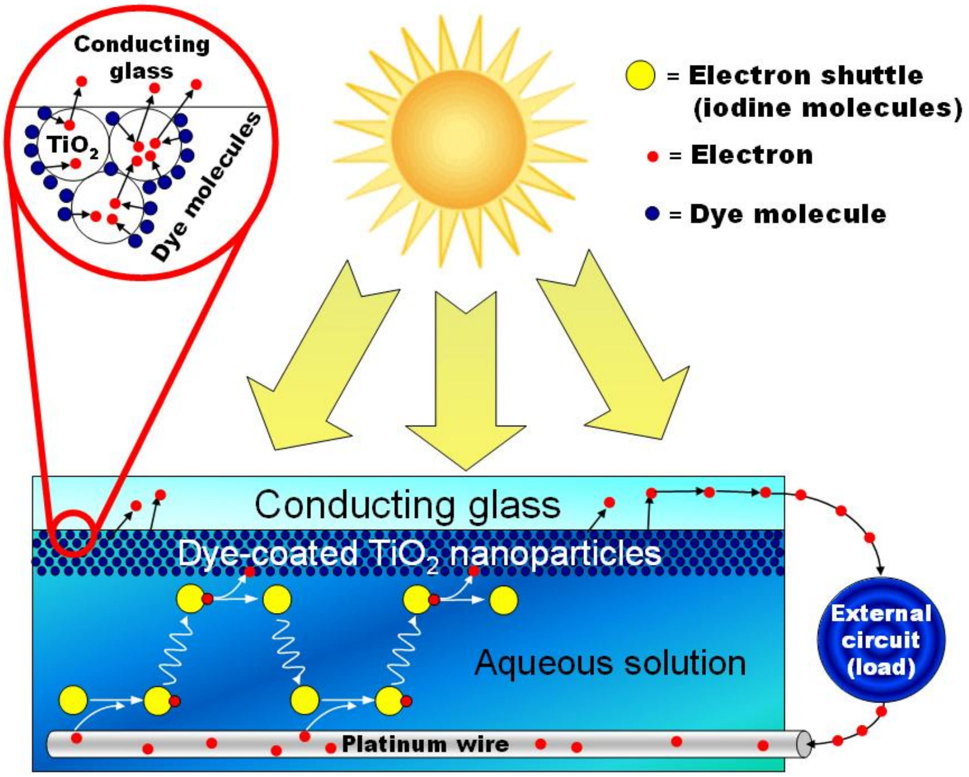

Figure 1.11: Representation of Gratzel cell.

The Gratzel cell consists of four primary components: the transparent conducting and counter conducting electrodes, the nanostructured wide bandgap semiconducting layer, dye molecules (sensitizers = S), and the electrolyte. Both the transparent conducting electrode and the counter electrode are coated with a thin, conductive, and transparent film. The TiO_2 surface is coated with dye to enhance light absorption. TiO_2 nanocrystals are used instead of a continuous layer to maximize the surface area for light absorption. The electrolyte is positioned between the electrodes.

When photons are absorbed, the dye molecules are excited from the highest occupied molecular orbital (HOMO) to the lowest unoccupied molecular orbital (LUMO) states. This excitation process is described by Equation 1.17. Upon excitation, an electron is injected into the conduction band of the wide bandgap semiconductor nanostructured TiO_2 film, causing the dye molecule (photosensitizer) to become oxidized, as represented by Equation 1.18. The injected electron is then transported between the TiO_2 nanoparticles and subsequently extracted to a load, delivering electrical energy, as shown in Equation 1.19. The electrons flow through the TiO_2 to the electrode, pass through an electric circuit, and finally reach the counter electrode. The electrolyte carries electrons back to the dye from the counter electrode. Electrolytes containing redox ions serve as electron mediators between the TiO_2 photoelectrode and the coated counter electrode. Thus, the oxidized dye molecules (photosensitizer) are regenerated by receiving electrons from the redox mediator ions, which are oxidized to tri-iodide ions. This regeneration process is depicted in Equation 1.20. For the HOMO level to effectively accept the donated electrons from the redox mediator, the energy difference between the HOMO and the redox chemical potential must be more positive . (80)

$$S + hv \rightarrow S^{*} \tag{1.17}$$

$$S^{*} \rightarrow S^{+} + e^{-} \tag{1.18}$$

$$S^{+} + e^{-} \rightarrow S \tag{1.19}$$

$$I^{-} - e^{-} \rightarrow I_3^{-} \tag{1.20}$$

Equation 1.17 shows that the excited electron is subsequently released from the excited dye and travels to the photoanode via the TiO_2 conduction band. Next, the electrolyte (I^-/I_3^-) donates an electron to the oxidised dye. An electron is gained by the oxidised electrolyte from the photocathode, and a current is created when the electron from the photoanode flows to the photocathode.

In Great Britain, the entire yearly electricity consumption is roughly 2.7 x 10^7 kW. and the total incident solar energy on a clear, sunny day is roughly 2.3 x 10^{11} kW. (81) Consequently, the demand to manufacture energy from other non-renewable sources would be greatly decreased if even a small portion of incident solar energy could be caught and transformed into a useful form. To make up for any future limitations of fossil fuels, it will be vital to create innovative, clean and efficient energy technologies.

Photosynthesis, which converts about 3% of the total solar energy incident onto the earth with an efficiency of 25 to 30% of light adsorbed, serves as an example of the potential for solar energy utilisation. It is astounding to learn that every year, photosynthetic organisms fix about 1.5 x 10^{11} tonnes of carbon, which is roughly ten times the world's current annual energy needs.

Despite, the poor effectiveness of TiO_2 systems at turning light into electrical energy, they work well in heterogeneous photocatalysis. Titanium dioxide-based wastewater remediation has the potential to drastically reduce water treatment costs in many nations that receive enough sunlight.

1.7 Doped TiO_2

Doping is the process of adding a foreign atom into a lattice structure that is either electron rich or electron deficient. The intra-band states shown in Figure 1.12 are the result of this difference in electron density. Because these states move the Fermi energy, they change the energy needed to form the charge carrier pair (e^- and h^+).

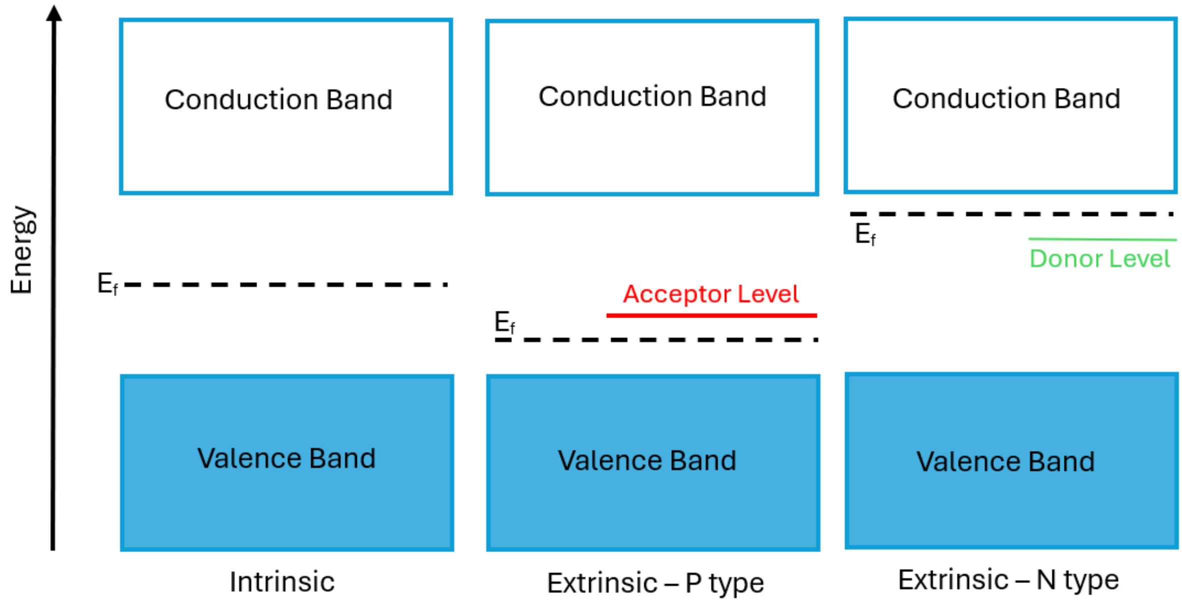

Figure 1.12: Intrinsic and extrinsic p- and n-type semiconductors demonstrating the Fermi shift.

Materials can be adjusted for their particular purposes via band gap modification, therefore, resulting in different excitation energies that would then match the energies of targeted applications. The primary function of the doping performed throughout this thesis is therefore related to its use as a photocatalyst. In addition to changing the extrinsic band gap, which can occasionally shorten the lifetime of these species by functioning as a site for both electron and hole trapping and encouraging recombination.

A brief overview of doped TiO_2 systems is provided here. Numerous studies have been conducted on doped TiO_2 systems, covering doping with transition metals, alkaline earth metals, and non-metals. (82-92)

1.7.1 Non-metal

The doping of titanium dioxide (TiO_2) with non-metals has been a topic of significant research interest, with nitrogen being the most extensively studied dopant. Since Sato's seminal 1986 report on nitrogen-doped TiO_2, researchers have focused on N-TiO_2 due to the observed reduction in the material's band gap energy. (83) This modification has been attributed to the introduction of substitutional nitrogen into the TiO_2 lattice, where nitrogen atoms occupy oxygen vacancies. This substitution causes the mixing of nitrogen and oxygen 2p states, which leads to the formation of mid-gap states and a consequent narrowing of the band gap. (82)

Some studies suggest that nitrogen atoms may instead occupy interstitial positions within the lattice. In this configuration, nitrogen forms localized 2p states just above the valence band, also contributing to the reduction in band gap energy (Figure 1.13). This interstitial doping model implies a different mechanism by which the electronic structure of TiO_2 is modified, leading to potential variations in the photocatalytic properties of the material. (84)

EPR investigations have detected two distinct nitrogen species in N-TiO_2, providing evidence for nitrogen's incorporation into the crystal lattice. (83) Through in-situ irradiation studies, these species have been identified as interstitial nitrogen (N_iO) and weakly physiosorbed molecular NO. Upon exposure to radiation, the signal for N_iO increases, indicating that an electron transitions from the diamagnetic $[N_iO]^-$ to the conduction band, creating $[N_iO]^\bullet$ radicals. This process is visually represented in Figure 1.14.

Furthermore, the concentration of these NiO radical species has been found to be dependent on the crystallite size of TiO_2. Specifically, smaller crystallites exhibit higher concentrations of N_iO radicals, highlighting the influence of nanoscale effects on the doping and properties of N-TiO_2. This size dependence suggests that the photocatalytic performance of nitrogen-doped TiO_2 can be optimized by controlling the crystallite size, making it a crucial parameter in the design and application of these materials in various environmental and energy-related technologies. (83)

Nitrogen is not the only popular non-metal doping technique, there are numerous reports for species like boron, carbon, and fluorine to mention a few, however, this work focused on replacing oxygen atoms with nitrogen.

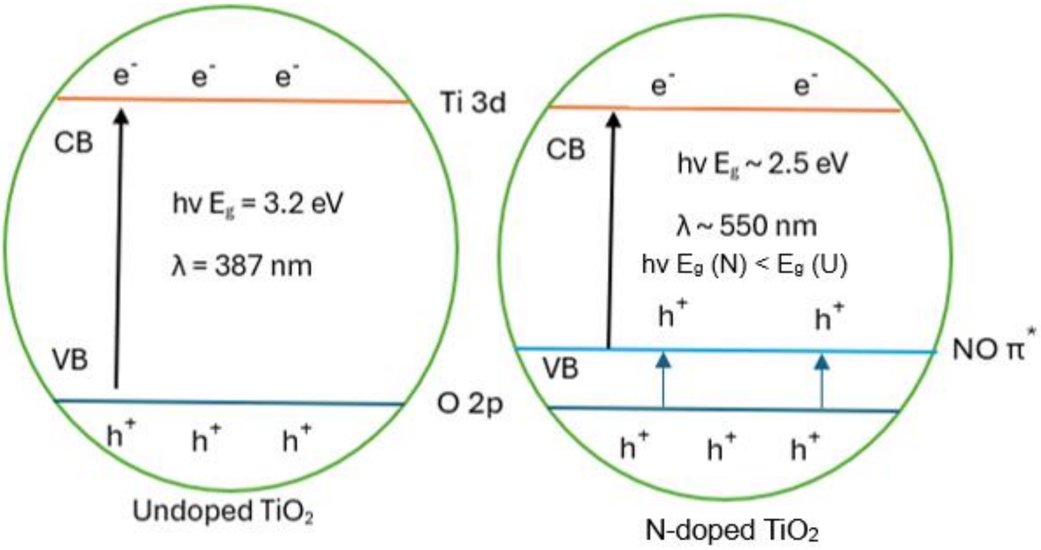

Figure 1.13: Band gap structures of undoped and doped TiO_2 displaying the intrinsic and extrinsic band gaps.

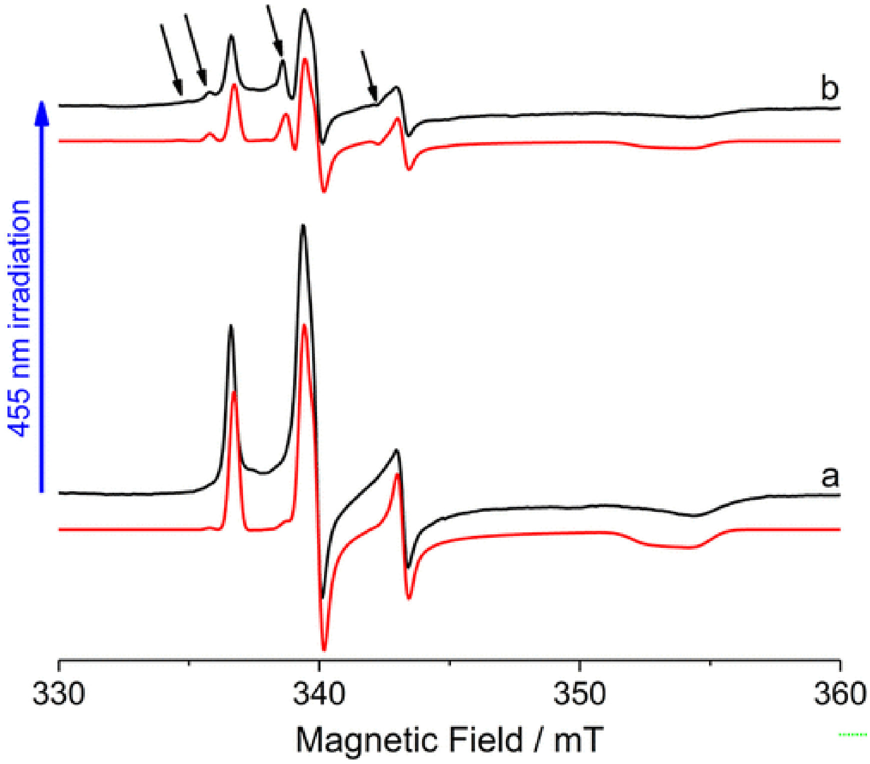

Figure 1.14. Experimental (black) and simulated (red) X-band CW EPR spectra of the $Ti_{0.909}W_{0.091}O_2N_x$ (a) dark and (b) during irradiation with a 455 nm LED light source. (83)

1.7.2 Metals

Extensive research has also been conducted on the use of metals, with particular emphasis on the platinum group metals because of their higher catalytic activity. More recently, the emphasis has switched to more environmentally friendly doping metals, such as tungsten, niobium, tantalum, etc, due to their low toxicity, recyclability and stable supply chain.

One metal that has gained interest in niobium. Niobium doping is useful for dye-sensitized solar cells and novel transparent conducting oxides (TCO). (95) The electronic effect of Nb was found to be the same as that of a fluorine doped system when a tetravalent titanium ion was replaced with a pentavalent niobium ion. Niobium doping causes the additional electron (Nb^{4+}) to localise on the Ti^{4+} once more, decreasing it and resulting in a paramagnetic Ti^{3+} that can be observed by EPR. (87) This only happens on anatase, EPR and XPS observations of the Nb^{4+} ion show that the additional electron stays localised on the dopant in Nb-TiO_2 (rutile). Nb doesn't suppress the phase transition like many other non-metals doped systems do, therefore some rutile is formed but anatase remains the dominating phase. The extrinsic band gap change was shown to be strongly correlated with the synthesis process, although overall, the band gap was found to not stray too far from the bare TiO_2. The Fermi level is located higher than it would be in the undoped sample. Studies on radiation indicated that the Nb dopant inhibits the generation of surface Ti^{3+}. (87, 95)

Tungsten is another common transition metal dopant, leading to a visible light response. The tungsten acts an electron scavenger and facilitates charge separation. When tungsten is doped into the TiO_2 lattice, it typically substitutes for titanium (Ti^{4+}) ions, resulting in the formation of tungsten in its +6 oxidation state (W^{6+}). (96) This substitution introduces localized states within the band gap of TiO_2, which can act as trapping sites for electrons. The W^{6+} ions capture photogenerated electrons, thereby reducing the electron-hole recombination rate and enhancing charge separation. The trapped electrons can then participate in photocatalytic reactions more effectively. Furthermore, the presence of tungsten in TiO_2 creates a heterojunction, where the conduction band of W^{6+} is slightly lower than that of Ti^{4+}. This band alignment facilitates the transfer of photogenerated electrons from the

TiO_2 conduction band to the tungsten ions, effectively separating the charge carriers. By acting as electron scavengers, tungsten ions help in maintaining a longer lifetime for the photogenerated holes, which can then oxidize organic pollutants or water molecules. This selective capture and stabilization of electrons by W^{6+} ions significantly reduce the probability of electron-hole recombination. Both W^{6+} and W^{4+} have been detected in the TiO_2 matrix by XPS, and XRD as both techniques demonstrated that the substitutional doping of W^{4+} caused the anatase unit cell to expand. W-TiO_2 was shown to maintain the present phase's polymorph of anatase. As W^{4+} has a similar ionic radius to Ti^{4+} the structure of the polymorph is not significantly disrupted, however small changes to the lattice parameters are observed. It has been suggested that there is an excitation of 3d electron from W^{4+} into the TiO_2 conduction band. This electron transfer then enables surfaces reactions. Tungsten improves TiO_2 catalytic activity via charge separation when there is a dispersed concentration of the dopant.

Tantalum atoms typically substitute for titanium atoms in the TiO_2 lattice due to their similar ionic radii (Ti^{4+} 0.605 Å, Ta^{5+} 0.64 Å). This substitution introduces Ta^{5+} ions into the lattice, which affects the electronic structure and introduces new energy states within the band gap. (97) The presence of Ta^{5+} ions in the TiO_2 lattice enhances charge separation by creating localized energy states that can trap photogenerated electrons. This reduces the recombination rate of electron-hole pairs and extends the lifetime of charge carriers, which is crucial for effective photocatalysis. The impact of tantalum on the photocatalytic activity of TiO_2 that has been annealed at 1373 and 1673 K in air is presented in this work. It was demonstrated that for the specimens annealed at 1373 K, the inclusion of tantalum increased the photocatalytic activity of TiO_2. On the other hand, Ta-doped TiO_2 specimens that have been annealed at 1673 K show less activity. Tantalum's impact on photocatalytic performance at 1373 K has been explained by improved charge transfer and a concentration of titanium vacancies, which serve as active surface sites. It has also been demonstrated in this work that the photocatalytic performance was not significantly affected by the band gap reduction resulting from tantalum inclusion. The lowered surface segregation of tantalum was used to explain how annealing at 1673 K affected photocatalytic activity.

1.7.3 Self-Doping

Oxygen vacancies and Ti^{3+} species are present in reduced TiO_2 (TiO_{2-x}). Where the oxygen vacancies have energy levels between 0.75 and 1.18 eV below the conduction band, they exhibit a visible light absorption for photocatalytic applications. It was hypothesised that by creating a valence band beneath the conduction band, more vacancies would cause the extrinsic band gap to shrink. (98)

1.7.4 Co-doped

Although doping modifies materials to increase their photocatalytic activity, studies have also shown that co-doping may be more advantageous. Co-doping has been used with both metals and non-metals. (83, 99, 100)

Numerous oxidation states of ions are present in these systems, the majority of which are paramagnetic (unpaired electron). Therefore, to comprehend these systems, electron paramagnetic resonance spectroscopy (EPR) will be used. Through hyperfine analysis, EPR not only makes it possible to determine whether dopants are present and in what state of oxidation, but it also makes it possible to learn about the dopants nearby surroundings. This thesis will focus on the co-doping approach with a metal (W or Ta) and a non-metal (N) and examine their effect in the materials' structure and catalytic ability.

1.8 Conclusion

The chapter on titanium dioxide presents an in-depth exploration of its structural, electronic, and surface properties, emphasizing its applications in photocatalysis. As a widely used metal oxide, TiO_2 plays a critical role in environmental purification, solar energy conversion, and hydrogen production due to its chemical stability and photocatalytic capabilities. However, one of the major challenges in harnessing TiO_2 for photocatalytic applications is its limited absorption of visible light, as its bandgap excitation occurs primarily in the UV region, which comprises only about 4% of solar irradiation.

When TiO_2 is irradiated with photons of energy greater than its bandgap, electron-hole pairs are generated, which can participate in reactions with surface adsorbates. A significant area of research focuses on the interaction between photogenerated charge carriers and surface-adsorbed oxygen, leading to the formation of various oxygen radicals. Oxygen is the most commonly used oxidizing agent in photocatalytic reactions, making the study of different oxygen radicals formed during photoirradiation particularly relevant. TiO_2 is extensively employed as a photocatalyst for the remediation of atmospheric pollution, underscoring the importance of understanding the mechanisms involved in the photodegradation of organic pollutants in the presence of TiO_2.

Throughout the chapter, several structural modifications aimed at improving the photo response of TiO_2 under visible light are discussed. Doping, both with metal elements like tungsten (W) and tantalum (Ta), and with non-metal elements such as nitrogen (N), emerges as a key strategy for optimizing the TiO_2 performance. These dopants can alter the electronic properties, introduce new states in the band gap, and promote more efficient charge carrier separation, leading to enhanced photocatalytic activity.

The chapter delves into the differences between the two polymorphs of TiO_2 (anatase and rutile) and their relative photocatalytic efficiencies. Anatase, with its lower surface energy and greater thermodynamic stability at the nanoscale, typically exhibits higher photocatalytic activity than rutile, especially for applications like volatile organic compound degradation. The relationship between surface energy and reactivity is critical, as anatase forms smaller particles, which enhances its surface-area-to-volume ratio, further improving its photocatalytic performance.

The significance of surface structure and bulk defects in TiO_2 is another key focus. Bulk defects such as oxygen vacancies and titanium interstitials can influence charge carrier dynamics, either enhancing or hindering photocatalytic efficiency. Surface reactivity, particularly in relation to crystallographic facets, is shown to be essential for optimizing TiO_2's performance. The chapter highlights how the (001) and (101) facets of anatase, as well as the (110) and (001) facets of rutile, exhibit different reactivities, affecting the migration and separation of photogenerated charge carriers.

The chapter also examines various reactions catalysed by TiO_2, such as the photo-oxidation of glycerol and the degradation of organic pollutants like toluene. These reactions serve as models for understanding the mechanisms of photocatalysis, electron-hole dynamics, and the role of surface modifications in improving efficiency.

1.9 References

(1) Z. Li, S. Wang, J. Wu, W. Zhou, *Renewable and Sustainable Energy Reviews*, 2022, **156,** 111980.

(2) R. Asahi, T. Morikawa, T. Ohwaki, K. Aoki, Y. Taga, *Science*, 2001, **293**, 269.

(3) E. J. Minay, A. R. Boccaccini, *Biomaterials, Artificial Organs and Tissue Engineering*, 2005, 15-25, Woodhead Publishing Series in Biomaterials.

(4) M. S. S. Danish, A. Bhattacharya, D. Stepanova, A. Mikhaylov, M. L. Grilli, M. Khosravy, T. Senjyu, *Metals,* 2020, **10**(12), 1604.

(5) H. Tan, *Comprehensive Structural Integrity*, 2003, 414 – 448.

(6) P. Perrot, *A to Z of Thermodynamics*, Oxford University Press, 1998.

(7) U. Diebold, *Surf Sci. Rep*., 2003, **48**, 53.

(8) H. G. Brittain, G. Barbera, J. DeVincentis, A. W. Newman, *Analytical Profiles of Drug Substances and Excipients,* 1992, **21,** 659-691.

(9) A. D. Paola, M. Bellardita, L. Palmisano, *Catalysts* 2013, **3**(1), 36-73.

(10) W. Liu, L. Lü, H. Yue, B. Liang, C. Li, *Journal of Alloys and Compounds,* 2017, **705**, 572-580.

(11) M. J. Gázquez, S. M. P. Moreno, J. P. Bolívar, *Metal Oxides,* 2021, 311-335.

(12) Z. Wang, X. Wang, H. Wang, X. Chen, W. Dai, X. Fu, *Applied Catalysis B: Environmental,* 2020, **277**, 119169.

(13) J. Zhang, Q. Xu, Z. Feng, M. Li, C. Li, *Angewadte Chemie International Edition*, 2008, **47**, 1766.

(14) P. Oruç, N. Turan, S. Cavdar, N. Tuğluoğlu, H. Koralay, *J Mater Sci: Mater Electron,* 2023, **34**, 498.

(15) B. O'Regan, M. Gratzel, *Nature*, 1991, **353**, 737.

(16) A. L. da Silva, D. Hotza, R. H. R. Castro, *Applied Surface Science*, 2017, **393**, 103-109.

(17) J. Whitehead, *Titanium Compounds* (Inorganic), Kirk Othmer : Encyclopedia of Chemical Technology, John Wiley, 1983, **23**, 131.

(18) J. Barksdale, *Titanium – Its Occurrence, Chemistry and Technology*, 2nd Editio, Roland Press Co (New York), 1966.

(19) J. Yang, Y. Zhang, Z. Hong, R. Ma, D. Zhang, X. Wang, C. Sun, Z. Hu, *Thin Solid Films,* 2012, **520**(7), 2651-2655.

(20) A. Fujishima, K. Honda, *Nature*, 1972, **238**, 37.

(21) B. O'Regan, M. Gratzel, *Nature*, 1991, **353**, 737.

(22) F. Parrino, L. Palmisano, *Titanium Dioxide (TiO2) and Its Applications*, 2020, Elsevier.

(23) M.J. Gázquez, J.P. Bolívar, R. Garcia-Tenorio, F. Vaca, *Materials Sciences and Applications,* 2014, **05**(07), 441–458.

(24) A.J. Haider, Z.N. Jameel, I.H.M. Al-Hussaini, *Energy Procedia*, 2019, **157,** 17–29.

(25) D. Ziental, B. Czarczynska-Goslinska, D.T. Mlynarczyk, A. Glowacka-Sobotta, B. Stanisz, T. Goslinski, L. Sobotta, *Nanomaterials*, 2020, **10**(2), 387.

(26) Y. Zhu, J. Shi, Z. Zhang, C. Zhang, X. Zhang, *Analytical Chemistry*, 2001, **74**(1), 120–124.

(27) P.J. Cameron, L.M. Peter, *J. Phys. Chem. B* 2003, **107,** 51, 14394–14400.

(28) M. Y. Byun, Y. E. Kim, J. H. Baek, J. Jae, M. S. Lee, *RSC Adv*, 2021, **12**(2), 860–868.

(29) M. Čaplovičová, P. Billik, Ľ. Čaplovič, V. Brezová, T. Turáni, G. Plesch, P. Fejdi, *Applied Catalysis B: Environmental* 2012, **117–118**, 224-235.

(30) G. Liu, H. G. Yang, J. Pan, Y. Q. Yang, G. Q. Lu, H. M. Cheng, *Chem Rev.* 2014, **114**(19), 9559-612.

(31) U. Diebold, N. Ruzycki, G. S. Herman, A. Selloni, *Catal. Today*, 2003, **85**, 93–100.

(32) M. Chen, J. Ma, B. Zhang, F. Wang, Y. Li, C. Zhang, H. He, *Applied Catalysis B: Environmental*, 2018, **223**, 209-215.

(33) J. Pan, G. Liu, Se*miconductors and Semimetals*, 2017, **97**, 349-391.

(34) H. Zhang, P. Sun, X. Fei, *et al.*, *Nat Commun*, 2024, **15**, 4453.

(35) X. He, F. Zhu, L. Dong, H. Guo, X. Liu, G. Ren, X. Ma, *Applied Catalysis A: General*, **664**, 119353.

(36) M. Ramamoorthy, D. Vanderbilt, R.D. King-Smith, *Phys. Rev. B*, 1994, **49**, 16721.

(37) F. Pellegrino, F. Sordello, M. Minella, C. Minero, V. Maurino, *Catalysts,* 2019, **9**, 32.

(38) B. Wei, F. Tielens, M. Calatayud, *Nanomaterials,* 2019, **9**, 1199.

(39) Z. Lai, F. Peng, H. Wang, H. Yu, S. Zhang, H. Zhao, *J. Mater. Chem. A,* 2013, **1,** 4182-4185.

(40) L. Hou, Z. Guan, T. Liu, C. He, Q. Li, J. Yang, *International Journal of Hydrogen Energy*, 2019, **44**, 8109-8120.

(41) C. Xiao, B. A. Lu, P. Xue, N. Tian, Z. Y. Zhou, X. Lin, W. F. Lin, S. G. Sun, *Joule,* 2020, **4**(12), 2562-2598.

(42) S. Kimura, M. Tsukada, *Applied Surface Science,* 1998, **130–132**, 587-592.

(43) R. G. A. Wills, F. C. Walsh, *Electrochimica* ,2010, **55,** 6342-6351.

(44) J. Chen, F. Qiu, W. Xu, S. Cao, H. Zhu, *Applied Catalysis A: General*, 2015, **495**, 131-140.

(45) H. Haerudin, S. Bertel, R. Kramer, *J. Chem. Soc. Faraday Trans.*, 1998, **94**, 1481.

(46) U. Diebold, *Mat. Res. Soc. Symp. Proc.*, 2001, **654**, AA5.1.1.

(47) E. Yagi, R.R. Hasiguti, M. Aono, *Phys. Rev. B*, 1996, **54**, 7945.

(48) H.B. Huntington, G.A. Sullivan, *Phys. Rev. Lett.*, 1965,**14**, 177.

(49) R. Schaub, E. Wahlstrom, A. Ronnau, E. Lasgsgaard, I. Stensgaard, F. Besenbacher, *Science*, 2003, **299**, 377.

(50) H. Idriss, *Chem Catalysis*, 2022, **2**(7), 1549-1560.

(51) W. Gopel, G. Rocker, R. Feierabend, *Phys. Rev. B,* 1983, **28**, 3427.

(52) J.M. Pan, B.L. Maschhoff, U. Diebold, T.E. Madey*, J. Vac. Sci and Tech.*, 1992, **10**, 2470.

(53) R.L. Kurtz, R. Stockbauer, T.E Madey, E. Roman, J.L. de Segovia, *Surf. Sci.,* 1989, **218**, 178.

(54) G. Lu, A. Linsebigler, J.T. Yates Jr., *J. Phys. Chem.*, 1994, **98**, 11733.

(55) L.Q Wang, D.R. Baer, M.H. Englehard, A.N. Shultz, *Surf. Sci*., 1995, **344**, 237.
(56) H. Norenber, J.H. Harding, *Surf. Sci*., 2001, **473**, 151. 34
(57) J. Green, E. Carter, D. M. Murphy, *Chemical Physics Letters*, 2009, **477**(4–6), 340-344.
(58) R.I. Bickley, T. Gonzalez-Cameno, J.S. Lees, L. Palmisano, R.J.D. Tilley, *J. Solid State Chem*., 1991, **92**, 178.
(59) D.C. Hurum, A.G. Agrios, K.A. Gray, T. Rajh, M.C. Thumauer, *J. Phys. Chem. B*, 2003,**107**, 4545.
(60) D.C. Hurum, A.G. Agrios, S.E. Crist, K.A. Gray, T. Rajh, M.C. Thumauer, *J. Elect. Spec. and Rel*. *Phen*, 2006,**150**, 155.
(61) S.H. Szczepankiewicz, J.A. Moss, M.R. Hoffmann, *J. Phys. Chem. B*, 2002, **106**, 2922.
(62) T. Berger, M. Sterrer, O. Diwald, E. Knozinger, D. Panayotov, T.L. Thompson, J.T. Yates Jr. *J. Phys. Chem. B,* 2005,**109**, 6061.
(63) J.M. Coronado, A. J. Maira, J. C. Conesa, K. L.Yeung, V. Augugliaro, J. Soria, *Langmuir,* 2001, **77**, 5368.
(64) A. Lewis, J. Hopkins, D. Carslaw, J. Hamilton, B. Nelson, G. Stewart, J. Dernie, N. Passant, T. Murrells, *Philosophical Transactions of the Royal Society of London. Series A, Mathematical and Physical Sciences,* 2020, **378.**
(65) Y. Nosaka, M. Kishimoto, J. Nishino, *J. Phys. Chem. B*, 1998,**102**, 10279.
(66) Y. Nosaka, K. Koenuma, K. Ushida, A. Kira, *Langmuir,*1996,**12**, 736.
(67) A.J. Maira, K.L. Yeung, J. Soria, J.M. Coronado, C. Belver, C.Y. Lee, V. Augugliaro, *App. Catal B*, 2001, **29**, 327.
(68) S.M. Tichapondwa, J.P. Newman, O. Kubheka, *Physics and Chemistry of the Earth, Parts A/B/C,* 2020, **118–119**, 102900.
(69) M.N. Abellán, R. Dillert, J. Giménez, D. Bahnemann, *Journal of Photochemistry and Photobiology A: Chemistry*, 2009, **202**(2–3), 164-171.
(70) Z. Barbieriková, D. Dvoranová, V. Brezová, *Catalysis Today*, 2018, **313**, 106-113.
(71) X. Gu, K. Zhou, Y. Li, J. Yao, *RSC Adv,* 2016, **6**, 16314.
(72) A. Fujishima, K. Honda, *Nature*, 1972, **238**, 5358, 37.
(73) H. Yaghoubi, N. Taghavinia, E. K. Alamdari, *Surface and coatings technology*, 2010, **204**, 1562.
(74) Y. R. Smith, R. S. Ray, K. Carlson, B. Sarma, M. Misra, *Materials*, 2013, **6**, 2892-2957.
(75) M.A. Fox, M.T. Dulay, *Chem. Rev*., 1993, **93**, 341.
(76) E. Borgarello, J. Kiwi, M. Gratzel, E. Pelizzetti, M. Visca, *J. Am. Chem. Soc*., 1982,**104**, 2996.
(77) A. N. Banerjee, *Nanotechnol Sci Appl*., 2011, **4,** 35-65.
(78) K. Hashimoto, H. Irie A. Fujishima, *Japanese journal of applied physics*, 2005, **44**, 8269.
(79) Y. Xing, L. E, L. Lai, D. Zhao, J. Wang, *J Mater Sci: Mater Electron,* 2021, **32**, 5156–5164.

(80) S. Y. Huang, G. Schlichthorl, A. J. Nozik, M. Gratzel, A. J. Frank, *The Journal of Physical Chemistry B*, 1997, **101**, 1576.

(81) Statista Research Department, Jun 28, 2024, accessed March 2024.

(82) H. Saito, Y. Nosaka, *The Journal of Physical Chemistry C*, 2014, **118**, 24648.

(83) A. Folli, J. Z. Bloh, K. Armstrong, E. Richards, D. M. Murphy, L. Lu, C. J. Kiely, D. J. Morgan, R. I. Smith, A. C. Mclaughlin, D. E. Macphee, *ACS Catalysis* 2018, **8**, 6927.

(84) W. Zhao, W. Ma, C. Chen, J. Zhao, Z. Shuai, *Journal of the American Chemical Society*, 2004, **126**, 4782.

(85) G. Liu, C. Han, M. Pelaez, D. Zhu, S. Liao, V. Likodimos, N. Ioannidis, *Nanotechnology*, 2012, **23**, 294003.

(86) A. M. Czoska, S. Livraghi, M. Chiesa, E. Giamello, S. Agnoli, G. Granozzi, E. Finazzi, C. D. Valentin, G. Pacchioni, *The Journal of Physical Chemistry C*, 2008, **112**, 8951.

(87) J. Biedrzycki, S. Livraghi, E. Giamello, S. Agnoli, G. Granozzi, *The Journal of Physical Chemistry C*, 2014, **118**, 8462.

(88) W. Kim, T. Tachikawa, H. Kim, N. Lakshminarasimhan, P. Murugan, H. Park, W. Choi, *Applied Catalysis B: Environmental*, 2014, **147**, 642.

(89) D. Dvoranova, V. Brezova, M. Mazur, M. A. Malati, *Applied Catalysis B: Environmental*, 2002, **37**, 91.

(90) J. Talat-Mehrabad, M. Khosravi, N. Modirshahla, M. A. Behnajady, *Desalination and Water Treatment*, 2015, 1.

(91) H. Liu, Y. Wu, J. Zhang, *ACS Applied Materials Interfaces*, 2011, **3**, 1757.

(92) C. C. Yang, Y. H. Yu, B. van der Linden, J. C. S. Wu, G. Mu, *Journal of the American Chemical Society*, 2010, **132**, 8398.

(93) S. Sato, R. Nakamura, S. Abe, *Applied Catalysis A: General*, 2005, **284**, 131.

(94) H. Irie, Y. Watanabe, K. Hashimoto, *The Journal of Physical Chemistry B*, 2003, **107**, 5483.

(95) Y. Gao, S. A. Chambers, *Materials Letters*, 1996, **26**, 217.

(96) T. Saha, J. Podder, M. R. Islam, H. N. Das, *Optical Materials*, 2022, **133**, 113065.

(97) P. Riza, K. Kavinarmatha, S. Parthiban, *Journal of Molecular Structure*, 2023, **1277**, 134869.

(98) C. Minero, G. Mariella, V. Maurinno, E. Pelizzetti, *Langmuir*, 2000, **16**, 2632.

(99) O. Diwald, T. L. Thompson, E. G. Goralski, S. D. Walck, J. T. Yates, *The Journal of Physical Chemistry B*, 2004, **108**, 52.

(100) Y. Cong, F. Chen, J. Zhang, M. Anpo, *Chemistry Letters*, 2006, **35**, 7, 800.

Chapter 2. An introduction to Solid State Chemistry

2.1 An introduction to Solid State Chemistry

Characteristic properties of solids such as the electronic conductivity, magnetic, optical, and surface properties are determined by the behaviour of the electrons situated in the solid. This demonstrates that many of the physical properties of solids are attributed to the nature of the bonding and the electron interactions within them. Thus, the study of solids and the factors that determine their structure and properties is of great interest in the scientific community. Studies that have furthered the understanding of the electronic structure of solid materials have relied on the electronic theory of valency, as it provides the basis for the advanced understanding of chemistry. Even though several theoretical approaches have been used to describe bonding in solids, the main two that have been developed are the free electron theory and the molecular orbital theory. (1) Despite the advantages that the free electron theory brings to the discussion of metals, it insufficiently portrays the conditions between the other two important classes of solid compounds, non—metals and semiconductors.

Solid state chemistry is a subject of great relevance to modern catalysis, as it forms the backbone of understanding a plethora of crucial photocatalytic reactions. Therefore, a comprehension of the diversity and complexity of structure types is central to an appreciation of solid-state chemistry. This includes the description and classification of the structures, along with a working knowledge of space groups, in addition to an evaluation of the factors that influence and control them. As TiO_2 is a vastly used catalyst, it is important to understand the electronic properties of this material to a great detail.

Understanding band theory, semiconductor nature, bonding in transition metals, surface band bending, and defects is crucial for interpret the behaviour of TiO_2, particularly in its applications in photocatalysis. In TiO_2, band theory explains the electronic structure by describing the conduction and valence bands. The band gap between these bands determines material’s ability to absorb light and participate in electron transfer processes. As explained in Chapter 1 TiO_2 has a wide band gap (~3.0 to 3.2 eV), making it suitable for photocatalytic applications under UV light, as the energy of the absorbed photons can excite electrons from the valence band to the conduction band. TiO_2 can be treated as an intrinsic semiconductor due to its pure state, but it is often doped to create extrinsic semiconductors. Doping TiO_2 with elements like nitrogen (N) introduces new energy levels within the band gap, enhancing its visible light absorption and catalytic efficiency. In p-type TiO_2, holes act as the majority carriers, while in n-type, electrons dominate. The formation of p-n junctions in TiO_2 leads to band bending at the junction. Band bending is vital for charge separation, which drives electron-hole pairs to different regions, reducing recombination and enhancing the efficiency of devices like solar cells. Defects, such as oxygen vacancies in TiO_2, play a significant role in its electrical and catalytic properties. These vacancies can create localized states within the band gap, altering conductivity and enhancing photocatalytic activity by trapping electrons or holes.

Overall, a deep understanding of these concepts is essential for optimizing the performance of TiO_2 in various advanced technological applications.

2.2 Band Theory

The high electrical conductivity of metals is due to the presence of delocalized valence electrons. These electrons are not bound to specific atoms or ions, allowing them to move freely throughout the metallic structure. In contrast, valence electrons in ionic and covalent bonds are localized to particular atoms or ions, restricting their mobility. (2) Band theory helps explain the electronic structures of metals, semiconductors, and other solids. The key differences among these materials lie in whether their valence bands are fully or partially occupied and in the size of the energy gaps between the fully occupied and empty bands.

Band theory can be described via two different approaches, the physical and chemical. (3) The physical approach extends the models first defined in the free electron theory to include quantum mechanics and Fermi-Dirac statistics, whereas in the chemical approach the concepts utilised in molecular orbital theory are applied to infinite 3-D structures. Both approaches will be discussed in detail on this chapter.

2.2.1 The Physical approach

Sommerfeld's free electron theory suggests a metal is regarded as a potential well, Figure 2.1, this could be analogous to the concept of a particle in a box used in quantum mechanics. Taking into consideration what is happening inside the potential well, the present electrons are moving freely. (4-6) Hence using the electron theory, the available energy levels the electrons may occupy can be calculated. These levels can be described through the quantized energy levels that are filled from the lowest and up, following the principle of 2 electrons per level. The corresponding energy is called the Fermi Energy (E_f). (7) A well-known physical factor that is often used during the study of solids is the Fermi level, it is the highest available level to filled at absolute zero, represents the sharp cut off boundary between occupied (below E_f) and unoccupied (above E_f) orbitals and is direct consequence of Fermi-Dirac distribution. If there are orbitals close to the Fermi level, then the uppermost electrons at those orbitals require little energy to get excited. Hence there are electrons that have a higher mobility, giving rise to the electrical conductivity. The energy of the upper most occupied orbital in a partially filled valence band corresponds to the Fermi level of a metal.

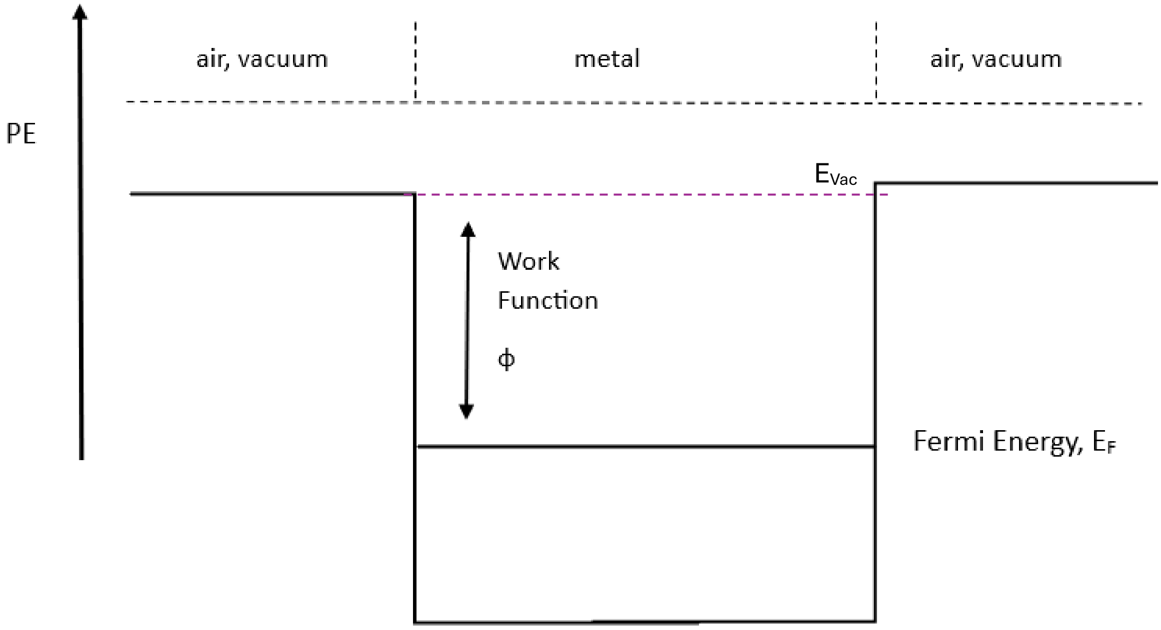

Figure 2.1: Based on the free electron theory, schematic representation of electrons in a potential well.

The drift of electrons that are in half-occupied states close to E_f cause the high electrical conductivity that characterises metals. Electrons that are in doubly occupied states at lower energies in the valence band cannot undergo any net migration in a particular direction, whereas those in singly occupied levels are free to move. Therefore, two mobile electrons rise from the promotion from a full level below E_f to an empty one above E_f. As the free electron theory is an over-simplification, recently more refined theories have been employed that study the potential within a molecule to be periodic. The potential energy of the electrons is at a minimum in zones of positive charge applied by cations within the molecule, due to coulombic attraction, and is at a maximum halfway between adjacent nuclei. (8) Due to the periodicity of potential, solved by the Schrodinger equation, an uninterrupted continuum of energy levels, described by the density of states Figure 2.2, is inaccurate.

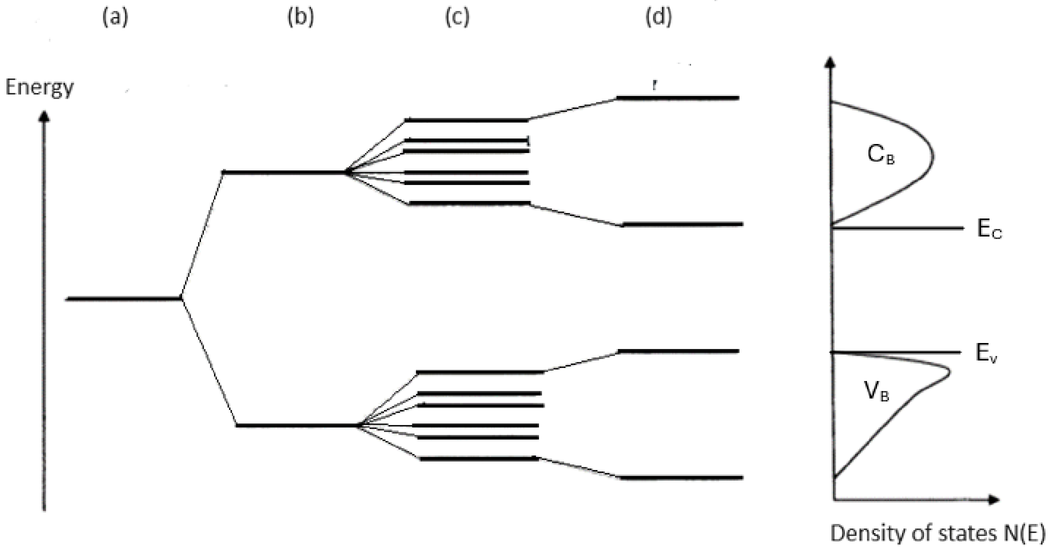

Figure 2.2: Schematic representation of orbital energies for (a) an atom, (b) a small molecule, (c) a large molecule and (d) a solid. The density of states [N(E)] corresponds to (d) a solid.

Considering semiconductors, only specific bands of energies are permitted, with the lowest and fully occupied level by valence electrons to be classified as the valence band. The next unoccupied or partially occupied level of electrons is defined as the conduction band. The limits of the upper and lower energies of these bands are indicated as E_v and E_c in Figure 2.2, respectively. The spacing between the valence and conduction bands, where there are no allowed energy levels, is termed the bandgap, and the value of this has a large effect on the chemistry of the semiconductor. (3) Similar conclusions about the existence of energy bands in solids are obtained either from both the molecular orbital and periodic potential approaches. From both theories, a similar model exists with bands of levels for the valence electrons. In some materials, overlap of different bands occurs. In others, a forbidden gap exists between energy bands.

2.2.1a Work Function

The work function, φ, is defined as the minimum energy required to remove the uppermost valence electrons from the potential well, Fermi level, from a material and locate it in a vacuum at an infinite distance away. Additionally, the work function is analogous to the ionisation potential of an isolated atom. It is important to consider the work function when studying thermionic emission, Schottky barrier formation and photoelectric emission. It is important to note that there are multiple different methods that are used to calculate the value of the work function, however, they all commonly yield different answers, even when applied to the same example.

In addition to the aforementioned, the work function is an extremely sensitive measurement of the state of a surface, with grain boundaries, defects and adsorbates all causing large changes in φ. Due to these reasons, the absolute values are often not found through literature research, instead literature is mainly focused on relative values and predominantly changes of Φ caused by surface manipulation. (9)

Within the studied solid the normal reference point for energy is the Fermi level, whereas outside of the solid the natural zero of energy is the vacuum level, E_{vac}, Figure 2.1. E_{vac} is the energy of an electron at rest, and at a significant distance from any electrical charge. The relationship between the two described energies is given by the work function (Figure 2.1) and defined from the Equation 2.1: (10-12)

$$\varphi = \mathrm{E}_{\mathrm{Vac}} - \mathrm{E}_{\mathrm{F}} \tag{2.1}$$

2.2.1b Fermi-Dirac Distribution Function

The Fermi-Dirac distribution (a version of the Boltzmann distribution) is used to calculate the population, P, of an energy level at a given temperature considering the effect of the Pauli principle, Equation 2.2: (12)

$$\mathrm{P} = \frac{1}{\mathrm{e}^{(\mathrm{E}-\mu)/\mathrm{kT}}+1} \tag{2.2}$$

where μ defines the chemical potential which is the energy of the level for P = ½, E defines the energy level and kT the Boltzmann distribution. The shape of the Fermi - Dirac distribution is presented in Figure 2.3 Recognizing that for energies much greater than the chemical potential, the Fermi-Dirac distribution simplifies to an exponential decay, is important because it provides a clearer understanding of the electron occupancy behaviour at high energies. This simplification is particularly useful in the study of semiconductors, such as TiO_2, at finite temperatures, facilitating easier and more intuitive analyses of electronic properties, thus, resulting in the Equation 2.3:

$$\mathrm{P} \sim \mathrm{e}^{-(\mathrm{E}-\ \mu)/\mathrm{kT}} \tag{2.3}$$

From the aforementioned equation the population currently resembles the Boltzmann distribution, hence decaying exponentially with the rise of energy. Therefore, the higher the temperature the longer the exponential tail will be. (13)

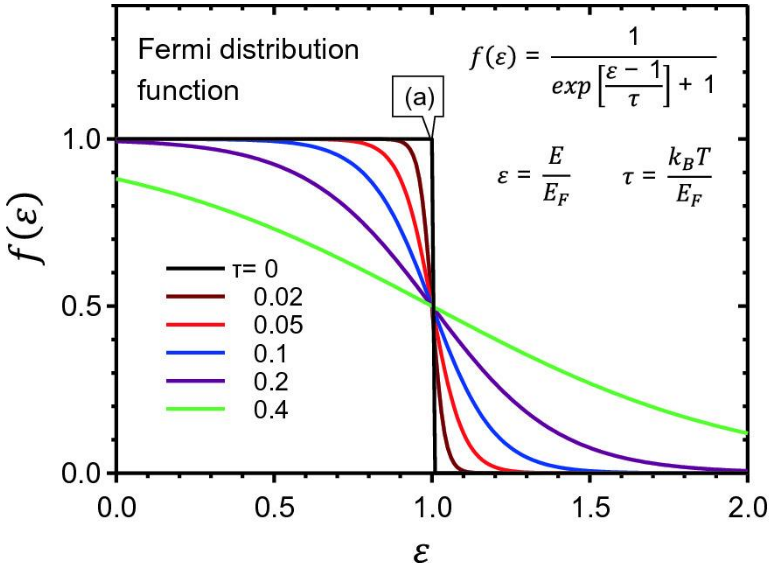

Figure 2.3: The Fermi-Dirac distribution function, which gives the population of the levels at temperature T = 0 (absolute zero) and two higher temperatures where $T_2 > T_1 > T = 0$ K. The high—energy tail decays exponentially towards zero. The curves are labelled with the value μ/kT.

Where E_F is the Fermi level, E is the energy of the energy of the level under consideration, k_B is the Boltzmann constant, and T is the temperature.

The number of electrons per energy level can be calculated by multiplying the density of states for the energy level by the probability of its occupation, described by the Fermi-Dirac distribution, thus resulting in the Equation 2.4:

$$n(E,T) = n(E)f(E,T) \tag{2.4}$$

2.2.2 The chemical approach

The chemical approach to band theory is to extend molecular orbital theory, usually applied to small finite sized molecules, toward infinite 3-D structures. The orbitals in molecules are approximated by the linear combinations of atomic orbitals approach. In a diatomic molecule, an atomic orbital from atom one overlaps with an atomic orbital on atom two resulting in the formation of two molecular orbitals, Figure 2.4, which are delocalised over both atoms. (14)

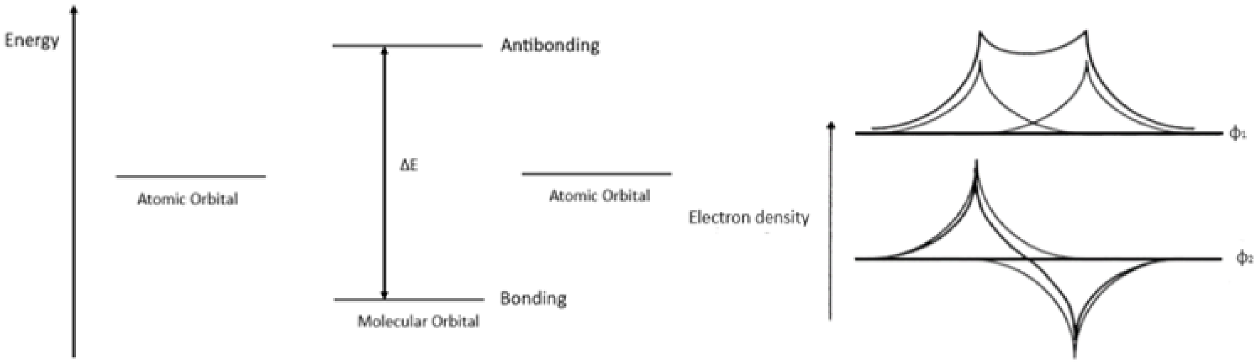

Figure 2.4: As described by the linear combinations of atomic orbitals approach this is a diagram for the formation of bonding and antibonding combinations of 2s—orbitals and their corresponding electron density distributions. (15)

The simplest example for a diatomic molecule to consider is the H_2 molecule, as it only contains two electrons that have linear combination of the 1s orbitals. One of the molecular orbitals, is identified as ‘bonding’ and has lower energy than that of the atomic orbitals, where the other, is identified as ‘antibonding’ and is of higher energy than the atomic orbitals. Therefore, specific to the H_2 example, the two possible combinations of the atomic orbitals, X_A and X_B are given by the following equation and the orbitals are delocalised over both of the H atoms, Equations 2.5 and 2.6:

$$\Phi_1 = \mathrm{X}_A + \mathrm{X}_B \tag{2.5}$$

$$\Phi_2 = \mathrm{X}_A - \mathrm{X}_B \tag{2.6}$$

The electron density for these orbitals is shown in Figure 2.4. The non—evenly distribution of the molecular orbitals over all participating energy levels is described via the density states, N(E), which defines that the N(E)δE is the number of allowed energy levels per unit volume of the solid, in the energy range E to E + δE and that N(E) is zero in the forbidden band gaps. (11) It is important to note that there are regions of energies which are void of molecular orbitals termed the bandgap; the density of states within the bandgap of the solid is zero.

It can be seen that the electron density is improved in the region between the nuclei for Φ_1, which leads to a favourable attractive potential. Therefore, Φ_1 is a bonding molecular orbital with energy lower than either of the original atomic orbitals. In contrast, the electron density is decreased in the region between the nuclei for Φ_2, hence this is an antibonding orbital with energy higher than the original atomic orbitals. The degree of overlap between the atomic orbitals determines the bonding interaction between the two orbitals. Therefore, for molecular orbitals to be effectively achieved it is required that the combined atomic orbitals are similar in energy and have the correct relative symmetry, which means that a σ type orbital will not overlap with π type orbitals. (16)

Across all constituent atoms in the molecule are extended molecular orbitals, the number of which is equal to the number of the valence atomic orbitals of the concerned atom. Henceforth, with the increase of the molecular weight, more atomic orbitals become involved, thus, the number of molecular orbitals increases and therefore, the energy between the levels reduces. As the energy spacing between the molecular orbitals in solids is small enough to be considered negligible, it is assumed that the molecular orbitals form continuous bands of energy levels. Within allowed bands the population of orbitals varies, which means that more orbitals can exist together at some energies compared to others. Additionally, some energy regions have no orbitals, corresponding to a gap between bands.

In the case of metals, they can be considered as infinitely large molecules in which a significant number of energy levels i.e. molecular orbitals, are present. The valence or outer electrons from atoms are placed in the valence band following a similar way to the one suggested by the molecular theory. Based on the filling levels of the bands the electronic arrangement effects different properties. In contrast, the lowest energy unoccupied band is located just above the valence band, this band is termed as the conduction band. (2) The energy gap is, therefore, defined as the separation between the valence and the conduction band. The size of the energy gap dictates the overall electronic properties of the metal.

2.3 TiO_2 Photocatalysis

Photocatalysis is a process in which light energy usually from the ultraviolet (UV) or visible spectrum, is used to accelerate a chemical reaction in the presence of a catalyst. In this context, a catalyst is a substance that increases the rate of a chemical reaction without itself undergoing any permanent chemical change. This catalyst, typically a semiconductor, facilitates the formation of reactive species that can drive the reaction forward, making photocatalysis a powerful tool in environmental and energy applications, such as water splitting, pollutant degradation, and CO_2 reduction. Titanium dioxide is one of the most widely studied and utilized photocatalysts due to its stability, non-toxicity, and strong oxidative power when activated by ultraviolet (UV) light.

The key to photocatalysis is the use of a photocatalyst, which is often a semiconductor material. (17) Semiconductors have a unique electronic structure characterized by a valence band (VB) filled with electrons and an empty conduction band (CB) separated by an energy gap called the bandgap (E_g). When the semiconductor absorbs photons with energy equal to or greater than its bandgap, electrons (e^-) are excited from the valence band to the conduction band, leaving behind positively charged holes (h^+) in the valence band. This process can be described by the Equation 2.7:

$$\text{Semiconductor} + h\nu \rightarrow e_{CB}^- + h_{VB}^+ \qquad (2.7)$$

Here, hv represents the energy of the absorbed photon, where h is Planck's constant and v is the frequency of the light.

The mechanism of photocatalysis with TiO_2 begins when TiO_2 absorbs photons with energy equal to or greater than its band gap, which is approximately 3.2 eV for the anatase phase and 3.0 eV for the rutile phase, corresponding to UV light. This photon absorption excites an electron from the valence band to the conduction band, creating an electron-hole pair (e^-/h^+). The electron (e^-) in the conduction band and the hole (h^+) in the valence band can migrate to the surface of the TiO_2 particle and participate in redox reactions with adsorbed species.

The holes can oxidize water or hydroxide ions (OH^-) to produce hydroxyl radicals ($^{\bullet}OH$), which are highly reactive and can decompose organic pollutants. The electrons can reduce molecular oxygen (O_2) to form superoxide anions ($O_2^{\bullet -}$), which can further participate in oxidative reactions. This dual oxidative and reductive capability makes TiO_2 a potent photocatalyst for degrading a wide range of contaminants, including organic dyes, pollutants, and even bacteria. (18)

A specific example of TiO_2 photocatalysis is the degradation of the organic dye methylene blue (MB). When TiO_2 is illuminated with UV light in the presence of methylene blue, the dye molecules adsorb onto the TiO_2 surface. The photogenerated electrons and holes in the TiO_2 then initiate a series of redox reactions leading to the breakdown of methylene blue into less harmful substances such as carbon dioxide and water. Studies have shown that anatase TiO_2 is particularly effective in this application due to its higher photocatalytic activity compared to the rutile phase. (19)

In environmental remediation, TiO_2 photocatalysis has been employed for the treatment of wastewater containing various organic pollutants. For instance, the photocatalytic oxidation of phenol, a common industrial pollutant, has been extensively studied. Under UV light, TiO_2 can efficiently degrade phenol into less toxic compounds, such as carbon dioxide and water, through the action of generated hydroxyl radicals ($^{\bullet}OH$) and superoxide anions ($O_2^{\bullet -}$). (20)

Additionally, TiO_2 photocatalysis is used in self-cleaning surfaces. For example, TiO_2 coatings on glass and building materials can decompose organic dirt and microbial contaminants when exposed to sunlight, maintaining cleanliness with minimal maintenance. The self-cleaning property is a result of the photocatalytic degradation of organic matter and the superhydrophilicity of TiO_2, which causes water to spread evenly across the surface and wash away loosened dirt. (21)

Advancements in TiO_2 photocatalysis also include modifications to enhance its activity under visible light, as undoped TiO_2 is primarily active under UV light, which constitutes only a small fraction of the solar spectrum. One approach is doping TiO_2 with non-metal elements, such as nitrogen, carbon, or sulphur, which introduces states within the band gap that allow visible light absorption. Nitrogen-doped TiO_2, for example, has shown improved photocatalytic activity under visible light for the degradation of pollutants (22), discussed in Chapter 1.

Another significant development is the use of TiO_2 in the form of nanomaterials, such as nanoparticles, nanorods, and nanotubes. These nanostructured TiO_2 materials exhibit enhanced surface area, better charge separation, and increased active sites for photocatalytic reactions. For instance, TiO_2 nanotubes have been shown to possess higher photocatalytic efficiency compared to conventional TiO_2 nanoparticles due to their unique morphology and electronic properties. (23)

Moreover, TiO_2 photocatalysis is explored in solar fuel production, such as hydrogen generation through water splitting. When TiO_2 is irradiated with light, the photogenerated electrons can reduce water to produce hydrogen gas, while the holes oxidize water to form oxygen gas. Efforts to improve the efficiency of this process include coupling TiO_2 with other semiconductors to form heterojunctions, which can enhance charge separation and extend light absorption into the visible region. (24)

In conclusion, TiO_2 photocatalysis is a versatile and powerful technology with applications ranging from environmental cleanup to energy production. The ongoing research and development of TiO_2-based materials and their modifications aim to further improve their efficiency and extend their applicability under different light conditions. The future of TiO_2 photocatalysis holds great promise for addressing various environmental and energy challenges.

2.4 Nature of Semiconductor

Considering semiconductors, the E_F will be located in the energy gap between the valence and the conduction bands. However, the exact location should be identified and assigned accurately. The movement of electrons, caused by excitation when a photon with greater energy than the target bandgap is incident, results in a positive hole. The number of the charge carriers is dependent on temperature, at 0 K a semiconducting crystal will not conduct electricity. However, in addition to the temperature, the number of charge carriers in a semiconductor can be manipulated and controlled by doping the material, thus improving the conducting properties by introducing charged impurities or defects. In the case of doping, this can also affect and control the electronic properties of the semiconductor, as it controls the concentration of both carries (electrons and holes) and the position of the Fermi level in the semiconductor. (25) The aforementioned result in two categories for semiconductors. If doping has taken place the semiconductor is known as extrinsic, while undoped semiconductors are stated as intrinsic.

2.4.1 Intrinsic Semiconductors

In its pure form a semiconductor is called intrinsic, meaning that holes and electrons are solely created by thermal excitation across the band gap. Therefore, the Fermi level is halfway between the valence and conduction bands. As the temperature is increased a finite number of electrons can now reach across the band gap to the conduction band giving rise to electrical conduction. The concentration of electrons and holes must always be equal as thermal excitation of an electron creates a corresponding hole. (7, 14) Therefore, in an intrinsic semiconductor the amount of charge carriers can be controlled either by the temperature or the magnitude of the band gap in the material. The population of the conduction band is given by the Equation 2.8:

$$P \approx e^{-(E-E_F)/kBT} \qquad (2.8)$$

2.4.2 Extrinsic Semiconductors

Elements and compounds which require adjustment to lower the band gap, can be improved by doping with impurities, thus controlling the number of charge carriers, these types of semiconductors are known as extrinsic semiconductors. The process of doping involves removing a known small quantity of the original lattice element and replacing them with another element with more or less electrons than the original atom. (25) As a result of the presence of dopant atoms the electric conductivity of the semiconductor increases and can be described by the Equation 2.9:

$$\sigma = \mathrm{n}\,\mu_{\mathrm{e}}\mathrm{e} + \mathrm{p}\,\mu_{\mathrm{h}}\mathrm{e} \qquad (2.9)$$

where n and p are the concentrations of charge carriers, and μ_e and μ_h are their mobilities. The doping element must have levels similar to those of the host. Two forms of extrinsic semiconductors may be formed in this way, p-type, and n-type semiconductors.

2.4.2.1 p-type semiconductor

In p-type materials the p indicates that the electrical conductivity results from positive holes. Once an original lattice element is replaced with an atom containing fewer valence electrons, the bonds between the original and the new elements will be electron deficient, thus creating a doped p-type semiconductor. (2, 7,10, 11, 14, 26, 27) Applied band theory can describe that discrete levels or atomic orbitals are formed just above the top of the valence band as demonstrated in Figure 2.5, and thus this level is known as the acceptor level due to its capability of accepting an electron. The Fermi Level is shifted from the halfway point between the acceptor level and the valence band. (2, 7, 26-29) Thus, mobile positive holes in the valence band and therefore electrical conductivity in the semiconductor are a result of the thermal promotion of electrons from the valence band into the acceptor level.

One way to achieve p-type conductivity in TiO_2 is by doping it with elements that introduce holes as the majority carriers. When TiO_2 is doped with nitrogen, nitrogen atoms substitute for oxygen atoms in the lattice. Nitrogen has one less valence electron compared to oxygen, creating a hole (a positive charge carrier) in the process. This can effectively convert TiO_2 into a p-type semiconductor. (30)

Nitrogen atoms replace oxygen atoms in the TiO_2 lattice (Equation 2.10), resulting in the creation of holes.

$$TiO_2 + N \rightarrow TiO_{2-x}N_x + O_x \qquad (2.10)$$

Doping with nitrogen can narrow the band gap of TiO_2, improving its visible light absorption and making it useful for photocatalytic applications, such as degradation of organic pollutants. Thus, the introduction of nitrogen creates holes, making it a p-type semiconductor. The energy level associated with the N — Ti bond does not form part of the valence band as instead forms a discrete 'acceptor' energy level just above the top of the valence band as illustrated in Figure 2.5.

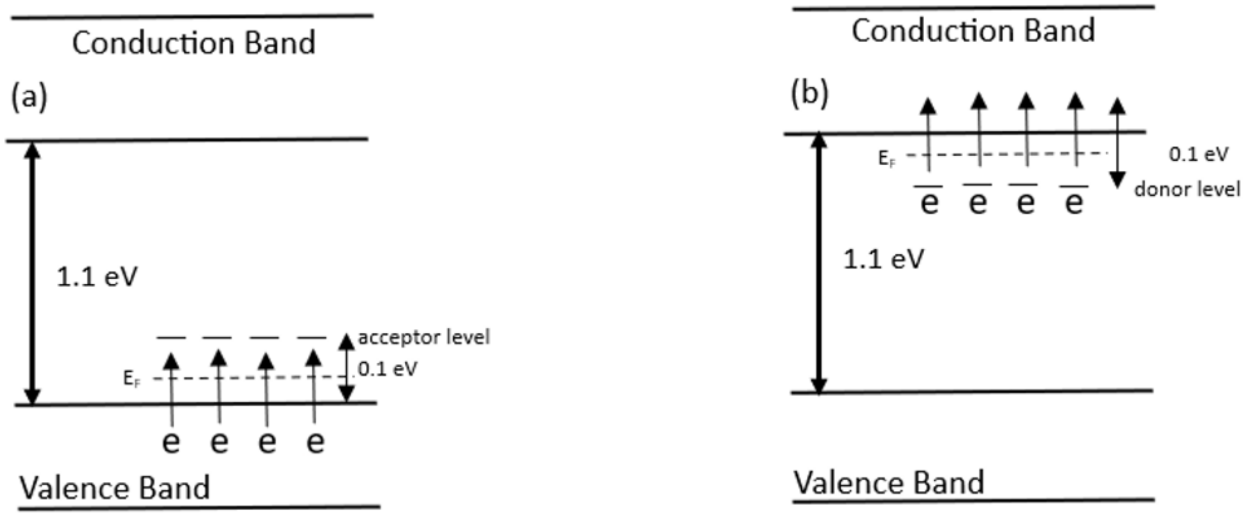

Figure 2.5: Demonstration of the donor and acceptor levels in an extrinsic semiconductor. (a) a p-type semiconductor and (b) a n-type semiconductor.

2.4.2.2 n-type semiconductor

In n-type materials the n indicates that the electrical conductivity results from negatively charged electrons. Once an original lattice element is replaced with an atom containing one extra valence electron and will have sufficient thermal energy to be elevated up in the conduction band where they can move freely, as shown in Figure 2.5. Thus, therefore electrical conductivity in the n-type semiconductor is a result of easily promoted electrons into the conduction band. (2, 7,10, 11, 14, 26, 27)

An example of an n-type semiconductor can be achieved by doping TiO_2 with elements that have more valence electrons than titanium. This doping introduces extra electrons into the material, which increases its electrical conductivity. One n-type dopant for TiO_2 is tungsten (W). When tungsten is substituted for titanium in the TiO_2 lattice, the extra electrons from tungsten contribute to n-type conductivity. In W-doped TiO_2, some of the titanium atoms in the TiO_2 crystal lattice are replaced by tungsten atoms. Titanium has a valence of +4, whereas tungsten can have a valence of +6. When W^{6+} replaces Ti^{4+} in the lattice, it donates an extra electron, creating an n-type semiconductor. (25) The additional electrons provided by the dopant atoms lie in energy levels, referred to as donor levels, situated lower from the bottom of the conduction band, as shown in Figure 2.5.

Extrinsic semiconductors have higher conductivities when compared to their analogous similar intrinsic ones at normal temperatures. Controlling the concentration of doping can accurately control the extrinsic semiconductors conductivity. Therefore, materials with desired values of conductivity may be custom designed. On the other hand, with intrinsic semiconductors, the conductivity is vastly dependent on temperature, stray impurities, and band gap size.

The thermal excitation of electrons is dominated by the Fermi-Dirac distribution function. At low temperatures the E_F represents the boundary between filled and empty levels therefore, in a non—metallic solid it must lie in the gap between the valence and conduction bands. (29) Considering that for a pure solid the density of states in the valence and conduction bands are assumed to be equal; the Fermi level is therefore placed midway in the energy gap, Equation 2.11:

$$E_F = \frac{(E_V - E_c)}{2} \qquad (2.11)$$

An n-type semiconductor has more electrons in the conduction band than holes in the valence band, while a p-type has more holes than electrons, the extra electrons or in the case of the p-type semiconductor extra holes cause a shift of the Fermi level away from its ideal mid gap position as shown in Figure 2.6.

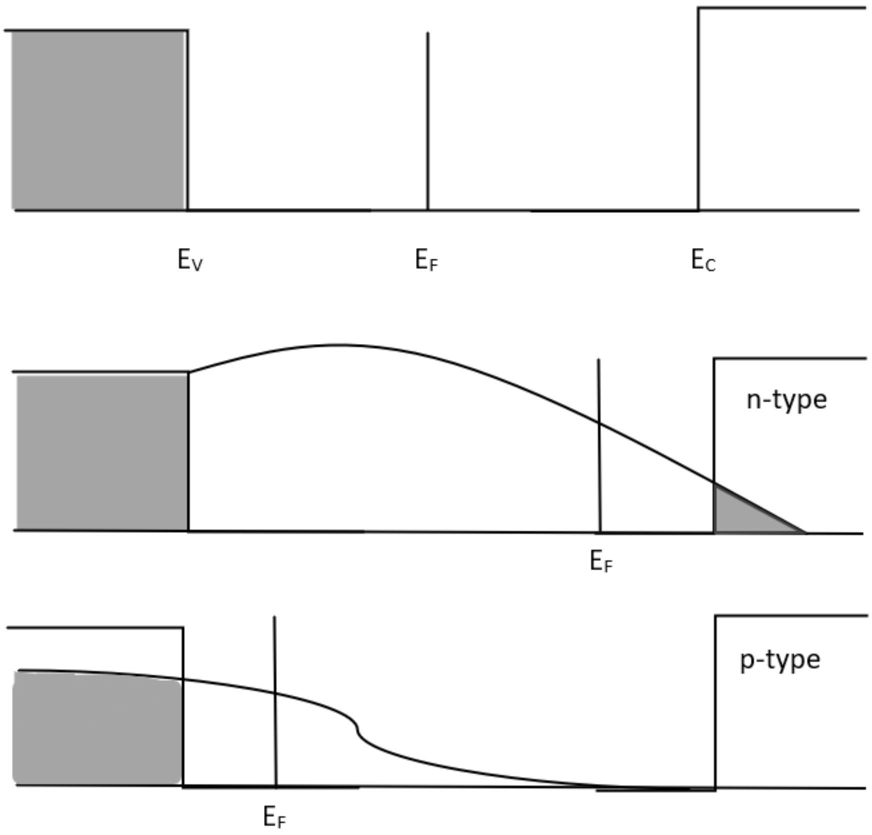

Figure 2.6: Representation of the Fermi level movement in n—type and p—type semiconductors. Shading indicates occupied energy levels.

2.4.4 p-n junction

A p-n junction is a fundamental building block of semiconductor technology, formed by joining p-type and n-type semiconductors. The p-type semiconductor, such as N-TiO_2, is rich in holes (positive charge carriers), while the n-type semiconductor, W – TiO_2, has an abundance of electrons (negative charge carriers). When these two materials are brought together, they form a depletion region at the interface where charge carriers diffuse and recombine, creating a built-in electric field. This electric field is crucial because it allows the p-n junction to rectify current, meaning it permits current to flow more easily in one direction than the other. This rectifying behaviour is the basis for many electronic devices, including diodes and transistors. (31) Thus, if the valence and conduction bands of the two regions are level the Femi level be different on each side, Figure 2.5.

Designing effective p-n junctions for photocatalysis involves selecting appropriate dopants in order to optimise the TiO_2 interface properties. The dopants chosen for the p and n sides should have appropriate band gaps that match the energy levels required for the desired photocatalytic reaction. (19) Proper band alignment is essential to ensure efficient charge separation. The conduction band of the n-type material should ideally align with the reduction potential of the reaction, while the valence band of the p-type material should align with the oxidation potential. (32) Lastly, modifying the surface properties of the p-n junction can enhance the adsorption of reactants and improve catalytic activity. This can, also, be achieved through doping, creating nanostructures, or adding co-catalysts that facilitate specific reactions. (24)

Photocatalysis refers to the acceleration of a photoreaction in the presence of a catalyst. Semiconductor materials are often used as photocatalysts because they can absorb light and generate electron-hole pairs, which can participate in chemical reactions. The p-n junction can play a significant role in enhancing photocatalytic efficiency. When light is absorbed by a semiconductor photocatalyst, electrons in the valence band are excited to the conduction band, leaving behind holes in the valence band. In a p-n junction, the built-in electric field at the depletion region can drive the separation of these photo-generated electron-hole pairs. Electrons are driven towards the n-type side, while holes are driven towards the p-type side. This efficient separation reduces the likelihood of recombination, where electrons and holes would otherwise neutralize each other without participating in any chemical reaction. (33) P-n junctions offer a powerful means of enhancing photocatalytic processes through efficient charge separation and reduced recombination of electron-hole pairs and can be used in a range of environmental photocatalytic processes, such as water splitting, CO_2 reduction and VOC degradation. For water splitting, when a p-n junction is exposed to light, the separated electrons and holes can participate in redox reactions at the surface of the semiconductor. Electrons reduce water to hydrogen gas, while holes oxidize water to oxygen gas. This process can be enhanced by the efficient charge separation provided by the p-n junction, improving the overall efficiency of hydrogen production. (24) Another significant application is the photocatalytic reduction of carbon dioxide (CO_2) to valuable hydrocarbons. P-n junctions can facilitate the separation of charge carriers, allowing electrons to reduce CO_2 while holes oxidize a sacrificial agent. This process mimics photosynthesis and has the potential to convert greenhouse gases into useful fuels, contributing to sustainable energy solutions. (34) Photocatalytic degradation of pollutants can be significantly improved using p-n junctions and will be a focus in this work. For example, titanium dioxide (TiO_2) is a well-known photocatalyst, but its efficiency can be limited by rapid recombination of electron-hole pairs. Creating a p-n junction with TiO_2 can help in the effective separation of charges, thus enhancing its photocatalytic activity. This method can be employed to degrade organic pollutants, dyes, and even bacteria in wastewater treatment processes. (32)

2.4.5 Band bending

Band bending is a fundamental concept in semiconductors that describes the variation of the energy levels (bands) near the surface or interface of a semiconductor material. This phenomenon is crucial for understanding the behaviour of semiconductors in various applications, including photocatalysis. Titanium dioxide (TiO_2) is a widely studied photocatalyst, and its effectiveness can be significantly influenced by band bending. In an ideal, infinite semiconductor crystal, the conduction band and valence band are flat, indicating uniform energy levels throughout the material. However, at surfaces, interfaces, or in the presence of external fields, these energy levels can bend. Band bending occurs due to the redistribution of charge carriers (electrons and holes) near the surface or interface, leading to the formation of an electric field within the semiconductor, Figure 2.7. (35)

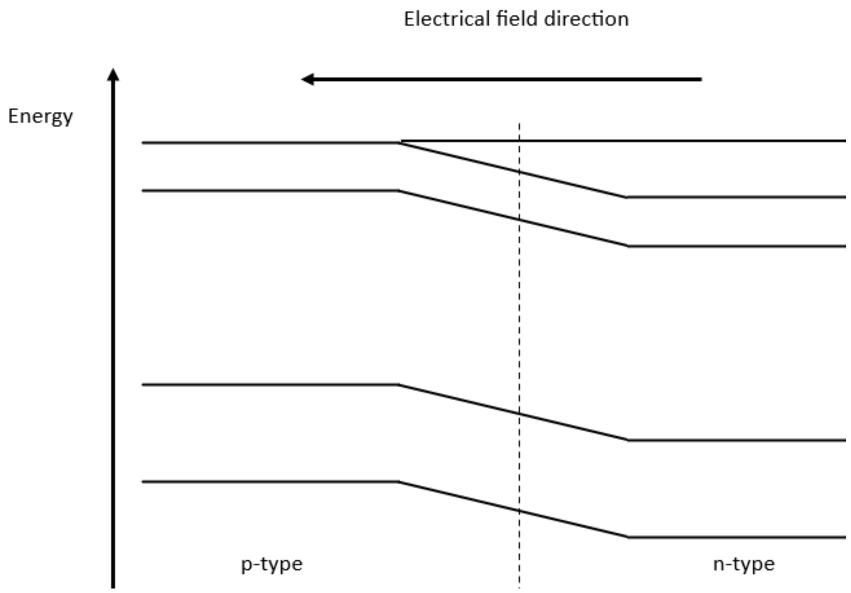

Figure 2.7: Band bending in a p—n junction.

Titanium dioxide is a prominent photocatalyst used in applications such as water splitting, pollutant degradation, and hydrogen production. The efficiency of TiO_2 in these applications is closely tied to its electronic properties, particularly the behaviour of charge carriers. Band bending plays a critical role in enhancing the photocatalytic performance of TiO_2. (36) One of the primary challenges in photocatalysis is the recombination of photogenerated electron-hole pairs. Band bending can enhance charge separation by creating an internal electric field that drives electrons and holes in opposite directions. For instance, at the surface of TiO_2, band bending can promote the migration of electrons to the surface while pushing holes into the bulk, reducing the likelihood of recombination. Depositing noble metals (such as Pt, Au, or Ag) on the surface of TiO_2 can form Schottky barriers. The metal acts as an electron sink, capturing photogenerated electrons and preventing their recombination with holes. This process increases the lifetime of charge carriers and enhances the photocatalytic activity. The band bending at the TiO_2-metal interface is crucial for this charge separation mechanism. Forming p-n junctions by coupling TiO_2 with p-type semiconductors (such as N- TiO_2) can create built-in electric fields that facilitate charge separation. Similarly, heterojunctions with other n-type semiconductors (W- TiO_2) can also induce band bending that enhances charge carrier dynamics. These junctions can be engineered to optimize the band alignment and maximize the photocatalytic efficiency. Modifying the surface of TiO_2 with dopants can introduce surface states that influence band bending. For example, doping TiO_2 with elements like nitrogen or carbon can create mid-gap states that alter the band structure and enhance visible light absorption. The resultant band bending can improve charge separation and increase photocatalytic activity under visible light. Applying an external electric field to TiO_2 can also enhance photocatalysis by inducing band bending. This approach can be used to control the direction of charge carrier migration, further reducing recombination rates and improving efficiency. (37)

In the context of TiO_2 photocatalysis, band bending enhances charge separation, reduces recombination, and improves overall photocatalytic efficiency. Applications of band bending in TiO_2 photocatalysis can demonstrate the importance of understanding the changes that occur during this process. Band bending can improve the separation of photogenerated electrons and holes, enhancing the efficiency of the water-splitting process. Schottky barriers formed with metal co-catalysts can further aid in capturing electrons and reducing recombination, leading to higher hydrogen production rates. TiO_2 is used for the degradation of organic pollutants in water and air. Effective charge separation due to band bending increases the generation of reactive species (such as hydroxyl radicals) that attack and break down pollutants. Surface modifications that induce favourable band bending can significantly enhance the degradation rates of various contaminants. TiO_2-based photocatalysts are also employed in solar energy conversion applications. The enhanced charge separation due to band bending improves the efficiency of converting solar energy into chemical energy, such as in dye-sensitized solar cells (DSSCs). Optimizing band bending through surface engineering and junction formation is important for maximizing solar energy conversion efficiency. (38)

2.5 TiO_2: Bonding in transition metals

In general, most inorganic materials are more structurally complex than metals and semiconducting elements. Taking into consideration band theory, it can provide an additional insight into the structures, bonding and properties of inorganic solids. Inorganic materials have also received less theoretical attention of the type involving band structure calculations. Consequently, their band structures are often known only by approximation.

In transition metal compounds the bonding is best described as a mixture between ionic and covalent bonding. Thus, an interesting and varied range of electronic behaviour is observed as a result of the partially filled d bands of the transition metals. The basic energy level diagram for a transition metal oxide has a valence band of O 2p character and a conduction band of metal character. For the pre-transition elements the conduction band is usually constructed from s or p orbitals, in the case of TiO_2 the orbitals comprising the conduction band are d orbitals. The d—orbitals of the transition metal ions have five-fold degeneracy in the free ions. Due to these different directional properties of the five orbitals produce different bonding interactions with nearby atoms. This is known as crystal-field or ligand-field splitting and is important in all transition metal oxides. With reference to the molecular orbital approach, the valence band is referred to as the bonding combination of oxygen and metal orbitals, and the conduction band as the antibonding combination. However, the characterisation of oxygen 2p valence band and metal d is more useful as it gives a clearer indication of the atomic orbital constituents. (39)

Octahedral is the most common coordination geometry for transition metal ions in oxides. The orbitals on the transition metal split into two groups according to their symmetry properties. The doubly degenerate e_g orbitals have lobes of maximum density pointing towards the ligand and three t_{2g} orbitals pointing away, demonstrated in Figure 2.8.

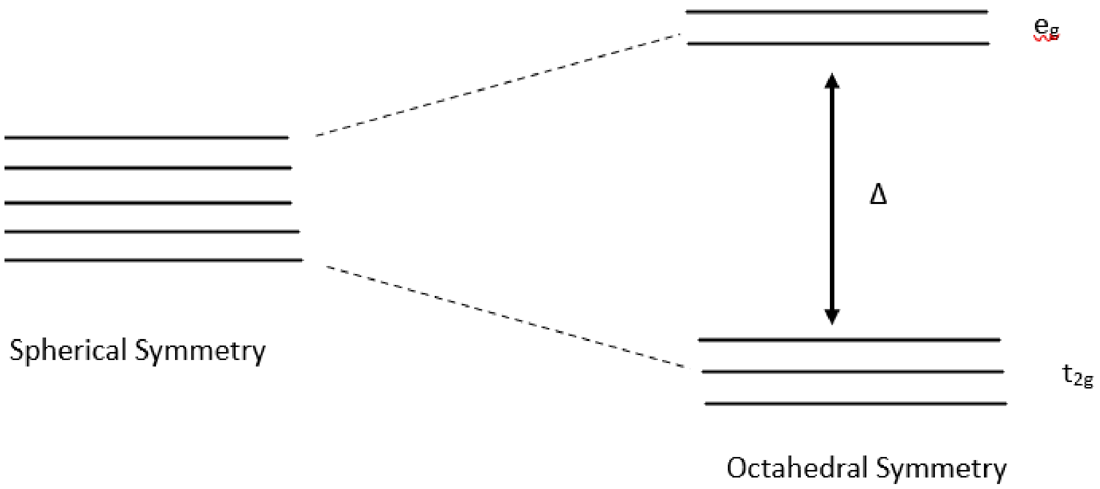

Figure 2.8: Transition metal ion d orbitals in an octahedral site result in orbitals with crystal field splitting.

In insulators the conduction band is empty, whereas for the early transition metals with a d^n configuration above d° the conduction band will be occupied. Stoichiometric d^0 oxides are, therefore, good insulators and have no excitations at energies less than the band gap. Considering TiO_2 for example, the Ti^{4+} cations have d° configuration and therefore there is no electrical conduction. This compound has a filled valence band of predominately O 2p character and a gap between this and the conduction band as shown in Figure 2.9. This studied gap of around 3.1 eV suggests an appreciable covalent mixing between the atomic orbitals and metal orbitals. Thus, the metal d conduction band acts as an antibonding combination. The description in terms of oxygen and a metal is informative, as it indicates the principal atomic orbital constituents of each level.

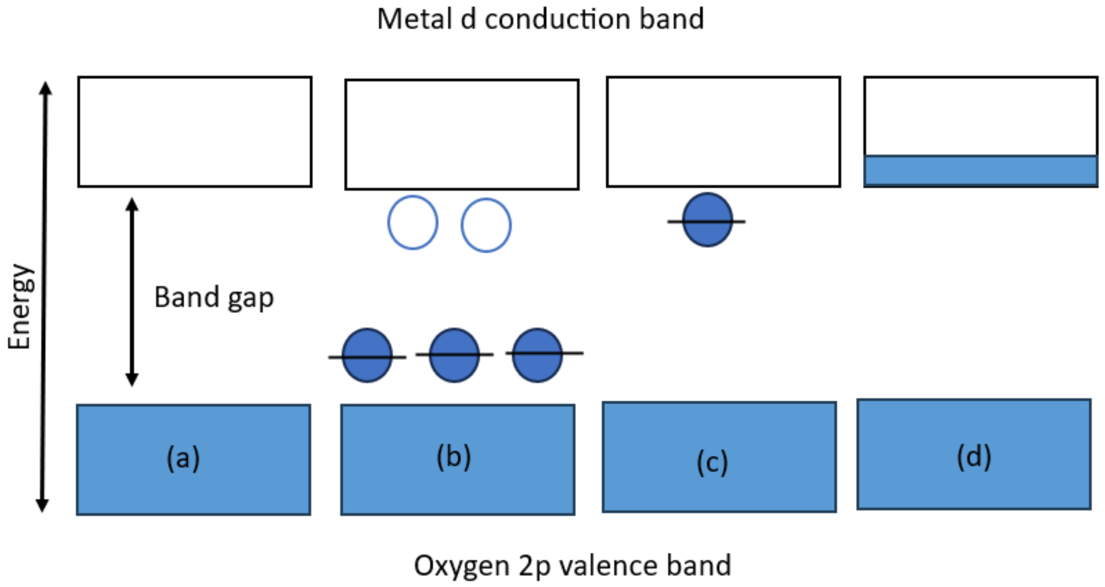

Figure 2.9: Qualitative electron energy—level diagrams for transition metal oxides. (a) bands of a d^0 compound with a gap between the oxygen 2p valence band and the empty metal d^0 conduction band; (b) the localised d levels appropriate to a transition metal impurity and to a magnetic insulator; (c) a donor level associated with a non—stoichiometric oxide and (d) the partially filled conduction band of a metallic oxide.

However, if the compound is reduced to form Ti^{3+} cations, with a d^1 configuration, there is a partial occupancy of the conduction band, and thus, the compound exhibits electrical conduction. As shown in Figure 2.9 where the gap between the occupied valence band and the unoccupied conduction band is designated as the bandgap, specifically for TiO_2 the bandgap is approximately 3 eV. This is identified as a small bandgap and is indicative of a significant covalent mixing between the oxygen and titanium atomic orbitals.

As a result of the interaction of the metal orbitals with the surrounding ligand orbitals, the d orbitals of a transition metal oxide are split in energy. The d orbitals which point directly towards the ligands (forming σ combinations) have a larger degree of overlap than orbitals pointing between the ligands (that form π combination), and therefore have a greater contribution to the ligand field splitting. The order of the d orbitals energy level is dependent on the geometry of the ligands surrounding the transition metal atom; considering that the geometry of TiO_2 around the Ti^{4+} cation is octahedral, the corresponding ligand field splitting is shown in Figure 2.8.

2.5.1 Surface band bending

Surface band bending refers to the variation in energy levels (conduction and valence bands) at the surface of a semiconductor compared to its bulk. This bending is caused by the redistribution of charge carriers (electrons and holes) due to surface states, adsorbed species, or external influences such as electric fields. The result is the formation of an electric field within the surface region of the semiconductor, which significantly affects its electronic and optical properties. Mechanisms leading to surface band bending include surface states, charge transfer, work function differences and doping (discussed in Chapter 1). Surface states are energy levels introduced within the bandgap by surface imperfections, defects, or adsorbed molecules. Adsorption of molecules such as oxygen or water on TiO_2 can introduce surface states that trap charge carriers, leading to band bending. For example, oxygen adsorption can create an upward band bending by capturing electrons, forming a surface depletion layer. Associated with this accumulation layer is a downward bending of the bands, as shown in Figure 2.10. They can trap charge carriers, creating an electric field that leads to band bending. Charge transfer occurs when the semiconductor surface interacts with other materials and results in a redistribution of charge carriers and causing band bending. Contact with materials having different work functions can lead to charge transfer, creating an electric field and band bending at the interface. Lastly, variations in doping concentration near the surface can also induce band bending as the Fermi level adjusts to the local charge carrier density. Specifically, the surface band bending of TiO_2 plays a crucial role in its photocatalytic efficiency by influencing charge carrier dynamics. (40) Doping TiO_2 with elements like nitrogen can create surface states and induce band bending. Nitrogen-doped TiO_2 shows enhanced visible light absorption and photocatalytic activity due to the introduction of mid-gap states and favourable band bending.

Additionally, n-type behaviour in an oxide is a result of slight reduction, which leaves extra electrons in the solid. Examples of this behaviour is found in compounds such as ZnO, SnO2 and TiO_2. In the ground state the electrons are trapped by the lattice defect, however, the electrons become more mobile in the conduction band at higher temperatures. Reduction can be accompanied by formation of interstitial metal atoms, or by oxygen vacancies. An interstitial cation in the lattice will give a positive potential that has the ability to trap an electron in a bound orbital just below the conduction band edge. (41) The unbalanced positive charge at an oxide vacancy also forms a trap. In the case of TiO_2, an n-type semiconductor, when there are surface states located in the bandgap there is transfer of electrons from the donor levels of the surface region in the surface states. Thus, resulting in a depletion layer where an electrostatic field is formed from the unbalanced positive charge of the ionised donors, causing the shift of the band energies, as shown in Figure 2.10.

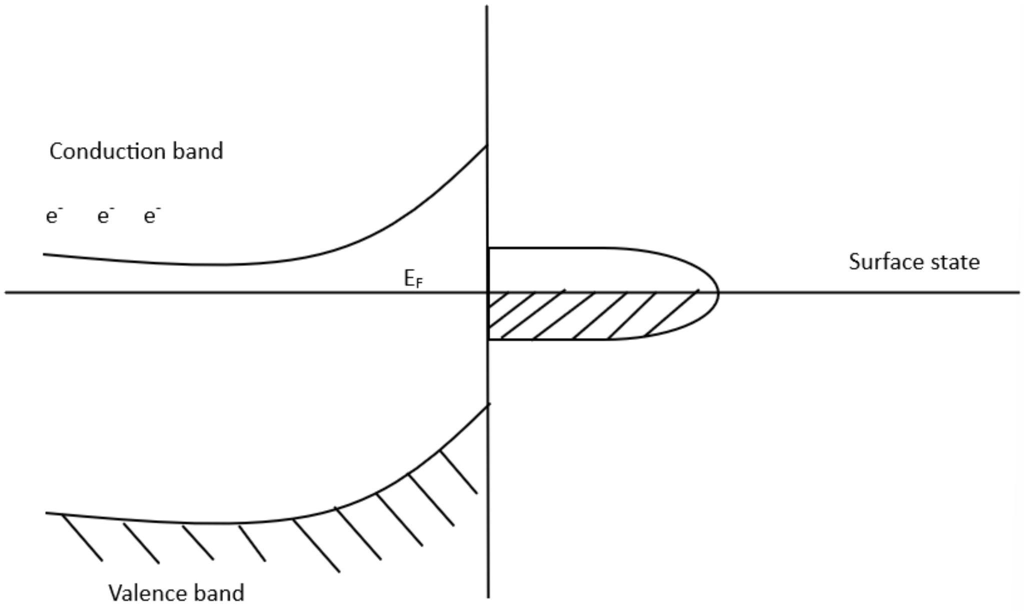

Figure 2.10: Band bending due to a surface state on a n—type semiconductor such as TiO_2.

2.5.2 Defects

Defects in TiO_2 are essential for tailoring its properties to suit specific applications, such as photocatalysis. By controlling the type, concentration, and distribution of defects, TiO_2 can be optimized for enhanced performance in photocatalysis, energy conversion, sensors, and other advanced technologies. Understanding and manipulating defects is a key aspect of materials science that enables the development of more efficient and effective TiO_2 - based materials.

The chances of the crystal structure of a material to be completely perfect are slim, as commonly they will contain a form of imperfection or defects. Specifically, for metal oxide chemistry, defects play an important role as they are the cause leading to variations in the electronic structure of the solid, hence, affecting the electrical and mechanical properties of overall system. (42) The presence of defects in a sample produces an increase in the overall entropy of the system, therefore, it is dictated by thermodynamics, that all crystals must contain a certain number of defects at non—zero temperatures and, in accordance with the Boltzmann distribution, the number of defects increases with temperature. In order to calculate the energy, given by E_V, required to create a defect in a crystal containing N atoms the equilibrium number of vacancies at a temperature T can be calculated from Equation 2.12:

$$N = Ne^{(-\frac{E_V}{kT})} \tag{2.12}$$

The surface of a solid is inheritably a break in the periodicity of the structure and thus, the origin of large changes in electronic structure. The number of electrons or holes occupying defect sites, along with the energy levels associated with these defects, are key factors in the formation of defects and the resulting changes to the electronic structure of the solid. The rise of electronic levels within the bandgap of the solid close to the edges of the valence and conduction bands themselves is produced due to the defects, hence their presence signifies their pivotal role. The electronic properties associated with defects depend upon both the energy levels relative to the band edges of the ideal crystal in addition to the number of electrons occupying the defect levels. Defects that the energy required to excite the charge carriers into the corresponding band is low often result in an increase in electrical conductivity. An interesting contribution may arise from the unoccupied energy levels, as they could also be introduced in the bandgap region from the defects possibly acting as trapping centres for charge carriers. (43)

There are two significant factors that complicate the study of defects. The first is the presence of defects that results in imbalances in charge over the total entity of the solid, in order to compensate for these other defects must be present. The second factor takes into consideration the structural relaxations and rearrangements which accompany the formation of any defect.

2.5.2.1 Vacancies as point defects

A vacancy, or Schottky defect, is the simplest type of defect in a crystal lattice, where an atom is missing from its site in the lattice. In the approximate space of the defect there will be some atomic rearrangement or reconstruction to account for the vacancy, Figure 2.11. However, a solid must maintain charge balance thus, defects occur in pairs; for example, following the stoichiometry of a solid, there are an equal number of cation and anion vacancies present. The presence of vacancies allows the diffusion of atoms through the lattice of the crystal, as the energy required for an atom to move into an adjacent vacancy site, i.e. leaving its own site vacant, is very small. (44) Therefore, the overall diffusion of atoms follows one direction, while vacancy creation in follows the opposite direction.

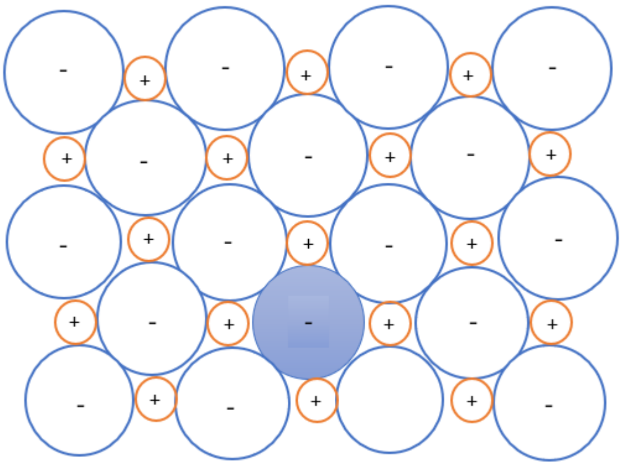

Figure 2.11: A lattice vacancy.

The electrons and holes generated at these vacancies can be responsible for changing the oxidation state of the metal in the lattice, thinking about TiO_2, where electrons positioned at an oxygen vacancy reduce the Ti^{4+} metal ions to Ti^{3+}. The degree of defect formation can often be associated to the ease of reduction or oxidation of the transition metal. (45) The loss of an oxygen anion from the surface of a crystal lattice results in a decrease in the coordination number of the neighbouring cations. For example, TiO_2 possible sites for an oxygen vacancy, either a bridging oxygen ion or one from the main plane of the surface. Considering the loss of a bridging oxygen, two 6—fold coordinated Ti^{4+} cations are reduced to 5—fold coordinated; whereas in the latter case, two 5—fold coordinated cations become 4—

fold. As it is commonly known, this reduction in coordination number is accompanied by an increase in chemical reactivity. (46)

2.6 Conclusion

The importance of solid-state chemistry with regards to synthesis, structure, properties, and applications has been highlighted through this chapter, with a particular reference to TiO_2. Of a great importance is the study of the electronic structure of the solids. The electrical conductivity of a material is characterised by the number of free charge carriers available to allow passage of electric current. As showed the electronic structure of metals, semiconductors and other solids can be described in terms of band theory. In a conductor there is a high number of free electrons, since conduction electrons are delocalised in the valence band. When a material has close to zero free conduction electrons, it is characterised as an insulator. Semiconductors are identified as the materials with charge numbers and are in—between conductors and insulators, these materials allow electric current to pass. Semiconductors are split into two groups, pure form semiconductors, whose conductivity is controlled by the magnitude of the band gap and semiconductors whose conductivity is controlled by the addition of dopants, also known as intrinsic and extrinsic, respectively. From the latter semiconductors, two types could be form, n- and p-type, depending on the nature of the dopant. These semiconductors can be utilised in a vast range of devices such as transitions, silicon chips, photocells, etc. Additionally, as discussed through the chapter, lot of these solid-state devices also use extrinsic semiconductors in the form of p-n junctions. The main focus of this thesis is on metal oxides, therefore on insulators and semiconductors. The electrical conductivity of metal oxides depends on a variety of factors including identity of the metal and the crystal system. TiO_2 with the d^0 configuration may be classed as a borderline insulator but can be readily reduced or doped to become a semiconductor.

2.7 References

(1) J. M. Galbraith, S. Shaik, D. Danovich, B. Braïda, W. Wu, P. Hiberty, D. L. Cooper, P. B. Karadakov, T. H. Dunning Jr., *J. Chem. Educ.*, 2021, **98**, 12, 3617–3620.

(2) P. A. Cox, *The Electronic Structure and Chemistry of Solids*, 1987, Oxford Science Publications.

(3) K.W. Böer, U.W. Pohl, *The Origin of Band Structure. In: Semiconductor Physics*, 2022, Springer

(4) A. Sommerfield, Z. *Physik*, 1928, **47**, 1.

(5) J. P. McKelvey, *Solid state and semiconductor Physics*, Ed R. E. Krieger, 1966, New York, NY: Harper Row.

(6) T. Jeon, Z. Jiangquan, D. Grischkowsky, *Applied Physics Letters*, 2005, **86**, 16904.

(7) A R. West, *Solid Chemistry and its Applications*, 1994, Wiley.

(8) T. Jahnke, U. Hergenhahn, B. Winter, R. Dörner, U. Frühling, P. V. Demekhin, K. Gokhberg, L. S. Cederbaum, A. Ehresmann, A. Knie, A. Dreuw, *Chem. Rev.* 2020, **120** (20), 11295–11369.

(9) K. Takeuchi, A. Suda, S. Ushioda, *Surface Science,* 2001, **489**, (1–3), 100-106.

(10) S. Dunn, *Reactions and Characteristics of Solids*, 2000, The Royal Society of Chemistry ISBN : 978 – 0 – 85404 – 612 – 6 .

(11) P. Atkins, J. de Paula, *Physical Chemistry*, 2009, 9th Edition, Wiley.

(12) J. R. Hook, H. E. Hall, *Solid State Physics*, 1991, 2nd Edition, Wiley.

(13) S. C. Kim, A. S. Arun, M. E. Ahsen, R. Vogel, G. Stolovitzky, *Proc Natl Acad Sci*, 2021, **118**(34).

(14) A.R. West, *Basic Solid State Chemistry*, 1999, Wiley, Sussex.

(15) R. F. Nalewajski, D. Szczepanik, J. Mrozek, *Advances in Quantum Chemistry*, 2011, **61,** 1-48.

(16) J. Autschbach, *J. Chem. Educ,* 2012, **89** (8), 1032–1040

(17) M. A. Hassaan, M. A. El-Nemr, M. R. Elkatory, S. Ragab, V. C. Niculescu, A. E. Nemr, *Top Curr Chem*, 2023, **381**(6), 31.

(18) X. Zhao, G. Zhang, Z. Zhang, *Environment International*, 2020, **136**, 105453.

(19) X. Chen, , S. S. Mao, *Chemical Reviews*, 2007, **107**(7), 2891-2959

(20) Hoffmann et al., 1995 M. R. Hoffmann, S. T. Martin, W. Choi, D. W. Bahnemann, *Chemical Reviews*, 1995, **95**(1), 69-96.

(21) A. Fujishima, T. N. Rao, D. A. Tryk, *Journal of Photochemistry and Photobiology C: Photochemistry Reviews*, 2008, **1**(1), 1-21.

(22) R. Asahi, T. Morikawa, T. Ohwaki, K. Aoki, Y. Taga, *Science*, 2001, **93**(5528), 269-271.

(23) M. Zhou, J. Yu, B. Cheng, *Journal of Hazardous Materials*, 2007, **137**(3), 1838-1847.

(24) A., Kudo, Y. Miseki, *Chemical Society Reviews*, 2009, **38**(1), 253-278.

(25) A. Folli, J. Z. Bloh, E. P. Beukes, R. F. Howe, D. E. Macphee, *J. Phys. Chem. C,* 2013, **117** (42), 22149–22155.

(26) E. M. McCash, *Surface Chemistry*, 2001, Oxford University Press ISBN: 9780198503286.

(27) L. Smart, E. Moore, *Solid State Chemistry*, An introduction, 2nd Edition, 1996, Chapman and Hall.

(28) S. Dunn, *Reactions and Characterisation of Solids*, RSC*,* 2000.

(29) P. Atkins, J. de Paula, *Physical Chemistry*, 7th Edition, Oxford, 2002.
(30) A. Panepinto, A. Krumpmann, D. Cornil, J. Cornil, R. Snyders, *Applied Surface Science*, 2021, **563**, 150274
(31) Streetman & Banerjee, 2006 *Devices,* 2006, Pearson Prentice Hall.
(32) W. J. Ong, L. L. Tan, Y. H. Ng, S. T. Yong, S. P. Chai, *Chemical Reviews*, 2016, **116**(12), 7159-7329.
(33) J. Yu, J. Low, W. Xiao, P. Zhou, M. Jaroniec, *Journal of the American Chemical Society*, 2013, **136**(25), 8839-8842.
(34) T. Inoue, A. Fujishima, S. Konishi, K. Honda, *Nature*, 1979, **277**(5698), 637-638.
(35) P. C. J. Clark, N. K. Lewis, J. C. R. Ke, R. Ahumada-Lazo, Q. Chen, D. C. J. Neo, E. A. Gaulding, G. F. Pach, I. Pis, M. G. Silly, W. R. Flavell, *Nanoscale,* 2021, 005436.
(36) M. Sakar, R. M. Prakash, T. O. Do, *Catalysts,* 2019, **9**(8), 680
(37) T. Lv, J. Li, N. Arif, L. Qi, J. Lu, Z. Ye, Y. J. Zeng, *Matter,* 2022, **5**(9), 2685-2721.
(38) Md. H. Miah, M. U. Khandaker, Md. B. Rahmanb, M. Nur-E-Alam, M. A. Islam, *RSC Adv.*, 2024, **14**, 15876-15906.
(39) H. Wang, T. Zhai, Y. Wu, T. Zhou, B. Zhou, C. Shang, Z. Guo, *Advanced Science*, 2023, **10**(22), 2301706.
(40) S. Ma, M. E. Reish, Z. Zhang, I. Harrison, J. T. Yates Jr, *J. Phys. Chem. C,* 2017, **121** (2), 1263–1271.
(41) K. Maeda, *Journal of Photochemistry and Photobiology C: Photochemistry Reviews,* 2011, **12**, 237-268.
(42) U. Diebold, *Surf Sci. Rep.*, 2003, **48**, 53.
(43) V. Etacheri, C. Di Valentin, J. Schneider, D. Bahnemann, S. C. *Pillai, Journal of Photochemistry and Photobiology C: Photochemistry Reviews,* 2015, **25,** 1-29.
(44) Shriver, Atkins, *Inorganic Chemistry*, 2006, 4th Edition, Oxford.
(45) R.L. Nelson, A.J. Tench, B.J. Harmsworth, *Trans. Faraday Soc.*, 1967, **63**,1427.
(46) M.A. Henderson, W.S. Epling, C.L. Perkins, C.F.H. Peden, U. Diebold, *J. Phys. Chem. B,* 1999,**103**, 5328.

Chapter 3. Brief Overview of the Electron Paramagnetic Resonance (EPR) Technique

3.1 Introduction

By analysing systems with unpaired electrons, Electron Paramagnetic Resonance (EPR) spectroscopy is a strong, non-destructive, and adaptable analytical method that can provide both structural and dynamic information. Although the first EPR experiment was carried out by Zavoisky in 1945 (1), the spectroscopic technique, which enables the examination of materials with unpaired electrons, derives theoretically from the fundamental properties of the electron spin discovered in the Stern-Gerlach experiment (1922). (2)

TiO_2-based materials can be treated to produce paramagnetic species that can be analysed using EPR studies providing unique insight into the electronic properties of TiO_2. There are great texts available for a more thorough review of EPR theory (3-9), but a brief summary is provided below.

3.2 Theory

3.2.1 Basic Zeeman interaction (EZI)

The Stern-Gelach experiment, which involved passing a beam of silver atoms ((Kr)$4d^{10}5s^1$)) through an inhomogeneous magnetic field provided direct experimental evidence for the intrinsic physical property of an electron, the electron spin (Figure 3.1). In the experiment, a beam of silver atoms was heated in an oven and directed through a non-uniform magnetic field created by a pair of magnets with opposite poles. The magnetic field gradient was designed to vary in strength along one spatial direction. The silver atoms were deflected into discrete beams, not a continuous spread. Specifically, the beam split into two distinct spots on a detector screen. This showed that the magnetic moment, and hence the angular momentum, was quantized and could only take on certain discrete values. (2) The primary interaction in EPR spectroscopy is the Zeeman effect, which splits the degenerate electron spin states in the presence of an external magnetic field.

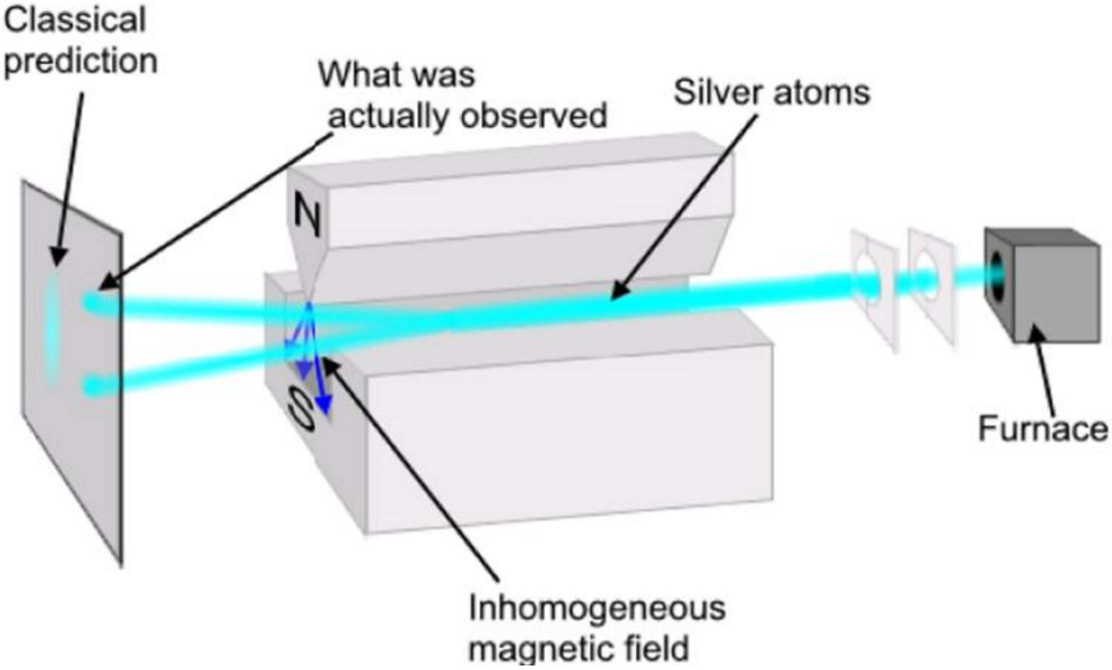

Figure 3.1: Depiction of the Stern-Gelach experiment (2).

The observation of two distinct spots on the collection plate was evidence of two quantised spin states, described as spin up and spin down (or α and β), respectively. Because of the mass difference between an electron and a proton, EPR, which depends on the magnetic moment created by the electron, exhibits heightened sensitivity to nuclear magnetic resonance (Equations 3.1 and 3.2). This is especially helpful when examining systems in which the number of paramagnetic species is naturally low.(10)

$$\mu_{\mathrm{N}} = \frac{e\hbar}{2m_p} \tag{3.1}$$

$$\mu_{\mathrm{B}} = \frac{e\hbar}{2m_e} \tag{3.2}$$

Where μ_N and μ_B are the magnetic moments for a neutron and electron respectively, m_p is the mass of the neutron = 1.67262 x 10^{-27} and m_e is the mass of an electron = 0.00091 x 10^{-27} kg.

The negative charge of an electron, which has the intrinsic characteristic of spin, is the origin of to these two spin states. (11) Equation 3.3 states that as this electric charge moves along an axis, a current is created, and the electron magnetic field is created.

$$\mu_S = \left(\frac{e\hbar}{4\pi m_e}\right)\boldsymbol{S} \qquad (3.3)$$

Where e = charge on the electron, $\hbar$ = reduced planks constant, m_e is the mass of the electron and **S** is the spin. This property is a vector and can be quantised in the units of $\hbar$ (Equation 3.4).

$$|\,\boldsymbol{S}\,| = \sqrt{s(s+1)} \qquad (3.4)$$

Where S = electron spin quantum number. Equation 3.4 predicts 2S+1 allowed projections along an arbitrary axis, which is typically the direction of the applied external magnetic field (B). Hence an electron with S=1/2 has two possible spin states μ_S =± ½. Therefore, the magnetic moment can be defined classically as follows: two states interact differently with an applied field, and this interaction is orientation dependent, as Figure 3.2 demonstrates.

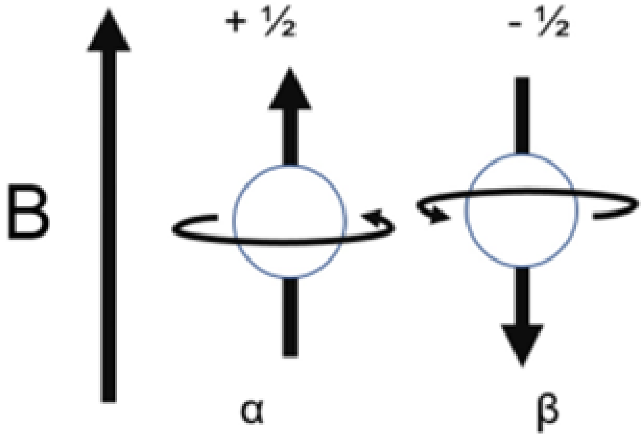

Figure 3.2: Degenerate states of μ with respect to the magnetic field B_0.

Equation 3.5 can be used to calculate the energy of aforementioned electronic states, which are caused by the magnetic moment as well as the external field. A magnetic dipole moment (μ_S), which is connected to the gyromagnetic ration (γ), is produced through a circulating current.

$$\mu_S = -\gamma \boldsymbol{S}\hbar = g_e \left(\frac{e\hbar}{2m_e}\right)\boldsymbol{S} \tag{3.5}$$

In this equation, g_e is the free-electron *g*-factor, a dimensionless value (approximately 2.0023) that adjusts the quantum electron's magnetic moment from what would be expected based on classical physics. Nevertheless, by representing the constants as the Bohr magneton (μ_B – Equation 3.6), this equation can be simplified.

$$\mu_S = -g_e \mu_B \boldsymbol{S} \tag{3.6}$$

The z-component of the magnetic moment (μ_z) along the direction of the applied magnetic field **B** is linked to the electron spin states m_s, resulting in two possible electron magnetic dipole moments, Equation 3.7, Figure 3.3.

$$\mu_z = -g_e \mu_B m_s \tag{3.7}$$

In the absence of an external magnetic field, it was demonstrated that the m_S levels are degenerate. However, this degeneracy is lifted when an external magnetic field is applied. The interaction energy (E) of the electron's magnetic moment with the magnetic field **B** is given by Equation 3.8 and demonstrated in Figure 3.3.

$$E = -\mu_B \boldsymbol{B} \tag{3.8}$$

When a magnetic field is applied, the two distinct m_S levels vary in response to the magnetic field's strength (Figure 3.3), termed the electron Zeeman effect (EZS). The magnetic field interacts with the two opposing spin states, which are either parallel or antiparallel to B. The energy difference can be calculated using Equations 3.9 – 3.11.

$$E = g_e \mu_B m_s B \tag{3.9}$$

$$\Delta E = \left(\frac{1}{2} g_e \mu_B B\right) - \left(-\frac{1}{2} g_e \mu_B B\right) \tag{3.10}$$

$$\Delta E = g_e \mu_B B \tag{3.11}$$

EPR probes the transition from one electronic state (m_S = -1/2) to the other (m_S = +1/2), via the absorption of electromagnetic radiation, as indicated in Figure 3.3.

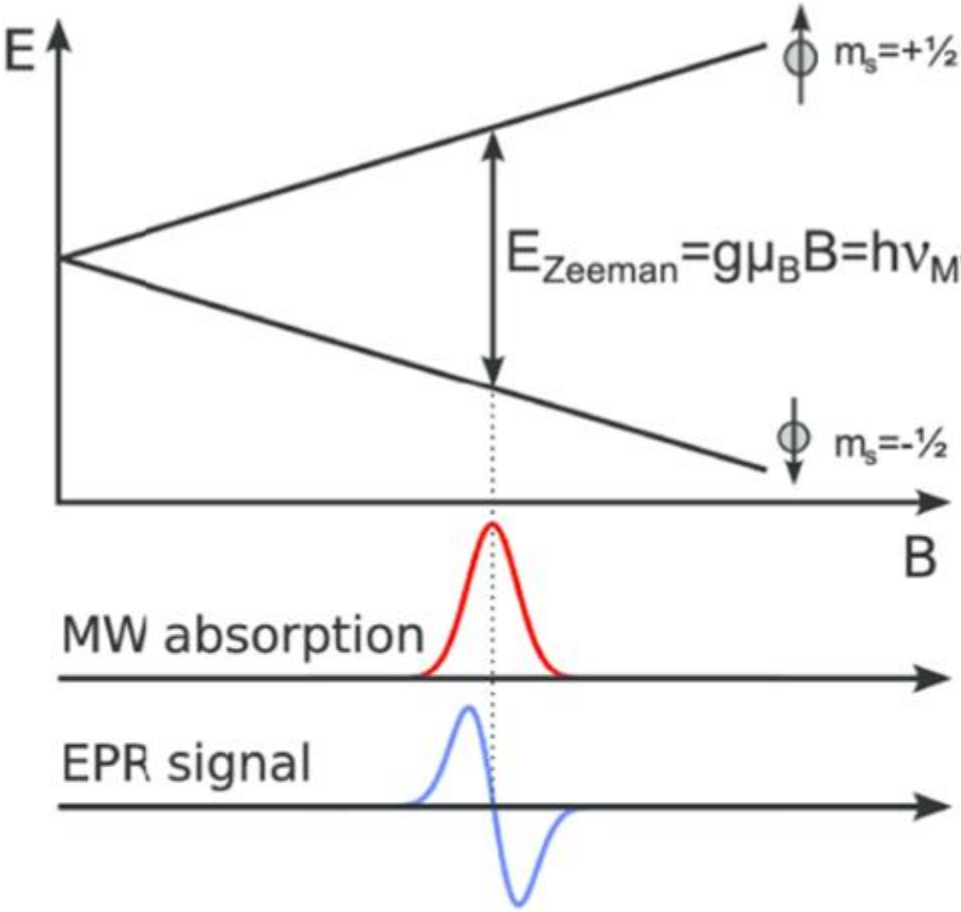

Figure 3.3: Loss of degeneracy of the spin up (α) and spin down (β) states upon the presence of an external magnetic field and 1st derivative and absorption profiles.

The relationship between energy (E) and applied field (B) is likewise described by Equation 3.9, however because of the chemical environment, each electron will experience a different magnetic field. Since there will be varying local fields in different settings, an effective field is created when an external field is applied. When calculating the interaction energy of an electron in an applied field, $\mathbf{B}_{\mathrm{eff}}$ usually takes the place of B, but in practice, it is more convenient to keep **B** because it is easier to measure and substitutes g_e with an effective g factor (Equation 3.12).

$$\boldsymbol{B_{eff}} = \left(\frac{\boldsymbol{g}}{g_e}\right)\boldsymbol{B} \qquad (3.12)$$

3.2.2 **g**-tensor Anisotropy

As previously stated, the spin orbit coupling and the extent of mixing from between the ground and excited states determine the *g* value. Anisotropy, or the orientation dependency of the *g* value, results from this mixing. The anisotropy averages out to produce g_{iso} in a completely symmetrical scenario (Figure 3.4 (a)), such as when samples are recorded in a solution phase with rapid tumbling (such that orientation with respect to the external field is averaged), samples in which the unpaired electron occupies an s-orbital, or if the electronic environment has T_d or O_h symmetry. However, for frozen solutions, powders, and single crystals, the *g* value changes depending on the orientation of the unpaired electron with respect to the external field. Every paramagnetic molecule has a distinct axis known as the principal axis system, which Figure 3.4 demonstrates. The combination of the g-values, denoted by the characters g_x, g_y, and g_z, result in the overall **g**-tensor. EPR spectra are often recorded in frozen solution or powder forms, and in these configurations, all potential orientations are summed. (10)

The angular dependence on the *g* value can now be described as Equation 3.13.

$$\mathrm{g}(\boldsymbol{\theta},\boldsymbol{\Phi}) = \sqrt{\mathrm{g}_x^2\sin^2\theta\cos^2\Phi + \mathrm{g}_y^2\sin^2\theta\sin^2\Phi + \mathrm{g}_z^2\mathrm{f}\cos^2\theta} \qquad (3.13)$$

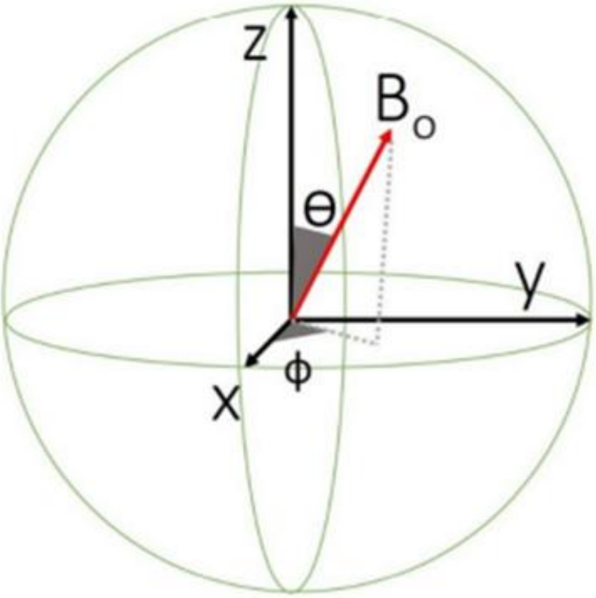

Figure 3.4: Angular dependence with respect to the *g* values.

This means that every electron in a solid (including frozen solutions) takes on a fixed orientation in relation to the applied magnetic field. As a result, the angle both within the xy plane (Φ) and between the xy plane and the z direction (θ) determines the g value. The g values vary as a result of variations in the applied magnetic field with respect to the principal axes. (10)

Since each paramagnetic centre's electrons can occupy any orientation relative to the field in a bulk sample, resonances originating from all possible orientations will be present in the recorded EPR spectrum. All orientations have the same probability in a polycrystalline environment, and the two types of spectra that are commonly observed are axial and orthorhombic (Figure 3.5 (b-c)).

i. Axial

Due to the energy differences between the electrons in the z and xy planes in an axial system, there are two distinct *g* values: *g* parallel ($g_{\parallel}$), which corresponds to the electrons in the z axis, and *g* perpendicular ($g_{\perp}$), which corresponds to the electrons aligned in the x and y axes. The absorption and first derivative profiles are displayed in Figure 3.5 (b and c). Nevertheless, the electron can be positioned anywhere between these two components and so give rise to resonances at all magnetic field positions between the spectrum extremes of $g_{\parallel}$ and $g_{\perp}$. The Jahn Teller effect is responsible for these peaks' relative positions. Since g values are proportional to energy because of the resonance equation, if there is a compression along the z axis, the z component g will have a larger energy than the xy component g. On the other hand, the g component's energy will decrease with elongation along the z axis. The orbital occupation is also indicated by the **g**-tensor: if a system is d^1-d^4, then $\mathbf{g}<g_e$, whereas if $\mathbf{g}>g_e$ then the system is d^5-d^9. (5) Utilising the information the **g**- tensor can provide, identification of paramagnetic centres in materials, such as TiO_2, becomes achievable. Thus, a deeper understanding of the materials and their potential are attainable.

ii. Orthorhombic

The unpaired electron in an orthorhombic system can be pointing in the direction of the x, y, or z axis, since $\Phi = 0 – 90^o$ and $\theta = 0 – 90^o$. On the other hand, resonances can arise at any magnetic field point between the spectral extremes of g_x, g_y, and g_z since the electron can be positioned anywhere between these three components. (12) Figure 3.5 (d) shows an example of the three components—g_x, g_y, and g_z—that are seen in the orthorhombic spectra.

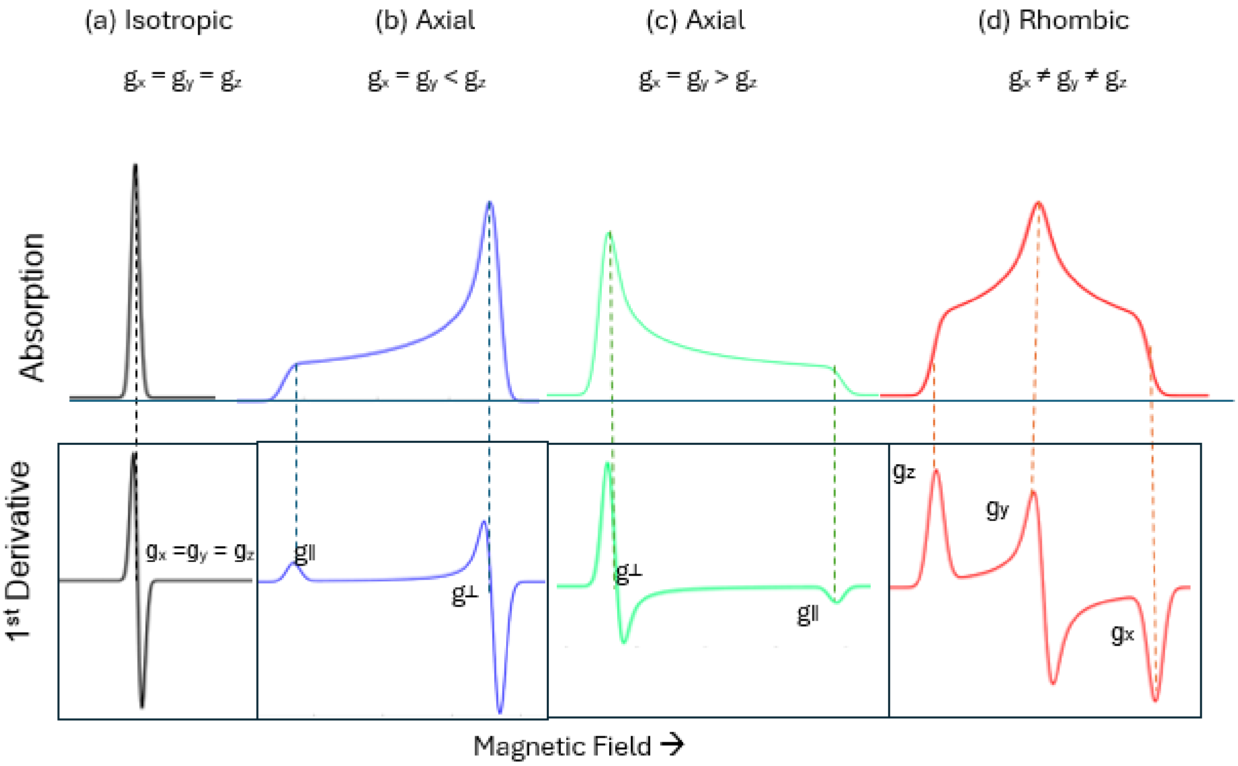

Figure 3.5: Diagrammatic representation of the resulting EPR spectra and the g tensor. The forms of the isotropic (a), axial (b, c), and rhombic (d) magnetic moments are represented by the upper solid bodies. These are the absorption curves underneath. On the bottom are the relevant EPR derivative curves.

The spectral characteristics of transition metal complexes differ from those of organic species. A paramagnetic substance is produced by a large number of transition metal ions, either alone in a solid matrix or in combination with an organic ligand in a metal complex. (8) Since the unpaired electron is usually restricted to a d-orbital with a large spin orbit coupling and exhibit a broad linewidth (discussed in 3.2.5).

The d-orbital splitting of d block elements is connected to their electron and magnetic characteristics. Five d-orbitals are known as d_{xy}, d_{xz}, d_{yz}, d_{z^2}, and $d_{x^2-y^2}$. The degeneracy of the orbitals is caused by the local environment, or the area around the ligands. (6)

Surrounding ligands generate an electric field, which destabilises the orbitals. Because they are directed directly towards the ligand, this increases the energy of the e_g levels, or d_{z^2} and $d_{x^2-y^2}$, in an octahedral (O_h) environment. As they are oriented between the ligands, the t_{2g} levels, or d_{xy}, d_{xz}, and d_{yz}, on the other hand, drop in energy. An energy gap is created as a result of this loss of degeneracy, and it grows as the electrostatic field does.

In addition, the spin orbit coupling, and Jahn-Teller distortions have an impact on this loss of orbital degeneracy. The severe instances (d^1, d^5, and d^9) are described in detail in the electron paramagnetic resonance primer. (10) Here, though, a brief description of the d^1 situation will be given. Given that the lone unpaired electron in a d^1 system is restricted to the d-orbitals, a deeper comprehension of λ, which characterises the degree of orbital mixing in spin orbit coupling, is necessary. This is due to the fact that spin orbit coupling to an empty orbital result in a negative contribution to the g value; hence, by taking the orbital orientation into account, the impacts on the g values can be investigated separately.

For instance, Ti^{3+} distortion lifts the degeneracy of the $d_{x^2-y^2}$ and d_{z^2}, resulting in the unpaired electron living on the d_{z^2} in a d^1 system with D_{2h} symmetry. Consequently, $g_e = g$ since there is no state mixing when the applied field is parallel to the z axis. On the other hand, mixing of the E_g states occurs when the applied field is perpendicular to the z axis. This explains why all g values in this symmetry (g = 2.0023, Equation 3.14 and 3.15) will be less than free spin, except for the d_{z^2} ground state. (11,13)

$$g_z = g_{\parallel} = g_e - (\frac{8\lambda}{E_{xy} - E_{x^2-y^2}}) \quad (3.14)$$

$$g_{xx}, g_{yy} = g_{\perp} = g_e - (\frac{2\lambda}{E_{xy} - E_{xy,xz}}) \quad (3.15)$$

Isotope abundance needs to be considered because of the significance of the spin orbit coupling on the spectral profiles. There are several isotopes of transition metals, and as these isotopes can display distinct spin angular moments, it is important to take this into account when interpreting spectra.

3.2.3 Nuclear Zeeman and Hyperfine Interaction

Sections 3.2.1 – 3.2.3 solely considered the interaction of the unpaired electron with the external magnetic field, however the nuclear environment of the paramagnetic species must also be taken into account in describing the full electronic character Equation 3.16 describes the energy of the angular momentum spin states (**I**) in the presence of a magnetic field.

$$\mathrm{E} = g_N \mu_\mathrm{N} \mathbf{IB} \quad (3.16)$$

Thus, additional splitting to the electron Zeeman interaction takes place in the presence of an external magnetic field; this process is referred to as nuclear Zeeman splitting (NZS) and results in additional splitting to the energy diagram (Figure 3.6) and terms to the Hamiltonian (Equation. 3.16, 3.18 and 3.19). The opposite charge of the nucleus compared with the electron results in the opposite ordering of the nuclear spin states.

The contact between the electron's magnetic moment and the nucleus produces a third interaction that needs to be considered, which is referred to as the hyperfine interaction. Insights into the electronic and nuclear environments of the paramagnetic species can be provided via the characterisation of the hyperfine coupling constant. (13) The splitting diagram, as seen in Figure 3.6, may be perturbed as a result of the interaction between these two fields, Equation 3.18.

The behaviour of the electron spins in a magnetic field can be described by the spin Hamiltonian. A spin Hamiltonian can be built by considering the hyperfine, nuclear Zeeman interaction, and electron Zeeman interaction, Equations 3.17-3.19. (14)

$$EZI\ H = g_e \mathrm{\mu_B} \mathbf{B} \tag{3.17}$$

$$NZI\ H = g_N \mathrm{\mu_N} \mathbf{IB} \tag{3.18}$$

$$HYP\ H = \mathbf{S} a_{iso} \mathbf{I} \tag{3.19}$$

These Hamiltonians can be combined to create equation 3.20, which represents the fundamental interactions seen in an EPR spectrum:

$$H = g_e \mu_B \mathbf{B} - g_N \mu_N \mathbf{IB} + \mathbf{S} a_{iso} \mathbf{I} \tag{3.20}$$

Other interactions, such as dipole-dipole and quadrupolar interactions, are not covered here as they are out of the scope of this thesis, however, there is excellent literature covering these.

The strength of the hyperfine interaction is related to two terms and provides insights into the surrounding environment.(15) The Fermi contact term is a specific component of the hyperfine interaction that arises when an electron's wavefunction has a nonzero probability density at the location of the nucleus. This interaction is particularly relevant for s-orbital electrons, where the electron density at the nucleus is significant. The Fermi contact term directly influences the strength of the isotropic hyperfine interaction. Hence, a stronger Fermi contact term indicates a closer proximity between the electron and nuclear spins, leading to a stronger hyperfine interaction. When the electron's wavefunction overlaps significantly with the nucleus, the hyperfine interaction is stronger. This is because the magnetic field generated by the electron's spin interacts more directly with the nuclear spin when they are in close proximity. The Fermi contact term, which represents the interaction when the electron is located inside the nucleus (as with s-orbital electrons), is a key factor in this relationship. Therefore, a stronger hyperfine interaction generally indicates that the electron is close to the nucleus.

In EPR spectroscopy, the selection rules for allowed transitions are primarily determined by the spin quantum number and the magnetic quantum number. The key selection rules are:

1. $\Delta m_S = \pm 1$: The magnetic quantum number of the electron spin (m_S) must change by ±1. This corresponds to the flipping of the electron spin, which is essential for the resonance condition in EPR.
2. $\Delta m_I = 0$: The magnetic quantum number of the nuclear spin (m_I) typically remains unchanged during the transition. However, in the presence of hyperfine interaction, transitions with $\Delta m_I = \pm 1$ may also be allowed, but these are generally weaker.

These rules mean that for an EPR transition to occur, the electron spin must change from one state to another (such as from m_S=+1/2 to m_S=−1/2), while the nuclear spin state generally stays the same.

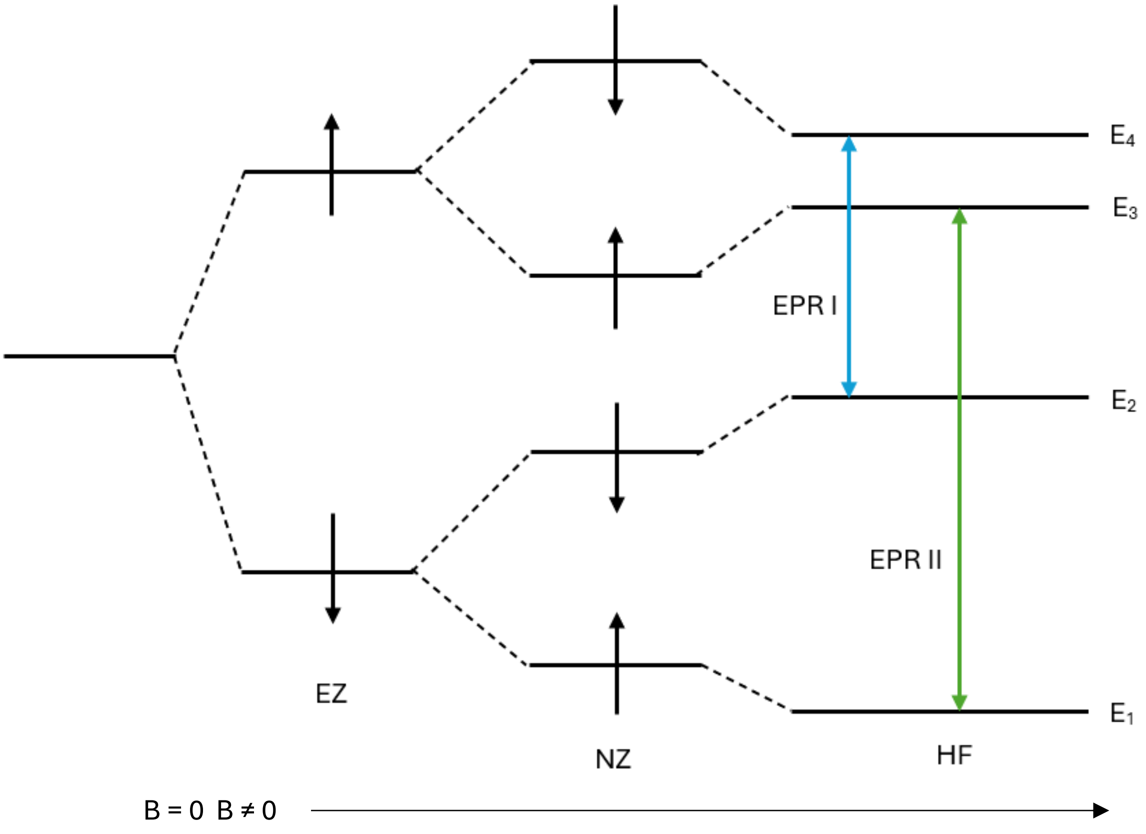

Figure 3.6: Energy level diagram for an S = ½, I = ½ spin system indicating the electron Zeeman (EZ) and nuclear Zeeman (NZ) levels and hyperfine (HF) perturbations. The allowed EPR transitions are labelled EPR I – EPR II.

Hyperfine splitting can be classified as either isotropic or anisotropic. (10) Isotropic hyperfine splitting refers to the case where the interaction between the nuclear and electronic magnetic moments is the same in all directions. This usually occurs in systems where the electron cloud surrounding the nucleus is spherically symmetric, meaning that the electron's wavefunction has no directional dependence. Anisotropic hyperfine splitting occurs when the hyperfine interaction depends on the direction relative to some axis, meaning the splitting varies with the orientation of the system. This anisotropy arises in systems where the electron distribution around the nucleus is not spherically symmetric (Equation 3.21).

$$a_{iso} = \left(\frac{8\pi}{3g_e g_N \mu_B \mu_N}\right) |\varphi(0)|^{2} \qquad (3.21)$$

Where $|\varphi(0)|^2$ is the square of the unpaired electron wavefunction's absolute value as determined at the nucleus. The electron density at the nucleus may be connected to the size of the detected hyperfine. On the other hand, in an anisotropic system, the electron is also affected by a dipole-dipole interaction that is related to the electron's distance from the nuclei (Figure 3.7, Equation 3.22).

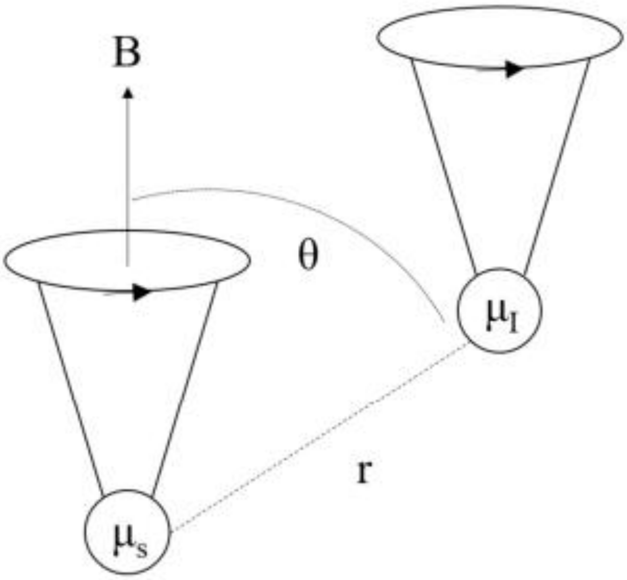

Figure 3.7: Classical dipole interaction between μ_s and μ_I as a function of distance and orientation.

$$E_{dip} = (\frac{\mu_0}{4\pi})\left(\frac{\mu_s\mu_I}{r^3}\right) - (3\frac{(\mu_s\boldsymbol{r})(\mu_0\boldsymbol{r})}{r^5}) \qquad (3.22)$$

Where **r** = vector relating the electron and nucleus magnetic moments and r= distance between the two species. However, in real systems there is a mix of these two hyperfine interactions. For example, in the case of TiO_2, an axial system, the a_{iso} is demonstrated in Equations 3.23 and 3.24.

$$\alpha_{iso} = \frac{A_\perp + A_\perp + A_\parallel}{3} \qquad (3.23)$$

$$B = a_{iso} - A_\perp \qquad (3.24)$$

3.2.4 Spin orbit coupling

Spin-orbit coupling is another significant interaction in EPR spectroscopy, especially for heavier elements with larger atomic numbers. This coupling between the electron's spin and its orbital motion can lead to shifts and splitting in the EPR spectrum, further enriching the information obtainable about the electronic structure. Electrons have an orbit angular momentum (**L**), equivalent to a circulating current. As a result, an orbital angular momentum is created, Figure 3.8.
The total magnetic moment of the electron is the vector sum of the spin and orbital angular momenta, Equation 3.25:

$$\boldsymbol{\mu} = \mu_B\,(\boldsymbol{L} + g_e\boldsymbol{S}) \qquad (3.25)$$

Although there is mixing between the ground and excited states, which results in a contribution from the spin orbit coupling. Because the atomic mass of the associated nucleus determines the magnitude of the spin orbit coupling, organic species that comprise C, O, N, and H have tiny spin orbit coupling and do not significantly diverge from g_e. On the other hand, heavier species, such metals, do stray from g_e because they produce larger spin orbit coupling

Considering the impact of orbital mixing, where $g_e\mu_B\mathbf{SB}$ is the electron Zeeman contribution, $\mu_B\mathbf{LB}$ is the orbital Zeeman contribution and $\lambda\mathbf{LS}$ is the spin orbit coupling contribution, with λ specifically being the spin orbit coupling constant, then the Hamiltonian Equation 3.20 can be re-written as Equation 3.26.

$$\widehat{H} = g_e\mu_B\mathbf{SB} + \mu_B\mathbf{LB} + \lambda\mathbf{LS} \qquad (3.26)$$

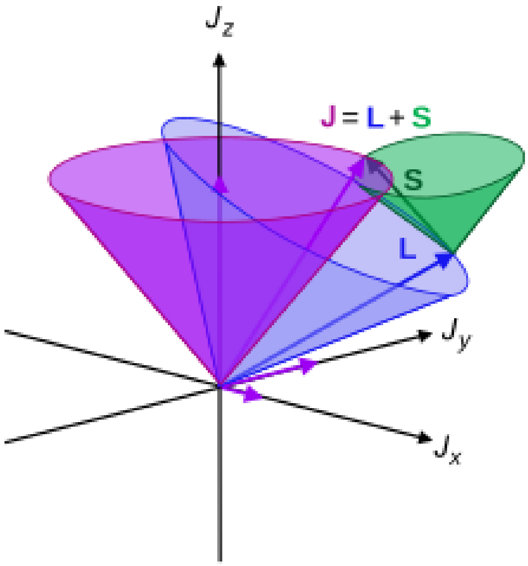

Figure 3.8: Angular momentum of an electron.

Therefore, the *g* value contains chemical information on the electron within the molecule and can be considered the electronic fingerprint of the paramagnetic species of interest.

In TiO_2, the Ti^{4+} ion is in a d^0 configuration, meaning that in a perfect crystal without defects or dopants, there are no unpaired electrons, and hence, no EPR signal would be observed. However, materials can present natural or induced defects, such as oxygen vacancies, interstitials, or doping with other elements can introduce Ti^{3+} (d^1) centres, which have an unpaired electron and are EPR active.

The Ti^{3+} ion in TiO_2 experiences significant spin-orbit coupling due to the relatively high atomic number of titanium. The spin-orbit coupling affects the EPR spectra by causing splitting of the energy levels associated with the unpaired electron in the Ti^{3+} ion. In a simple case, if the spin-orbit coupling is weak compared to the crystal field splitting, the EPR spectrum may show a single broad line, but as the spin-orbit coupling increases, more complex splitting patterns can emerge.

When Ti^{3+} centres are present in TiO_2, the EPR spectrum typically shows signals corresponding to the unpaired electron in the 3d orbital of Ti^{3+}. The observed EPR lines are affected by the interaction between the electron spin and the magnetic field, modulated by spin-orbit coupling.

In the rutile phase of TiO_2, the Ti^{3+} ion is in a slightly distorted octahedral environment. The spin-orbit coupling in this case causes the energy levels to split into multiple sub-levels, and the EPR spectrum reflects this by showing a characteristic multi-line pattern. The splitting pattern can provide information about the strength of the spin-orbit coupling, the crystal field, and the symmetry of the local environment around the Ti^{3+} ion.

3.2.5 Linewidth of EPR spectra

Linewidth is a critical parameter in EPR spectroscopy. Narrow lines are highly susceptible to saturation or distortion if incorrect spectrometer settings (such as power, time constant, or modulation amplitude) are used. However, when accurately recorded, these narrow lines provide excellent resolution of adjacent peaks with high sensitivity. In contrast, broad lines can be difficult to distinguish from the background, particularly if the signal intensity is low, and in some cases, very broad lines may not be detectable. Linewidth measurements also offer valuable insights into the structure and spin system. EPR spectroscopy commonly uses peak-to-peak linewidth (ΔBpp). For complex spectra, such as anisotropic patterns, directly extracting linewidth may not be feasible, but spectral simulations can still provide valuable linewidth information. Linewidth in EPR spectroscopy is typically determined by the spin–spin relaxation time T_2, with various relaxation pathways contributing to this effect. (10)

Different types of line broadening can be classified as either homogeneous or inhomogeneous. Homogeneous broadening occurs when all spins experience identical net magnetic fields, resulting in the same transition probability for each spin in the spin packet. In contrast, inhomogeneous broadening arises when each spin packet is subjected to slightly different net magnetic fields, leading to a superposition of individual components (each with a Lorentzian profile) that combine to form a Gaussian envelope for an absorption profile. Anisotropic EPR spectra in solid state, for example, often display inhomogeneously broadened lines due to the random orientations of radicals relative to the external magnetic field, resulting in a spectrum that reflects contributions from all possible orientations.(10, 16)

In many real systems, EPR lines are neither purely Lorentzian nor Gaussian but are best described by a Voigtian shape, a convolution of Lorentzian and Gaussian profiles. Inhomogeneous broadening is not related to dynamic processes but occurs when individual spins are in different environments or have different orientations with respect to the external magnetic field. EPR spectra of disordered paramagnetic species in the solid state are the sum of spectra for each orientation, leading to significantly broader spectra than those for each individual orientation an example of inhomogeneous broadening. Another important source of inhomogeneous broadening is strain effects, which refer to small variations in magnetic parameters (such as the components of g and A tensors) among individual radicals due to the inhomogeneous nature of the sample, potentially caused by defects in the solid matrix or slight conformational differences in the solid phase. (17) This is especially relevant for co-doped samples studied in this thesis as dopants are defect sources in the solid sample. The presence of slightly different conformations leads to a distribution of magnetic parameters, typically resulting in line broadening. Although this effect may seem minor, neglecting it can cause significant errors in spectrum simulations.

A different form of inhomogeneous broadening, unrelated to sample inhomogeneity, is due to weak, unresolved hyperfine interactions. This broadening is often observed in solid samples where the proximity of a large number of nuclei with non-zero spin (such as protons) results in very weak hyperfine interactions. Although these interactions are generally too weak to split the EPR lines, their combined effect causes line broadening and alters the lineshape, making it more Gaussian, as is typical of inhomogeneous broadening (Figure 3.9). (10,17)

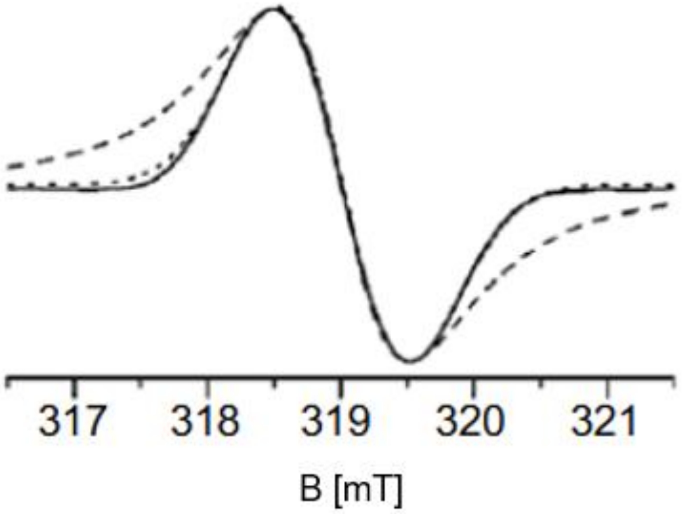

Figure 3.9: EPR spectrum demonstrating a nearly Gaussian shape due to many unresolved hyperfine interactions. For comparison, Gaussian and Lorentzian shapes are shown with dotted and dashed lines, respectively.

3.3 EPR of Defects in TiO_2

This work focus on the study of doped TiO_2 materials and the effect different synthetic pathways have on the materials as potential catalysts. Therefore, understanding the type and origin of EPR defects is of great importance in order to correctly characterise the samples. The paramagnetic defects in TiO_2 primarily include oxygen vacancies, titanium interstitials, and substitutional dopants. (18) EPR is particularly useful for studying surface and interface phenomena in TiO_2 which are crucial for its catalytic activity. Surface-bound species, such as adsorbed molecules and radicals, often exhibit unique EPR signals. These signals can reveal information about adsorption sites, surface defects, and the nature of chemical interactions at the surface. (19)

3.3.1 Oxygen Vacancies

One of the main focuses of EPR studies on TiO_2 is the investigation of surface defects, particularly oxygen vacancies. Oxygen vacancies are ubiquitous defects that can significantly affect the material's electronic properties and reactivity. EPR detects these vacancies by identifying the characteristic signals of trapped electrons, often associated with a g-factor around 2.003-2.004. (20) These paramagnetic centres arise because the missing oxygen atoms create localized states within the band gap.

The formation and concentration of oxygen vacancies can be influenced by factors such as annealing, doping, and irradiation. EPR studies have shown that UV irradiation increases the concentration of oxygen vacancies, which in turn enhances the photocatalytic activity of TiO_2. (21) By monitoring the EPR signals of these defects, researchers can optimize the processing conditions to maximize the photocatalytic performance.

These vacancies are paramagnetic due to the presence of unpaired electrons trapped in the lattice as a result of the missing oxygen atoms. The unpaired electrons in these defects exhibit resonance when subjected to a magnetic field, producing characteristic g-values that allow for detailed identification of different defect species in the material.

Oxygen vacancies in TiO_2 are complex and can exist in different charge states, such as neutral, singly ionised, or doubly ionised. These defects influence the material’s electronic and photocatalytic properties. The exact nature of these vacancies depends on the preparation method (e.g., thermal treatment, irradiation, doping) and the surrounding chemical environment.

3.3.1.1. Neutral Oxygen Vacancies

Neutral oxygen vacancies are the simplest type of vacancy. In these vacancies, two electrons are trapped in the vacancy left by the missing oxygen atom. These electrons are localized and can be detected by EPR. The EPR signal typically observed for neutral oxygen vacancies in TiO_2 appears with a *g*-value of around 2.003–2.004, which represents an electron localised in the vacancy, indicating the presence of a neutral oxygen vacancy in the TiO_2 lattice. This signal is associated with electrons trapped in shallow states near the conduction band edge.(22)

3.3.1.2. Singly Ionised Oxygen Vacancies

In a singly ionised oxygen vacancy, only one electron is trapped in the vacancy, with the second electron having been removed, usually through thermal excitation or interaction with neighbouring species. The *g*-value for singly ionized oxygen vacancies in TiO_2 is usually observed around 2.002–2.003. This is slightly lower than that for neutral vacancies due to the altered electronic environment around the vacancy. The lower *g*-value reflects the fact that there is only one electron in the vacancy, as opposed to the two in neutral vacancies, and this changes the resonance behaviour.(23)

3.3.1.3. Ti^{3+} Ions Adjacent to Oxygen Vacancies

When an oxygen vacancy forms in TiO_2, the electronic charge redistribution can sometimes result in the reduction of adjacent Ti^{4+} ions to Ti^{3+}. This process can occur because the missing oxygen atom leaves an excess of electrons in the lattice, some of which can localise on neighbouring titanium ions, converting them to Ti^{3+}. The EPR signal for Ti^{3+} ions in reduced TiO_2 shows a characteristic *g*-value of 1.94–1.98. These signals are usually seen alongside those for oxygen vacancies and are particularly common when TiO_2 is annealed in reducing atmospheres, such as hydrogen or vacuum. The Ti^{3+} signal is important because it indicates the presence of both oxygen vacancies and reduced Ti ions, which are closely linked in the defect structure.(24)

3.3.1.4. Surface Oxygen Vacancies

Surface oxygen vacancies differ from bulk vacancies in that they are located on the outermost layers of the TiO_2 particles or crystals. These defects are highly reactive and play a crucial role in photocatalysis and adsorption processes. The surface oxygen vacancies may show a slightly shifted *g*-value compared to bulk vacancies, often appearing around 2.004–2.005. The shift in g-value is due to the altered chemical environment at the surface, where the coordination of the atoms is different from that in the bulk. These vacancies are often associated with enhanced reactivity, particularly in photocatalytic applications, as they serve as active sites for chemical reactions involving adsorbed molecules.(24, 25)

3.3.2 Substitutional Dopants

Surface modifications and doping are common strategies to enhance the properties of TiO_2 for specific applications. EPR spectroscopy is instrumental in studying the effects of these modifications. For example, doping TiO_2 with transition metals such as tungsten (W) or tantalum (Ta) introduces new paramagnetic centres with unique EPR signatures. (26) These dopants can modify the electronic structure of TiO_2, influence the formation of oxygen vacancies, and alter the surface chemistry.

EPR studies on doped TiO_2 have revealed changes in the **g**-factor and hyperfine splitting, providing information about the local environment of the dopants and their interaction with the TiO_2 matrix. This understanding helps in fine-tuning the doping process to achieve desired electronic and catalytic properties.

3.3.4 Photocatalytic Activity

The photocatalytic properties of TiO_2 are closely related to the behaviour of charge carriers (electrons and holes) generated upon light irradiation. EPR can monitor these charge carriers, providing insights into the mechanisms of photocatalytic reactions. For instance, photo-generated electrons trapped at Ti^{4+} sites and holes trapped at oxygen sites can be detected and studied using EPR. (27) EPR can detect radical species generated during photocatalytic processes, such as reactive oxygen species (ROS). For example, hydroxyl radicals ($^{\bullet}OH$) and superoxide radicals ($O_2^{-\bullet}$) can be identified by their characteristic EPR signals. (28)

Photo-generated electrons can become trapped at Ti^{4+} sites, reducing them to Ti^{3+} ions. These trapped electrons are paramagnetic, making them detectable by EPR spectroscopy. The presence of trapped electrons at Ti^{3+} centres is typically observed in the EPR spectrum as a signal with a *g*-value of approximately *g* ≈ 1.96–1.98. This signal arises from the interaction of the unpaired electron in the 3d orbital of the Ti^{3+} ion. (24) The exact *g*-value can vary slightly depending on the local coordination and the surrounding defect environment. The EPR signal intensity can increase with light irradiation, indicating the generation of photo-excited electrons trapped at these sites.(29)

Simultaneously, photo-generated holes tend to become trapped at oxygen sites in the TiO_2 lattice. These holes can form oxygen radicals (O^- or O_2^-) when interacting with the oxygen atoms in the TiO_2 crystal structure. Holes trapped at oxygen sites (O^- centres) can be detected as EPR signals with g-values around *g* ≈ 2.002–2.004. This signal reflects the interaction of the unpaired electron in the oxygen 2p orbital with the hole trapped at the site. The *g*-value is similar to that of a free electron but slightly shifted due to the influence of the surrounding crystal lattice.(30)

EPR provides a non-invasive way to monitor the dynamics of charge carriers in real-time under light irradiation. By comparing the EPR spectra of TiO_2 in the dark and under illumination, the efficiency of the generated trap charge carriers can be observed. During photocatalysis, the photo-generated electrons and holes drive redox reactions that produce various radical species, which are highly reactive and responsible for degrading organic pollutants and initiating other photocatalytic processes. EPR is one of the few techniques capable of directly detecting these radical intermediates.

Hydroxyl radicals ($^{\bullet}OH$) are one of the most important and reactive species generated during TiO_2 photocatalysis. These radicals are formed when photo-generated holes (h^+) react with surface-adsorbed water molecules or hydroxyl groups. Hydroxyl radicals can be detected by EPR using spin-trapping techniques. Spin traps, such as 5,5-dimethyl-1-pyrroline N-oxide (DMPO), react with $^{\bullet}OH$ radicals to form a stable radical adduct, DMPO-OH, which exhibits a characteristic EPR spectrum. The EPR spectrum of DMPO-OH consists of a four-line hyperfine pattern due to the interaction of the unpaired electron with the nitrogen nucleus of the spin trap (I = 1), with a hyperfine coupling constant (A_N) of approximately 14.9 G. (31) The appearance and intensity of this signal provide information about the concentration of hydroxyl radicals generated during photocatalytic reactions.

Superoxide radicals ($O_2^{-\bullet}$) are formed when photo-generated electrons reduce molecular oxygen adsorbed on the TiO_2 surface. Superoxide radicals can also be detected using spin-trapping techniques. When a spin trap like DMPO is used, it reacts with $O_2^{-\bullet}$ to form a DMPO-OOH adduct, which exhibits a characteristic EPR signal. The EPR spectrum of DMPO-OOH consists of a six-line pattern due to hyperfine interactions with the nitrogen and hydrogen nuclei. Superoxide radicals can also be detected directly without spin trapping, often giving an isotropic EPR signal with $g \approx 2.00$–2.01. (31) This signal is indicative of the unpaired electron being located in a π^* antibonding orbital of the superoxide anion.

In addition to hydroxyl and superoxide radicals, other reactive oxygen species (ROS) such as peroxyl radicals ($ROO^\bullet$) may be generated during photocatalysis. These species play crucial roles in oxidation reactions and the breakdown of organic molecules. Although less common than $^\bullet OH$ and $O_2^{-\bullet}$, peroxyl radicals can also be detected using specific spin-trapping agents that stabilize these short-lived radical. The EPR signals provide insight into the types of ROS generated under specific photocatalytic conditions.

EPR studies provide a molecular-level understanding of the mechanisms behind photocatalytic reactions by directly monitoring the key intermediates—charge carriers and reactive radicals. This understanding is essential for optimizing TiO_2 photocatalysts in various applications.

The efficiency of photocatalytic processes depends largely on the separation of photo-generated electrons and holes. (32) EPR can track the formation of Ti^{3+} centres and oxygen radicals over time, allowing for the determination of the recombination rate of electron-hole. High recombination rates limit the efficiency of photocatalysis, as fewer electrons and holes are available to participate in redox reactions. Doping TiO_2 with elements such as nitrogen or tungsten can influence charge carrier dynamics. EPR studies have shown that certain dopants can reduce recombination rates by either acting as electron traps (e.g., Ti^{3+} centres) or promoting better charge separation. (33)

By identifying the reactive radical species generated during photocatalysis, EPR helps to clarify the specific pathways by which pollutants or contaminants are degraded. (34) For example, the detection of hydroxyl radicals suggests that the oxidation of organic molecules proceeds through highly reactive species that attack bonds in the target molecules. Similarly, the detection of superoxide radicals indicates the involvement of reduction processes, which can be important in processes like water splitting or CO_2 reduction. (35) Understanding the relative contributions of different radical species allows for the fine-tuning of reaction conditions to maximize the generation of the most reactive species.

The ability of EPR to monitor both charge carriers and radical intermediates enables detailed studies throughout this work of the degradation mechanisms of various pollutants. This allowed specific mechanistic pathways to be proposed based on the detection of radicals at different stages of the photocatalytic reaction.

3.4 Conclusion

EPR will be used in this thesis to examine the various titanium dioxide polymorphs. The variations in unit cell architectures will be specifically examined in relation to the variations in surface locations and activity. This is because TiO_2 is a widely used photocatalyst therefore, a better understanding of the surface activity would enable improved catalysis design, through co-doping. Specifically, the study will focus on molecular oxygen adsorption. Photogenerated charges have the ability to interact with adsorbed oxygen. It has been demonstrated that this interaction generates a wide variety of surface oxygen radicals that are detectable by EPR. Second, in order to replicate the impact of pollutant molecules on redox reactions with regard to environmental restoration, organic molecules will also be investigated. The alteration of titanium dioxide to increase the photo-efficiency is thus the subject of the second half of the thesis, with EPR used via solid state characterisation and via spin trap. Due to the sensitivity of the EPR parameters, many paramagnetic dopant species can be seen using EPR, allowing for the identification of the lattice position.

3.5 References

(1) E. Zavoisky, *J. Phys*, U.S.S.R., 1945, **9**, 211.

(2) W. Gerlach, O. Stem, *J Phys*, 1921, **8**, 110.

(3) A. Schweiger, G. Jeschke, *Principles of Pulse Electron Paramagnetic Resonance*, 2001, OUP, Oxford.

(4) J. A. Weil, J. R. Bolton, J. E. Wertz, *Electron Paramagnetic Resonance: Elementary Theory and Practical Applications*, 1994, John Wiley and Sons.

(5) F. E. Mabbs, D. Collison, *Electron Paramagnetic Resonance of d Transition Metal Compounds*, 1992, Elsevier.

(6) J. R Pilbrow, *Transition Ion Electron Paramagnetic Resonance*, 1990, Laredon Press, Oxford.

(7) P. W. Atkins, M. C. R. Symons, *The structure of Inorganic Radicals*, 1967, Elsevier, Amsterdam.

(8) M. Che, E. Giamello, *Spectroscopic Characterisation of Heterogenous Catalysts Part B, Stud. Surf. Sci. Catal.*, 1987, **57**, B265.

(9) V. Chechik, E. Carter, D. Murphy, *Electron paramagnetic resonance*, 2017, Oxford University Press.

(10) V. Chechik, E. Carter, D. Murphy, *Electron Paramagnetic Resonance*, Oxford University Press, 2016.

(11) G. Breit, I. I. Rabi, *Phys. Rev*. 1931, **38**, 2082.

(12) Atherton, N. M., *Principles of Electron Spin Resonance*, 1993, Ellis Horwood.

(13) M. J. Stephens, J. P. Auffray, *Chem. Phy*. 1959, **31**, 1329.

(14) D. M. Murphy, *EPR Spectroscopy in Chemistry*, 1997, Springer.

(15) A.L. Kleschyov, P. Wenzel, T. Munzel, *Journal of Chromatography* , 2007, **851**, 12-20.

(16) B. L. Bales, M. Peric, *The Jour. of Phys. Chem. B,* 1997, **101,** 43, 8707-8716.

(17) Z. Wilamowski *et al*, *Semicond. Sci. Technol.,* 2011, **26,** 064009.

(18) U. Diebold, *Surface Science Reports*, 2003, **48**, 5-8, 53-229.

(19) A. Fujishima, T. N. Rao, D. A. Tryk, *Photochemistry Reviews*, 2000, **1**, 1, 1-21.

(20) O. Carp, C. L. Huisman, A. *Reller, Photoinduced reactivity of titanium dioxide. Progress in Solid State Chemistry*, 2004, **32**, 1-2, 33-177.

(21) Y. Nosaka, A. Y. Nosaka, *ACS Energy Letters*, 2017, **1**, 3, 356-359.

(22) A. T. Brant, E. M. Golden, N. C. Giles, S. Yang, M. A. R. Sarker, S. Watauchi, M. Nagao, I. Tanaka, D. A. Tryk, A. Manivannan, and L. E. Halliburton, *Phys. Rev. B,* 2014, **89**, 115206.

(23) J. Chen, N. A. Bogdanov, D. Usvyat, W. Fang, A. Michaelides, A. Alavi, *J. Chem. Phys.,* 2020, **153**, 20, 204704.

(24) J. Green, E. Carter, D. M. Murphy, *Chem Phys Letters,* 2009, **477**, 4–6, 340-344.

(25) S. G. Wang, X. D. Wen, D. B. Cao, Y. W. Li, J. Wang, H. Jiao, *Surface Science*, 2005, **577**, 1, 69-76.

(26) W. Choi, A. Termin, M. R. Hoffmann, *J. Phys. Chem*., 1994, **98**, 13669-13679.

(27) M. R. Hoffmann, S. T. Martin, W. Choi, D. W. Bahnemann, *Chemical Reviews*, 1995, **95**, 1, 69-96.

(28) M. Che, A. J. Tench, *Advances in Catalysis*, 1983, **32**, 1-148.

(29) I. R. Macdonald, S. Rhydderch, E. Holt, N. Grant, J. Storey, R. F. Howe, *Catalysis Today*, 2012, **182**, 1, 39-45.

(30) K. Sobańska, A. Krasowska, T. Mazur, *et al.*, *Top Catal,* 2015, **58**, 796–810.

(31) J. Cadet, R. Teoule, *Photochemistry and Photobiology*, 1978, **28**, 661-665.

(32) R. Marschall, *Adv. Funct. Mater*., 2014, **24**, 2421-2440.

(33) K. Pandi, S. K. Lakhera, N. Bernaurdshaw, *Catalysis Today*, 2021, **370,** 161-172

(34) H. Jia, W. He, W. G. Wamer, X. Han, B. Zhang, S. Zhang, Z. Zheng, Y. Xiang, J. Yin, *The Journal of Physical Chemistry C,* 2014, **118**, 37, 21447-21456.

(35) M. Hayyan, M. A. Hashim, I. M. AlNashef, *Chemical Reviews,* 2016, **116**, 5, 3029-3085.

Chapter 4. Experimental

4.1 Introduction

In this chapter the materials, synthetic procedures, apparatus and experimental procedures used throughout the thesis will be detailed.

4.2 TiO_2 Synthesis

The synthetic procedures for the pure and co-doped TiO_2 materials discussed in this thesis are presented below.

Sample Labelling	Calcination method	Morphology	Metal dopant	Nitrogen source
F-A-undoped-TiO_2	Furnace	Anatase		
F-A-WN-TiO_2	Furnace	Anatase	Tungsten	Ammonia
F-A-WN(U)-TiO_2	Furnace	Anatase	Tungsten	Urea
F-A-TaN-TiO_2	Furnace	Anatase	Tantalum	Ammonia
F-A-TaN(U) -TiO_2	Furnace	Anatase	Tantalum	Urea
F-R-undoped-TiO_2	Furnace	Rutile		
F-R-WN-TiO_2	Furnace	Rutile	Tungsten	Ammonia
F-R-WN(U)-TiO_2	Furnace	Rutile	Tungsten	Urea
F-R-TaN-TiO_2	Furnace	Rutile	Tantalum	Ammonia
F-R-TaN(U) -TiO_2	Furnace	Rutile	Tantalum	Urea
MW-A-undoped-TiO_2	Microwave	Anatase		
MW-A-WN-TiO_2	Microwave	Anatase	Tungsten	Ammonia
MW-A-WN(U)-TiO_2	Microwave	Anatase	Tungsten	Urea
MW-A-TaN-TiO_2	Microwave	Anatase	Tantalum	Ammonia
MW-A-TaN(U) -TiO_2	Microwave	Anatase	Tantalum	Urea
MW-R-undoped-TiO_2	Microwave	Rutile		
MW-R-WN-TiO_2	Microwave	Rutile	Tungsten	Ammonia
MW-R-WN(U)-TiO_2	Microwave	Rutile	Tungsten	Urea
MW-R-TaN-TiO_2	Microwave	Rutile	Tantalum	Ammonia
MW-R-TaN(U) -TiO_2	Microwave	Rutile	Tantalum	Urea

4.2.1 Anatase and rutile (pure phase)

Titanium iso-propoxide (8 mL, Sigma-Aldrich) and propan-2-ol (8 mL) were mixed together. After thorough mixing, deionised water (8 mL, 18MΩ cm) was added dropwise to the solution. The white precipitate was re-dissolved upon further stirring. The solution was left at room temperature for 24 hrs, followed by oven drying at 343 K for a further 24 hrs for complete solvent removal.

4.2.2 W,N- TiO_2 (ammonia precursor)

Tungstic acid (>97% Sigma Aldrich, 0.08g) was dissolved in ammonia solution (35%, 40 mL). The solution was added dropwise to titanium iso-propoxide (10 mL, Sigma-Aldrich) held in an ice bath, followed by stirring for 1 hr. The solution was left for the solvent to evaporate in the fume cupboard for at least 24 hrs followed by oven dried for another 24 hrs at 343 K.

4.2.3 W,N- TiO_2, (urea precursor)

Titanium iso-propoxide (8 mL, Sigma-Aldrich) and propan-2-ol (8 mL) were mixed together. After thorough mixing warm deionised water, containing the required amount of urea (99% Sigma Aldrich) (4 mL, 18MΩ cm) was added dropwise to the solution. The white precipitate was re-dissolved upon further stirring. Further deionised water (4 mL, 18MΩ cm) was then added to the solution, containing tungstic acid (>97% Sigma Aldrich, 0.08g). The solution was stirred for an hour. The solution was left for the solvent to evaporate in the fume cupboard for at least 24 hrs followed by oven dried for another 24 hrs at 343 K.

4.2.4 Ta,N- TiO_2 (ammonia precursor)

Tantalum ethoxide (>99% Sigma Aldrich,0.3 ml) was dissolved in ammonia solution (35%, 40 mL). The solution was added dropwise to titanium iso-propoxide (10 mL, Sigma-Aldrich) held in an ice bath. The solution was stirred for an hour. The solution was left for the solvent to evaporate in the fume cupboard for at least 24 hrs followed by oven dried for another 24 hrs at 343 K.

4.2.5 Ta,N- TiO_2, (urea precursor)

Titanium iso-propoxide (8 mL, Sigma-Aldrich) and propan-2-ol (8 mL) were mixed together. After thorough mixing warm deionised water, containing the required amount of urea (99% Sigma Aldrich) (4 mL, 18MΩ cm) was added slowly to the solution. The white precipitate was re-dissolved upon further stirring. Further deionised water (4 mL, 18MΩ cm) was then added to the solution, containing the tantalum ethoxide (>99% Sigma Aldrich, 0.3 ml). The solution was stirred for an hour. The solution was left for the solvent to evaporate in the fume cupboard for at least 24 hrs followed by oven dried for another 24 hrs at 343 K.

4.2.6 Calcination processes

The dry powders were ground in an agate mortar and then transferred into a ceramic crucible. The samples were calcined at 773 K and 1173 K for 2 hrs to obtain furnace calcined samples in the anatase and rutile phase, respectively. Samples calcined in the microwave furnace were calcined at the same temperatures for 2 hrs before cooling to RT, however, the main advantage of the microwave furnace is the drastic increase of the heating and cooling rate speed. For example, for an anatase sample it would require an overall of 10 – 12 hrs to obtain the final material powder (2 hrs to reach 773 K, 2 hrs remaining at the temperature and 6 – 8 hrs to cool down), whereas for a microwave calcined sample the overall process required 2.5 hrs (20 mins to reach 773 K, 2 hrs remaining at the temperature and 10 mins to cool down). For a rutile sample the furnace process increased in duration to 16 – 18 hrs overall as both the heating rate and the cooling time are longer. However, the rutile microwave samples were prepared within the same time scale as their anatase counterparts.

4.3 Reactions

4.3.1 Spin trap reactions

The EPR experiments were carried out using an EMX spectrometer and ex-situ irradiation was performed using a series of discrete wavelength LED lamps (see 4.5.5 for details). The suspensions were irradiated at 295 K with a UV or blue light (Table 4.1). The parameters for the EPR measurements used: microwave power of 10 mW, 10 scans with time constant of 5.12 ms, modulation frequency 100 kHz and 0.1 mT modulation depth.

Dimethyl sulfoxide (DMSO) was used as a solvent, at a volume of 1 mL, with 10 mg of catalyst and then 5 mM toluene and/or 5 mM paraformaldehyde (95%, Sigma Aldrich) were added and irradiated. After 5 min of irradiation 30 mM of the spin trap agent, *N*-*tert*-Butyl-α-phenylnitrone (PBN) (>98%, TCI) or 5,5-Dimethyl-1-pyrroline N-oxide (DMPO) (≥98%, Sigma Aldrich), were added and quickly the suspension was filtered and measured.

1 mL Deionised water, 100 µL glycerol (≥98%, Fisher Chemical) and the 10 mg of the catalyst were placed together and created a suspension that was irradiated under constant stirring. After 5 min of irradiation 30 mM DMPO was added and quickly the suspension was filtered and measured.

4.3.2 Photocatalytic reaction of glycerol transformation using the TiO_2 catalysts

In a two neck round bottom flask 40 mL of deionised water were placed, to that 100 µL of glycerol and 10 mg of catalyst were added. The flask was sealed and wrapped in aluminium foil, and the solution was purged with 1 bar of argon (Ar) for 30 mins. Once purging was completed the sample was transferred in the dark box, hovering over a stir plate. The stirring rate was set to 1000rpm and at 20 cm distance between the Pyrex flask and the xenon lamp. Using a syringe, gas aliquots of volume 300 µL were obtained and injected into the gas chromatographer.

4.4 Adsorbates

4.4.1 Gases

Oxygen (O_2) gas of 99.6 % purity was supplied by Argo International and was added via the vacuum manifold (described in 4.5.1) at 295 K, unless otherwise specified.

4.4.2 Liquids

The vapour pressure of two solvents were added to the cells. Toluene solvent was supplied by Sigma Aldrich and was of analytical grade. Dimethyl sulfoxide (≥99.9%) was provided by Honeywell.

4.5 Apparatus

4.5.1 Vacuum manifold

The sample treatment for solid-state EPR measurements was performed on the vacuum manifold (see schematic representation of the manifold in Figure 4.1), connected to a T-station 75 rotary pump. Base pressures of 10^{-4} mbar could be achieved, monitored by an Edwards or Leybold, Thermovac transmitter (TTR91R) wide range gauge. A mercury manometer or the Leybold gauge were used to measure the positive pressure of the gas added to the gas reservoir bulb. Using the gauge attached to the vacuum manifold the pressure of the gas added to the sample was able to be measured. The heat resistance lubricant Apiezon H was used to grease all non-fused joints, taps and connection points. Custom made cells with a glass bulb and vacuum connector, fused to a standard 4 mm EPR tube were used for sample treatment. The samples were heated in the glass bulb section using a thermostatically controlled electric furnace prior to transfer to the EPR tube section for measurement.

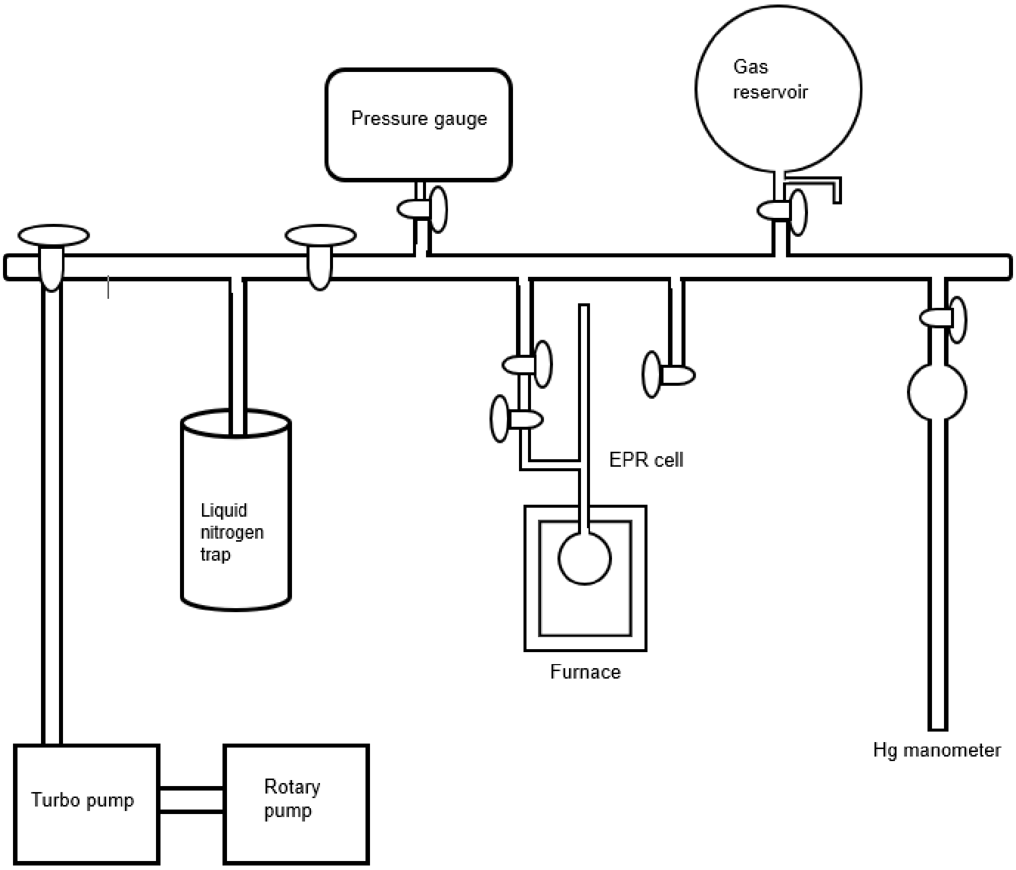

Figure 4.1: Schematic representation of the vacuum manifold that was used during this work.

4.5.2 Thermostatically controlled furnace

A thermostatically controlled furnace (Severn Furnaces Limited, TF38-2-12, 240 volts, 500 watts) used a thermocouple to maintain a stable temperature between 323 – 393 K.

4.5.3 Conventional furnace and Microwave controlled oven

The conventional furnace (Carbolite Furnaces CTF, 12/50, 220/240 volts, 1980 watts) used a rate of 5 K/min and with a 2-hour calcination period at a constant temperature of 773 K and 1173 K. The microwave oven (Milestone PYRO microwave ashing system 480T) calcined samples using the same rate and the calcination period remained 2 hrs.

4.5.4 EPR spectroscopy

The continuous wave (CW) EPR spectra were recorded using two instruments, an X-band Bruker EMX spectrometer and Bruker Elexsys E500 spectrometer. Both instruments utilised the high sensitivity HS0208 cavity, operating at 100 kHz modulation frequency, 0.1 – 0.3 mT modulation depth and 10 mW microwave power, and incorporated a variable temperature unit (100 – 293 K). All EPR simulations were performed using the Easyspin toolbox (version 6.0.0-dev.51) within MATLAB.(1)

4.5.5 Light sources

Two different light sources were used for the irradiation of the samples. The tunable light source (TLS) (TLS-55/72-X300) from Sciencetech Inc, was used to irradiate the samples in-situ when using the EMX spectrometer. Any other irradiations were performed using light emitting diode (LED) lamps, provided by Labino, with an output power range of 40 – 354 mW for the visible region wavelength and >16000 μW / cm^2 for UV wavelength (see Table 4.1).

Table 4.1: LED lamp properties used for the experiments.

LED	Wavelength / nm	Bandwidth / nm	Typical Output / V	Power / mW
UV	365	350- 395	0.212	>16 mW/cm^2
Blue	455	440- 460	0.353	354
Green	530	520- 530	0.126	127
Red	625	620- 645	0.208	209

For the photocatalytic experiments presented in Chapter 7 a xenon arc lamp (LOT Quantum Design MODEL: LSB520; see appendix A.1 for spectral output), enclosed in an arc lamp housing (LOT Quantum Design Model LSH102), was connected to a power supply (LSN 150/2).

4.6 Procedures

4.6.1 Dehydroxylation

Samples were initially evacuated to a base pressure of 10^{-4} mbar at 298 K, followed by heating at 323 K under dynamic vacuum for 12 hrs.

4.6.2 Addition of vapour pressures

Liquid solvents were transferred to the bulb section of the custom-made EPR cells and exposed to three freeze-pump-thaw cycles to remove dissolved oxygen prior to exposure of vapour pressures to solid samples. To achieve the desired vapour pressure, toluene and DMSO were heated at 313 K and 363 K, respectively.

4.6.3 Co-adsorption of mixture of gases to dehydroxylated surfaces

Following the same procedure as described in section 4.6.2 the vapour pressures of each gas was added to the vacuum line prior to sample exposure, thus allowing for mixing to occur and obtaining the desired ratio of ~ 10:1 mbar organic solvent to oxygen. In order to obtain the required ratio 3.5 mbar of molecular oxygen was mixed with 35 mbar of gas toluene or DMSO, which were acquired via vapour pressures by heating to 313 and 363 K respectively.

4.6.4 Irradiation

Irradiations took place both ex-situ and in-situ. Once the gas was in contact with the samples the cell was cooled at 77 K and irradiated with UV or blue light for 30 mins and then it was rapidly transferred to a pre-cooled cavity. The in-situ irradiation used the TLS and took place between the 100 – 298 K temperatures, while the ex-situ irradiation used the LED lamps and took place between 77 (liquid nitrogen) and 298 K. Unless stated otherwise, the irradiation for the spin trap measurements was 5 mins, while irradiation for the solid state EPR experiments lasted 30 mins. The irradiation of the samples during the photocatalytic reactions took place at 295 K for 1 hour, under constant stirring.

4.6.5 Superoxide generation through Irradiation

A sample with a dehydroxylated surface was exposed to 10 Torr of molecular oxygen at room temperature (298 K). The sample was irradiated at low temperature (77 – 100 K) for 30 mins and then the sample was quickly placed to a pre-cooled cavity. Spectra were obtained under and after evacuation of oxygen atmosphere, at low temperatures (77 – 100 K).

4.7 Characterisation Techniques

Acknowledgments go to Dr Greg Shaw who, due to COVID capacity and training restrictions, assisted in acquiring data for XRD, Raman, FTIR, UV-Vis and BET data.

Acknowledgments go to Dr David Morgan who acquired data for XPS.

4.7.1 X-Ray Diffraction

The X-Ray diffraction data was acquired using X'Pert pro (serial number DY2739 diffractometer) using the X'Pert High Score Plus software. The specific parameters used were as follows: geometry: Bragg-Brentano , 2θ: 10-100° with operating current of 40 mA and tension of 40 kV, step size: 0.0170, scan step time (s): 24.130, slits: 1/2; 1/2; 5 and anode: Cu.

4.7.2 X-Ray Photoelectron Spectroscopy

X-ray photoelectron spectroscopy (XPS) was performed using the Thermo Fisher Scientific K-alpha+ spectrometer. The samples were analysed applying a micro-focused monochromatic Al x-ray source (72 W) over an area of roughly 400 microns. The data was obtained at pass energies of 150 eV for survey scans and 40 eV for high resolution scans with steps of 1 and 0.1 eV, respectively. The charge neutralisation of each sample was completed via a combination of both low energy electrons and argon ions. CasaXPS (v2.3.26 PR1.0 N) was used to perform data analysis through Scofield cross sections.

4.7.3 Raman

Rama spectra for the samples were produced using the Renishaw inVia Raman microscope, with amodu-laser argon ion stellar-REN. The average power output was 25 mW for the lasers, with a beam diameter of 0.65 mm, a radiation emittance of 514 nm and an average exposure time of 5 secs, with the accumulation set to 10.

4.7.4 FTIR

All data for the samples were obtained using a Shimadzu IRAffinity – 1S Fourier transform infrared spectrophotometer with scans being in the range of 400 – 4000 cm^{-1}.

4.7.5 Brunauer – Emmett – Teller (BET)

For the BET analysis, after the samples were degassed at 120 °C overnight with a Quantachrome Flovac degasser and then weighed accurately before analysis using the Quantachrome Nova 2200e instrument. Surface areas were calculated via the BET method. Nitrogen porosimetry was performed with a 5-point, at -196 °C, over the range $P/P_o = 0.005 – 0.2$.

4.7.6 Solid State UV

The UV-Vis solid state spectra were obtained using the Cary Series UV-Vis spectrophotometer. The parameters used were of a 200-800 nm (%R) range, with scan rate of 198.00 nm/min, date internal of 0.330 nm, average time set at 0.100 sec and 2 number of scans. The resulting reflectance spectra were transformed into absorption spectra and then the %R was converted in absorbance (a.u.) by the Kubelka-Munk function (Equation 4.1):

$$F(R_\infty) = (1 - R_\infty^2)/(2R_\infty) \qquad (4.1)$$

4.7.7 Gas chromatography (GC)

A GC (Clarus 480) (a Perkin Elmer Clarus 480) with a thermal conductivity detector (TCD) and a 2MX1/8SilicoStol Molecular Sieve 5A 80/100PE 800NCCI SS column. Argon was used as the carrier gas. The conditions of the GC were as follows: flow rate of carrier gas was set to 30 ml / min, the injector port and column temperature was 150 °C and the detector temperature at 175 °C.

4.8 References

(1) EasySpin: https://easyspin.org/

(2) Labino Nova Torch, available at: Labino Forensic Crime Lights (MPXL & LED) Range - ALS (advanced-ndt.co.uk)

Chapter 5. Characterisation of the co-doped TiO_2

The electrical, crystallographic, and structural relationships for doped and co—doped TiO_2 semiconductor nanoparticles are explored in this chapter. Dopant inclusion, corresponding charge compensation, and their impact on charge carrier photostability are highlighted. This will be investigated on co—doped materials in this thesis and this section presents a comparison between the material's consequent activity and that of pristine TiO_2. The focus of the research is on the need for highly active catalysts that do not require costly and scarce platinum—group metals. As the introduction of a dopant could enhance the charge separation, which has an impact on the lifespan of charges. (1-7)

The dopants were selected because they have been demonstrated to increase the electron storage capacity (and lengthen electron discharge periods) in hetero-junction films and TiO_2-WO_3 mixed oxides. (8) The resulting experimental data of anatase and rutile WN- and TaN- co doped materials is contrasted with that of undoped anatase and rutile TiO_2 in the discussion that follows. Additionally, the effect of the source for the non-metal dopant was investigated as it has been shown that the precursor plays a role in the photocatalytic activity of the materials.

5.1 X-ray Diffraction (XRD)

X-ray diffraction (XRD) is employed to primarily analyse material attributes such as crystal structure, crystallite size, and strain. X-ray diffraction (XRD) is a powerful technique used to analyse the crystal structure of materials, but its ability to directly detect dopants, especially at low concentrations, is limited. However, XRD can provide indirect evidence of doping through several observable effects on the diffraction patterns of the host material.

Dopants often alter the lattice parameters of the host material due to differences in ionic radii between the dopant and the host atoms. This can cause shifts in the positions of the XRD peaks. For example, if a dopant ion is larger or smaller than the ion it replaces, the lattice will expand or contract, respectively. These changes can be quantified by Rietveld refinement, which allows for precise determination of lattice constants, where a (doped) ≠ a (undoped). The introduction of dopants can affect the crystallite size and introduce micro-strain in the material. For example, if Ta^{5+} (ionic radius ~0.64 Å) substitutes for Ti^{4+} (ionic radius ~0.605 Å) in TiO_2, it may cause an increase in the lattice parameters. Changes in lattice parameters due to doping can result in shifts of the XRD peaks. Additionally, the introduction of dopants can cause peak broadening due to the introduction of strain or defects in the crystal lattice, as the lattice will expand or contract slightly to accommodate the change of the metal atom sizes. (9) In some cases, dopants may not fully incorporate into the host lattice and can form secondary phases or compounds. These secondary phases will produce additional peaks in the XRD pattern, which can be identified and matched to known compounds and could occur for both tungsten and tantalum doped materials. For example, peaks corresponding to Ta_2O_5 may appear if tantalum does not completely integrate into the TiO_2 lattice, Equation 5.1 and peaks for WO_3 secondary phase are described from Equation 5.2.

$$TiO_2 + Ta \rightarrow TiO_2 + Ta_2O_5 \text{ (secondary phase)} \quad (5.1)$$

$$TiO_2 + W \rightarrow TiO_2 + WO_3 \text{ (secondary phase)} \quad (5.2)$$

The XRD patterns of the anatase co-doped samples are shown in Figure 5.1. All of the samples clearly show patterns typical of the anatase structure. The XRD patterns obtained for the $Ti_{1-y}W_yN_xO_2$ and $Ti_{1-y}Ta_yN_xO_2$ demonstrated the following peaks and Miller indices at 2θ (°) = 25.47 [101], 37.18 [103], 38.07 [004], 38.75 [112], 48.17 [200], 54.15 [105], 55.19 [211], 62.87 [201], 68.96 [116], 70.39 [220], 75.24 [215] and 76.11 [301] for all of the co-doped samples, all of which are characteristic of an anatase diffraction pattern. (10) Due to the absence of peaks between 2θ (°) = 25 – 35, especially between 23 – 25° (typically observed as three continuous peaks before the dominant TiO_2 peak), it can be concluded that there is no evidence of formation of either tungsten oxides WO_x or tungsten bronze W_xO_y structures. (11) Similarly, the absence of peaks in the 2θ (°) range of 20–55 indicates that no tantalum oxide structures, such as Ta_2O_5, were formed. (12) However, for the tantalum co-doped samples the peaks demonstrated a broadness that could be attribute to the extra strain present in the crystal structure due to the different size of tantalum. In XRD, the detection of dopants like tungsten, tantalum and nitrogen depends on the concentration of the dopants, the size of the dopant atoms relative to the host lattice atoms, and how the dopants integrate into the lattice structure. As N atoms are relatively small and depending on whether N substitutes for a lattice atom (such as oxygen) or occupies an interstitial position, the effect on the lattice parameter may be smaller and harder to detect via XRD. However, significant doping could lead to a measurable shift in peak positions or broadening due to lattice strain.

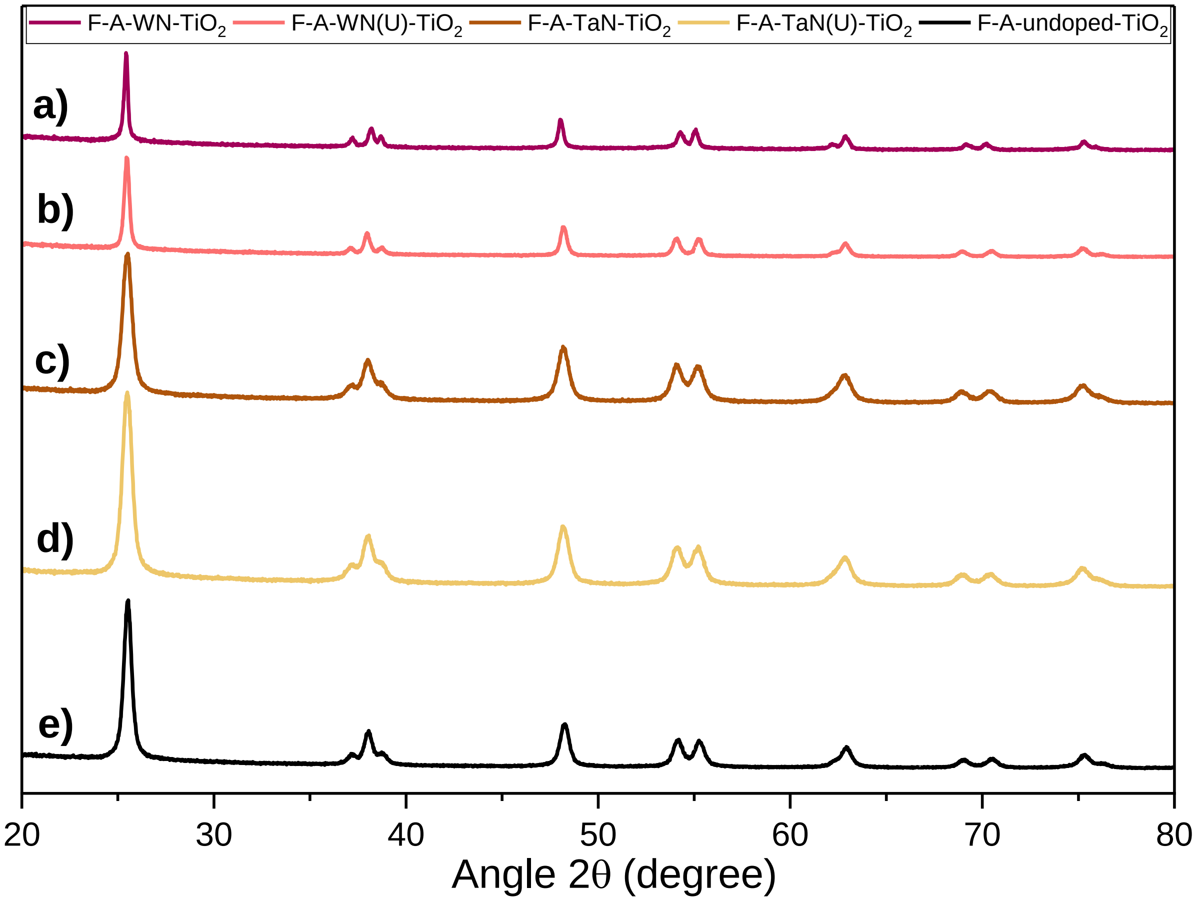

Figure 5.1: XRD pattern for the anatase co-doped TiO_2 a)F-A- WN-TiO_2, b) F-A-WN(U)-TiO_2, c) F-A-TaN-TiO_2, d) F-A-TaN(U)-TiO_2 and e) F-A-undoped-TiO_2.

The XRD patterns of the namely rutile co-doped samples are shown in Figure 5.2. The XRD patterns obtained for the $Ti_{1-y}W_yN_xO_2$ and $Ti_{1-y}Ta_yN_xO_2$ demonstrated a mixture of phases present in each sample. However, the diffraction pattern and Miller indices at peaks at 2θ (°) = 27.65 [110], 36.28 [101], 39.50 [200], 41.43 [111], 44.25 [210], 54.64 [211], 56.81 [220], 63.10 [002], 64.40 [310], 69.97 [301] and 70.15 [112] are characteristic of rutile. Additionally, for WN, TaN and TaN(U) samples the peaks and Miller indices observed at 2θ (°) = 25.53 [101], 37.18 [103], 38.07 [004], 38.75 [112], 48.17 [200], 54.15 [105], 55.19 [211], 62.87 [204], 68.96 [116], 70.39 [220], 75.24 [215] and 76.11 [301], are all characteristic of an anatase diffraction pattern. Similarly, with the anatase phase materials, there are no reflection peaks at 2θ (°) = 25-35 and at 2θ (°) = 20-55, thus, indicating the absence of tungsten and tantalum oxides, respectively. A rutilisation constraint is demonstrated by the presence of the anatase peak at 2θ (°) = 25.53 for WN, TaN and TaN(U) samples. These co-doped samples have demonstrated that the type and source of the dopants affect the rutilisation formation during the calcination process. The co-doped materials with Ta as their metal dopant presented a high constraint in achieving full rutilisation, compared to the W co-doped that managed to achieve complete or near complete rutilisation. The biggest difference is demonstrated between the WN(U), having the least affect with no observable anatase peaks, and the TaN(U), which exhibits almost a 50% anatase — 50% rutile mixture, as demonstrated from Rietveld refinement calculations.

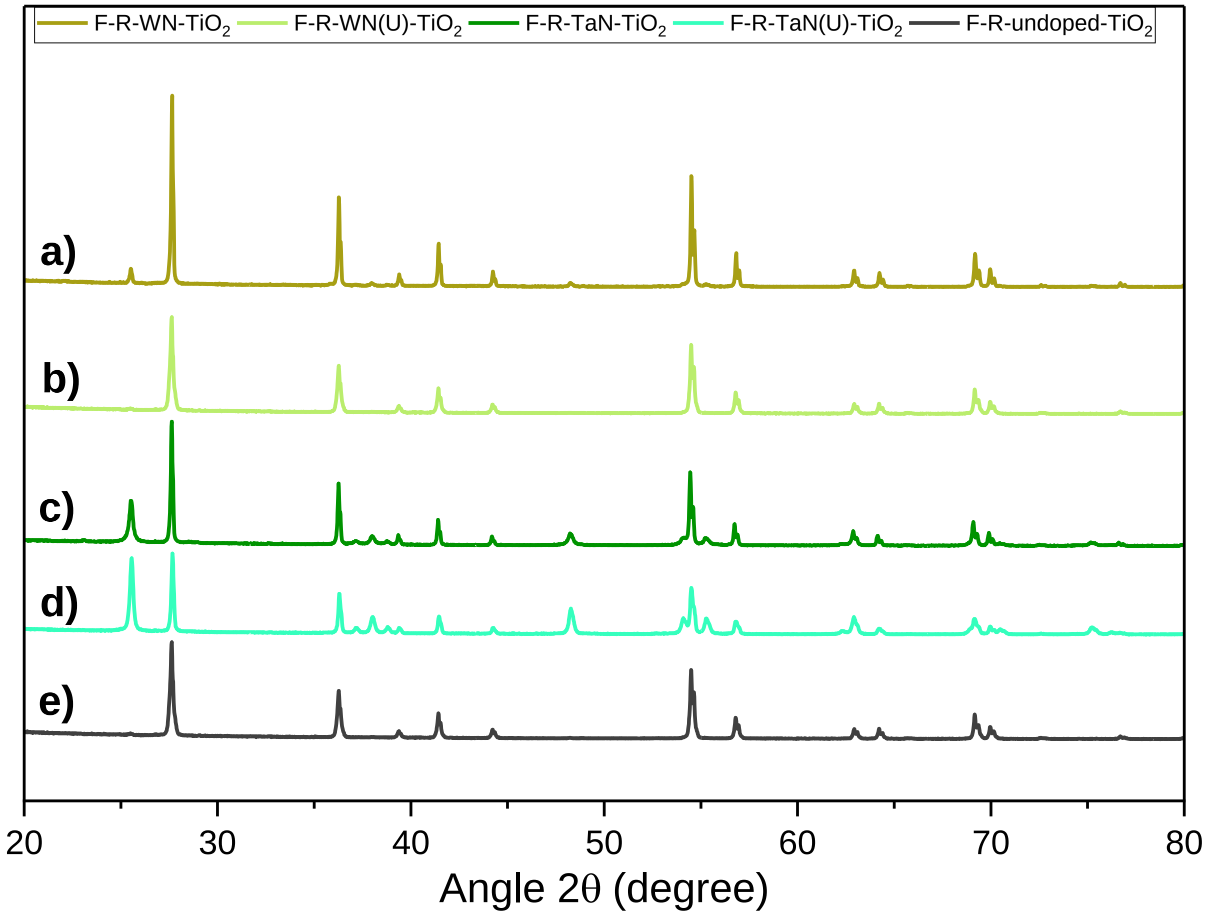

Figure 5.2: XRD pattern for the rutile co-doped TiO_2 a) F-R-WN-TiO_2, b) F-R-WN(U)-TiO_2, c) F-R-TaN-TiO_2, d) F-R-TaN(U)-TiO_2 and e) F-R-undoped-TiO_2.

Rietveld refinement of all anatase and rutile samples indicated variations in the unit cell parameters shown in Table 5.1 which demonstrates an increased strain in the unit cell. This is predominantly attributed to the different size of the cations, W^{5+} = 0.620 Å and Ta^{5+} = 0.640 Å, compared to the Ti^{4+} = 0.605 Å. Peak splitting refers to the appearance of two or more closely spaced peaks where you would normally expect only one. When XRD peaks do not show any splitting or superstructure, it indicates that the crystal maintains a high degree of uniformity in its lattice. The lattice remains regular and undisturbed by factors such as doping. Thus, the lack of splitting or formation of superstructure in the XRD spectra demonstrated that the incorporation of W and Ta atoms did not affect the symmetry when they were added to into the lattice.

If the concentration of W or N dopants is very low, the changes to the lattice parameter might be too small to be detected by XRD. In such cases, the overall structure may remain nearly unchanged, and other characterization techniques like XPS (X-ray photoelectron spectroscopy) could be more useful for confirming the presence of dopants.

Table 5.1: A comparison of the refined structural parameters for the co-doped TiO_2 samples, including the parameters for undoped anatase and rutile.

Sample	Anatase Unit Cell/ Å		Rutile Unit Cell/ Å		% Morphology	
	a = b	c	a = b	c	Anatase	Rutile
F-A-undoped-TiO_2	3.799	9.539	—	—		
F-A-WN-TiO_2	3.789	9.480	—	—	100.00	—
F-A-WN(U)-TiO_2	3.794	9.519	—	—	100.00	—
F-A-TaN-TiO_2	3.802	9.474	—	—	100.00	—
F-A-TaN(U)-TiO_2	3.798	9.475	—	—	100.00	—
F-R-undoped-TiO_2	—	—	4.594	2.959		
F-R-WN-TiO_2	3.788	9.519	4.592	2.957	7.37	92.63
F-R-WN(U)-TiO_2	3.787	9.518	4.593	2.959	2.00	98.00
F-R-TaN-TiO_2	3.787	9.519	4.598	2.962	25.12	74.88
F-R-TaN(U)-TiO_2	3.788	9.520	4.597	2.961	45.03	54.97

5.2 X-ray Photoelectron Spectroscopy (XPS)

In XPS analysis of co-doped samples, the primary focus was on identifying the presence of both dopants and confirming their relative concentrations. Understanding the chemical states of the dopants is crucial, as it reveals their oxidation states and how they interact with the host material. Additionally, verifying the composition of the host material alongside the dopants is important for a complete analysis. XPS can also help detect any interactions or chemical bonding between the dopants that might affect the material's overall properties. The uniformity of doping across the surface is another key factor, as is determining whether the dopants are concentrated at the surface or distributed throughout the bulk. Furthermore, any shifts in binding energies can provide insights into changes in the material's electronic structure due to co-doping, helping to better understand its impact on properties such as catalytic activity. (13)

The XPS spectra for the anatase samples are presented in Figure 5.3 (a — d), displaying the O (1s), Ti (2p), N (1s), W (4d) and Ta (4d) and W (4f) and Ta (4f) core levels, respectively. The metal 4f region (around 35-40 eV) demonstrates overlaps between the three metals (Appendix A.2.1), therefore the 4d (220-270 eV) region is used for characterisation. XPS quantification for the total contribution of the metal and nitrogen elements was performed and the results are presented in Table 5.2.

The core level spectra for the O (1s) region, Figure 5.3a, exhibits the presence of the lattice Ti—O at 530.1 eV, with two smaller shoulders at 530.5 eV and 532.2 eV, corresponding to hydroxide and carbonate, respectively.(14) The carbonate peak is present for the WN-, TaN- and TaN(U)-TiO_2 samples. Both the hydroxide and the carbonate peaks are attributed to handling the samples in air.

Figure 5.3b signals are representative of Ti peaks. The peaks at 458.9 eV and 464.7 eV are attributed to Ti $2p_{3/2}$ and Ti $2p_{1/2}$ states (doublet separation of around 6 eV), confirming the presence of the Ti^{4+} species present in the lattice of the TiO_2. The satellite peak at 472.4 eV is attributed to the Ti $2p_{3/2}$ with a 13.5 eV shift from the main peak, which is created due to the sudden changes in Coulombic potential as the ejected electron passes through the valence band.(15) From the comparison of atomic percentage (Casa2326-PR1-0) of the oxygen and titanium levels a ratio of 1.96 for O/Ti is calculated.

Typical XPS peaks for nitrogen doped TiO_2 are found between 396 – 404 eV and are largely affected by the preparation methods and conditions of the sample. Commonly, peaks around 397 eV are associated with N^{2-} anions that substitute oxygen in the TiO_2 lattice, whilst peaks featured around 399.5 eV present a smaller chemical shift and can be attributed to an interstitial nitrogen. (16) For the Ta-containing samples there is an overlap of the nitrogen peaks with the Ta $4p_{3/2}$ signal. From the N (1s) region shown in Figure 5.3c, the W- containing samples demonstrated only one N (1s) peak at 399.4 eV which is produced from an interstitial site of a nitrogen bound to hydrogen. For the tantalum co-doped samples only, the N (1s) peak at 397.1 eV is indicative of substitutional N doping in the lattice. Additionally, the signal at 404.4 eV, for these samples, is attributed to Ta $4p_{3/2}$, which demonstrates the presence of Ta at the surface of the nanoparticles.

The core levels presented in the metals d region (Figure 5.3d) can be utilised to give an insight, for the W (4d) and Ta (4d) core levels. The Ta $4d_{5/2}$ and $4d_{3/2}$ peaks appear at 230.2 eV and 241.8 eV, respectively. These peaks confirm the introduction of tantalum dopant, at least at the surface of the material. The peaks at 247.3 eV and 259.8 eV are contributions from the W $4d_{5/2}$ and $4d_{3/2}$ electronic states, respectively, again representing the incorporation of the tungsten dopant. The intensities for the F-A-TaN-TiO_2 and F-A-TaN(U)-TiO_2 samples demonstrate that more tantalum is incorporated in the material synthesised from ammonia. (17)

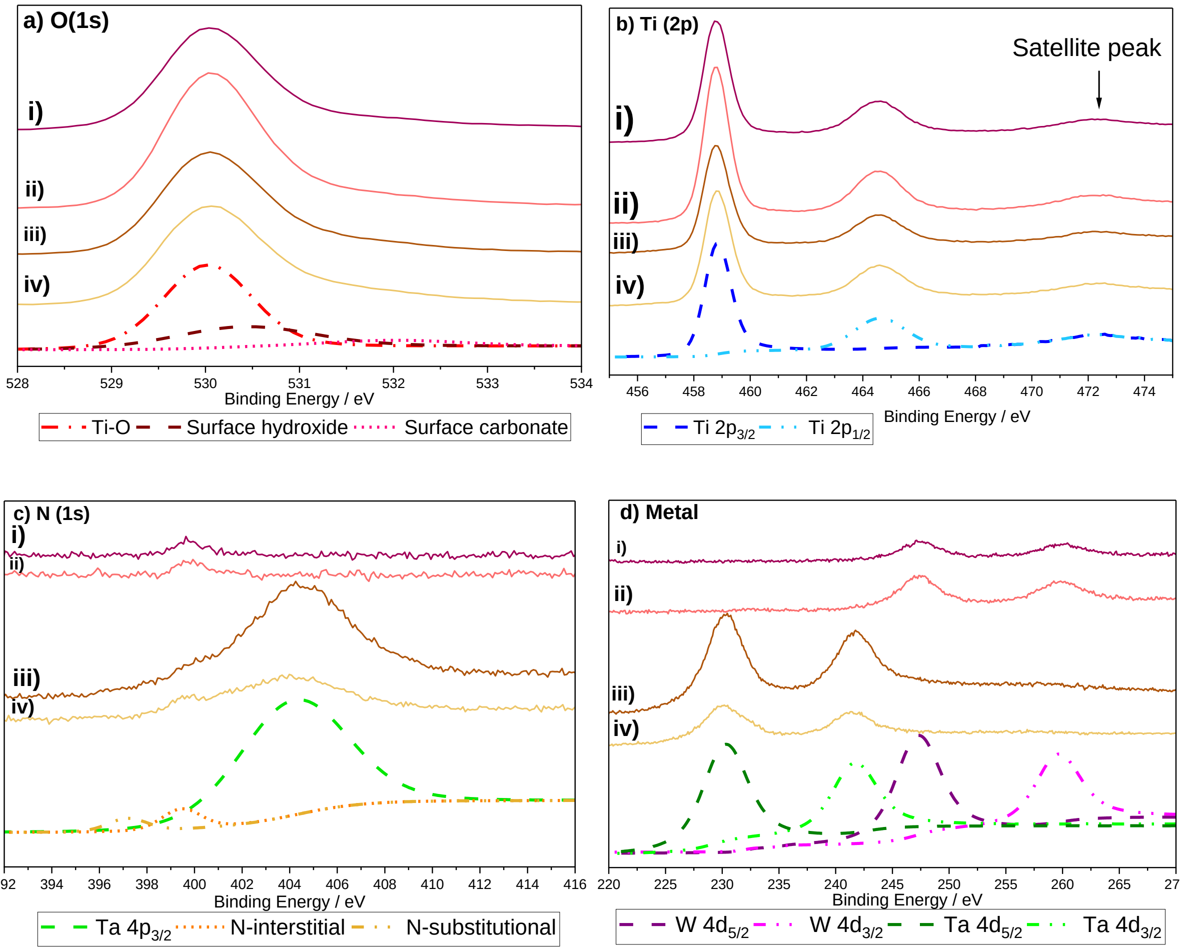

Figure 5.3: XPS spectra showing the (a) O (1s), (b) Ti (2p), (c) N (1s) and (d) metal core levels for the anatase co-doped TiO_2, namely i) F-A-WN-TiO_2, ii) F-A-WN(U)-TiO_2, iii) F-A-TaN-TiO_2 and iv) F-A-TaN(U)-TiO_2.

Table 5.2: XPS quantification of the atomic percentage concentration for each dopant from the binding energies for the O 1s, Ti 2p, N 1s and metal 4d for the anatase samples.

Sample	Dopant Atomic %		Sample	Dopant Atomic %	
	W	Nitrogen		Ta	Nitrogen
F-A-WN-TiO_2	0.36	5.97	**F-A-TaN-TiO_2**	0.83	9.66
F-A-WN(U)-TiO_2	0.52	3.36	**F-A-TaN(U)-TiO_2**	0.61	4.12
F-R-WN-TiO_2	0.59	4.76	**F-R-TaN-TiO_2**	0.77	12.7
F-R-WN(U)-TiO_2	0.97	3.84	**F-R-TaN(U)-TiO_2**	0.89	5.51

From Table 5.2 the formula for the anatase $Ti_{1-y}W_yN_xO_2$ for the ammonia and urea precursors become $Ti_{0.9964}W_{0.0036}N_{0.0597}O_2$ and $Ti_{0.9948}W_{0.0052}N_{0.0336}O_2$, respectively. While the $Ti_{1-y}Ta_yN_xO_2$ for the ammonia and urea precursors become $Ti_{0.9917}Ta_{0.083}N_{0.0996}O_2$ and $Ti_{0.9939}Ta_{0.0061}N_{0.0412}O_2$, respectively. For the rutile $Ti_{1-y}W_yN_xO_2$ for the ammonia and urea precursors become $Ti_{0.9941}W_{0.0059}N_{0.0476}O_2$ and $Ti_{0.9903}W_{0.0097}N_{0.0384}O_2$, respectively. While the $Ti_{1-y}Ta_yN_xO_2$ for the ammonia and urea precursors become $Ti_{0.9923}Ta_{0.0077}N_{0.0996}O_2$ and $Ti_{0.9911}Ta_{0.0089}N_{0.0551}O_2$, respectively. The aimed nitrogen theoretical was 25%, it was set high as nitrogen is small and during calcination it burns off and escapes from the material. While the theoretical metal dopants percentage was 1%.

The XPS spectra for the corresponding rutile samples are presented in Figure 5.4 (a — d), displaying the O (1s), Ti (2p), N (1s), W (4d) and Ta (4d) core levels, respectively. XPS quantification for the total contribution of each element was performed and is listed in Table 5.2. The core level spectra for O (1s), Ti (2p) and metal (4d) present the very similar peaks as the anatase samples, in particular the following binding energies: 530.1 eV (Ti—O), 530.6 eV (surface hydroxide), 532.4 eV (surface carbonate), 458.8 eV (Ti $2p_{3/2}$), 464.6 eV (Ti $2p_{1/2}$), 472.3 eV (Ti satellite), 230.2 eV (Ta $4d_{5/2}$), 242.6 eV (Ta $4d_{3/2}$), 247.5 eV (W $4d_{5/2}$) and 260.1 eV ($4d_{3/2}$).

Figure 5.4c demonstrates two N associated peaks for all samples and for the Ta doped samples there is an overlap of the nitrogen peaks with the Ta $4p_{3/2}$ signal at 404.4 eV which demonstrates the presence of Ta at the surface of the nanoparticles. The N (1s) peak at 399.4 eV for the F-R-WN-TiO_2 sample, originates from an interstitial site of a nitrogen bound to hydrogen. While F-R-WN(U)-TiO_2 presented the smallest peak at this binding energy. The F-R-WN-TiO_2, F-R-TaN-TiO_2 and F-R-TaN(U)-TiO_2 samples exhibited a second N (1s) peak at 397.1 eV, indicative of substitutional N doping in the lattice.

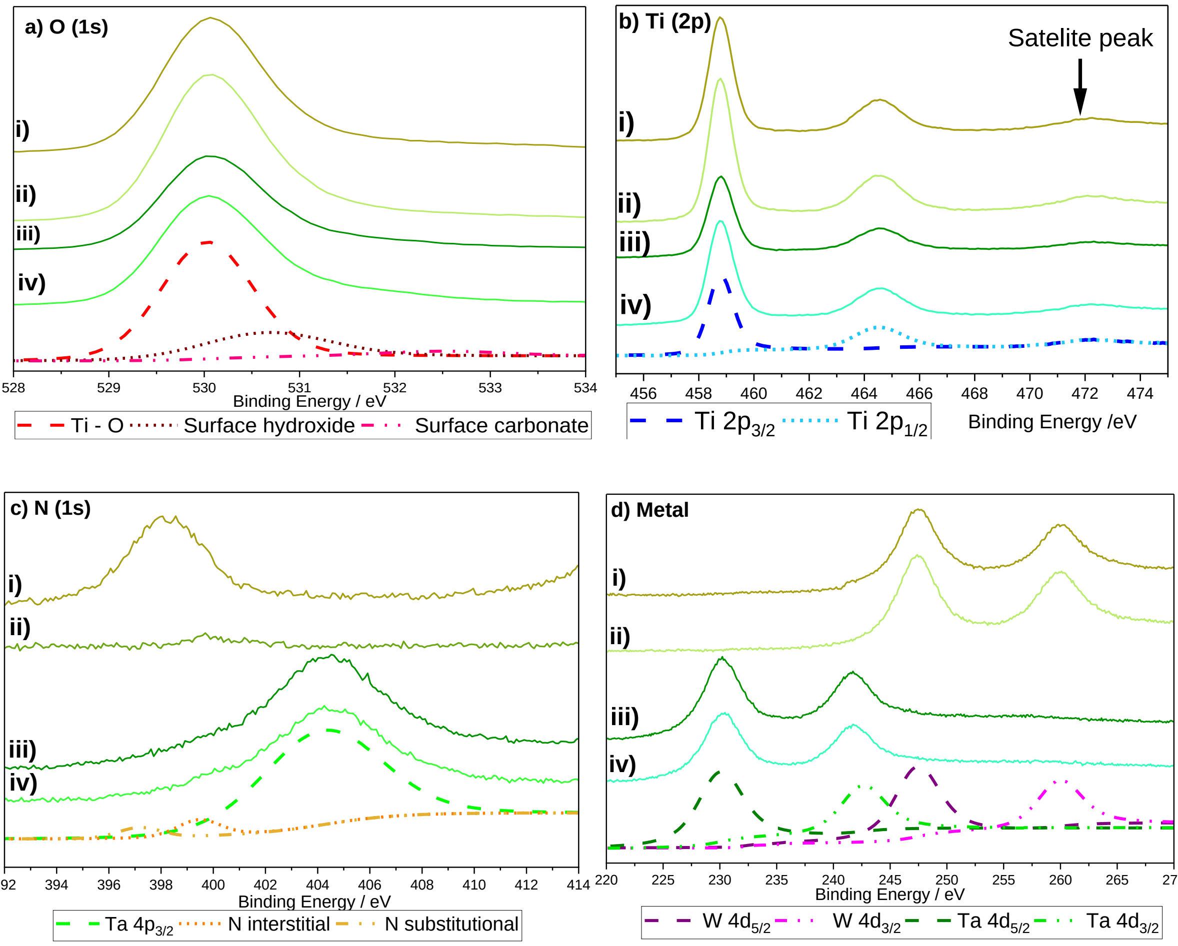

Figure 5.4: XPS spectra showing the (a) O (1s), (b) Ti (2p), (c) N (1s) and (d) metal core levels for the rutile co-doped TiO_2, namely i) F-A-WN-TiO_2, ii) F-A-WN(U)-TiO_2, iii) F-A-TaN-TiO_2 and iv) F-A-TaN(U)-TiO_2.

5.3 UV—Vis Diffuse Reflectance Spectroscopy

The absorbance spectra of the compounds as a solid are obtained using ultraviolet-visible (UV-Vis) spectroscopy. The wavelength range of 800–200 nm is covered by the UV-Vis region of energy for the electromagnetic spectrum, which covers 1.5–6.2 eV. Data from UV-Vis spectroscopy can provide both qualitative and quantitative information about a particular material. UV-Vis of the co-doped samples was utilised to examine the optical properties and understand the impact of doping on the material. This method determined changes in the band gap energy by analysing the absorbance spectra. The technique identified intra-band states introduced by doping and observed as additional absorption features. For materials intended for photocatalysis, UV-Vis spectroscopy is useful in evaluating the light absorption range and efficiency, which could be enhanced or modified by the co-doping process of the samples. In undoped TiO_2 the optical band gap occurs due to the electronic transition O 2p → Ti 3d and is representative of the intrinsic band gap of the semiconductor. (18) When dopants, such as W, Ta and N, are introduced intra-bands states are exhibited as well, hence creating the extrinsic band gap with the metal dopants offering an acceptor level and the non-metal dopant offering a donor level.

UV-VIS data for all materials is presented in Figure 5.5. For the synthesised F-A-undoped-TiO_2 and F-R-undoped-TiO_2 the bandgaps were calculated as 3.20 eV and 3.00 eV, respectively, and agreed with literature.(19) The higher band gap of anatase is attributed to the phase's electronic structure, which is more favourable for electron transport. In UV-Vis spectra, anatase absorbs UV light, but its band gap is too wide for effective visible-light absorption. Thus, anatase TiO_2 is primarily active under UV radiation, limiting its utility in visible-light-driven applications. Rutile's narrower band gap allows for some absorption in the visible range, though its photocatalytic activity is still predominantly UV-driven. The smaller band gap is due to rutile's more compact crystal structure, which influences the energy required to excite electrons from the valence band to the conduction band.(20)

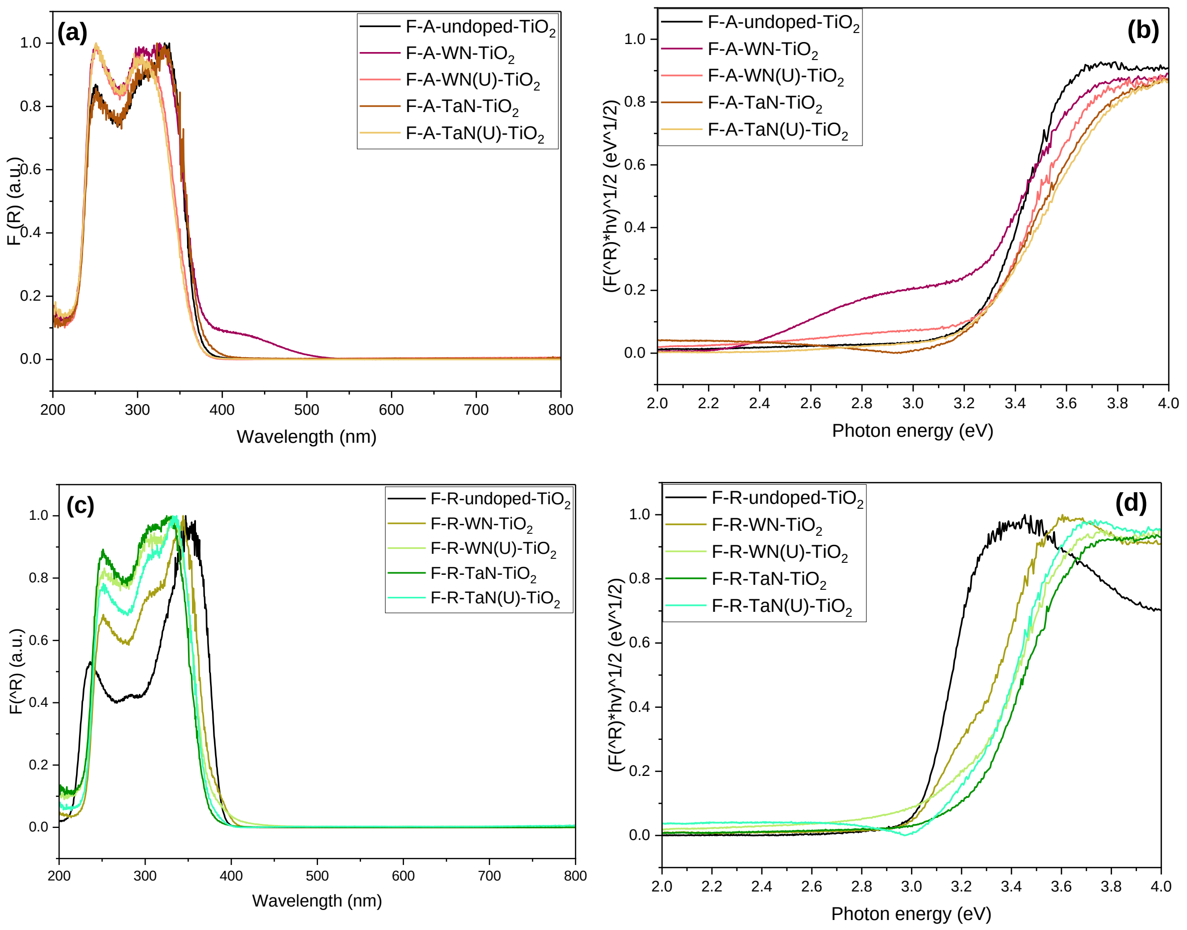

Figure 5.5: (a, c) UV-Vis absorption spectra of the co-doped materials and (b, d) corresponding Tauc plots for the representative samples (top-anatase, bottom-rutile).

All of the anatase samples containing nitrogen from the ammonia precursor displayed a yellow colour that was more pronounced at the lower (773 K) calcination temperature. The UV–Vis absorption results show that the more pronounced colouration is the result of the absorption edge extending into the visible range. The nitrogen containing samples have an extra absorption band in the 400–500 nm range in addition to the band gap. The absorption peak at 358 nm corresponds to the indirect bandgap of the undoped material, with different values expected for the two phases. Upon nitrogen doping, an additional absorption appears at 438 nm, signifying a sub-bandgap transition, Figure 5.5(a). This feature is responsible for the yellow coloration observed in the doped samples. The results of solid-state UV spectroscopy for the anatase co-doped materials are shown on the Table 5.3, the absorption spectra and the corresponding tauc plots can be found in Figure 5.5. The anatase W-containing samples exhibited a greater decrease of the E_{gap} through the introduction of sub-bandgap states thus, bringing the individual optical band gap into the visible light region. In contrast, the Ta-containing samples exhibit only a smaller decrease in the E_{gap} when compared to F-A-undoped-TiO_2, indicating that the photocatalytic capabilities remain predominantly in the UV absorption region.

Compared to the corresponding anatase samples (which as mentioned were an obvious yellow colour), the rutile samples were slight off-white colours. The results of solid-state UV spectroscopy for the rutile co-doped materials are listed in Table 5.3, the absorption spectra and the corresponding tauc plots can be found in Figure 5.5. Once doping occurred the band gap of the rutile co-doped sample demonstrated an increase of their E_{gap}, approaching values closer with anatase (3.20 eV). This slight increase could be attributed to the small increase in the crystal structure and the presences of anatase crystalline phase, both of which can were detected via XRD. Both W-based co-doped samples had a smaller weight percentage of anatase compared to both Ta-based, which agrees with the two different trends of the E_{gap} increase. The samples containing tungsten as the metal doping exhibited only a relatively small increase of the E_{gap} of up to 0.08 eV, in comparison to the undoped material with 3.00 eV. A larger increase is observed for Ta-containing materials with the E_{gap} reaching an increase of up to 0.20 eV, compared to the F-R-undoped-TiO_2.

F-A-WN-TiO_2 has a significant impact on the anatase phase, reducing the E_{gap} from 3.20 eV to 2.85 eV. This change suggests that the doping effectively modifies anatase’s electronic structure, enhancing visible light absorption and making it more suitable for photocatalytic applications, as doping introduces intra-band states. In contrast, F-R-WN-TiO_2 has little effect, with the band gap remaining around 3.01 eV. The difference in response suggests that anatase's more flexible crystal structure better accommodates the dopant, while rutile's compact lattice limits the doping influence on the band gap. The F-A-WN(U)-TiO_2 demonstrates a smaller degree of the E_{gap} when compared to F-A-WN-TiO_2, indicating that the electronic structure remains similar to that of the F-A-undoped-TiO_2, demonstrated via the calculations from the XRD Rietveld refinement. The F-R-WN(U)-TiO_2 demonstrated a slight increase reaching the 3.08 eV, indicating a similar crystal structure to that of F-R-WN-TiO_2 and of the F-R-undoped-TiO_2.

In contrast to the W-based co-doped materials, the F-A-TaN-TiO_2 and F-A-TaN(U) -TiO_2 have a E_{gap} value close to that of undoped TiO_2 at 3.22 eV and 3.19 eV, respectively, indicating that the tantalum incorporation had little effect on the band gap in anatase. In rutile, however, tantalum doping increases the band gap significantly to 3.19 eV and 3.20 eV corresponding to the F-R-TaN-TiO_2 and F-R-TaN(U) -TiO_2. This increase suggests that tantalum interacts differently with the rutile structure, which is proven through the XRD data, as the data presented the presence of a mixture of anatase and rutile phases.

Table 5.3: UV-Vis optical gap of furnace anatase and rutile co-doped samples.

Sample	**E_{gap} (eV)**	**E_{gap} error (eV)**
F—A—undoped—TiO_2	3.20	0.02
F—A—WN—TiO_2	2.85	0.11
F—A—WN(U)—TiO_2	3.10	0.08
F—A—TaN—TiO_2	3.22	0.07
F—A—TaN(U)—TiO_2	3.19	0.07
F—R—undoped—TiO_2	3.00	0.02
F—R—WN—TiO_2	3.01	0.07
F—R—WN(U) —TiO_2	3.08	0.11
F—R—TaN—TiO_2	3.19	0.10
F—R—TaN(U) —TiO_2	3.20	0.09

5.4 Raman Spectroscopy

For Raman spectroscopy performed on TiO_2 there are three dominant modes observed: E_g mode is mainly the result of the symmetric stretching vibration of O-Ti-O, the B_{1g} mode is produced by the symmetric bending vibration of O-Ti-O and the A_{1g} mode is caused by the anti—symmetric bending vibration of O-Ti-O. Raman modes arise due to the vibration of the molecular bond, this means that different crystal facets make different contributions to the active modes. (21) The {101} facet is the most thermodynamically stable facet of anatase TiO_2. In naturally formed or synthesized TiO_2 nanoparticles, this facet is dominant because it minimizes surface energy. The {101} facet's bonding modes has mainly saturated 6c—Ti and 3c—O and unsaturated 5c—Ti and 2c—O modes on the surface. Despite being stable, the {101} is less reactive than the {001} facet. For the {001} facet, the bonding modes on the surface are unsaturated 5c—Ti and 2c—O.(22) The atoms on this facet are undercoordinated, meaning they have unsaturated bonds, which makes them more chemically active. The {101} 6c—Ti and 3c—O demonstrate a symmetric stretching vibration, while the {001} 5c—Ti and 2c—O tend to exhibit the symmetric and the anti—symmetric bending vibrations. These facets are of primary interest because they are the most commonly exposed surfaces in TiO_2 materials, and they exhibit distinct reactivity, bonding configurations, and vibrational modes, which strongly influence the material's overall performance in applications like photocatalysis. (23)

Four Raman active modes, E_g (146 cm^{-1}), B_{1g} (393 cm^{-1}), A_{1g} (516 cm^{-1}) and E_g (611 cm^{-1}) are observed, which are indicative of the anatase phase and are present in all of the co—doped samples, Figure 5.6. The introduction of dopants caused a variable blue shift in all of the peaks when compared to undoped anatase, caused by the formation of defects. The E_g mode at 146 cm^{-1} is almost identical to the undoped anatase TiO_2 (144 cm^{-1}), suggesting minimal distortion to the lattice for this low-energy vibrational mode. The B_{1g} mode at 393 cm^{-1} has shifted slightly compared to the undoped 399 cm^{-1} and could be attributed to the influence of the dopant atoms, likely causing slight modifications in the Ti-O bond strength or bond angle. The A_{1g} mode at 516 cm^{-1} is close to the F-A-undoped-TiO_2 mode at 513 cm^{-1}, implying that this symmetric stretching mode was not strongly affected by the co-dopants. The E_g mode at 611 cm^{-1} demonstrated a shift from the F-A-undoped-TiO_2 at 639 cm^{-1}.(24) This larger shift could suggest increased lattice distortion, possibly due to the presence of the metal dopant atoms in the TiO_2 lattice, which has a much larger atomic radius than titanium. This could induce strain in the lattice and resulting to a more significant shift in this high-energy mode.

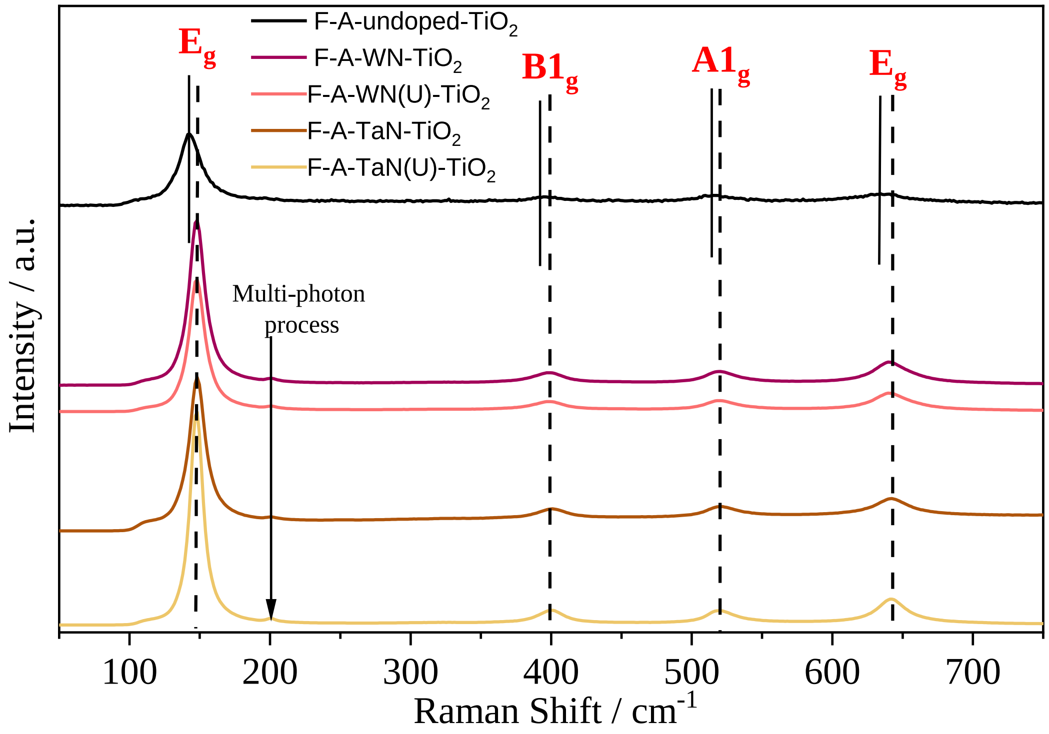

Figure 5.6: Raman spectra for the anatase co-doped TiO_2 a) F-A-undoped-TiO_2, b) F-A-WN-TiO_2, c) F-A-WN(U)-TiO_2, d) F-A-TaN-TiO_2 and e) F-A-TaN(U)-TiO_2.

The {110} facet’s bonding modes has mainly saturated 6c—Ti and 3c—O and unsaturated 5c—Ti and 2c—O modes on the surface, while for the {100} facet, the bonding modes on the surface are unsaturated 5c—Ti and 2c—O. The modes are attributed to the same vibrations as anatase, which means that 6c—Ti and 3c—O are caused due to the symmetric stretching vibration, while the 5c—Ti and 2c—O arise from the symmetric and the anti-symmetric bending vibrations. These facets are of key interest since they are the ones commonly exposed surfaces in rutile TiO_2 materials, and they strongly influence the material's vibrational modes.

The Raman data for the rutile materials is shown in Figure 5.7. The decrease of the high frequency E_g mode, between anatase and rutile is observed as a consequence of the increased calcination temperature. Three Raman active modes, E_g (141 cm^{-1}), E_g (443 cm^{-1}), A_{1g} (611 cm^{-1}) and the multi-photon process (234 cm^{-1}) which correspond to the rutile phase are present in all of the samples.

The introduction of dopants caused a red shift in all of the peaks, which is an opposite result to the blue shift observed previously for the anatase materials. In the co-doped TiO_2 samples, the E_g mode at 141 cm^{-1} is typically associated with the symmetric stretching vibrations of Ti-O bonds, which generally appear around 144 cm^{-1}. The observed peak at 141 cm^{-1}, being slightly lower than the usual value, suggests minor distortions or alterations in the Ti-O bond environment due to doping. Similarly, the E_g mode at 443 cm^{-1} in rutile TiO_2 is normally found around 446 cm^{-1} and corresponds to the symmetric stretching of Ti-O bonds. The peak at 443 cm^{-1}, although close to the typical value, indicates that co-doping with W and N has introduced changes in the lattice or bond strength. The A_{1g} mode, involving symmetric stretching of Ti-O bonds, demonstrated a peak at 611 cm^{-1}, indicating a minor impact of co-doping on this vibrational mode compared to the 612 cm^{-1} in undoped rutile TiO_2. The multiphoton peak at 234 cm^{-1}, which is atypical for rutile TiO_2, may indicate complex interactions involving multiple photon processes. This peak could be related to higher-order Raman scattering or additional vibrational modes introduced by W, Ta and N doping, potentially suggesting increased defect density or structural strain. (25) The appearance of noise in the spectra, further, validates the presence of weak Raman scattering that could be originated from the added dopants.

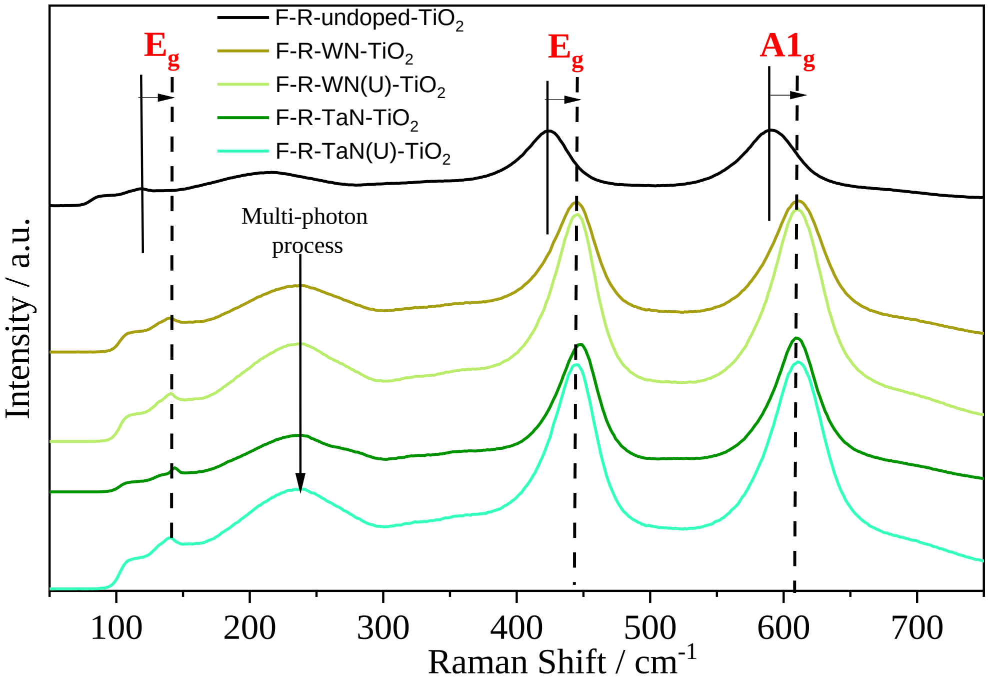

Figure 5.7: Raman spectra for the rutile co-doped TiO_2 a) F-R-undoped-TiO_2, b) F-R-WN-TiO_2, c) F-R-WN(U)-TiO_2, d) F-R-TaN-TiO_2 and e) F-R-TaN(U)-TiO_2.

5.5 Fourier Transform Infrared Spectroscopy (FTIR)

The FTIR spectra of the anatase samples are presented in Figure 5.8. The weak or absent FTIR peaks in undoped TiO_2 are likely due to low polarizability and weak dipole moment changes in Ti-O bonds, along with low defect density and high lattice symmetry. The stronger peak at 1735 cm^{-1} was attributed to bending vibrations of O–H, and at 3438 cm−1 was stretching vibrations O–H and the 1438 cm^{-1} is assigned to the bending vibration mode of N-H group formed during doping. Nitrogen incorporation into the TiO_2 lattice (either substitutionally or interstitially) introduces new bands, such as N-Ti stretching vibrations. If nitrogen is incorporated substitutionally (replacing oxygen in the lattice), these vibrations can cause shifts in the typical Ti-O-Ti vibrations. The peak at 1363 cm^{-1}, which was produced by –Ti–O–N–Ti– (–Ti–NO_x) stretching vibrations, indicates that N atoms were incorporated into the TiO_2 crystal lattice. (26, 27) The intense peak at 1215 cm^{-1} arises from the Ti-N vibrations caused due to the incorporation of N atoms into the lattice of the TiO_2. The peak around 3015 cm^{-1} arises from the N-H bending vibration. The low intensity peak at 1095 cm^{-1} is due to the C-N bending vibrations that are a result from the synthetic pathway. (26)

The significantly higher FTIR O–H intensity in co-doped TiO_2 compared to undoped TiO_2 can be explained by several factors related to changes in surface properties and crystal structure due to doping. Co-doping with elements like nitrogen, tantalum, or tungsten often leads to increased surface hydroxylation, as the introduction of defects such as oxygen vacancies or lattice strain enhances the material's ability to adsorb water and form hydroxyl groups, as demonstrated through XRD analysis. These defects, combined with lattice distortion caused by dopant atoms, create active sites where water can adsorb and dissociate more easily, resulting in stronger O–H signals. (27)

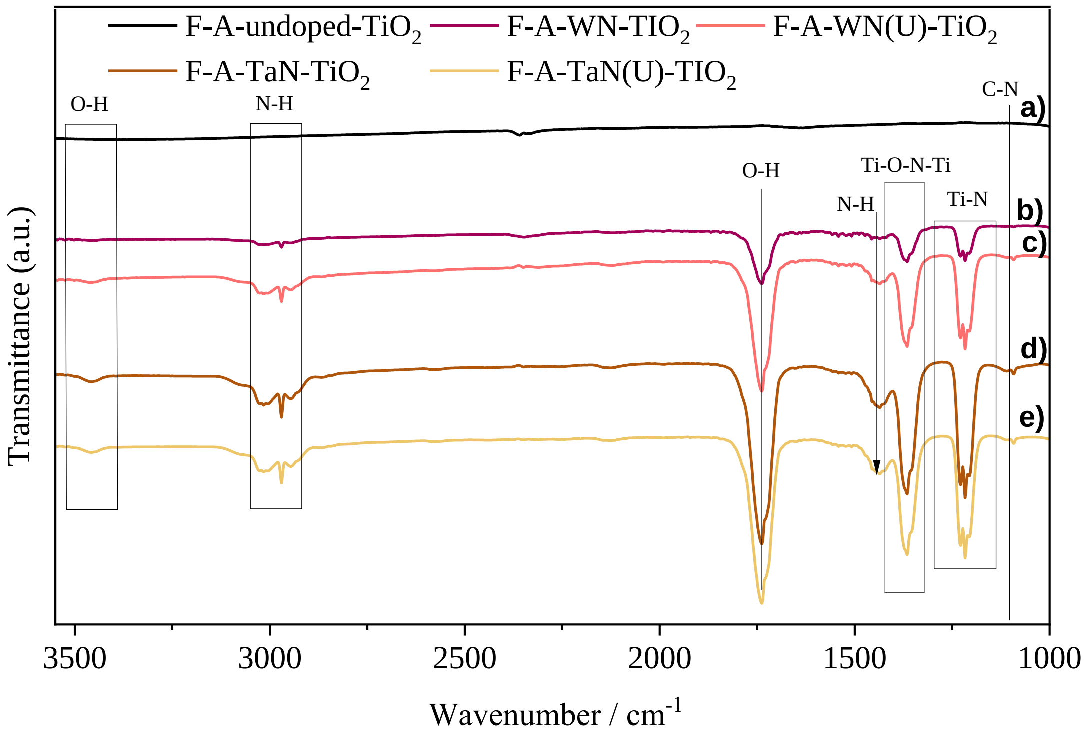

Figure 5.8: FTIR spectra for the anatase co—doped TiO_2 a) F-A-undoped-TiO_2, b) F-A-WN-TiO_2, c) F-A-WN(U)-TiO_2, d) F-A-TaN-TiO_2 and e) F-A-TaN(U)-TiO_2.

Similarly to the anatase undoped material the peaks for F-R-undoped-TiO_2 present low intensities. The intensities of the absorption characteristic peaks, arising from doping, are decreased with the increased calcination temperature (1173 K) required for rutilisation, which is due to a result of a smaller uptake of nitrogen, as seen in Table 5.2. This also explains the lack of the peak associated with surface water absorbance at around 3450 cm^{-1}.The FTIR spectra in Figure 5.9 presents the main peaks rising from the rutile samples, which show some similarity with the anatase data presented in Figure 5.8.

The peak at 1733 cm^{-1} is attributed to O–H bending vibrations. (27) The low intensity peak at 1436 cm^{-1} is assigned to the bending vibration of the N–H group producing as a result from the doping. The lower intensity compared to the corresponding anatase materials is a result of the higher calcination temperature used. (28) The peak at 1365 cm^{-1}, associated with the stretching vibrations of –Ti–O–N–Ti– (or –Ti–NO_x), suggests that nitrogen atoms were incorporated into the TiO_2 crystal structure. The intense peak at 1220 cm^{-1} is attributed to Ti–N vibrations, indicating the incorporation of nitrogen into the TiO_2 lattice. (26) The peak around 3005 cm^{-1} is due to the N-H bending vibrations. (29)

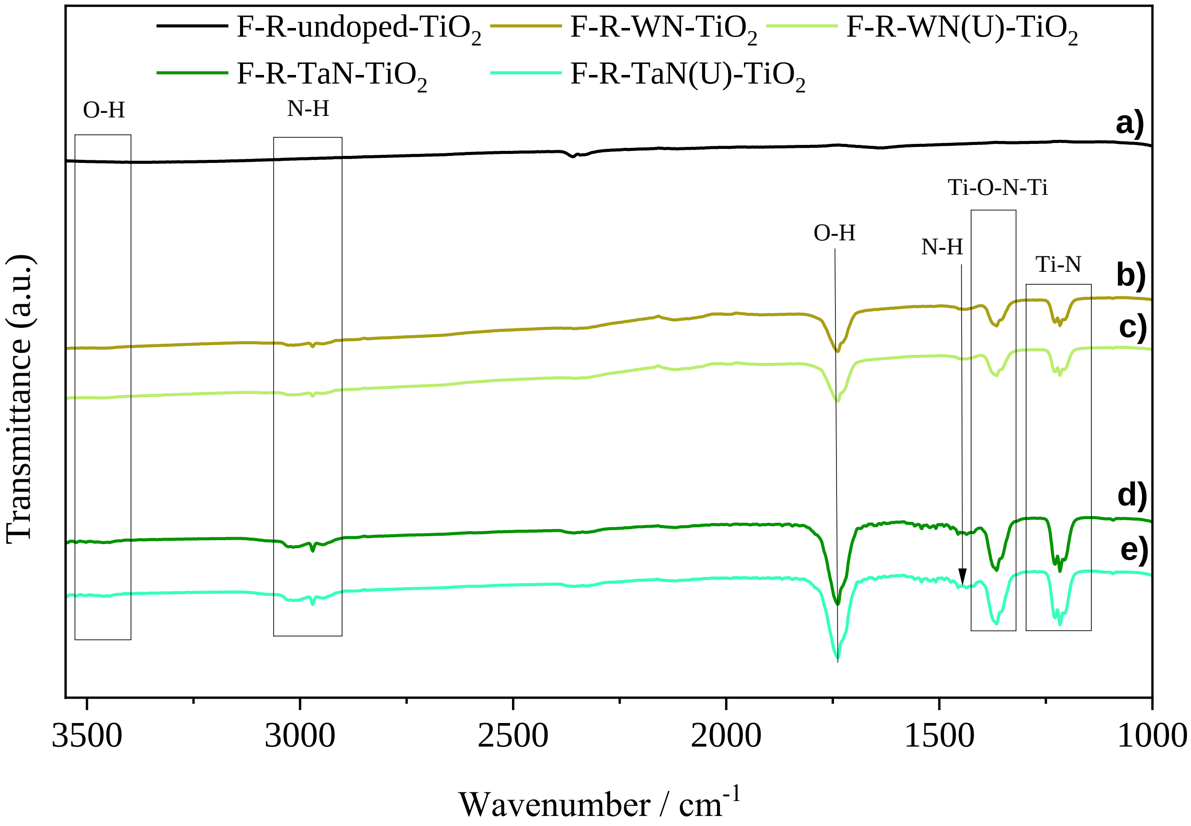

Figure 5.9: FTIR spectra for the rutile co—doped TiO_2 a) F-R-undoped-TiO_2, b) F-R-WN-TiO_2, c) F-R-WN(U) -TiO_2, d) F-R-TaN-TiO_2 and e) F-R-TaN(U)-TiO_2.

The lower FTIR intensities in rutile TiO_2 compared to anatase can be explained by several structural and surface-related differences between the two polymorphs, which were demonstrated via XRD and BET. Rutile has a more compact and dense crystal structure, which limits the vibrational freedom of Ti–O bonds, leading to weaker vibrational signals, whereas anatase's more open structure allows for stronger vibrational modes. Additionally, anatase typically has a higher surface area, increasing the number of surface hydroxyl groups that contribute to stronger O–H vibrational peaks in FTIR. Rutile, with a lower surface area, adsorbs fewer hydroxyl groups, resulting in weaker intensities. Furthermore, rutile's higher optical absorption in the infrared region also dampens the intensity of vibrational modes in FTIR. These factors combined with the increase in the calcination temperature result in rutile exhibiting lower FTIR intensities compared to anatase.

5.6 BET

BET analysis following N_2 adsorption isotherms on the anatase $Ti_{1-y}W_yN_xO_2$ and $Ti_{1-y}Ta_yN_xO_2$ was performed providing specific surface areas and their corresponding particle size for each sample, see Figure 5.10 and Table 5.4. The specific surface area of undoped anatase is 46.59 m^2g^{-1}, in line with previous literature reports. (30) There is a significant increase in surface area for the F-A-WN-TiO_2 sample of 88.17 m^2g^{-1}, and an even larger increase when urea is used as the precursor. The specific surface area of the F-A-TaN-TiO_2 is again larger than the undoped material, however the trend of sample size with choice of nitrogen precursor is reversed for the tantalum containing samples, for which the larger particle size is observed for the materials using ammonia as precursor. The F-A-WN(U)-TiO_2 sample has the largest surface area of all materials.

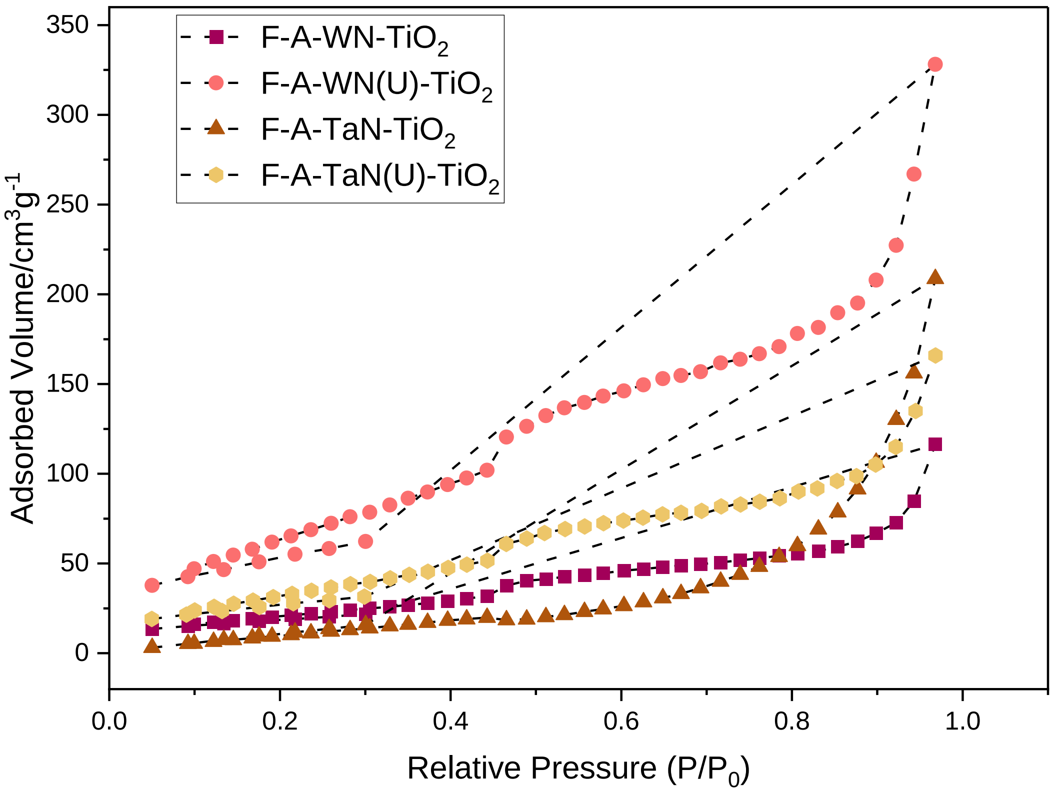

Figure 5.10: BET plot for the anatase co-doped TiO_2 a) F-A-WN-TiO_2, b) F-A-WN(U)-TiO_2, c) F-A-TaN-TiO_2 and d) F-A-TaN(U)-TiO_2.

Table 5.4: BET surface area for the anatase and rutile undoped and co—doped samples.

Sample	**S_{BET} ($m^2 \cdot g^{-1}$)**	**V_p [a] ($cm^3 \cdot g^{-1}$)**	**d [b] (nm)**	**N/W**
F-A-undoped-TiO_2	46.59	0.019	—	
F-A-WN-TiO_2	88.17	0.065	6	16.58
F-A-WN(U)-TiO_2	197.13	0.219	6	6.46
F-A-TaN-TiO_2	143.25	0.146	6	11.64
F-A-TaN(U)-TiO_2	123.27	0.129	5	6.75
F-R-undoped-TiO_2	40.20	0.005	—	
F-R-WN-TiO_2	92.55	0.112	6	8.07
F-R-WN(U)-TiO_2	107.27	0.285	4	3.96
F-R-TaN-TiO_2	96.44	0.164	6	16.49
F-R-TaN(U)-TiO_2	103.26	0.227	5	6.19

BET analysis following N_2 adsorption isotherms on the rutile co-doped samples was performed providing specific surface areas and their corresponding particle size for each sample, Figure 5.11 and Table 5.4. The specific surface area of undoped rutile is 40.20 m^2g^{-1}, in line with previous literature reports. (31) There is a significant increase in surface area for the F-R-WN-TiO_2 and F-R-TaN-TiO_2 samples of 92.55 m^2g^{-1} and 96.44 m^2g^{-1}, respectively. While the largest increase is observed from the F-A-WN(U)-TiO_2 reaching 197.13 m^2g^{-1}. The specific surface area of the F-R-WN(U)-TiO_2 and F-R-TaN(U)-TiO_2 is larger than the undoped and the materials that used ammonia as a nitrogen precursor. The F-R-WN(U)-TiO_2 sample has the largest surface area of all the rutile materials, 107. 27 m^2g^{-1}, correspondingly to the anatase materials. The introduction of dopants could result in a reduction in particle size which leads to a higher surface area because smaller particles have a greater surface-to-volume ratio. Considering both the N/W ratio calculated from XPS and the S_{BET} (Table 5.4) it is observed that a higher N content relative to W results in lower surface area, demonstrating a doping effect. Whereas, for the Ta materials the higher N content relative to Ta does not necessarily increase the surface area.

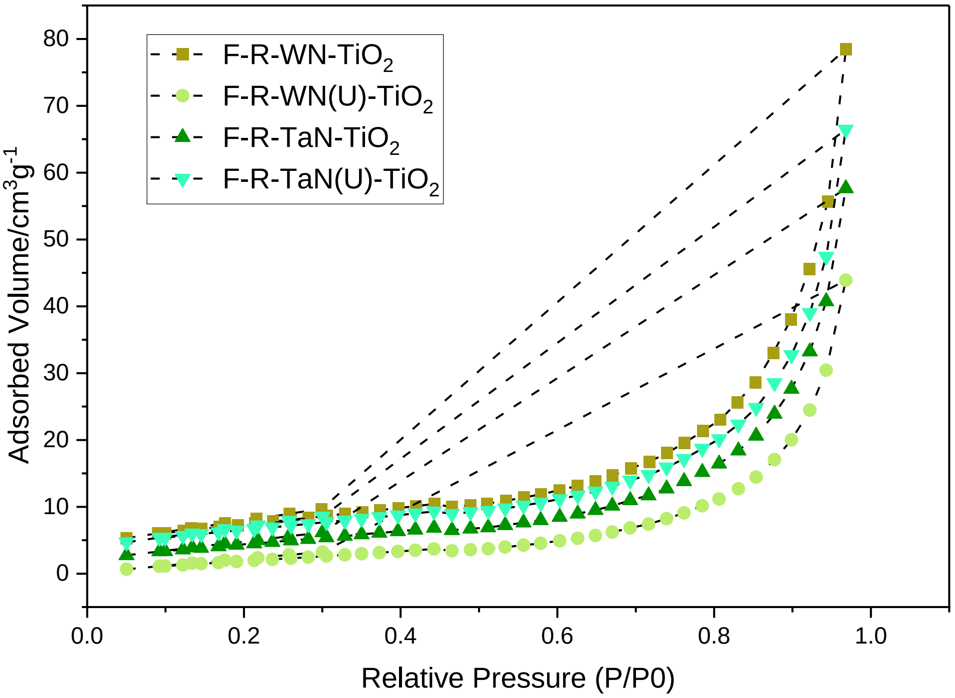

Figure 5.11: BET plot for the rutile co-doped TiO_2 a) F-R-WN-TiO_2, b) F-R-WN(U)-TiO_2, c) F-R-TaN-TiO_2 and d) F-R-TaN(U)-TiO_2.

The increase in specific surface area for all of the doped materials in comparison to their undoped counterparts is explained due to the restriction in crystallite growth caused via dopant introduction into the TiO_2 lattice, thus creating smaller particles. In the absence of dopants, TiO_2 crystallites typically grow larger during synthesis. As the crystallite size increases, the surface area decreases due to the reduced number of exposed surfaces available for interactions (since fewer, larger particles aggregate more easily). This results in a relatively lower specific surface area. When dopants are introduced into the TiO_2 lattice, they typically act as crystallisation inhibitors. Dopants distort the lattice and disrupt the regular arrangement of Ti and O atoms, which inhibits the growth of TiO_2 crystallites during the calcination or annealing processes. The reduced crystallite size leads to a higher surface area due to an increase in the number of exposed surfaces per unit mass. The literature explains this phenomenon based on the idea that dopant atoms act as nucleation sites or interrupt normal growth patterns. (32,33) For a co-doped material, transition metal dopants (W, Ta) or non-metal dopants (N) often occupy interstitial or substitutional positions within the TiO_2 lattice, which leads to strain in the lattice. This strain inhibits long-range crystallisation, thus producing smaller crystallites.

5.7 Microwave Calcined Samples

As it has been shown through the rest of this chapter, the properties of each sample can be affected by the precursor used for each dopant. The calcination step is the other point during the synthesis that could affect the physio-chemical properties of the samples. As an exploration of the importance of heating methods on sample preparation, microwave calcination was also performed on select materials as it offers clear advantages including reduced time requirements, lower reaction temperatures, evenly distributed heating across the sample, energy efficiency, high purity products, and environmental friendliness. (34, 35) For these samples XRD, XPS and UV-Vis analyses were performed. However corresponding Raman, FTIR and BET datasets are not available due to COVID-related time constraints.

The XRD patterns of the $Ti_{1-y}W_yN_xO_2$ and $Ti_{1-y}Ta_yN_xO_2$ anatase and rutile co-doped samples are shown in Figure 5.12 and 5.13, respectively. All of the samples clearly show patterns typical for the anatase and rutile structures. Peaks and corresponding Miller indices are demonstrated at 2θ (°) = 25.55 [103], 37.18 [101], 38.05 [004], 38.76 [112], 48.26 [200], 54.17 [105], 55.28 [211], 62.90 [204], 69.01 [116], 70.47 [220], 75.26 [215] and 76.21 [301] are characteristic of an anatase diffraction pattern. Additionally, the undoped and three ((WN), (WN(U)) and (TaN) of the co—doped samples the peaks and Miller indices observed at 2θ (°) = 27.67 [110], 36.33 [101], 39.44 [200], 41.48 [210], 44.30 [111], 54.56 [211], 56.85 [220], 62.99 [002], 64.45 [310], 69.98 [301] and 70.19 [112] are characteristic of rutile. The absence of peaks between 2θ (°) = 25–35, suggests no formation of tungsten oxides (WO_x) or tungsten bronze (W_xO_Y) structures. (11) Similarly, the lack of peaks in the 2θ (°) range of 20–55 indicates that no tantalum oxide structures were present. (12) However, in the tantalum co-doped samples, the peaks displayed broadening, which can be attributed to additional strain in the crystal structure caused by the size difference of tantalum atoms.

The diffraction pattern and Miller indices at 2θ (°) = 27.67 [110], 36.33 [101], 39.44 [200], 41.48 [111], 44.30 [210], 54.67 [211], 56.85 [220], 62.99 [002], 64.45 [310], 69.98 [301] and 70.19 [112] are characteristic of rutile. Additionally, for the following two co-doped samples (WN(U) and (TaN)) the peaks and Miller indices observed at 2θ (°) = 25.61 [101], 39.39 [112], 54.56 [105], 62.91 [204], 69.11 [116], 70.25 [220] and 76.71 [301], are all characteristic of an anatase diffraction pattern. From the presence of peaks between 2θ (°) = 25 – 35, especially three continuous peaks before the TiO_2 dominant peak between 23 to 25, it can be concluded that there is evidence of formation of either tungsten oxides WO_x structures. The peaks and Miller indices relating to the WO_x appear at 2θ (°) = 23.42, 23.93, 24.66, 33.5 and 34.49 for only the rutile W-based co-doped samples. The absence of peaks within the 2θ (°) range of 20–55 confirms the lack of formation of tantalum oxide structures.

These co-doped samples have demonstrated that the calcination pathway affects the rutilisation formation during the calcination process for both the anatase and rutile polymorphs, with the majority of the samples forming rutile phase materials. Rietveld refinement indicated variations in the unit cell parameters shown in Table 5.5 which demonstrates an increased strain in the unit cell. Despite, the formation of oxide superstructures when tungsten atoms were incorporated into the lattice the unit cell parameters indicate that the overall morphology remained the same as the undoped materials.

Table 5.5: A comparison of the refined structural parameters for the co—doped TiO_2 samples prepared via microwave calcination, including the parameters for undoped anatase and rutile.

Sample	**Anatase Unit Cell/ Å**		**Rutile Unit Cell/ Å**		**% Morphology**	
	a = b	**c**	**a = b**	**c**	**Anatase**	**Rutile**
A-undoped	3.799	9.539	4.594	2.959	69.87	30.13
A-WN	3.783	9.510	4.591	2.955	91.38	8.62
A-WN(U)	3.784	9.511	4.592	2.954	97.43	2.57
A-TaN	3.795	9.514	4.595	2.961	85.17	14.83
A-TaN(U)	3.796	9.515	—	—	100.00	—
R-undoped	—	—	4.594	2.959		
R-WN	—	—	4.593	2.956	—	100.00
R-WN(U)	3.786	9.524	4.591	2.957	2.31	97.69
R-TaN	3.789	9.522	4.597	2.961	1.93	98.07
R-TaN(U)	—	—	4.596	2.962	—	100.00

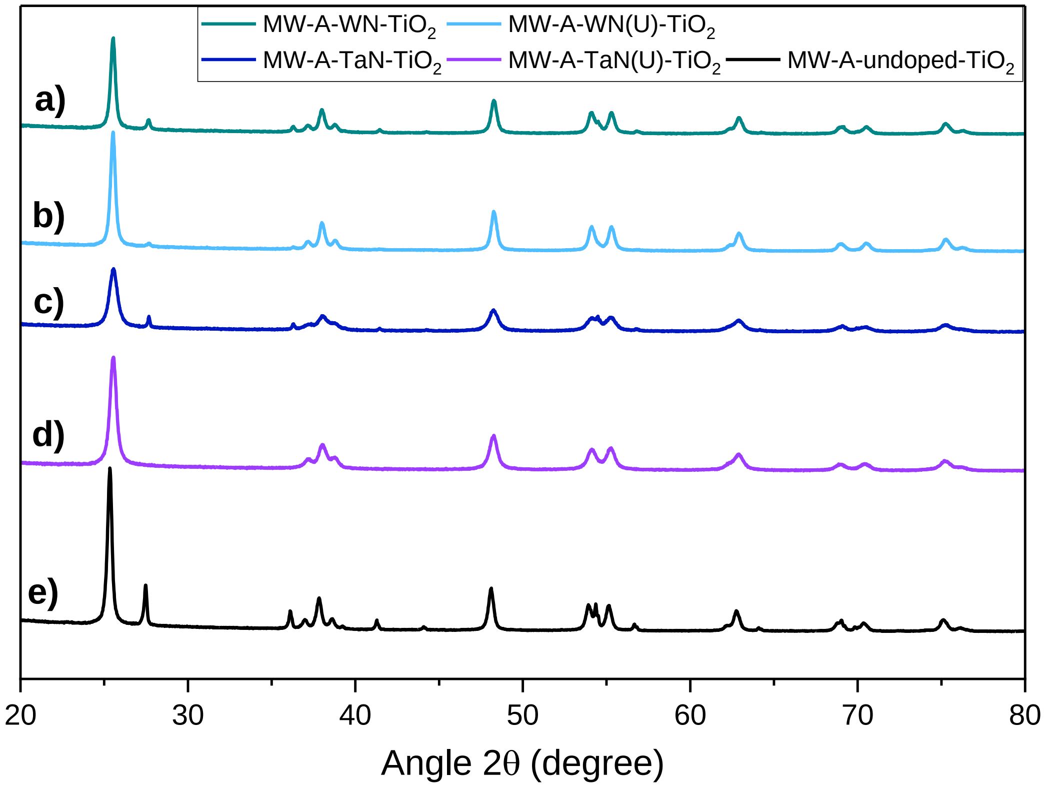

Figure 5.12: XRD pattern for the microwave anatase co-doped TiO_2 a) MW-A-WN-TiO_2, b) MW-A-WN(U)-TiO_2, c) MW-A-TaN-TiO_2, d) MW-A-TaN(U)-TiO_2 and e) MW-A-undoped-TiO_2.

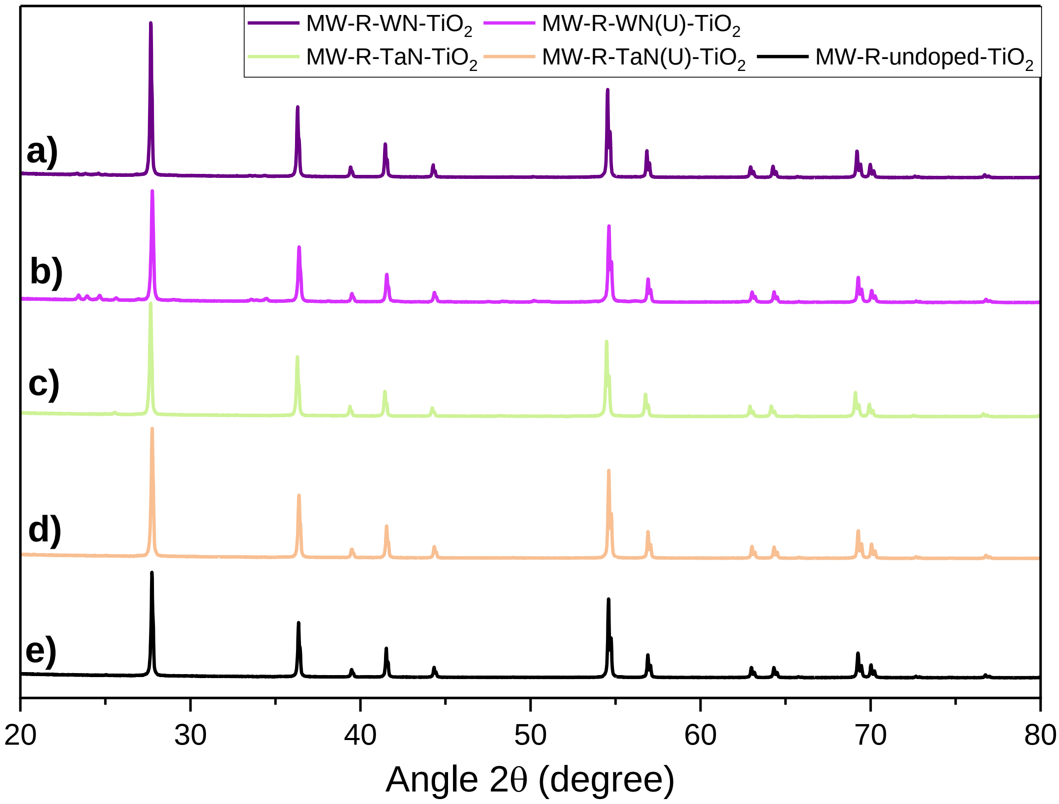

Figure 5.13: XRD pattern for the microwave anatase co-doped TiO_2 a) MW-R-WN-TiO_2, b) MW-R-WN(U)-TiO_2, c) MW-R-TaN-TiO_2, d) MW-R-TaN(U)-TiO_2 and e) MW-R-undoped-TiO_2.

The results of solid-state UV spectroscopy for the anatase and rutile co-doped materials for the calculated E_{gap} are shown on the Table 5.6 and the absorption spectra and the corresponding tauc plots can be found in Figure 5.14. Compared to the corresponding furnace calcined anatase samples, the nominated rutile samples where slight off-white colours. The anatase samples using urea as a nitrogen source as the non-metal doping exhibited a higher decrease of the band gap. Once doping had occurred the band gap of the rutile sample demonstrated a decrease up to 0.11 eV, demonstrating an opposite trend to the furnace samples. This could be explained by the fact that when using a microwave for the calcination the rutilisation is more complete, as demonstrated previously by the XRD results. The samples containing tungsten as the metal dopant exhibited a higher decrease of the band gap, thus bringing their individual optical band gap into the visible light region. On the other hand, the samples containing tantalum as their metal dopant exhibited a smaller decrease in the band gap. The band gaps for the MW-A-WN-TiO_2 (3.26 eV) and MW-A-TaN-TiO_2 (3.22 eV) samples are closest to that of pure TiO_2, indicating limited band gap reduction by WN and TaN doping under microwave calcination in air. However, the MW-A-WN(U)-TiO_2 (3.04 eV) and MW-A-TaN(U)-TiO_2 (3.03 eV) samples led to a notable narrowing of the band gap, enhancing visible light absorption. In contrast, the MW-R-WN-TiO_2 (3.01 eV) and MW-R-TaN-TiO_2 (2.98 eV) exhibiting lower values compared to their anatase counterparts. The combination of rutile calcination and the use of urea as a nitrogen precursor produced the most significant reduction in the band gap, with MW-R-WN(U)-TiO_2 reaching 2.90 eV, which may result in enhanced photocatalytic activity under visible light. WN doping generally resulted in a slightly greater band gap reduction than TaN doping, indicating its higher efficacy in narrowing the band gap across both synthesis methods. Overall, MW-R-WN(U)-TiO_2 appears to be the most promising candidate for applications in photocatalysis due to its significantly reduced band gap, which will be discussed in Chapter 7.

Table 5.6: UV-Vis absorption data, including optical gap of microwave co—doped samples.

Sample	E_{gap} (eV)	E_{gap} error (eV)
MW-A-undoped-TiO_2	3.21	0.04
MW-A-WN-TiO_2	3.26	0.08
MW-A-WN(U)-TiO_2	3.04	0.13
MW-A-TaN-TiO_2	3.22	0.07
MW-A-TaN(U)-TiO_2	3.03	0.07
MW-R-undoped-TiO_2	3.00	0.03
MW-R-WN-TiO_2	3.01	0.09
MW-R-WN(U)-TiO_2	2.90	0.10
MW-R-TaN-TiO_2	2.98	0.09
MW-R-TaN(U)-TiO_2	3.00	0.07

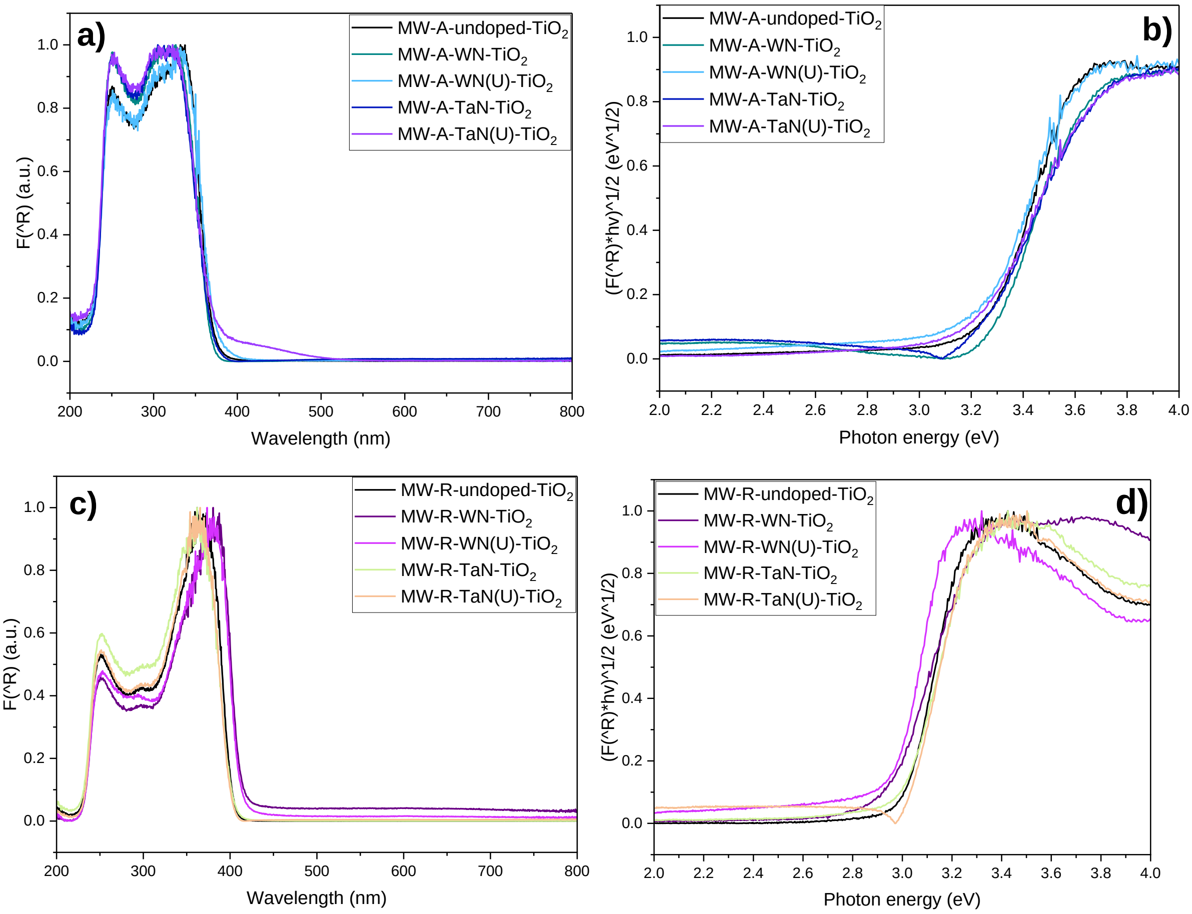

Figure 5.14: (a, c) UV-Vis absorption spectra of the co-doped materials and (b, d) corresponding Tauc plots for the representative samples (top-anatase, bottom-rutile).

The XPS binding energy peaks for the anatase and rutile samples for the O (1s), Ti (2p), W (4d) and Ta (4d), and W (4f) and Ta (4f) core levels from their corresponding contributions were very similar to that of the furnace anatase and rutile samples, respectively (Appendix A.2.2 and A.2.3). XPS quantification for the total contribution of each element was performed using CasaXPS and can be seen in Table 5.7.

While the majority of the core level spectra present very similar peaks as the anatase furnace samples, there are significant changes in the N (1s) core level region. From the N (1s) region, Figure 5.15, two N associated peaks are revealed for all samples and for the Ta doped samples there is an overlap of the nitrogen peaks with the Ta $4p_{3/2}$ signal. Tungsten co—doped samples demonstrated the N (1s) peak at 399.17 eV which is produced from an interstitial site of a nitrogen bound to hydrogen. (36, 37) The intensity of this signal is more pronounced for the samples that used urea as the nitrogen source. The second N (1s) peak at 401.34 eV (38) is indicative of N–O bonds and is present in the Ta—based samples, which will be discussed through solid state electron paramagnetic resonance (EPR) spectroscopy, discussed in Chapter 6. Additionally, the signal at 404.4 eV is attributed to Ta $4p_{3/2}$, which supports the presence of Ta at the surface of the materials. (17)

Similarly to the trend observed for the anatase samples, the core level spectra show very similar peaks as the rutile furnace samples. Still, the N (1s) region demonstrates contributions attributed to different profiles. From the N (1s) region, Figure 5.16, only one N associated peak is revealed for all samples, while the overlap of the nitrogen peaks with the Ta $4p_{3/2}$ signal for the Ta doped samples there is present only for the TaN(U) co-doped samples. The MW-R-WN(U)-TiO_2 samples demonstrated the N (1s) peak at 399.3 eV which is produced from an interstitial site of a nitrogen bound to hydrogen. The intensity of this signal is more pronounced for the samples that used urea as the nitrogen source. Additionally, the signal at 404.2 eV is attributed to Ta $4p_{3/2}$, which explains the presence of Ta at the surface of the nanoparticles. The MW-R-WN-TiO_2 and MW-R-TaN-TiO_2 samples demonstrated no peaks. This could indicate that during the calcination process the nitrogen and tantalum is completely removed from the surface, thus XPS is not able to detect anything.

From Table 5.7 the formula for the anatase $Ti_{1-y}W_yN_xO_2$ for the ammonia and urea precursors become $Ti_{0.9948}W_{0.0052}N_{0.0631}O_2$ and $Ti_{0.9932}W_{0.0068}N_{0.0764}O_2$, respectively. While the $Ti_{1-y}Ta_yN_xO_2$ for the ammonia and urea precursors become $Ti_{0.9913}Ta_{0.087}N_{0.0584}O_2$ and $Ti_{0.9902}Ta_{0.0098}N_{0.0523}O_2$, respectively. Additionally, from Table 5.7 the rutile $Ti_{1-y}W_yN_xO_2$ for the ammonia and urea precursors become $Ti_{0.9951}W_{0.0049}N_{0.0597}O_2$ and $Ti_{0.9924}W_{0.0076}N_{0.0194}O_2$, respectively. While for the rutile samples the $Ti_{1-y}Ta_yN_xO_2$ for the ammonia and urea precursors become $Ti_{0.9966}Ta_{0.0034}N_{0.0456}O_2$ and $Ti_{0.9902}Ta_{0.0098}N_{0.0628}O_2$, respectively. The aimed nitrogen and metal theoretical values were 25% and 1%, respectively, following the same calculations as for the furnace materials.

Table 5.7: XPS quantification of the atomic percentage concertation for each dopant from the binding energies for the O 1s, Ti 2p, N 1s and metal 4d for the anatase samples.

Sample	Dopant Atomic %		Sample	Dopant Atomic %	
	W	Nitrogen		Ta	Nitrogen
MW-A-WN-TiO_2	0.52	6.31	**MW-A-TaN-TiO_2**	0.87	5.84
MW-A-WN(U)-TiO_2	0.68	7.64	**MW-A-TaN(U)-TiO_2**	0.98	5.23
MW-R-WN-TiO_2	0.49	5.97	**MW-R-TaN-TiO_2**	0.34	4.56
MW-R-WN(U)-TiO_2	0.76	1.94	**MW-R-TaN(U)-TiO_2**	0.98	6.28

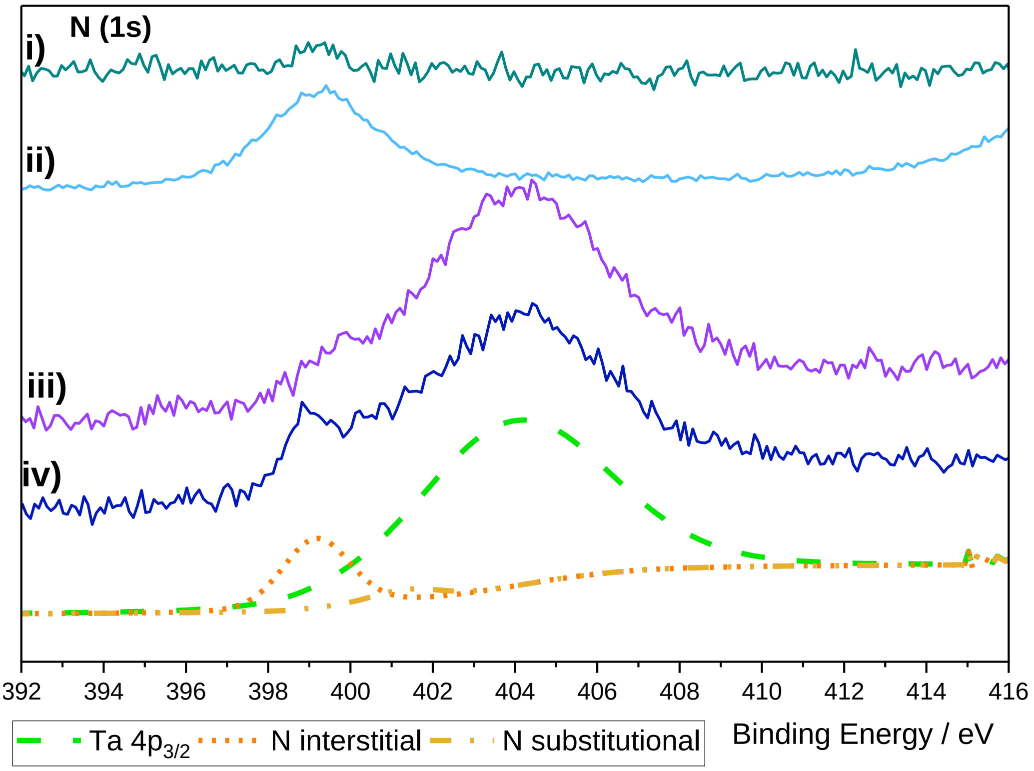

Figure 5.15: XPS pattern for the N (1s) region of the microwave anatase co-doped TiO_2 i) MW-A-WN-TiO_2, ii) MW-A-WN(U)-TiO_2, iii) MW-A-TaN-TiO_2 and iv) MW-A-TaN(U)-TiO_2.

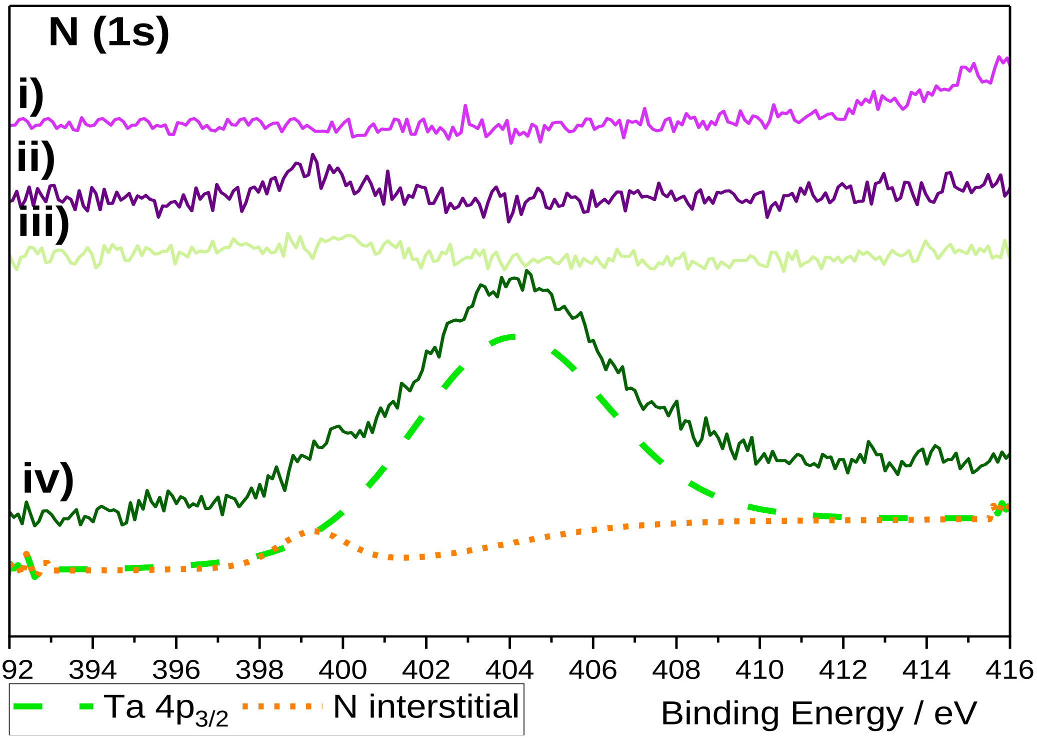

Figure 5.16: XPS pattern for the N (1s) region of the microwave anatase co-doped TiO_2 i) MW-R-WN-TiO_2, ii) MW-R-WN(U)-TiO_2, iii) MW-R-TaN-TiO_2 and iv) MW-R-TaN(U)-TiO_2.

5.8 Conclusion

From the analysis of data accumulated via the different characterisation techniques it is concluded that the desired co-dopants of W and N and Ta and N were successfully introduced into the TiO_2 via a sol-gel synthetic pathway. XPS was employed for surface study of these materials, which demonstrated the effectiveness of the calcination methods and of the choice for the dopants. The most interesting region of XPS was proven to be the N (1s) region, as it demonstrated the existence of different nitrogen species that will be further investigated via EPR in the next chapter. An additional region of interest was that of the metal region, as it confirmed the incorporation of the metal dopants. The addition of the two dopants for each system resulted in the narrowing of the optical band gap for the furnace anatase and microwave anatase and rutile calcined tungsten materials, notably due to the introduction of interstitial N_iO. This was specifically proven via the UV-Vis analysis of the Kubelka-Munk plots. Additionally, UV-Vis demonstrates the different effects the choice of metals has in the decrease of the band gap, with tungsten presenting a better response than tantalum in the anatase samples for both the furnace and the microwave calcined samples. Furthermore, UV-Vis proved the improvement of the microwave calcined materials the rutile samples, as they all demonstrated a narrowing of the optical gap, with the tungsten-based ones still demonstrating a higher decrease. XRD assisted in understanding the patterns that UV-Vis analysis showed, as the furnace samples for the rutile morphology were proven to be a mixture of anatase and rutile. XRD was also able to prove that the use of a microwave oven promotes the rutilisation of TiO_2 and has the ability to fully convert doped samples, Table 5.8. This is of great significance as the addition of dopants could inhibit the change from one morphology to the other, as it is seen herein since the addition of tantalum created mixtures of the phases.

Table 5.8: Comparing microwave and furnace materials.

Sample	XRD	XPS	UV
Furnace	Microwave materials achieved better rutilisation, with rutile phase present in anatase samples. The presence of tungsten superstructure was observed in the microwave samples.	no major differences	no major differences
Microwave			

In microwave-treated samples, a small amount of rutile phase was present in the materials with a desired anatase morphology, suggesting that the materials were reaching the rutile phase at a lower temperature. This phenomenon was attributed to the different heating mechanism, as microwave calcination heats the material internally through dielectric loss, whereas in a conventional furnace, heat is transferred from the external surroundings. Additionally, microwave samples exhibited a tungsten superstructure, indicating possible structural rearrangements or phase segregation due to the distinct heating process. Conversely, for samples intended to achieve a rutile morphology via furnace calcination, residual anatase was observed, suggesting an incomplete phase transition. No major differences were found between furnace and microwave samples in terms of surface composition (XPS) and optical properties (UV-Vis). This suggests that while the bulk morphology (XRD) was significantly affected based on the calcination process, the surface chemistry and electronic structure remained largely unchanged between the two synthesis methods. The improved rutilisation in microwave-treated samples could impact photocatalytic efficiency, as rutile phases may influence charge separation. BET, Raman and FTIR further confirmed the differences that arise from the incorporation of dopants into the lattice. It has been, therefore, demonstrated that doped materials present desirable characteristics which can be exploited in photocatalytic reactions.

5.9 References

(1) A. Folli, J.Z. Bloh, K. Armstrong, E. Richards, D.M. Murphy, L. Lu, C.J. Kiely, D.J. Morgan, R.I. Smith, A.C. Mclaughlin, D.E. Macphee, *ACS Catalysis*, 2018, **8**, 6927.

(2) K.Y. Jung, S.B. Park, S.K. Ihm, *Applied Catalysis B: Environmental*, 2014, **51**, 239.

(3) D. Pant, G. Van-Bogaert, L. Diels, K. Vanbroekhoven, *Sustainable Energy Fuels*, 2018, **2**, 2674.

(4) Y.H. Peng, G.F. Huang, W.Q. Huang, *Advanced Powder Technology*, 2012, **23**, 8.

(5) N. Bsiri, M.A. Zrir, A. Bardaoui, M. Bouacha, *Ceramics Interanational*, 2016, **42**, 10599.

(6) R.S. Dubey, S. Singh, *Physics*, 2017, **7**, 1283.

(7) A. Folli, J.Z. Bloh, A. Lecaplain, R. Walker, D.E. Macphee, *Phys. Chem.*, 2015, **17**, 4849.

(8) M. S. Sharifiyan, A. Fattah-alhosseini, M. Karbasi, *Applied Surface Science Advances*, 2023, **18**,100541.

(9) K. Amarsingh Bhabu, A. Kalpana Devi, J. Theerthagiri, *et al.*, *J Mater Sci: Mater Electron,* 2017, **28**, 3428–3439.

(10) J. Kasetsart, P. Limsuwan, B. Ngotawornchai, Nat. Sci., 2008, 42, 357–361.

(11) I. Székely, Z. Kovács, M. Rusu, T. Gyulavári, M. Todea, M. Focșan, M. Baia, Z. Pap, *Catalysts,* 2023, **13**, 1015.

(12) M.A.A. Talip, N.S. Khairir, R.A. Kadir, et al., *J Mater Sci*: *Mater Electron*, 2019, **30**, 4953–4966.

(13) P. Simon, V.G. Baldovino-Medrano, R. Wojcieszak, X-Ray Photoelectron Spectroscopy (XPS): Principles and Application for the Analysis of Photoactive Materials, Springer Handbooks. Springer, Cham, 2022.

(14) A. Bumajdad, M. Madkour, *Physical Chemistry Chemical Physics*, 2014, **16**, 7146.

(15) A. Kubala-Kukuś, D. Banaś, I. Stabrawa, K. Szary, D. Sobota, U. Majewska, J. Wudarczyk-Moćko, J. Braziewicz, M. Pajek, *Spectrochimica Acta Part B: Atomic Spectroscopy,* 2018, **145**, 43-50.

(16) M. Gratzel, Photoelectrochemical Cells, *Nature*, 2001, **414**, 338.

(17) V. Kumaravel, M. Barbara Maccioni, S. Mathew, S. J. Hinder, J. Bartlett, M. Nolan, S. C. Pillai, *The Journal of Physical Chemistry C,* 2022, **126**, 4, 2285-2297.

(18) S.M. Rasul, D.R. Saber, S.B. Aziz, *Results in Physics*, 2022, **38**, 105688.

(19) X. Song. L. Gao, *Langmuir*, 2007, **23**, 23, 11850-11856

(20) A. Folli, J.Z. Bloh, D.E. Macphee, *Journal of Electroanalytical Chemistry*, 2016, **780,** Pages 367-372.

(21) V. Vrakatseli, E. Farsari, D. Mataras, *Micromachines*, 2020, **11**, 616.

(22) U. Balachandran, N.G. Eror, *Journal of Solid State Chemistry*, 1982, **42**, 3, 276-282.

(23) O. Frank, M. Zukalova, B. Laskova, J. Kürti, J. Koltaib, L. Kavan, *Physical Chemistry Chemical Physics,* 2012, **14**, 14567-14572.

(24) V. Tamilselvan, D. Yuvaraj, R. Rakesh Kumar, K. Narasimha Rao, *Applied Surface Science*, 2012, **258**, 10, 4283-4287.

(25) S. Challagulla, K. Tarafder, R. Ganesan, et al., *Sci Rep*, 2017, **7**, 8783.

(26) D. Huang, S. Liao, S. Quan, L. Liu, Z. He, J. Wan, *Journal of Non-Crystalline Solids*, 2008, **33**, 3965-3972.

(27) Ó.R. Andrade, V. Rodríguez, R. Camarillo, F. Martínez, C. Jiménez, J. Rincón, *Nanomaterials*, 2022, **12**, 11, 1793.

(28) Wenbin Zhou aH.M. Ngo, A.U. Pawar, J. Tang, Z. Zhuo, D.K. Lee, K.M. Ok, Y.S. Kang, *Nanomaterials,* 2022, **12**, 2626.

(29) Y., Bouachiba, F. Hanini, A. Bouabellou, F. Kermiche, A. Taabouche, M. Bouafia, S. Amara, S. Sahli, K. Boukheddaden, *International Journal of Nanoparticles*, 2013, **6**, 169.

(30) I. Hernández-Perez, A.M. Maubert, L. Rendón, P. Santiago, H. Herrera-Hernández, L. Díaz-Barriga Arceo, V. Garibay Febles, E. Palacios González, L. González-Reyes, *International Journal of Electrochemical Science*, 2012, **7**, 9, 8832-8847.

(31) T. Dhandayuthapani, R. Sivakumar, R. Ilangovan, *Surfaces and Interfaces*, 2016, **4**, 59-68.

(32) J. Yu, W. Wang, B. Cheng, *Chem. Asian J*., 2010, **5**, 2499-2506.

(33) J. G. Yu, W. G. Wang, B. Cheng, *Chemistry*, 2010, **5**, 12, 2499–2506.

(34) M. Bomio, P. Lavela, R. L. Tranquilin, F. Villela da Motta, J. L. Tirado, *Journal of Electroanalytical Chemistry*, 2023, **930**, 117157.

(35) J. Maragatha, S. Rajendran, T. Endo, *et al.*, *J Mater Sci: Mater Electron,* 2017, **28**, 5281–5287.

(36) A. Kubiak, M. Zalas, M. Cegłowski, *Sci Rep,*2024, **14**, 12617.

(37) A.N. Kadam, R.S. Dhabbe, M.R. Kokate, Y.B. Gaikwad, K.M. Garadkar, *Spectrochimica Acta Part A: Molecular and Biomolecular Spectroscopy,* 2014, **133**, 669-676.

(38) M.S. Azami, W.I. Nawawi, A.H. Jawad, M.M. Ishak, K. Ismail, *Sains Malays*, 2017, **46**, 8, 1309-1316.

Chapter 6. EPR Solid State Characterisation

Prior to a discussion of the changes observed upon irradiation in the samples, it is pertinent to first provide a full description of the different EPR active centres observed in the each as-synthesised material, under the same conditions. Therefore, the material was measured after the surface was dehydroxylated, molecular oxygen was added to the cell, followed by irradiation at the desired wavelength (or in the case of dark no irradiation) and then the excess atmosphere was evacuated prior to measuring.

6.1 Tungsten and Nitrogen co-doped samples

EPR can be used to determine the precise characteristics of the active species in a material under different condition. For these specific materials the species that are responsive to visible light are of great interest. While N-doped TiO_2 is a thoroughly researched and characterised oxide semiconductor, the effect of different nitrogen sources for the WN-co doped TiO_2 is presented through clear and distinct EPR spectra of the samples.

Figure 6.1 displays the spectra of the F-A-WN-TiO_2 under different photoirradiation conditions, namely in the absence of light and during exposure to the following wavelengths of (a) 625 nm (b), 530 nm (c), 455 nm (d) and 365 nm (e). These wavelengths were selected as they are representative of the sunlight visible range wavelengths, with red light at 625 nm, 530 nm green, 455 nm blue and 365 nm UV. When exposed to light, the EPR signal undergoes changes in comparison to the signal from the sample that was not exposed to light.
The simulations for the dark and irradiated spectra are presented in Figures 6.2 and 6.3, respectively, and allow for the extraction of the distinctive EPR parameters. The characteristics of the EPR signals can be explained by five distinct EPR active centres (four associated with nitrogen species and a Ti^{3+}), as shown in Figures 6.2 and 6.3.

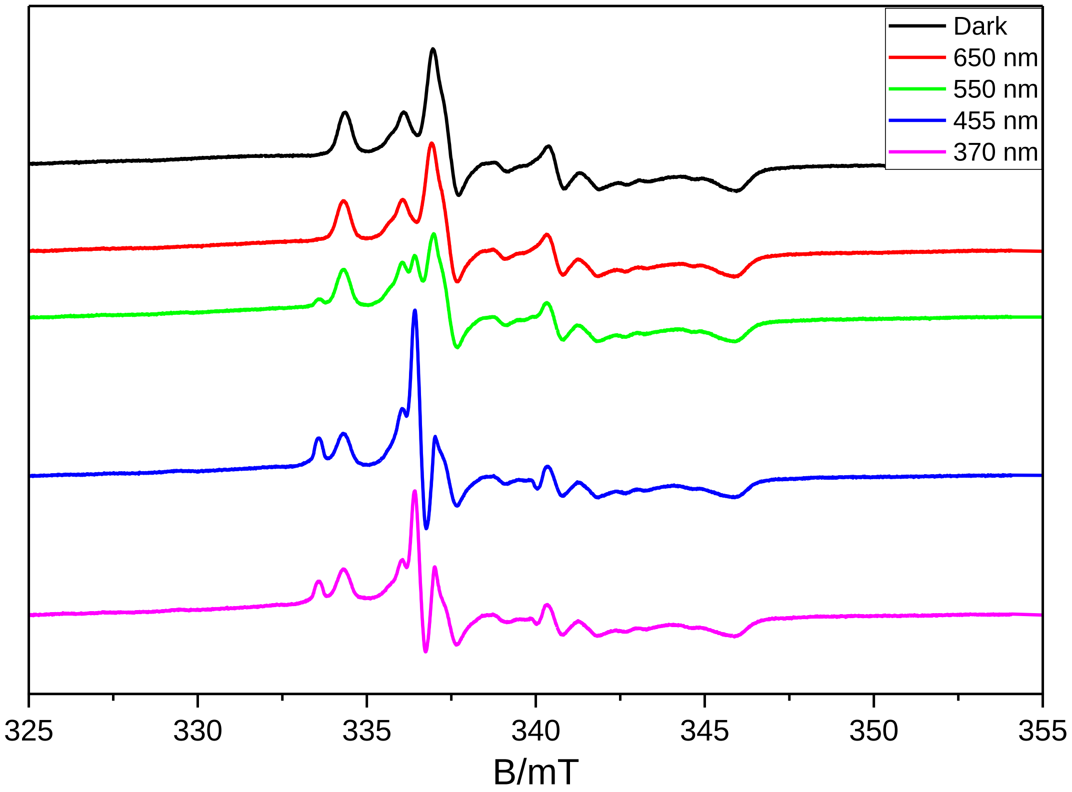

Figure 6.1: EPR spectra in the dark (a) and under in situ irradiation with 625 nm wavelength visible light (b), 530 nm wavelength visible light (c), 455 nm wavelength visible light (d) and 365 nm wavelength visible light (e) for the F-A-WN-TiO_2 sample.

Table 6.1 reports the **g** and **A** tensors of the Sys1, Sys2, Sys3, Sys4, Sys5, Sys6 and Sys8 and the species associated with those denotations. The presence of the paramagnetic centre labelled Sys1 in sol-gel synthesised co-doped TiO_2 can be attributed to the adsorption of molecule NO,(1,2), an 11-electron π radical in the adsorbed form, which is frequently seen in the cavities of the unit cell. This species demonstrates an anisotropic g tensor with rhombic symmetry. A resolvable hyperfine structure in each component of the **g**-tensor is developed when the unpaired electron is coupled with the nonzero nuclear spin ^{14}N (nuclear spin $I = 1$, signal multiplicity $2I + 1 = 3$). The values listed agree well with those that have been published elsewhere.(1,2) In the free-spin region, the EPR spectrum of NO in the gas phase is typically not visible; however, when the molecule is polarized and weakly adsorbed at $T < 170$ K on a cationic surface centre, it becomes visible. (3)
The presence of the EPR profile after each sample was evacuated under dynamic vacuum (ca. 10^{-4} mbar) and at 393 K for a minimum of 12 hours, indicates that the NO is encapsulated in bulk and subsurface micro voids (or closed

pores) created during the synthetic process rather than adsorbed on the sample's exposed surface. (2)

An interstitial N chemically coupled to a lattice O ion forms the paramagnetic centre labelled Sys2, which is composed of a $[N_iO]^•$ (5) group with one electron in the π* anti-bonding (1) singly occupied molecular orbital (SOMO). The $[N_iO]^•$ is essentially an intra band gap $NO^{2—}$ state that displays an anisotropic **g** tensor, see Table 6.1. More information about the paramagnetic centres labelled Sys1 and Sys2 have been covered elsewhere. (1,5)

There is a third paramagnetic centre, labelled Sys3. The interaction of paramagnetic $NO^{2—}$ with W produces $[N_iO]W^•$. Tungsten has five naturally occurring nuclides, with their following natural abundance: ^{180}W (0.12%), ^{182}W (26.50%), ^{183}W (14.31%), ^{184}W (30.64%), and ^{186}W (28.43%). Four $[N_iO]W^•$ isotopomers (^{180}W, ^{182}W, ^{184}W, and ^{186}W) have zero nuclear spins and are hence EPR-equivalent. (8) Only ^{183}W can produce super hyperfine structures when coupled with free $NO^{2—}$ electrons. Therefore, the total signal of the Sys3 centre consists of two components: a W-close range $NO^{2—}$ signal with super hyperfine splitting that accounts for 14.31% of ^{183}W that couples to the unpaired electron, and a close-range W-$NO^{2—}$ signal without super hyperfine couplings (connected to the four equivalent isotopomers). (9) The highly polarizing W^{6+} ion in this W–O–N close-range arrangement pushes electron density away from the lattice oxygen, increasing the N 2p character of the π* anti-bonding SOMO of the $N_iO^•$ unit, that is, the spin density linked to the unpaired electron is more confined to the N atom when compared to the N_2 centre.(10) Table 6.1 demonstrates the decrease of the g values (smaller g_{iso}) and the rise of the A values (larger a_{iso}), relative to the N_2 centre.

The fourth nitrogen associated signal is characterised by an orthorhombic EPR profile and an anisotropic hyperfine structure, which is caused by the coupling of the two nitrogen atoms, therefore, this signal is attributed to the paramagnetic $N_2^{—}$. This signal is only present for the samples with nitrogen sourced from ammonia solution at the anatase polymorph, therefore, this signal is a result of the synthetic pathway as the $N_2^{—}$ gets trapped in the voids of the material and the calcination temperature isn't high enough to completely remove it.

In addition to the nitrogen related signals, an axial signal is observed for the Ti^{3+} centres.

Table 6.1: **g** and **A** tensors for EPR centres Sys1, Sys2, Sys3 and Sys4, Ti^{3+}, $O_2^{—}$ and trapped hole for the F-A-WN-TiO_2.

Species	g_{xx}	g_{yy}	g_{zz}	A_1 **[MHz]**	A_2 **[MHz]**	A_3 **[MHz]**
NO (Sys1)	2.001 ± 0.002	1.998 ± 0.003	1.921 ± 0.005	2.8	92.5 ± 1.5	26.9
$N_iO^{2—}$ (Sys2)	2.0051 ± 0.0025	2.0044 ± 0.0021	2.0037 ± 0.0026	6.5	15.7	89.7 ± 1.5
W-$NO^{2—}$ (Sys3)	2.001 ± 0.002	2.000 ± 0.0018	1.999 ± 0.0023	(^{14}N) 45.1 ± 1.5 (^{183}W) 44.8 ± 1.3	22.4 ± 1.5 2.8	140.5 ± 3.5 154.1 ± 3.5
$N_2^{—}$ (Sys4)	2.004 ± 0.0031	2.002 ± 0.002	1.954 ± 0.0024	3.4	60.3 ± 2.5	15.7
Ti^{3+} (Sys5)	1.999 ± 0.001	1.999 ± 0.001	1.950 ± 0.005			
$O_2^{—}$ (Sys8)	2.024 ± 0.015	2.008 ± 0.002	2.002 ± 0.004			
Trapped hole (Sys6)	2.016 ± 0.011	2.007 ± 0.005	2.007 ± 0.004			

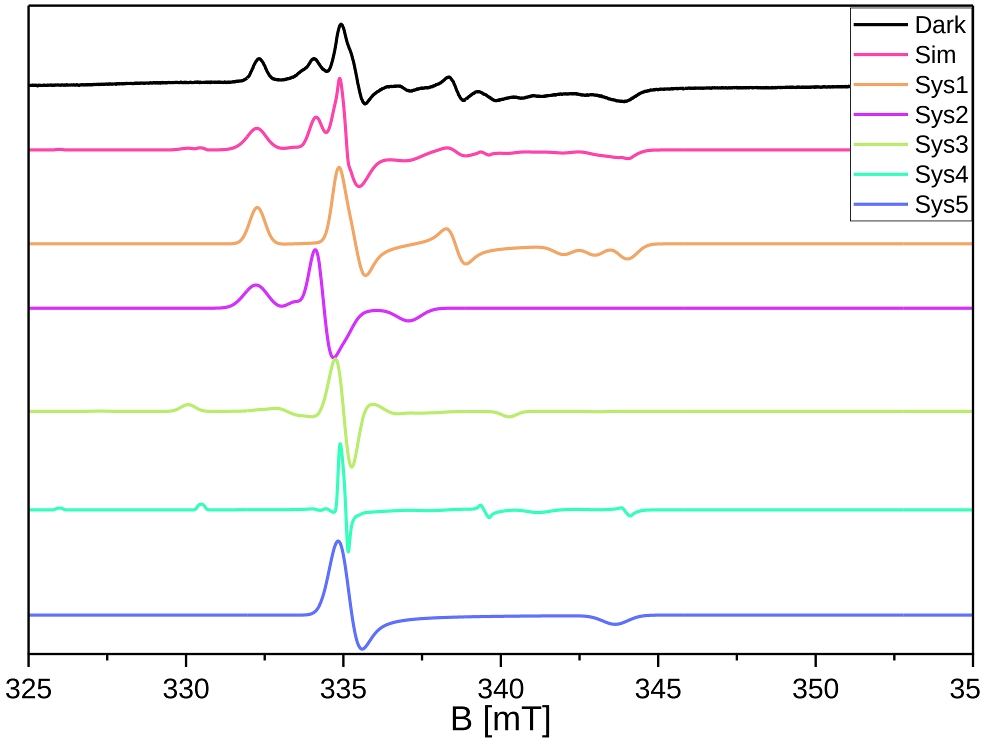

Figure 6.2: Experimental (black) and simulated (sim) dark spectra for F-A-WN-TiO_2 sample, including NO (Sys1), $N_iO^{2—}$ (Sys2), W-$NO^{2—}$ (Sys3), $N_2^{—}$ (Sys4) and Ti^{3+} (Sys5) (The scale for the individual species is set at 100% weight here, see Table 6.2 for specific contributions).

Having identified the nature of the EPR active species, we can now explain the change from the dark to the light-irradiated spectra in Figure 6.1. As in the case of N doping only, a large fraction of the nitrogen centres is diamagnetic before light irradiation, carrying two paired electrons in the highest occupied molecular orbital. (5) They can be seen as a $[N_iO]^-$,intra band gap NO^{3-} states, and, similarly, $[N_iO]W^-$ characterized by close range N−W coupling. The dark spectrum (Figure 6.1 (a)) is therefore dominated by the signal of adsorbed molecular NO (1,2) (Sys1 centre), which is formed and encapsulated during the doping stage of the synthesis. There are no observable differences between the dark spectrum and the 625 nm (red light) spectrum. However, as the wavelength is decreased and starts to approach the UV region, the appearance of changes in the spectra become more distinct. Upon irradiation with 530 nm, 455 nm and 365 nm, electron transitions $NO^{3-} \rightarrow$ CB occur, leaving behind a much larger quantity of paramagnetic NO^{2-} states that can be easily detected by EPR (Table 6.2). Overall, the signal of the adsorbed molecular NO does not significantly change, but the considerable formation of paramagnetic $[N_iO]^\bullet$ and $[N_iO]W^\bullet$ centres are responsible for the new profile of the EPR spectrum (Figure 6.1 (e)) together with the increased intensity.

In addition to the increase of the $[N_iO]^\bullet$, the presence of the superoxide centre is seen after irradiation of the sample in oxygen atmosphere, thus, causing photogeneration, Table 6.2. Molecular oxygen, (around 10 Torr) was added to a clean surface for the co-doped sample and then the closed cell was irradiated for 30 minutes at 77 K (liquid nitrogen), under O_2 atmosphere. After irradiation the O_2 atmosphere was evacuated prior to measurement. This signal displays an orthorhombic EPR profile. (11) As it has been reported, the magnitude of the g_{zz} component is primarily controlled by the local electric field gradient at the surface adsorption site (Ti^{4+}), which reduces the degeneracy of the two π^* antibonding orbitals to a degree that depends on the strength of the electric field gradient. These g_{zz} values for TiO_2 typically vary from 2.026 to 2.018, (11), with some slight variations based on the sample's physicochemical properties (phase, morphology, particle size, etc.) and sample treatment, presented in the discussion of this Chapter.

The weights of the different species contributions are presented in Table 6.2 for the different wavelengths, therefore, assembling the overall EPR profile of the sample at the different wavelengths.

Table 6.2: Percentage weight distribution of each species for each irradiation wavelength for the F-A-WN-TiO_2.

Wavelength	**Paramagnetic species percentage weight contribution**						
	NO	**N_iO^{2-}**	**W-NO^{2-}**	**N_2^-**	**Ti^{3+}**	**O_2^-**	**Trapped hole**
Dark	46.9	10.8	5.3	5.3	28.6	0	0
625 nm	47.8	9.7	5	5.5	28.7	0	0
530 nm	50.3	16.8	2.5	8.4	16.8	5.2	0
455 nm	46.3	14.6	4.2	5.4	24.4	5.1	0
365 nm	40.4	23.2	0.6	5.4	13.5	14.9	2

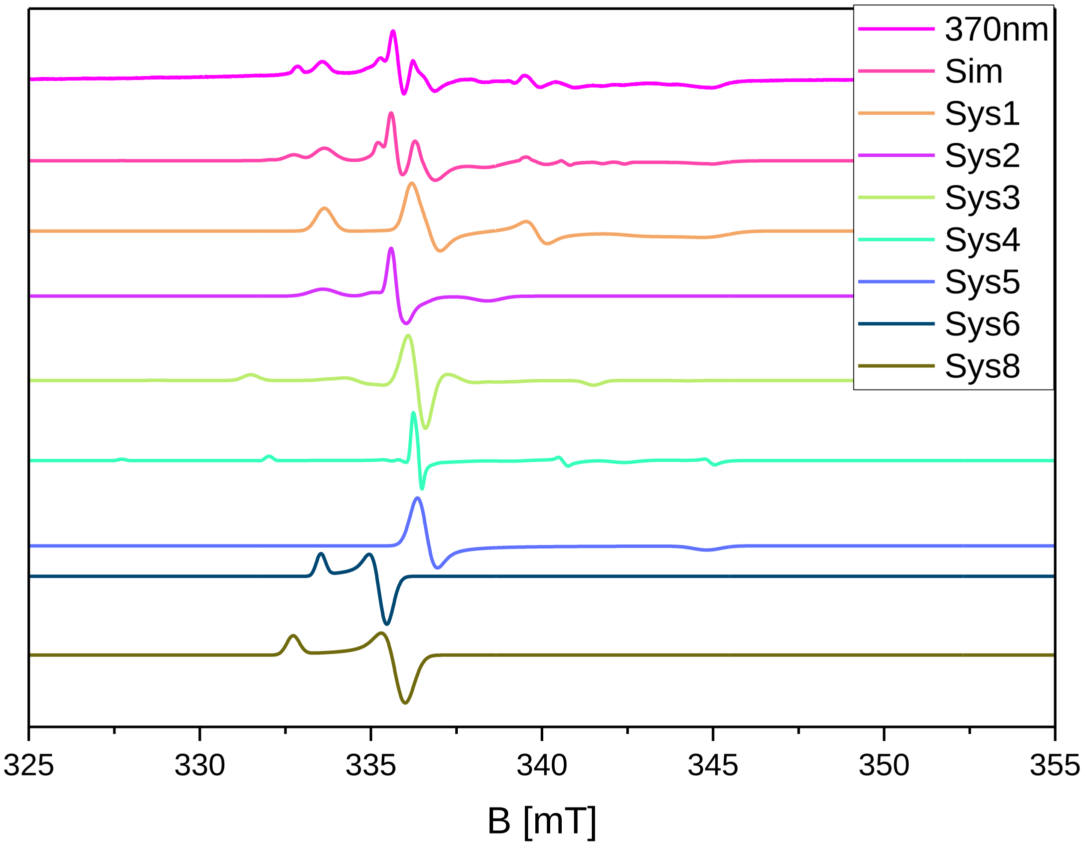

Figure 6.3: Experimental (black) and simulated (sim) 365 nm irradiated spectra for F-A-WN-TiO_2 sample, including NO (Sys1), N_iO^{2-} (Sys2) W-NO^{2-} (Sys3), N_2^- (Sys4), Ti^{3+} (Sys5), trapped hole (Sys6) and O_2^- (Sys8) (The scale for the individual species is set at 100% weight here, see Table 6.2 for specific contributions).

Figure 6.4 shows the spectra of the F-R-WN-TiO_2 under different photoirradiation conditions, specifically, in the absence of light and during exposure to the following wavelengths of 625 nm (b), 530 nm (c), 455 nm (d) and 365 nm (e).

The EPR spectrum obtained under 365 nm irradiation presents differences in the contributing signals.

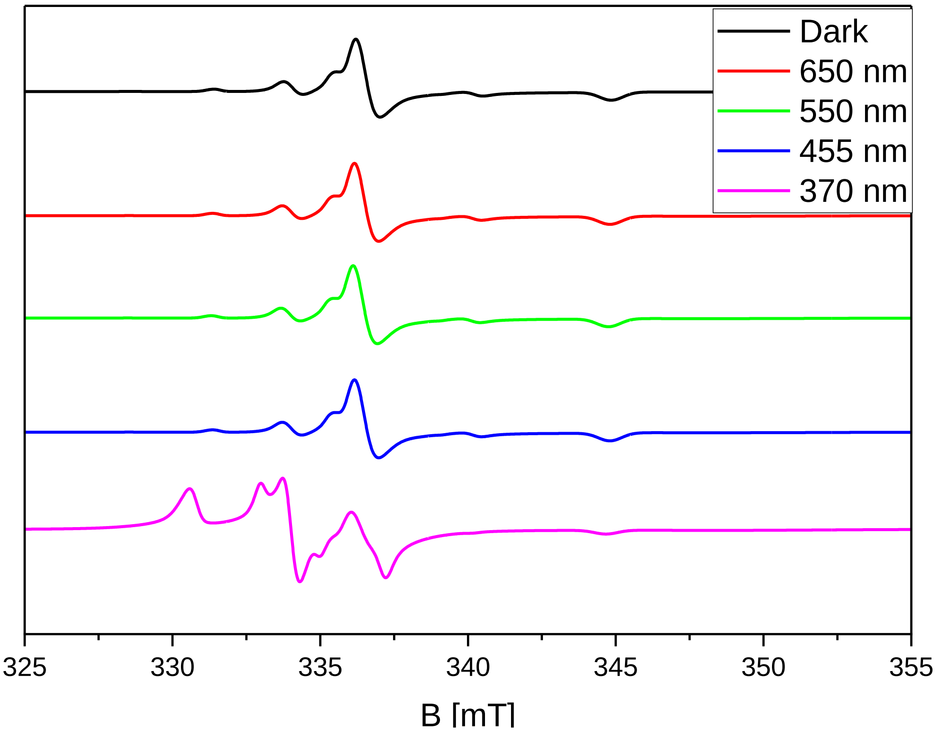

Figure 6.4: EPR spectra in the dark (a) and under in situ irradiation with 625 nm wavelength visible light (b), 530 nm wavelength visible light (c), 455 nm wavelength visible light (d) and 365 nm wavelength visible light (e) for the F-R-WN-TiO_2 sample.

The simulations for the dark and irradiated spectra are presented in Figures 6.5 and 6.6, respectively, and allow for the extraction of the distinctive EPR parameters. The characteristics of the EPR signals can be explained by four distinct EPR active centres (four associated with nitrogen species and a Ti^{3+}), as shown in Figures 6.5 and 6.6 and have been described and the **g** and **A** tensors are presented in the Table 6.3. Table 6.3 describes Sys1, Sys2, Sys3 and Sys5 and the species associated with those denotations.

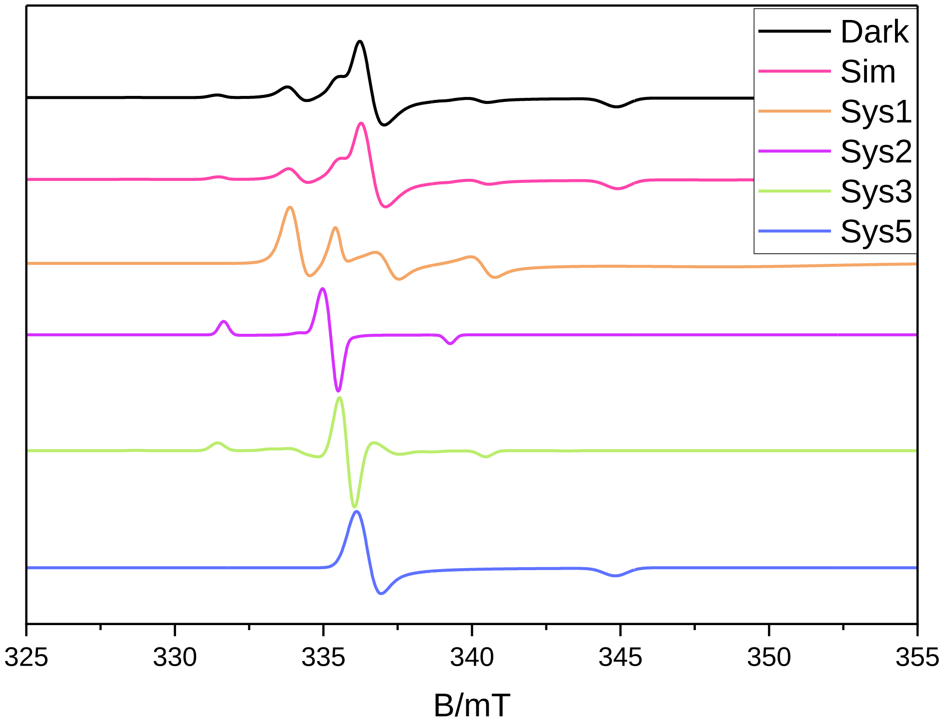

Figure 6.5:Experimental (black) and simulated (sim) dark spectra for F-R-WN-TiO_2 sample, including NO (Sys1), N_iO^{2-} (Sys2), W-NO^{2-} (Sys3), and Ti^{3+} (Sys5) (The scale for the individual species is set at 100% weight here, see Table 6.4 for specific contributions).

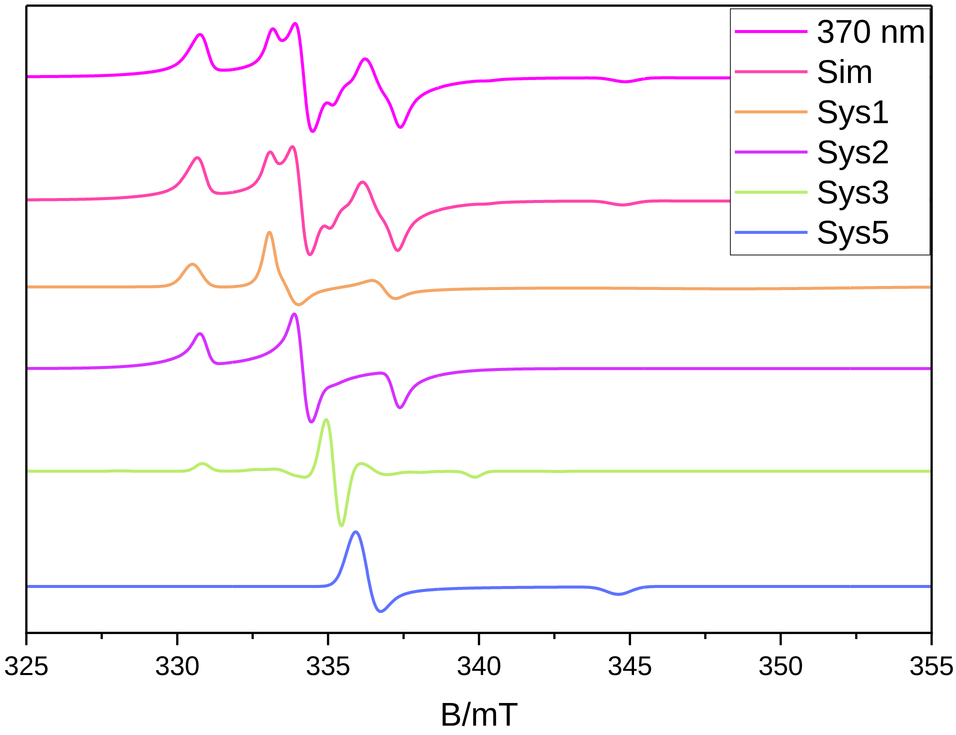

Figure 6.6: Experimental (black) and simulated (sim) 365 nm irradiated spectra for F-R-WN-TiO_2 sample, including NO (Sys1), N_iO^{2-} (Sys2), W-NO^{2-} (Sys3) and Ti^{3+} (Sys5) (The scale for the individual species is set at 100% weight here, see Table 6.4 for specific contributions).

Table 6.3: **g** and **A** tensors for EPR centres Sys1, Sys2 and Sys3 and Ti^{3+} for the F-R-WN-TiO$_2$.

Species	g_{xx}	g_{yy}	g_{zz}	A_1 **[MHz]**	A_2 **[MHz]**	A_3 **[MHz]**
NO (Sys1)	2.0013 ± 0.0026	1.9971 ± 0.0027	1.922 ± 0.0043	2.8	92.5 ± 1.7	26.9
N$_i$O^{2-} (Sys2)	2.0052± 0.0024	2.0041 ± 0.0023	2.0034 ± 0.0027	6.5	15.7	89.7 ± 2.1
W-NO^{2-} (Sys3)	2.001 ± 0.0016	2.000 ± 0.0017	1.999 ± 0.0021	(^{14}N)45.1 ± 1.3	22.4	140.5 ± 3.1
				(^{183}W)44.8 ± 1.4	2.8	154.1 ± 3.7
Ti^{3+} (Sys5)	1.988 ± 0.002	1.988 ± 0.002	1.950 ± 0.005			

As mentioned, no differences were detected between the dark spectrum and the spectra under 625 nm, 530 nm and 455 nm. However, as the wavelength is decreased and in the UV region, the appearance of changes in the spectra become more distinct. With the most important difference being the contribution of N$_i$O^{2-}, as it increased by almost 97% under 365 nm irradiation. A large fraction of the nitrogen centres is diamagnetic before light irradiation, with two paired electrons in the highest occupied molecular orbital. Upon irradiation with UV light, the electron transitions NO^{3-}→ CB occur, leaving behind a higher EPR detectable quantity of paramagnetic NO^{2-} states. The weights of the different species contributions are presented in Table 6.4 for the different wavelengths, therefore, assembling the overall EPR profile of the sample all of the irradiation wavelengths.

Table 6.4: Percentage weight distribution of each species for each irradiation wavelength for the F-R-WN-TiO$_2$.

Wavelength	**Paramagnetic species percentage weight contribution**			
	NO	**N$_i$O^{2-}**	**W-NO^{2-}**	**Ti^{3+}**
Dark	38.4	1.1	5.6	54.9
625 nm	36.2	1.3	5.8	56.7
530 nm	37.5	1.4	5.2	55.9
455 nm	36.6	1.6	5.1	56.7
365 nm	10.9	49.2	0.9	29.0

Figure 6.7 displays the spectra of the F-A-WN(U)-TiO_2 under different irradiation conditions, explicitly in the absence of light and under irradiation at the following wavelengths of 625 nm (b), 530 nm (c), 455 nm (d) and 365 nm (e). When exposed to light, the EPR signal goes through changes in comparison to the signal from the sample that was not exposed to light.

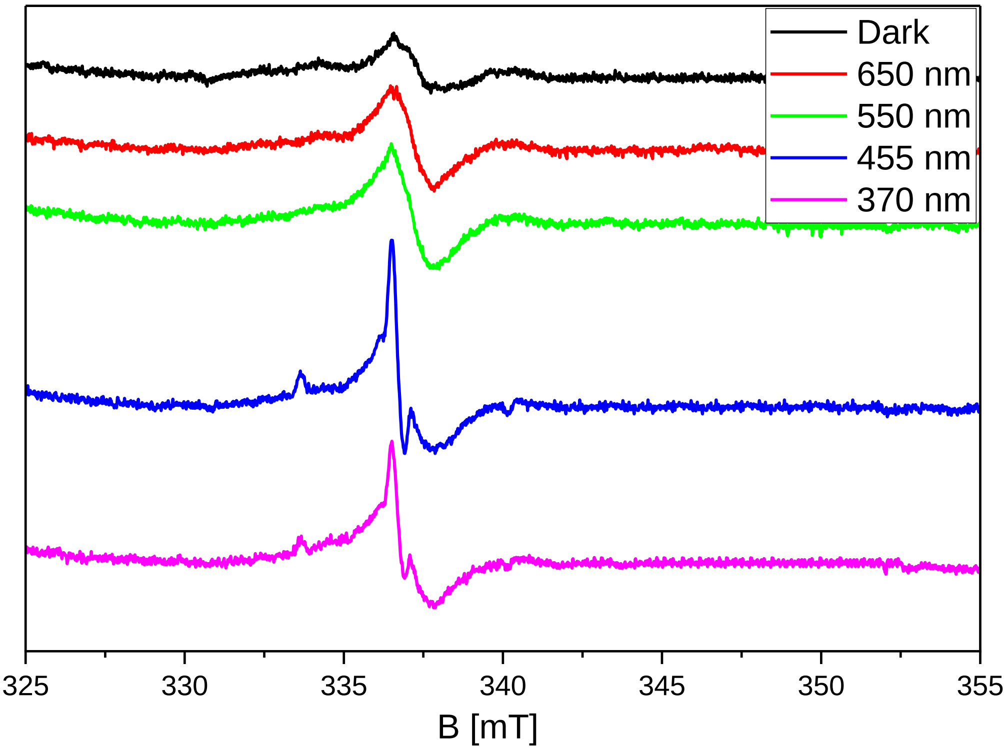

Figure 6.7: EPR spectra in the dark (a) and under in situ irradiation with 625 nm wavelength visible light (b), 530 nm wavelength visible light (c), 455 nm wavelength visible light (d) and 365 nm wavelength visible light (e) for the F-A-WN(U)-TiO_2 sample.

The simulations for the dark and irradiated spectra are presented in Figures 6.8 and 6.9, respectively, and allows for the extraction of the distinctive EPR parameters. The characteristics of the EPR signals can be explained by one nitrogen distinct EPR active centre (Sys2), as shown in Figure 6.7 which has been described earlier, and the **g** and **A** tensors are shown in Table 6.5. In addition to the nitrogen related signal the broadened axial signal for the Ti^{3+} centre is observed. Table 6.5 describes of the Sys2 and Sys5 and the species associated with those denotations.

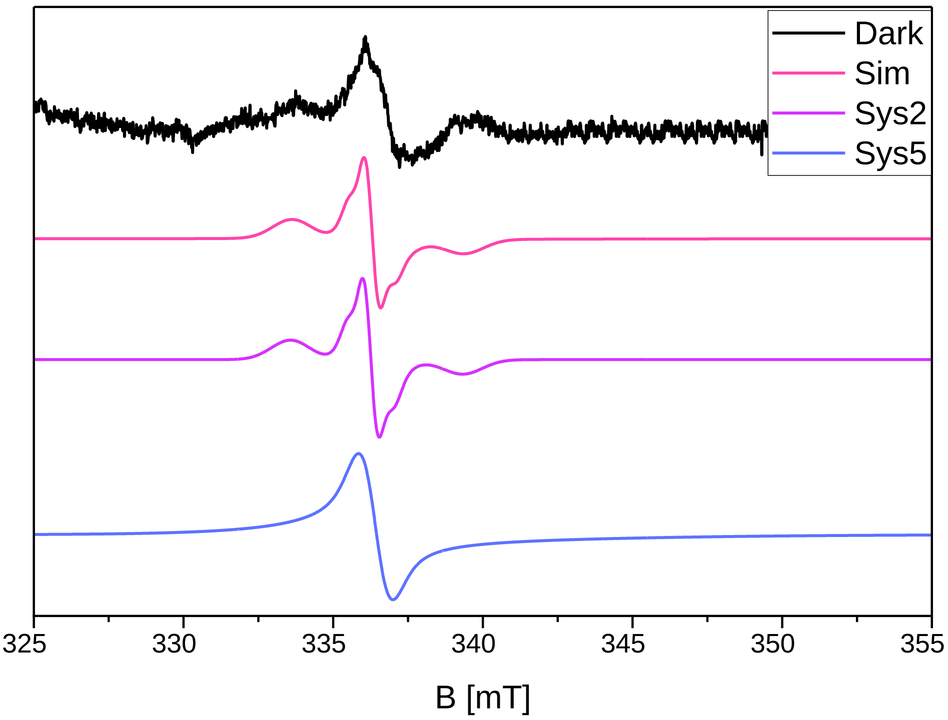

Figure 6.8: Experimental (black) and simulated (sim) dark spectra for F-A-WN(U)-TiO_2 sample, including N_iO^{2-}(Sys2) and Ti^{3+} (Sys5) (The scale for the individual species is set at 100% weight here, see Table 6.6 for specific contributions).

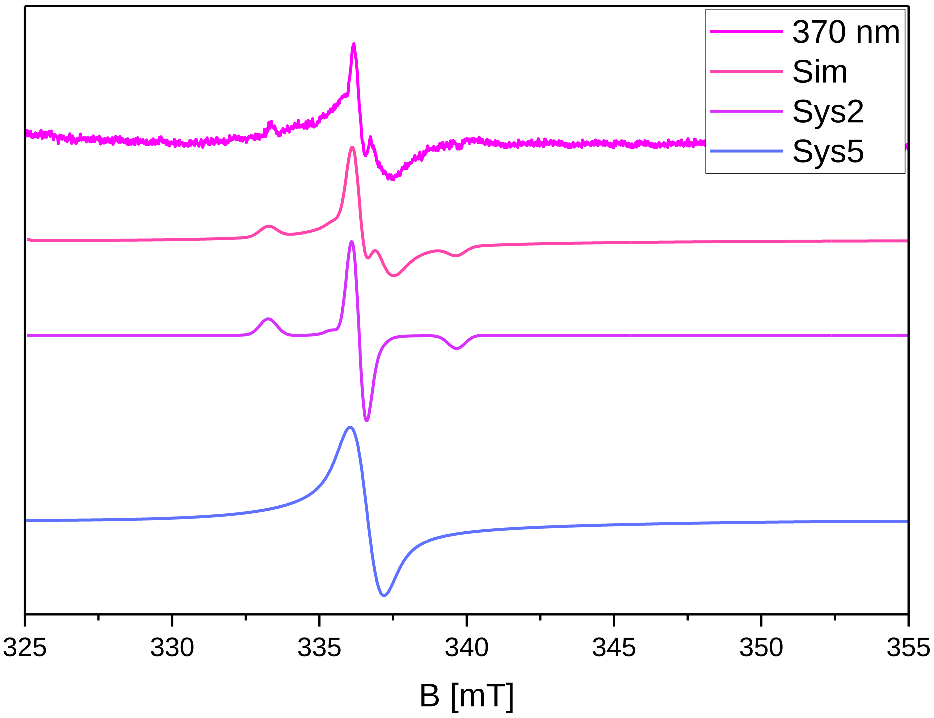

Figure 6.9: Experimental (black) and simulated (sim) 365 nm irradiated spectra for F-A-WN(U)-TiO_2 sample, including N_iO^{2-} (Sys2) and Ti^{3+} (Sys5) (The scale for the individual species is set at 100% weight here, see Table 6.6 for specific contributions).

Table 6.5: **g** and **A** tensors for EPR centres Sys2 and Ti^{3+} for the F-A-WN(U)-TiO_2.

Species	g_{xx}	g_{yy}	g_{zz}	A_1 **[MHz]**	A_2 **[MHz]**	A_3 **[MHz]**
$N_iO^{2—}$ (Sys2)	2.0015 ± 0.0025	1.9975 ± 0.0025	1.924 ± 0.004	2.8	92.4 ± 2.5	26.8
Ti^{3+} (Sys5)	1.999 ± 0.0015	1.999 ± 0.0015	1.950 ± 0.005			

There are no observable differences between the dark spectrum and the 625 nm (red light) and 530 nm (green light) spectra. With the decreased of the wavelength, starting to approach the UV region, the appearance of changes in the spectra become more distinct. At 455 nm (blue light) and 365 nm (UV light) the presence of the interstitial N chemically coupled to a lattice O ion forms the paramagnetic centre labelled Sys2 is distinctly observed at an increased amount. This sample greatly demonstrates the case of the large fraction of the nitrogen centres that are diamagnetic before light irradiation, carrying two paired electrons in the highest occupied molecular orbital. They can be seen as a $[N_iO]^{—}$,intra band gap $NO^{3—}$ states,(8). Upon irradiation with visible blue and UV light, the aforementioned explained electron transitions $NO^{3—} \rightarrow$ CB occur, leaving behind a higher EPR detectable quantity of paramagnetic $NO^{2—}$ states. The contributions of the different species for wavelengths are presented in Table 6.6, resulting in the overall EPR profile of the sample.

Table 6.6: Percentage weight distribution of each specie for each irradiation wavelength for the F-A-WN(U)-TiO_2.

Wavelength	**Paramagnetic species percentage weight contribution**	
	$N_iO^{2—}$	**Ti^{3+}**
Dark	20	80
625 nm	21	79
530 nm	22	78
455 nm	80.4	19.6
365 nm	82.5	17.5

Figure 6.10 shows the spectra of the F-R-WN(U)-TiO_2 under different photoirradiation conditions, specifically in the absence of light and during exposure the following wavelengths of 625 nm (b), 530 nm (c), 455 nm (d) and 365 nm (e). When exposed to visible light, the EPR signal does not undergo any changes in comparison to the signal from the sample that was not exposed to light. Prior to a discussion of the lack of changes observed upon irradiation in the sample, it is pertinent to first provide a full description of the different EPR active centres observed.

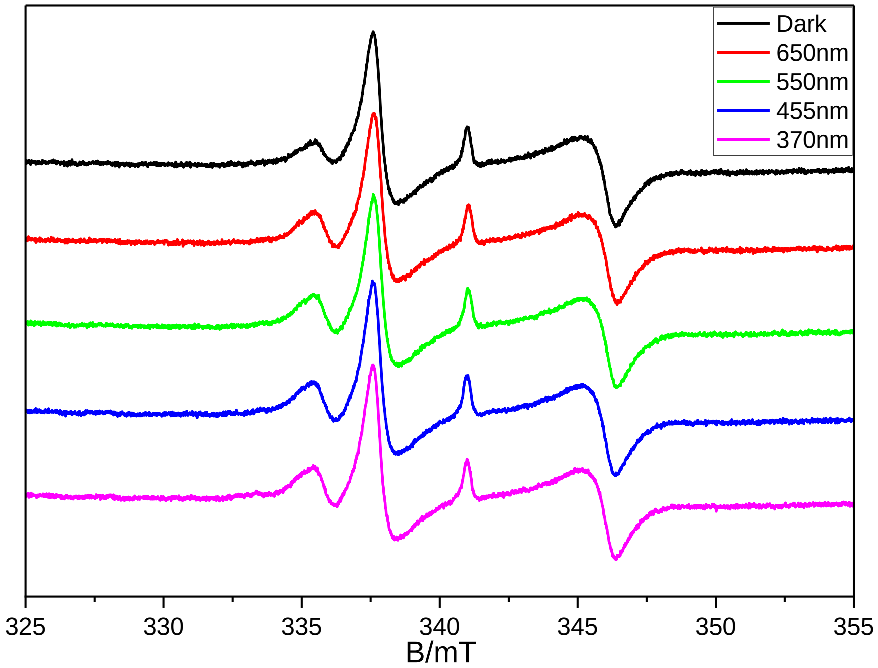

Figure 6.10: EPR spectra in the dark (a) and under in situ irradiation with 625 nm wavelength visible light (b), 530 nm wavelength visible light (c), 455 nm wavelength visible light (d) and 365 nm wavelength visible light (e) for the F-R-WN(U)-TiO_2 sample.

The simulation for the dark spectrum is seen in Figures 6.11 and allows for the extraction of the distinctive EPR parameters.

The characteristics of the EPR signals obtained can be explained by two distinct EPR active centres (one nitrogen associate and the Ti^{3+}), as shown in Figure 6.11. The nitrogen associated species is the molecular NO, that has been described and denotated a Sys1, with g_{xx} = 2.0011, g_{yy} = 1.9976 and g_{zz} = 1.922 and A_1 = 2.8, A_2 = 92.3 and A_3 = 26.8 MHz. As mentioned, the broadened axial signal for the Ti^{3+} centre is observed, with g_{xx} = g_{yy} = 1.985 and g_{zz} = 1.949. The weight contributions of the two species remain constant across all the wavelengths, with the NO weight percentage at 85% and the Ti^{3+} weight percentage at 15%.

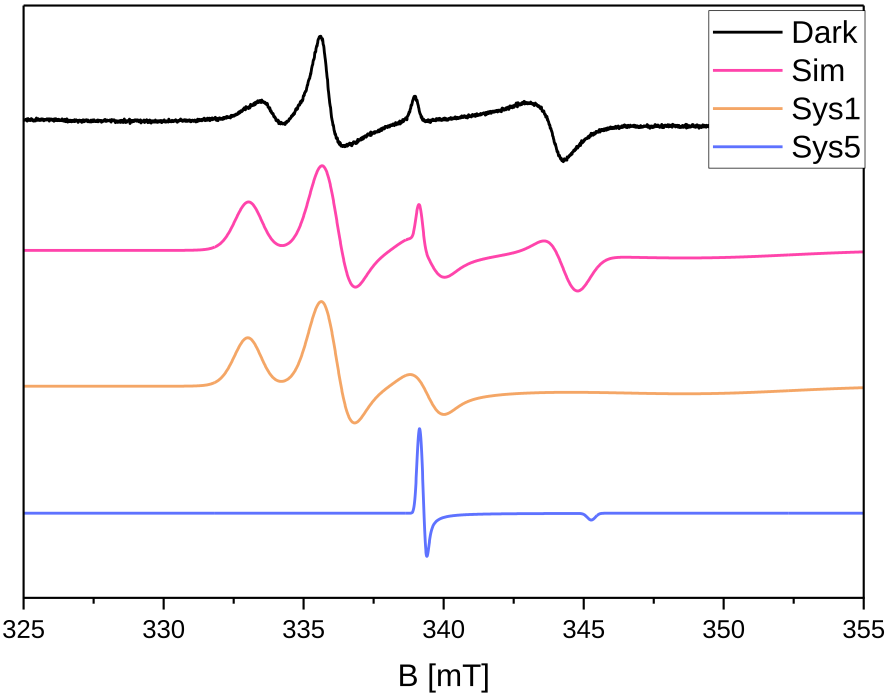

Figure 6.11: Experimental (black) and simulated (sim) dark spectra for F-R-WN(U)-TiO_2 sample, including NO (Sys1), Ti^{3+} (Sys5) (The scale for the individual species is set at 100% weight here, specific contributions are stated in text).

6.2 Tantalum and Nitrogen co-doped samples

The effect of different metal dopant, tantalum, was investigated in this thesis, resulting in the TaN- co-doped TiO_2 materials, which through their distinct characterised EPR spectra present their capabilities as photocatalysts.

Figure 6.12 displays the spectra of F-A-TaN-TiO_2 under different photoirradiation conditions, specifically, in the absence of light and under the following wavelengths of 625 nm (b), 530 nm (c), 455 nm (d) and 365 nm (e). When exposed to light, the EPR signal becomes stronger and the specie contribution ratio changes. The simulation for the dark and irradiated spectra is presented in Figures 6.13 and 6.14, respectively. The characteristics of the EPR signals can be assigned to four EPR active centres (three nitrogen associate and the Ti^{3+}) distinct, as shown in Figure 6.13.

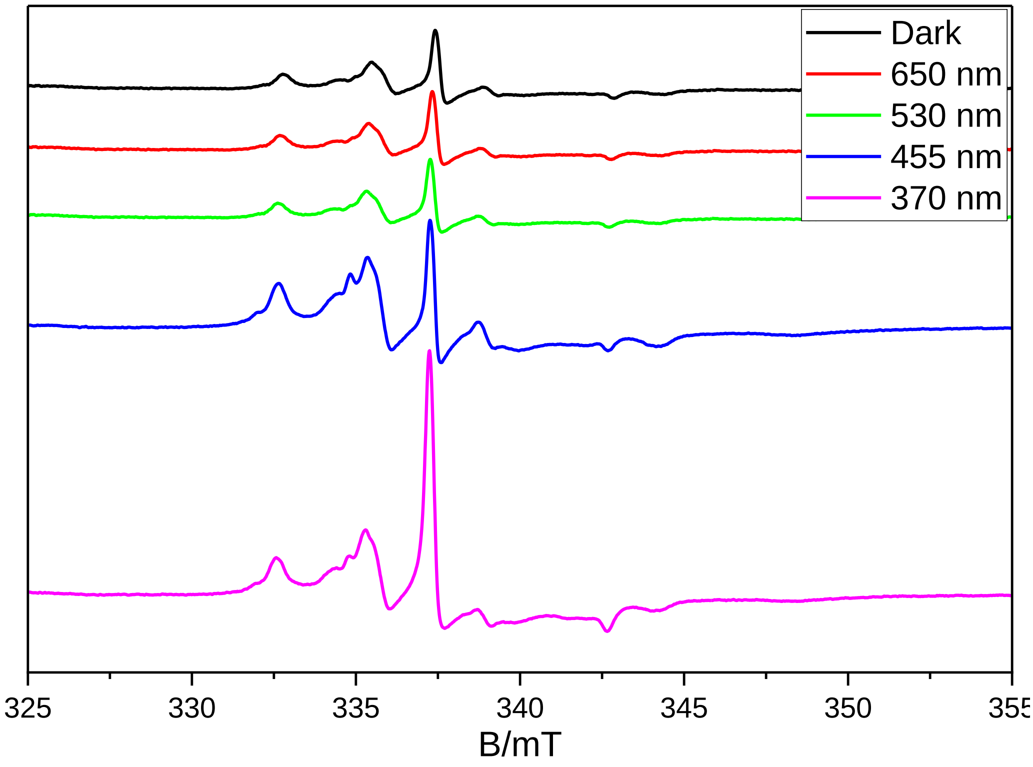

Figure 6.12: EPR spectra in the dark (a) and under in situ irradiation with 625 nm wavelength visible light (b), 530 nm wavelength visible light (c), 455 nm wavelength visible light (d) and 365 nm wavelength visible light (e) for the F-A-TaN-TiO_2 sample.

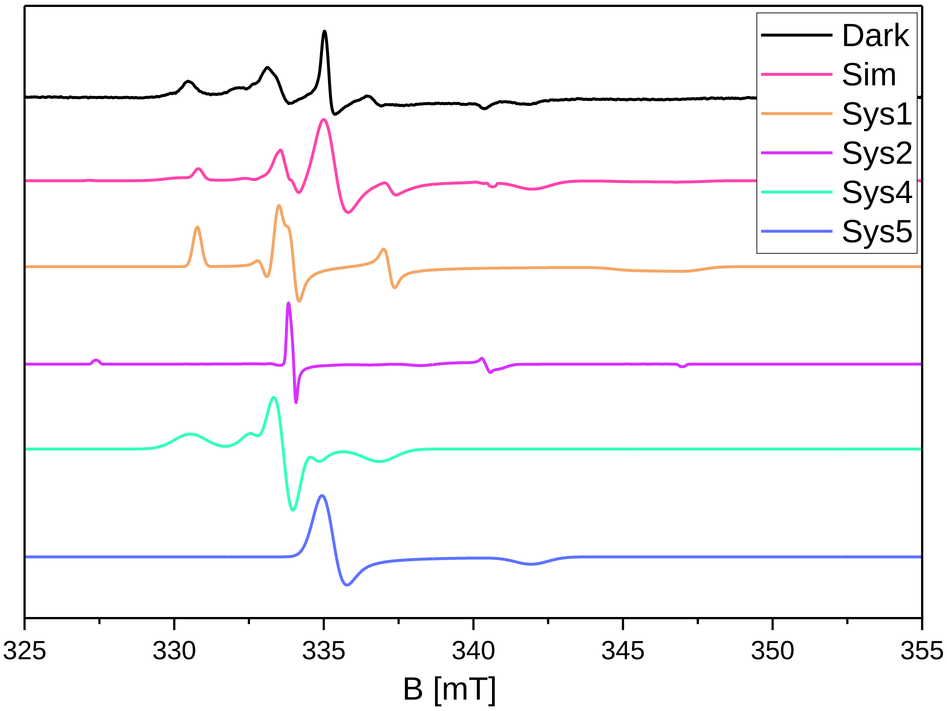

Figure 6.13: Experimental (black) and simulated (sim) dark spectra for F-A-TaN-TiO_2 sample, including NO (Sys1), N_iO^{2-} (Sys2), N_2^- (Sys4) and Ti^{3+} (Sys5) (The scale for the individual species is set at 100% weight here, see Table 6.8 for specific contributions).

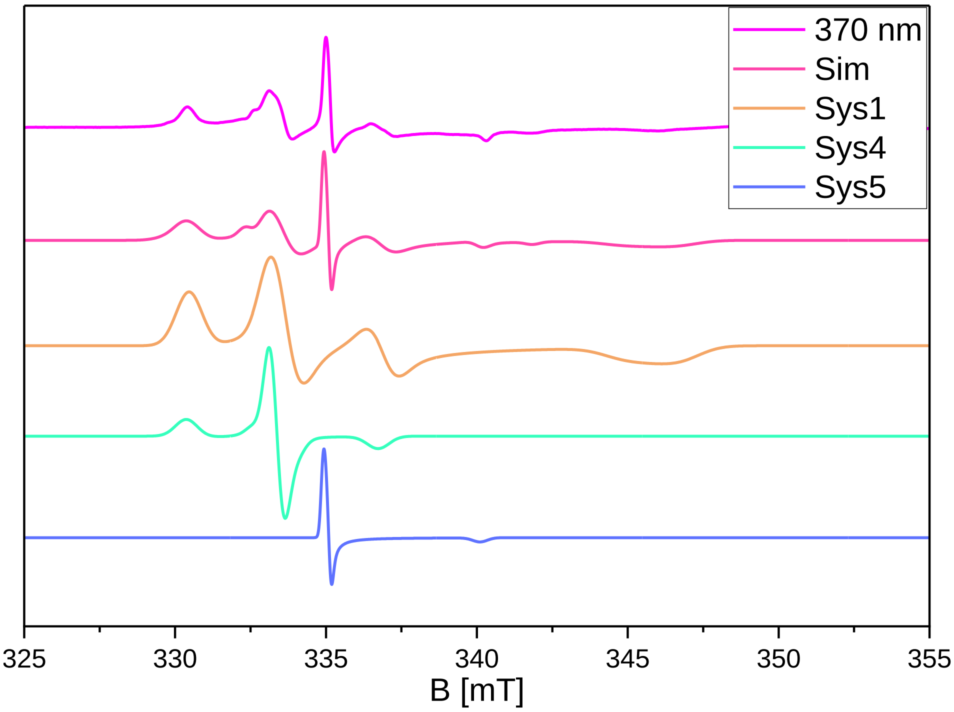

Figure 6.14: Experimental (black) and simulated (sim) 365 nm irradiated spectra for F-A-TaN-TiO_2 sample, including NO (Sys1), N_2^- (Sys4) and Ti^{3+} (Sys5) (The scale for the individual species is set at 100% weight here, see Table 6.8 for specific contributions).

Table 6.7: **g** and **A** tensors for EPR centres Sys1, Sys2 and Sys4 and Ti^{3+} for F-A-TaN-TiO$_2$.

Species	g_{xx}	g_{yy}	g_{zz}	A_1 [MHz]	A_2 [MHz]	A_3 [MHz]
NO (Sys1)	2.001 ± 0.002	1.998 ± 0.0024	1.925 ± 0.0055	2.8	92.5 ± 1.9	26.9
N_iO^{2-} (Sys2)	2.005 ± 0.0027	2.004 ± 0.0023	2.003 ± 0.0024	6.5	15.7	89.4 ± 1.5
N_2^{-} (Sys4)	2.0043 ± 0.0024	2.0023 ± 0.0024	1.957 ± 0.0019	3.4	60.3 ± 2.7	15.7
Ti^{3+} (Sys5)	1.996 ± 0.002	1.996 ± 0.002	1.950 ± 0.0058			

Table 6.7 reports the **g** and **A** tensors of the Sys1, Sys2, Sys4 and Sys5 and the species associated with those denotations. The paramagnetic centre labelled Sys1 presence has be attributed to the adsorption of molecule NO,(6-10), which has been described at the earlier in the chapter. This specie demonstrates an anisotropic **g** tensor with rhombic symmetry and hyperfine structure as explained in the WN- co–doped samples. The values that are displayed agree well with those that have been published in the literature.(9) As mentioned, NO is not visible at room temperature; however, once the weakly adsorbed molecule is polarised on a cationic surface and at temperatures below 170 K it becomes detectable. (1) The NO is encapsulated in bulk and subsurface micro voids created during synthesis rather than adsorbed on the exposed surface which is noticeable from the profile of the signal after treatment of the sample at 393 K for more than 12 hours, ca. 10^{-4} mbar. (4)

The interstitial N chemically coupled to a lattice O ion forms the paramagnetic centre labelled Sys2, which is composed of a [N$_i$O]• (4) is present .

The last nitrogen associated signal is characterised by an orthorhombic EPR profile and an anisotropic hyperfine structure, which is caused by the coupling of the two nitrogen atoms, therefore, this signal is attributed to the paramagnetic N_2^-. This signal is only present for the samples with nitrogen sourced from ammonia solution at the anatase morph, therefore, this signal is a result of the synthetic pathway as the N_2^- gets trapped in the voids of the material and the calcination temperature isn't high enough to completely remove it. In addition to the nitrogen related signals the axial signal for the Ti^{3+} centre is observed.

Having identified the nature of the EPR active species, we can now explain the change from the dark to the photo irradiated spectra in Figure 6.12 (e) . As in the case of rest of the doping systems, a large fraction of the nitrogen centres is diamagnetic before light irradiation. There are no observable differences between the dark spectrum, the 625 nm (red light) and 530 nm (green light) spectra. The dark spectrum (Figure 6.12 (a)) is predominantly dominated by the signal of adsorbed molecular NO (1,9) (Sys1 centre). Light irradiation does not affect the quantity of paramagnetic $NO^{2—}$ states. As the wavelength is decreased and start to approach the UV region, the appearance of changes in the spectra are observed. This evident as the N_2^- signal contribution is decreased, reaching zero, with the decrease of the wavelength. The signal of the adsorbed molecular NO, $[N_iO]^\bullet$ and Ti^{3+} do not significantly change, but the change in the ratio of the paramagnetic centres is responsible for the new profile of the EPR spectrum (Figure 6.12 (d and e)).

The weights of the different species contributions are presented in Table 6.8 for the different wavelengths, therefore, assembling the overall EPR profile of the sample at the different wavelengths.

Table 6.8: Percentage weight distribution of each specie for each irradiation wavelength for F-A-TaN-TiO_2.

Wavelength	Paramagnetic species percentage weight contribution			
	NO	**$N_iO^{2—}$**	**$N_2^{—}$**	**Ti^{3+}**
Dark	28.8	16.1	1.6	53.5
625 nm	35.1	12.3	0.3	52.3
530 nm	31.7	17.1	0	51.2
455 nm	36.5	16.6	0	46.9
365 nm	37.1	17.3	0	45.6

Figure 6.15 shows the spectra of the F-R-TaN-TiO_2 under irradiation conditions, namely, in the absence of light and during exposure to the following wavelengths of 625 nm (b), 530 nm (c), 455 nm (d) and 365 nm (e). When exposed to visible and UV light, the EPR signal does not undergo any changes in comparison to the signal from the sample that was not exposed to light.

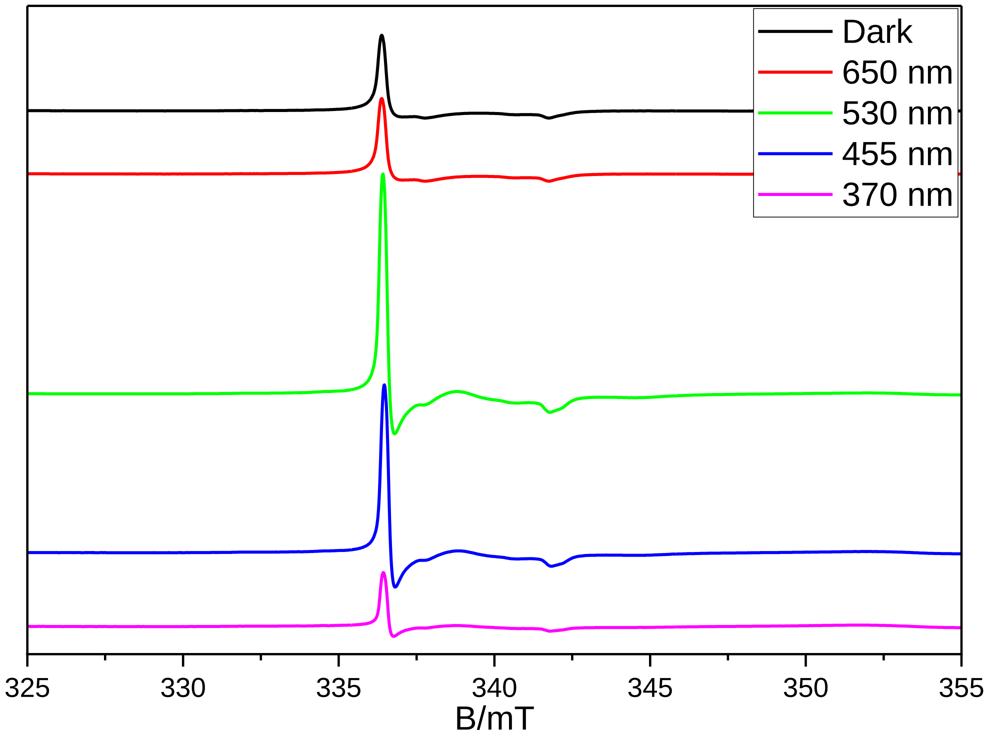

Figure 6.15: EPR spectra in the dark (a) and under in situ irradiation with 625 nm wavelength visible light (b), 530 nm wavelength visible light (c), 455 nm wavelength visible light (d) and 365 nm wavelength visible light (e) for the F-R-TaN-TiO_2 sample.

The simulation for the dark spectrum is seen in Figures 6.16 and allows for the extraction of the distinctive EPR parameters. The characteristics of the EPR signals obtained can be explained by two distinct EPR active centres (one nitrogen associate and the Ti^{3+}), as shown in Figure 6.15. The nitrogen associated species is the molecular NO, that has been described and denotated a Sys1, with g_{xx} = 2.001 g_{yy} = 1.9975 and g_{zz} = 1.919 and A_1 = 2.8, A_2 = 92.4 and A_3 = 26.8 MHz. As mentioned, in addition to the nitrogen related signal the broadened axial signal for the Ti^{3+} centre is observed, with g_{xx} = g_{yy} = 1.999 and g_{zz} = 1.951. In addition to the nitrogen related signal the broadened axial signal for the Ti^{3+} centre is observed. The weight contributions of the two species remain constant across all the wavelengths, with the NO weight percentage at 64.3% and the Ti^{3+} weight percentage at 35.7%.

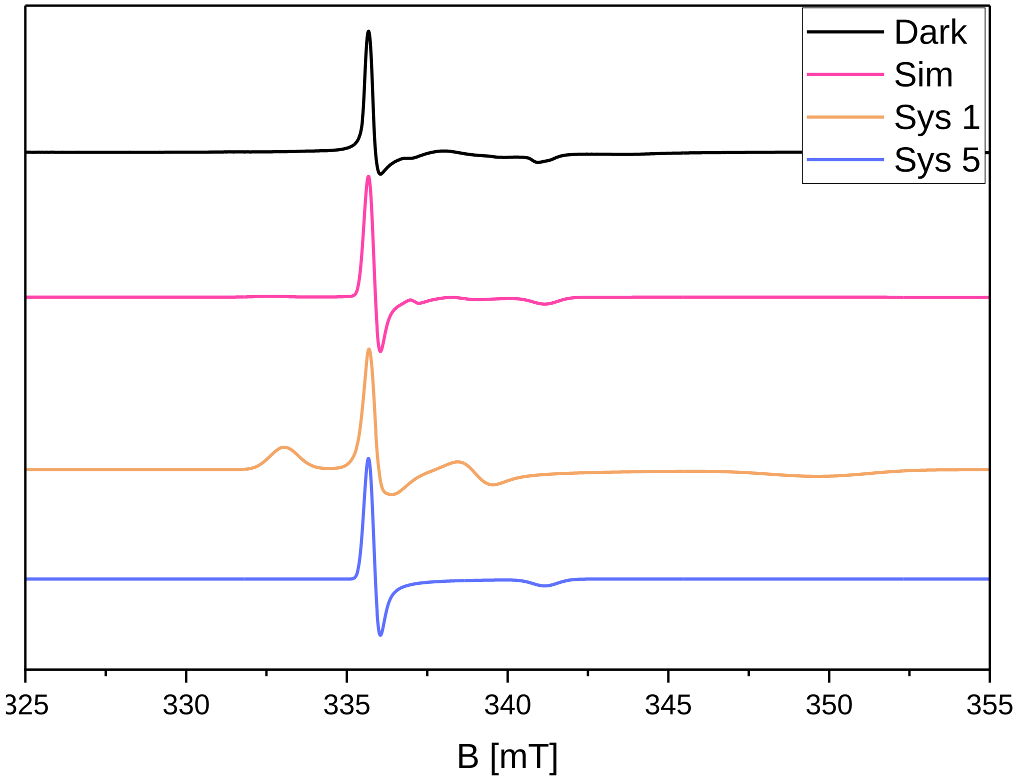

Figure 6.16: Experimental (black) and simulated (sim) dark spectra for F-R-TaN-TiO_2 sample, including NO (Sys1), and Ti^{3+} (Sys5) (The scale for the individual species is set at 100% weight here, specific contributions are stated in text).

Figure 6.17 displays the spectra of the F-A-TaN(U)-TiO_2 under different photoirradiation conditions, specifically, in the absence of light and under irradiation at the following wavelengths of 625 nm (b), 530 nm (c), 455 nm (d) and 365 nm (e). When exposed to light, the EPR signal undergoes changes in comparison to the signal from the sample that was not exposed to light.

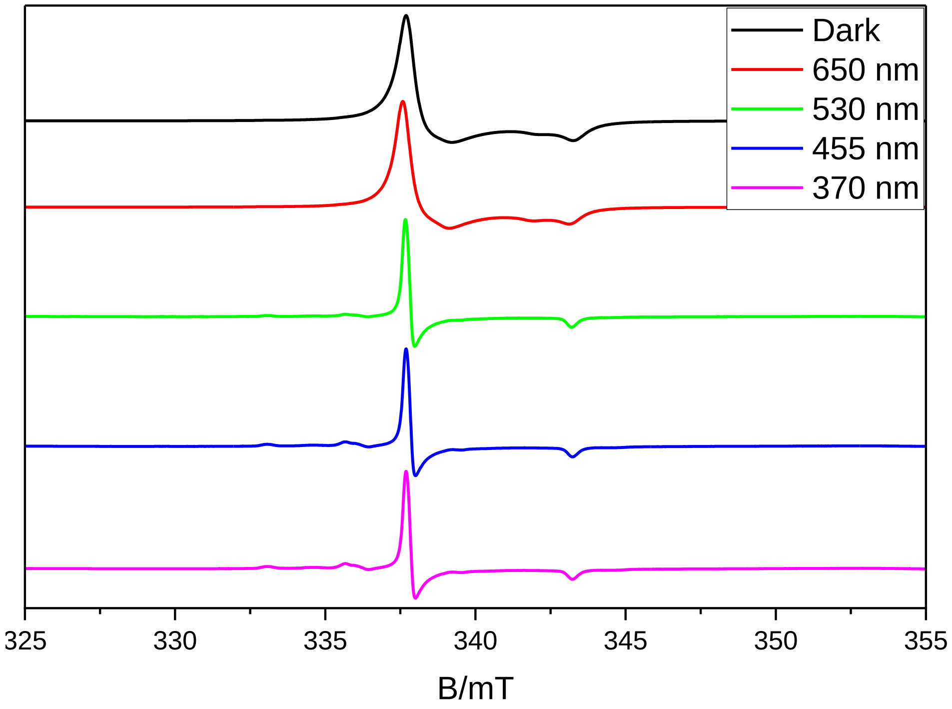

Figure 6.17: EPR spectra in the dark (a) and under in situ irradiation with 625 nm wavelength visible light (b), 530 nm wavelength visible light (c), 455 nm wavelength visible light (d) and 365 nm wavelength visible light (e) for the F-A-TaN(U)-TiO_2 sample.

The simulations for the dark and irradiated spectra it is presented in Figures 6.18 and 6.19, respectively, and allows for the extraction of the distinctive EPR parameters. The characteristics of the EPR signals obtained can be explained by three distinct EPR active centres (two nitrogen associate and the Ti^{3+}), as shown in Figure 6.17 (a). The characteristics of the EPR signals can be assigned to the molecular NO signal (Sys1) and the $[N_iO]^{\bullet}$ (Sys2), as shown in Figure 6.18 both of which have been described earlier, and the **g** and **A** tensors are shown in Table 6.9. Table 6.9 describes of the Sys1, Sys2 and Sys5 and the species associated with those denotations.

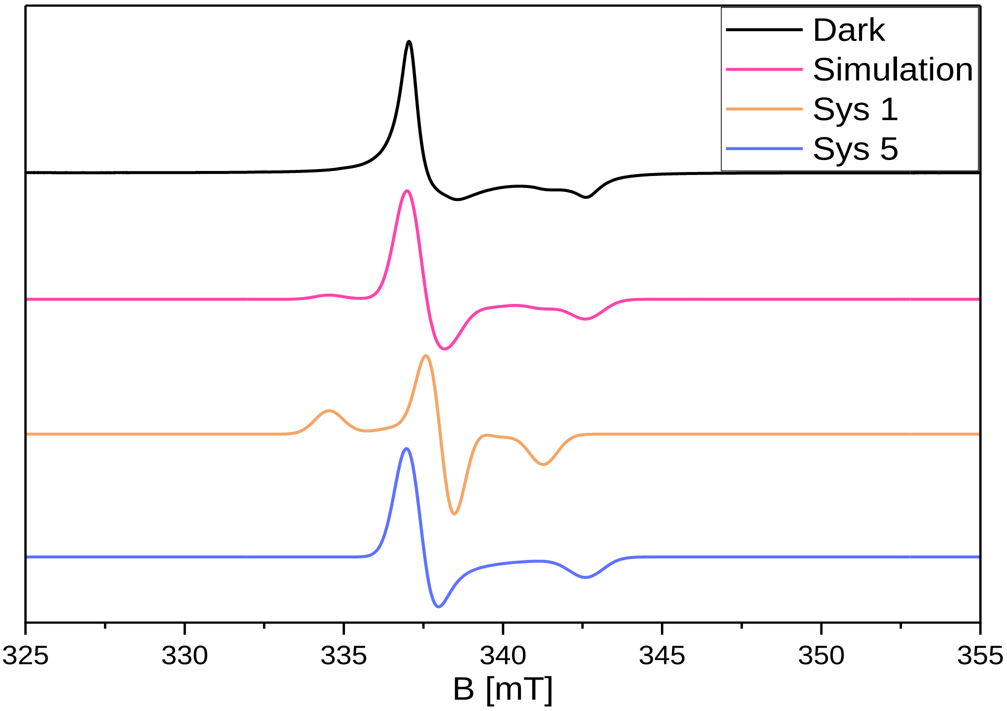

Figure 6.18: Experimental (black) and simulated (sim) dark spectra for F-A-TaN(U)-TiO$_2$ sample, including NO (Sys1) and Ti^{3+} (Sys5) (The scale for the individual species is set at 100% weight here, see Table 6.10 for specific contributions).

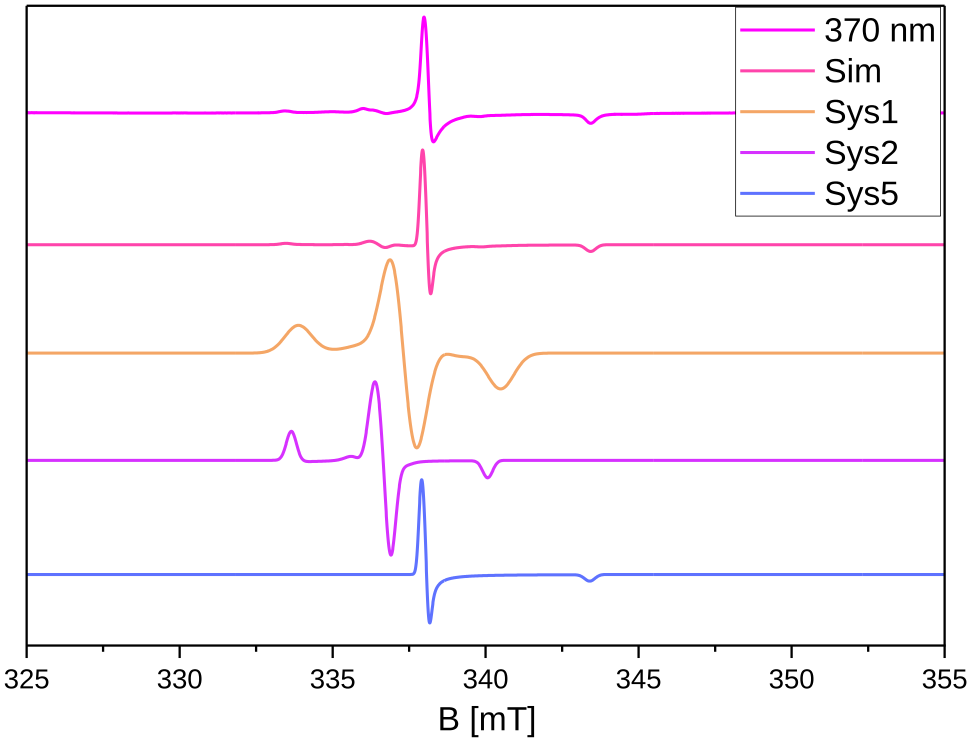

Figure 6.19: Experimental (black) and simulated (sim) 365 nm irradiated spectra for F-A-TaN(U)-TiO$_2$ sample, including NO (Sys1), N$_i$O^{2-} (Sys2) and Ti^{3+} (Sys5) (The scale for the individual species is set at 100% weight here, see Table 6.10 for specific contributions).

Table 6.9: **g** and **A** tensors for EPR centres Sys1, Sys2 and Ti^{3+} for the F-A-TaN(U)-TiO_2.

Species	g_{xx}	g_{yy}	g_{zz}	A_1 **[MHz]**	A_2 **[MHz]**	A_3 **[MHz]**
NO (Sys1)	2.0012 ± 0.0026	1.9979 ± 0.0026	1.927 ± 0.0038	2.8	92.7 ± 2.1	26.9
N_iO^{2-} (Sys2)	2.0037 ± 0.002	2.0044 ± 0.002	2.0029 ± 0.002	6.5	15.7	89.6 ± 1.9
Ti^{3+} (Sys5)	1.999 ± 0.002	1.999 ± 0.002	1.950 ± 0.0045			

There are no observable differences between the dark spectrum, the 625 nm (red light) and 530 nm (green light) spectra. With the decreased of the wavelength, starting to approach the UV region, the appearance of changes in the spectra become more distinct. At 455 nm (blue light) and 365 nm (UV light) the presence of the interstitial N chemically coupled to a lattice O ion forming the pre-described paramagnetic centre labelled Sys2, demonstrates a slight increase. As mentioned, in addition to displaying an anisotropic **g** tensor with rhombic symmetry, $[N_iO]^{\bullet}$ is essentially an intra band gap NO^{2-} state. The fraction of the nitrogen centres that are diamagnetic before light irradiation contribute a significant detectable quantity of paramagnetic NO^{2-} states upon irradiation with lower wavelengths, as the two paired electrons undergo the earlier described electron transition. The contributions of the different species for wavelengths are presented in Table 6.10, resulting in the overall EPR profile of the sample.

Table 6.10: Percentage weight distribution of each specie for each irradiation wavelength for the F-A-TaN(U)-TiO_2.

Wavelength	**Paramagnetic species percentage weight contribution**		
	NO	**N_iO^{2-}**	**Ti^{3+}**
Dark	10.0	5.9	84.1
625 nm	10.4	5.4	84.2
530 nm	10.9	5.3	83.8
455 nm	10.1	6.7	83.2
365 nm	9.0	9.0	82.0

Figure 6.20 shows the spectra of the F-R-TaN-TiO_2 under different irradiation conditions, namely, in the absence of light and during exposure to the following wavelengths of 625 nm (b), 530 nm (c), 455 nm (d) and 365 nm (e).

When exposed to visible light, the EPR signal does not undergo any changes in comparison to the signal from the sample that was not exposed to light.

The simulation for the dark spectrum is seen in Figures 6.21 and allows for the extraction of the distinctive EPR parameters.

The characteristics of the EPR signals obtained can be explained by two distinct EPR active centres (one nitrogen associate and the Ti^{3+}), as shown in Figure 6.20 (a). The nitrogen associated specie is the molecular NO, that has been described and denotated a Sys1, with g_{xx} = 2.001 g_{yy} = 1.9975 and g_{zz} = 1.921 and A_1 = 2.8, A_2 = 91.7 and A_3 = 26.8 MHz. In addition to the nitrogen related signal the broadened axial signal for the Ti^{3+} centre is observed, with g_{xx} = g_{yy} = 1.997 and g_{zz} = 1.948. As mentioned, in addition to the nitrogen related signal the broadened axial signal for the Ti^{3+} centre is observed. The weight contributions of the two species remain relatively similar across all the wavelengths, with the NO weight percentage at 83.3% and the Ti^{3+} weight percentage at 16.7%.

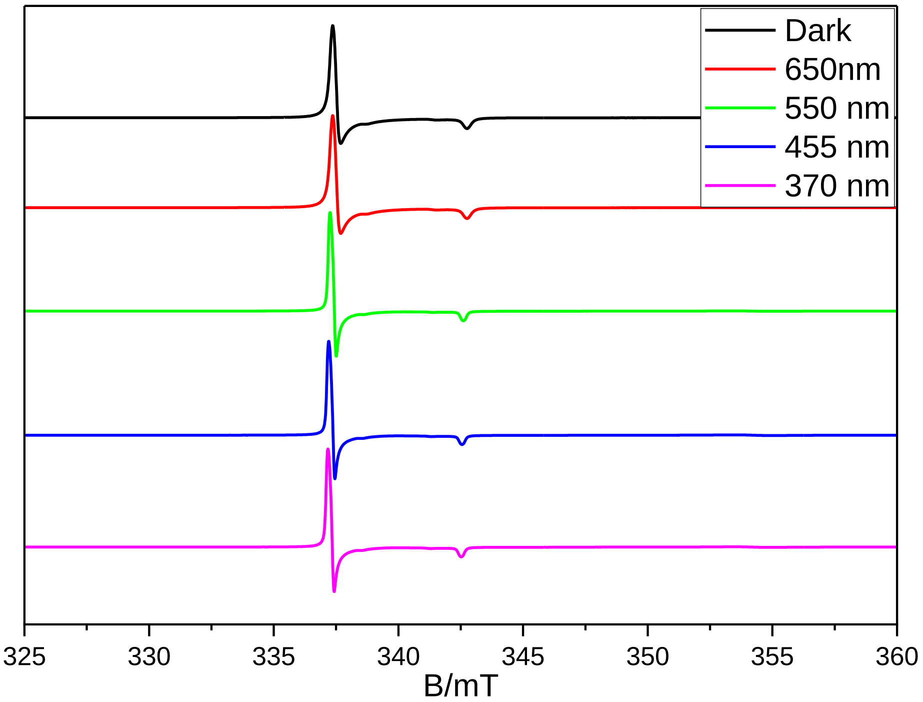

Figure 6.20: EPR spectra in the dark (a) and under in situ irradiation with 625 nm wavelength visible light (b), 530 nm wavelength visible light (c), 455 nm wavelength visible light (d) and 365 nm wavelength visible light (e) for the F-R-TaN(U)-TiO_2 sample.

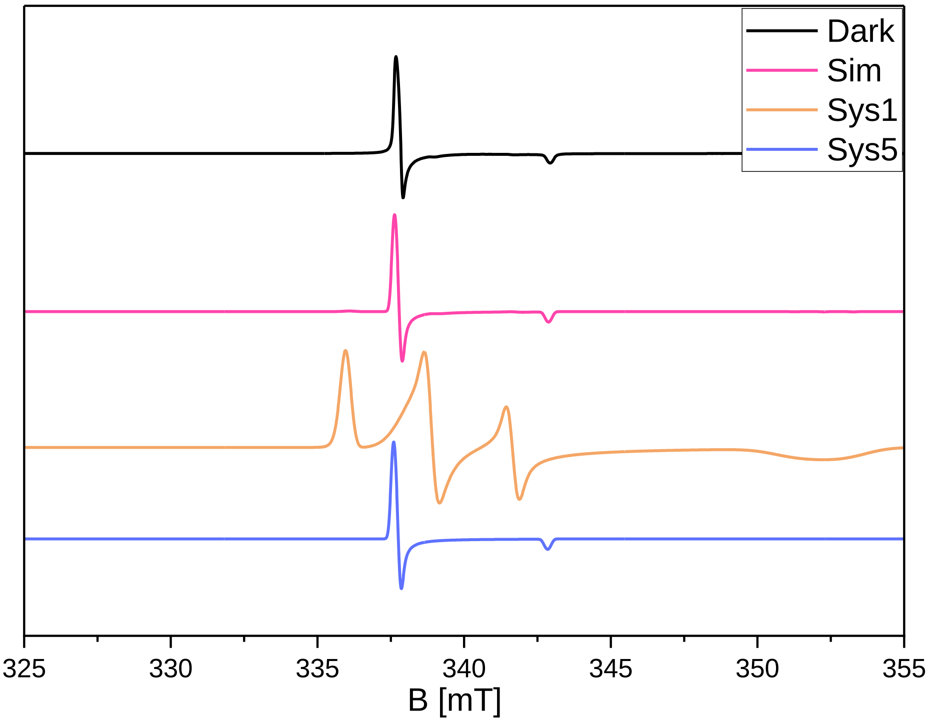

Figure 6.21: Experimental (black) and simulated (sim) dark spectra for rutile TaN(U)-TiO_2 sample, including NO (Sys1) and Ti^{3+} (Sys5) (The scale for the individual species is set at 100% weight here, specific contributions are stated in text).

One of the most distinct differences between the samples that used tungsten as a metal dopant compared to tantalum is the formation of the paramagnetic W-NO^{2-} specie. Additionally, the tungsten doped samples demonstrated the ability to form superoxide under visible light irradiation. An interesting point was presented based on the nitrogen source, as the samples that originated from the ammonia synthesis presented a nitrogen centre for the N_2^- specie. However, this species was only present for the anatase samples, which would indicate that the calcination temperature also, plays a role in its formation, as it affects the environment of the sample. All of the samples present a strong NO characteristic signal along with the constant presence of the Ti^{3+} signal. The difference between the EPR profiles gives an important insight into each sample's photocatalytic capabilities, as based on the species formed under irradiation, different environmental catalytic cycles can be specific targeted.

6.3 Microwave calcined co-doped samples, WN- and TaN- TiO_2

The microwave samples demonstrated significant differences compared to the furnace samples. The majority of the samples presented no differences between the dark and the irradiated spectra. The corresponding microwave calcined samples to all of the furnace samples once were investigated using EPR. For the MW-A-WN-TiO_2 and MW-A-TaN- TiO_2 co-doped samples obtained the EPR spectra revealed the presence of three (two nitrogen associate and the Ti^{3+}) characteristics signals. The MW-R-WN(U)-TiO_2 the EPR spectra revealed the presence of six (three nitrogen associate, Ti^{3+}, O_2^{-} and the trapped hole) characteristic signals.

Figure 6.22 displays the spectra of the MW-A-WN- co-doped sample, under different conditions, namely, in the absence of light and during exposure to the following wavelengths of 625 nm (b), 530 nm (c), 455 nm (d) and 365 nm (e).

When exposed to light, the EPR signal becomes stronger and undergoes changes in comparison to the signal from the sample that was not exposed to light. The simulations for the dark and irradiated spectra are presented in Figures 6.23 and 6.24, respectively, and allow for the extraction of the distinctive EPR parameters.

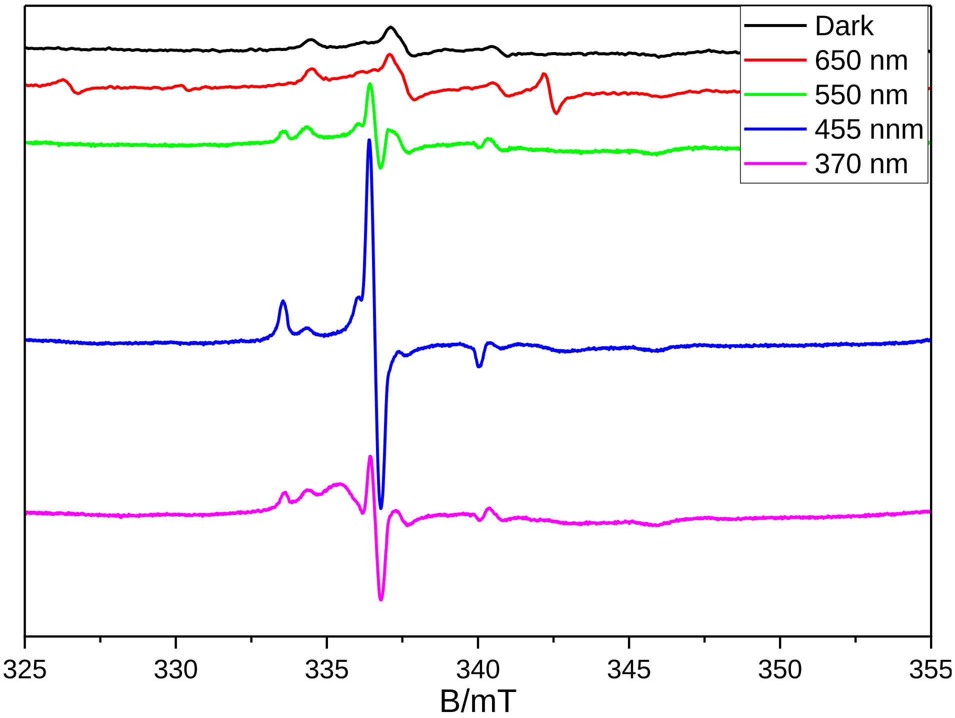

Figure 6.22: EPR spectra in the dark (a) and under in situ irradiation with 625 nm wavelength visible light (b), 530 nm wavelength visible light (c), 455 nm wavelength visible light (d) and 365 nm wavelength visible light (e) for the MW-A-WN-TiO_2 sample.

Table 6.11 reports the **g** and **A** tensors of the Sys1, Sys2, Sys5 and Sys8 and the species associated with those denotations. The paramagnetic centre labelled Sys1 presence can be attributed to the adsorption of molecule NO,(1) which was described earlier in the chapter. The interstitial N chemically coupled to a lattice O ion forms the paramagnetic centre labelled Sys2, which is described earlier in the chapter. The axial signal for the Ti^{3+} centre is, also, observed. The values that are displayed agree well with those that have been published elsewhere.(2,11) Having identified the nature of the EPR active species, we can now explain the change from the dark to the UV irradiated spectra in Figure 6.22 (e). As with the furnace co-doped samples, a significant portion of the nitrogen centres is diamagnetic before irradiation, containing two paired electrons in the highest occupied molecular orbital and appearing as $[N_iO]^{-}$,intra-band gap NO^{3-} states. (1,4) The dark spectrum (Figure 6.22 (a)) is dominated by the signal of adsorbed molecular NO (1,2 -10) (Sys1). Upon irradiation with visible light, electron transitions $NO^{3-} \rightarrow$ CB occur, leaving behind a much larger quantity of paramagnetic NO^{2-} states that can be easily detected by EPR. In addition to the increase of the $[N_iO]^{\bullet}$, the superoxide centre is seen once molecular oxygen was added to a clean surface, then irradiated for 30 minutes and then the excess atmosphere was evacuated. Thus, resulting in a signal displaying an orthorhombic EPR profile.

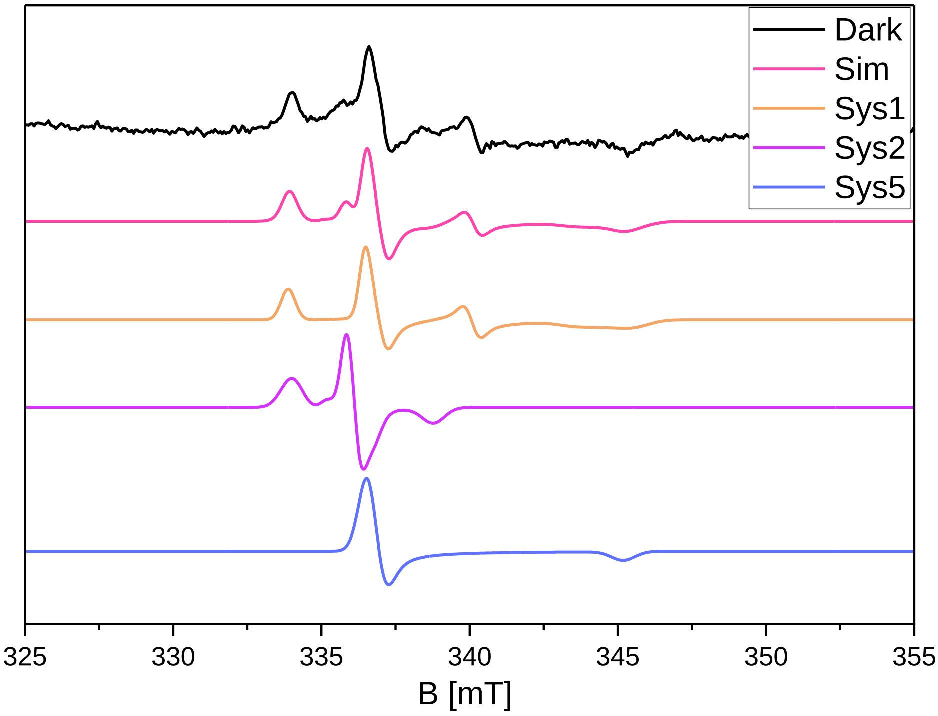

Figure 6.23: Experimental (black) and simulated (sim) dark spectra for MW-A-WN-TiO$_2$ sample, including NO (Sys1), N$_i$O^{2-} (Sys2) and Ti^{3+} (Sys5) (The scale for the individual species is set at 100% weight here, see Table 6.12 for specific contributions).

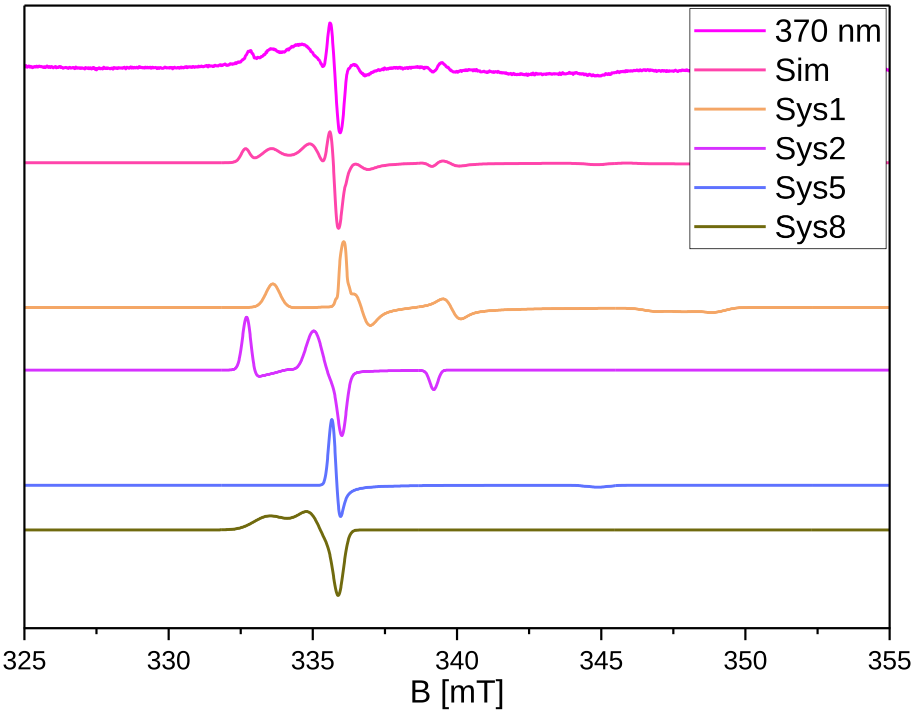

Figure 6.24: Experimental (black) and simulated (sim) 365 nm irradiated spectra for MW-A-WN-TiO$_2$ sample, including NO (Sys1), N$_i$O^{2-} (Sys2), Ti^{3+} (Sys5) and O$_2^-$ (Sys8), (The scale for the individual species is set at 100% weight here, see Table 6.12 for specific contributions).

Table 6.11: **g** and **A** tensors for EPR centres Sys1, Sys2, Ti^{3+} and O_2^{-} for the MW-A-WN-TiO_2.

Species	g_{xx}	g_{yy}	g_{zz}	A_1 [MHz]	A_2 [MHz]	A_3 [MHz]
NO (Sys1)	2.0013 ± 0.0024	1.9978 ± 0.0022	1.928 ± 0.0034	2.8	92.5± 1.9	26.9
N_iO^{2-} (Sys2)	2.0053 ± 0.002	2.0042 ± 0.0018	2.0033 ± 0.0025	6.5	15.7	89.7± 1.8
O_2^{-} (Sys8)	2.024 ± 0.018	2.008 ± 0.0025	2.002 ± 0.0034			
Ti^{3+} (Sys5)	1.999 ± 0.002	1.999 ± 0.002	1.950 ± 0.0048			

The weights of the different species contributions are presented in Table 6.12 for the different wavelengths, therefore, assembling the overall EPR profile of the sample at the different wavelengths.

Table 6.12: Percentage weight distribution of each specie for each irradiation wavelength for the MW-A-WN-TiO_2.

Wavelength	**Paramagnetic species percentage weight contribution**			
	NO	**N_iO^{2-}**	**Ti^{3+}**	**O_2^{-}**
Dark	73.2	8.9	17.9	0
625 nm	75.8	7.5	16.7	0
530 nm	74.9	7.7	17.4	0
455 nm	53.5	26.9	19.6	0
365 nm	46.6	13.4	16.6	23.4

Figure 6.25 displays the spectra of the TaN- co-doped sample, under different photoirradiation conditions, specifically, in the absence of light and under the following wavelengths of 625 nm (b), 530 nm (c), 455 nm (d) and 365 nm (e). When exposed to light, the EPR signal becomes stronger and undergoes changes in comparison to the signal from the sample that was not exposed to light.

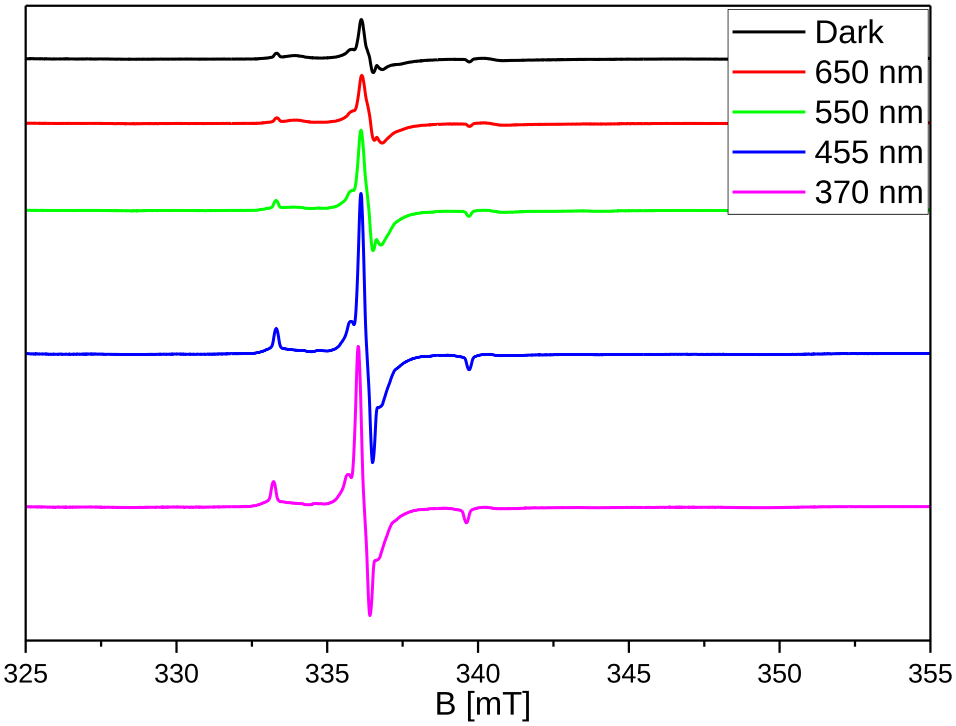

Figure 6.25: EPR spectra in the dark (a) and under in situ irradiation with 625 nm wavelength visible light (b), 530 nm wavelength visible light (c), 455 nm wavelength visible light (d) and 365 nm wavelength visible light (e) for the MW-A-TaN-TiO_2 sample.

The paramagnetic centre labelled Sys1 presence can be attributed to the adsorption of molecule NO,(1) which was described earlier in the chapter. Similarly to the rest of the co-doped samples, the NO is encapsulated in bulk and subsurface micro voids created during the synthetic process rather than adsorbed on the sample's exposed surface which is apparent from the profile of the signal after treatment of the sample at 393 K for at least 12 hours, (ca. 10^{-4} mbar). (10)

Table 6.13 reports the **g** and **A** tensors of the Sys1, Sys2 and Sys5 and the species associated with those denotations. Furthermore, interstitial N chemically coupled to a lattice O ion forms the paramagnetic centre labelled Sys2, which is described earlier in the chapter.

In addition to the nitrogen related signals the axial signal for the Ti^{3+} centre is a contributing signal. Having identified the nature of the EPR active species, we can now explain the change from the dark to the light-irradiated spectra in Figure 6.25 (e). The dark spectrum (Figure 6.25 (a)) is therefore dominated by the signal of adsorbed molecular NO (1) (Sys1). There are no observable differences between the dark spectrum and the 625 nm (red light) and 530 nm (green light) spectra. However, as the wavelength is decreased and start to approach the UV region, the appearance of changes in the spectra become more distinct. The most obvious change is the formation of a much larger quantity of paramagnetic NO^{2-} states that can be easily detected by EPR and are sources as the two paired electrons from diamagnetic nitrogen centres undergo already explained electron transitions.

The weights of the different species contributions are presented in Table 6.14 for the different wavelengths, therefore, assembling the overall EPR profile of the sample at the different wavelengths, Figures 6.26 and 6.27.

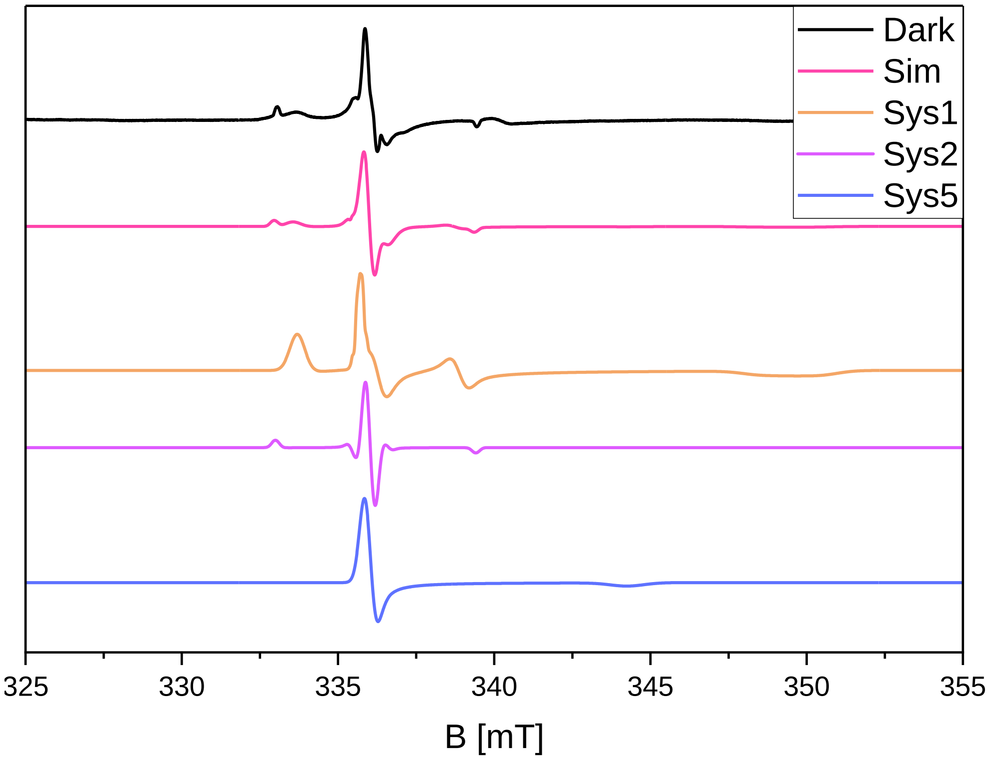

Figure 6.26: Experimental (black) and simulated (sim) dark spectra for MW-A-TaN-TiO_2 sample, including NO (Sys1), N_iO^{2-} (Sys2) and Ti^{3+} (Sys5) (The scale for the individual species is set at 100% weight here, see Table 6.14 for specific contributions).

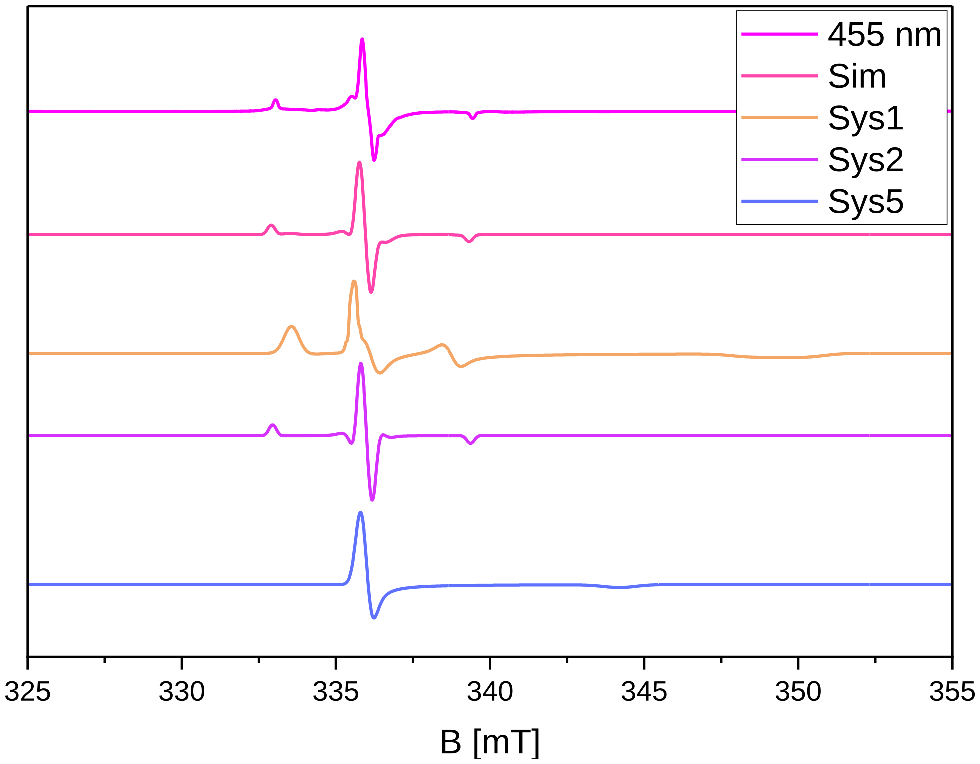

Figure 6.27: Experimental (black) and simulated (sim) 365 nm irradiated spectra for MW-A-TaN-TiO_2 sample, including NO (Sys1), N_iO^{2-} (Sys2) and Ti^{3+} (Sys5) (The scale for the individual species is set at 100% weight here, see Table 6.14 for specific contributions).

Table 6.13: **g** and **A** tensors for EPR centres Sys1, Sys2 and Ti^{3+} for the MW-A-TaN-TiO_2.

Species	g_{xx}	g_{yy}	g_{zz}	A_1 **[MHz]**	A_2 **[MHz]**	A_3 **[MHz]**
NO (Sys1)	2.0011 ± 0.0019	1.9982 ± 0.0023	1.9239 ± 0.0041	2.8	92.5± 2.1	26.9
N_iO^{2-} (Sys2)	2.0048 ± 0.0019	2.0038 ± 0.0024	2.0031 ± 0.0027	6.5	15.7	89.7± 1.7
Ti^{3+} (Sys5)	1.999 ± 0.002	1.999 ± 0.002	1.950 ± 0.0081			

Table 6.14: Percentage weight distribution of each specie for each irradiation wavelength for the MW-A-TaN-TiO_2.

Wavelength	**Paramagnetic species percentage weight contribution**		
	NO	**N_iO^{2-}**	**Ti^{3+}**
Dark	66.6	16.7	16.7
625 nm	64.2	20	15.8
530 nm	65.1	50.6	14.3
455 nm	33.4	55.6	11
365 nm	31.3	56.5	12.2

Figure 6.28 displays the spectra of the MW-R-WN(U)- co-doped sample, under different conditions, namely, in the absence of light and during exposure to the following wavelengths of 625 nm (b), 530 nm (c), 455 nm (d) and 365 nm (e). When exposed to light, the EPR signal becomes stronger and undergoes changes in comparison to the signal from the sample that was not exposed to light.

The simulations for the dark and irradiated spectra are presented in Figures 6.29 and 6.30, respectively, and allow for the extraction of the distinctive EPR parameters.

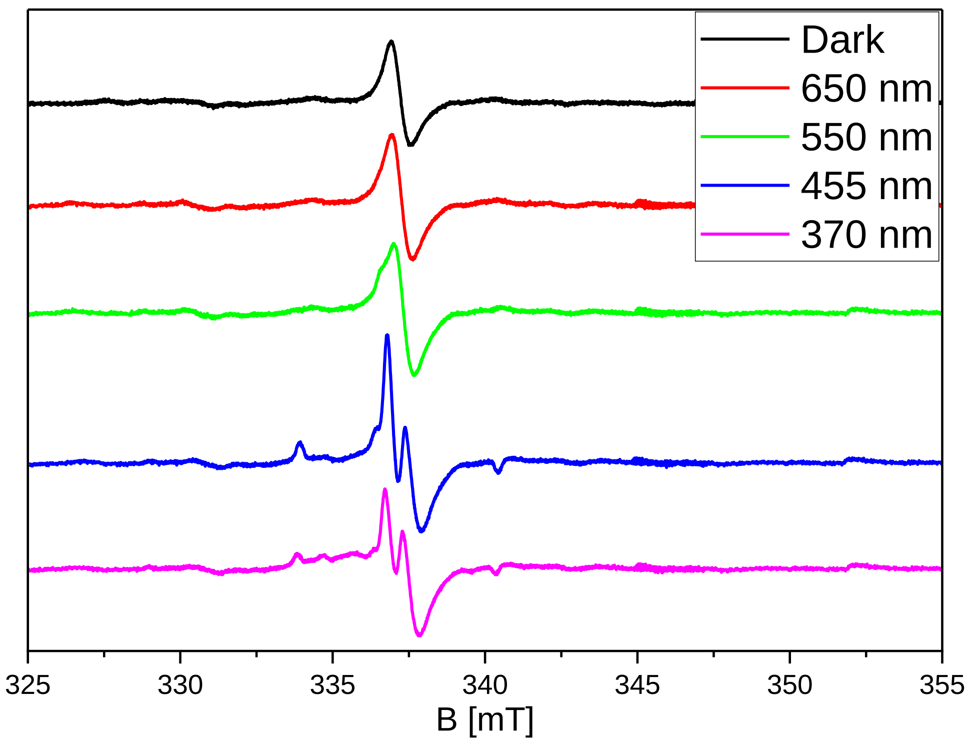

Figure 6.28: EPR spectra in the dark (a) and under in situ irradiation with 625 nm wavelength visible light (b), 530 nm wavelength visible light (c), 455 nm wavelength visible light (d) and 365 nm wavelength visible light (e) for the MW-R-WN(U)-TiO_2 sample.

The paramagnetic centre labelled Sys1 presence can be attributed to the adsorption of molecule NO,(1, 10) which is similar to the system that was described earlier in the chapter. Furthermore, interstitial N chemically coupled to a lattice O ion forms the paramagnetic centre labelled Sys2, which is described earlier in the chapter. There is a third paramagnetic centre labelled Sys3, that describes the interaction of paramagnetic NO^{2-} with W produces $[N_iO]W^{\bullet}$. As described earlier in the chapter the total signal of the Sys3 centre consists of two components: a W-close range NO^{2-} signal with super hyperfine splitting that accounts for 14.31% of ^{183}W that couples to the unpaired electron, and a close-range W-NO^{2-} signal without super hyperfine couplings. (9) In addition to the nitrogen related signals the axial signal for the Ti^{3+} centre is a contributing signal. Table 6.15 reports the **g** and **A** tensors of the Sys1, Sys2, Sys3, Sys5, Sys6 and Sys8 and the species associated with those denotations.

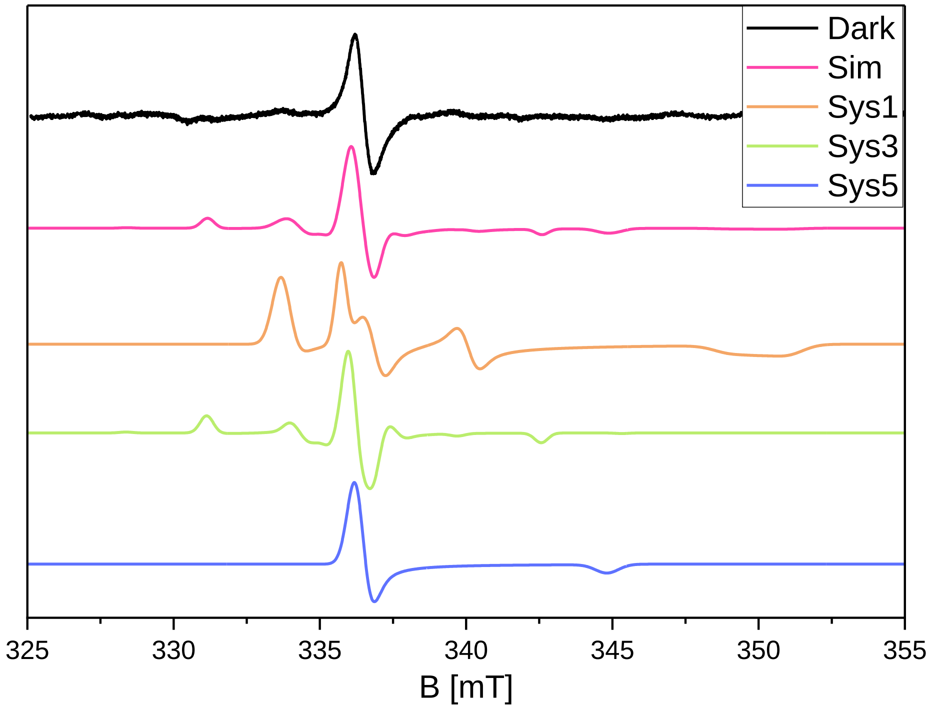

Figure 6.29: Experimental (black) and simulated (sim) dark spectra for MW-R-WN(U)-TiO_2 sample, including NO (Sys1), W-NO^{2-} (Sys3) and Ti^{3+} (Sys5) (The scale for the individual species is set at 100% weight here, see Table 6.16 for specific contributions).

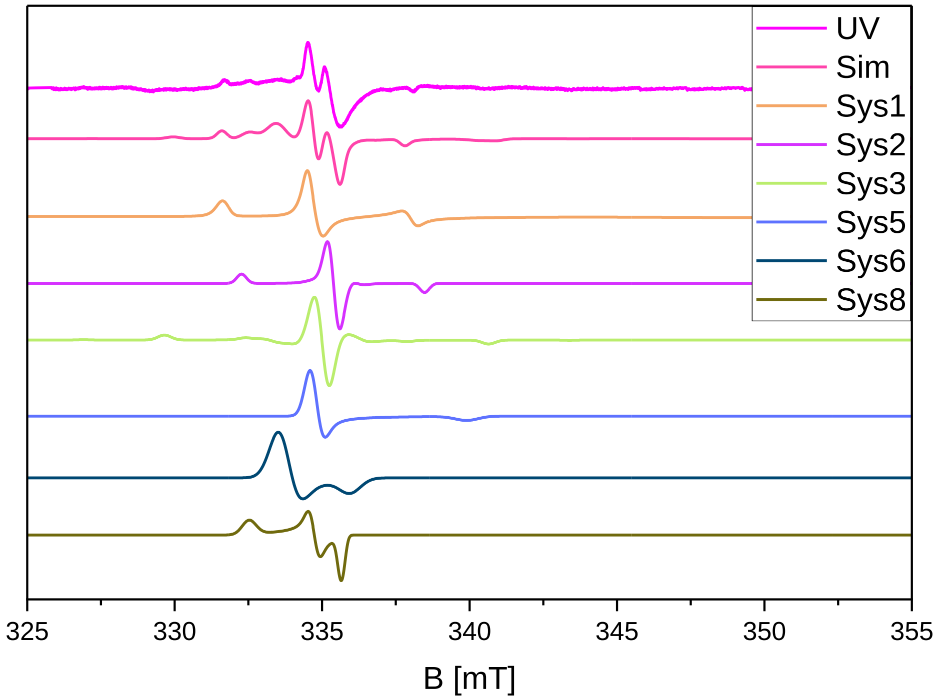

Figure 6.30: Experimental (black) and simulated (sim) 365 nm irradiated spectra for MW-R-WN(U)-TiO_2 sample, including NO (Sys1), N_iO^{2-} (Sys2) W-NO^{2-} (Sys3), Ti^{3+} (Sys5), trapped hole (Sys6) and O_2^- (Sys8) (The scale for the individual species is set at 100% weight here, see Table 6.16 for specific contributions).

Having identified the nature of the EPR active species, we can now explain the change from the dark to the light-irradiated spectra in Figure 6.28. The dark spectrum (Figure 6.28 (a)) is dominated by the signal of adsorbed molecular NO (Sys1), when considering the nitrogen centres. There are no observable differences between the dark spectrum and the 625 nm (red light) spectrum. With the decrease of the wavelength, the appearance of changes in the spectra become more distinct. Upon irradiation with 455 nm and 365 nm, electron transitions NO^{3-}→ CB occur, leaving behind a much larger quantity of paramagnetic NO^{2-} states that can be easily detected by EPR (Table 6.16). Overall, the signal of the adsorbed molecular NO undergoes a significant change, but the considerable formation of paramagnetic $[N_iO]^{2-}$ and $[N_iO]W^{2-}$ centres are responsible for the new profile of the EPR spectrum (Figure 6.28 (e)) together with the increased intensity.

In addition to the increase of the $[N_iO]^{2-}$, the presence of the superoxide centre is seen after irradiation of the sample in oxygen atmosphere followed by evacuation prior to measuring, thus, causing photogeneration. (11)

The weights of the different species contributions are presented in Table 6.16 for the different wavelengths, therefore, assembling the overall EPR profile of the sample at the different wavelengths.

Table 6.15: **g** and **A** tensors for EPR nitrogen Sys1, Sys2, Sys3, Ti^{3+}, O_2^{-} and trapped hole for the MW-R-WN(U)-TiO$_2$.

Species	g_{xx}	g_{yy}	g_{zz}	A_1 [MHz]	A_2 [MHz]	A_3 [MHz]
NO (Sys1)	2.002 ± 0.002	1.999 ± 0.003	1.923 ± 0.005	2.8	90.5 ± 1.5	26.9
N_iO^{2-} (Sys2)	2.0053 ± 0.0025	2.0041 ± 0.0021	2.0034 ± 0.0026	6.5	15.7	86.7 ± 1.5
W-NO^{2-} (Sys3)	2.002 ± 0.002	2.001 ± 0.0018	1.998 ± 0.0023	45.1 ± 1.5 44.8 ± 1.3	22.4 ± 1.5 2.8	145.5 ± 3.5 151.1 ± 3.5
Ti^{3+} (Sys5)	1.998 ± 0.001	1.998 ± 0.001	1.951 ± 0.005			
O_2^{-} (Sys8)	2.022 ± 0.015	2.007 ± 0.002	2.003 ± 0.004			
Trapped hole (Sys6)	2.015 ± 0.011	2.005 ± 0.005	2.005 ± 0.004			

Table 6.16: Percentage weight distribution of each species for each irradiation wavelength for the MW-R-WN(U)-TiO_2.

Wavelength	Paramagnetic species percentage weight contribution					
	NO	N_iO^{2-}	W-NO^{2-}	Ti^{3+}	O_2^-	Trapped hole
Dark	33.4	0	11.7	54.9	0	0
625 nm	35.7	0	9.6	54.7	0	0
530 nm	31.3	3.9	8.9	55.9	0	0
455 nm	21.9	14.4	8.3	55.4	0	0
365 nm	15.2	22.2	6.4	40.1	10.1	6

For the MW-A-WN(U)-TiO_2 and MW-A-TaN(U)-TiO_2 co-doped samples no changes were observed between the dark and the irradiated spectra. Only the presence of a very broad signal, attributed to the Ti^{3+} is seen in Figures 6.31 and 6.32, explained in the discussion of this Chapter.

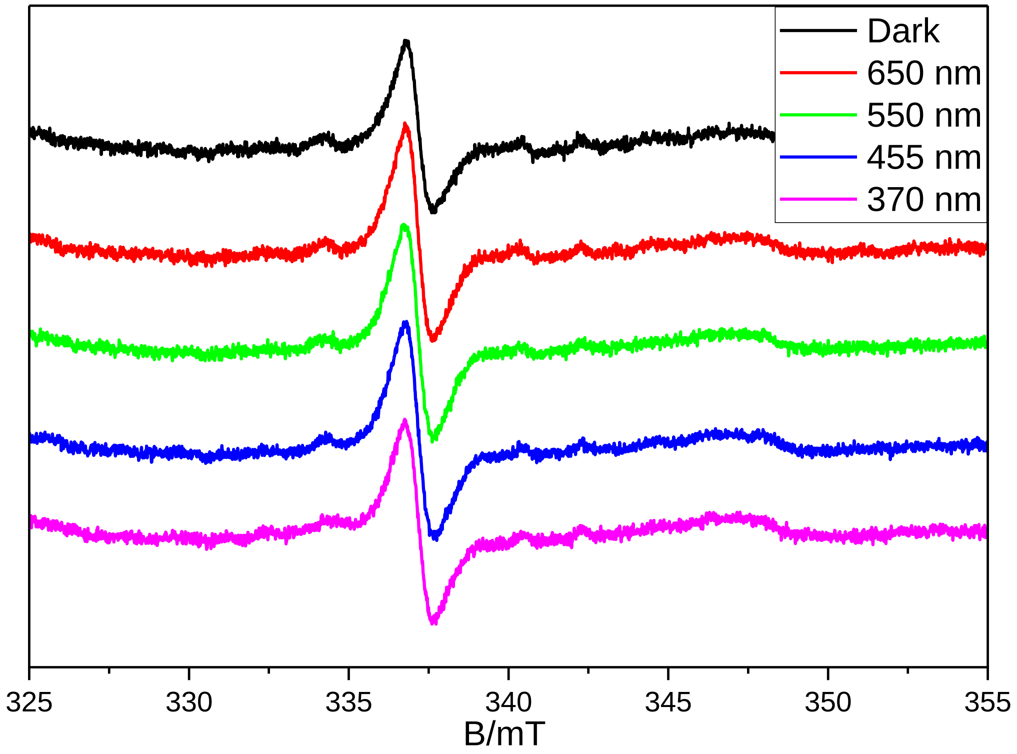

Figure 6.31: EPR spectra in the dark (a) and under in situ irradiation with 625 nm wavelength visible light (b), 530 nm wavelength visible light (c), 455 nm wavelength visible light (d) and 365 nm wavelength visible light (e) for the MW-A-WN(U)-TiO_2 sample.

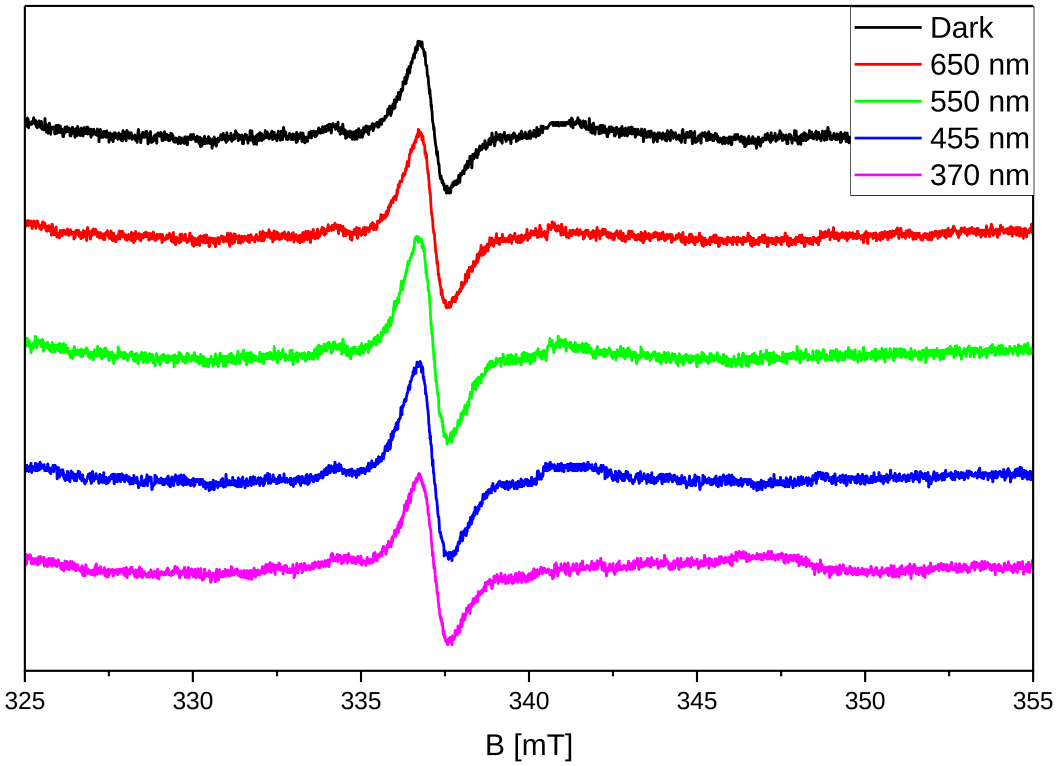

Figure 6.32: EPR spectra in the dark (a) and under in situ irradiation with 625 nm wavelength visible light (b), 530 nm wavelength visible light (c), 455 nm wavelength visible light (d) and 365 nm wavelength visible light (e) for the MW-A-TaN(U)-TiO_2 sample.

A similar trend was observed for all three rutile co-doped samples and are presented in Figures 6.33, 6.34 and 6.35, with the signal being attributed to a very broad Ti^{3+}.

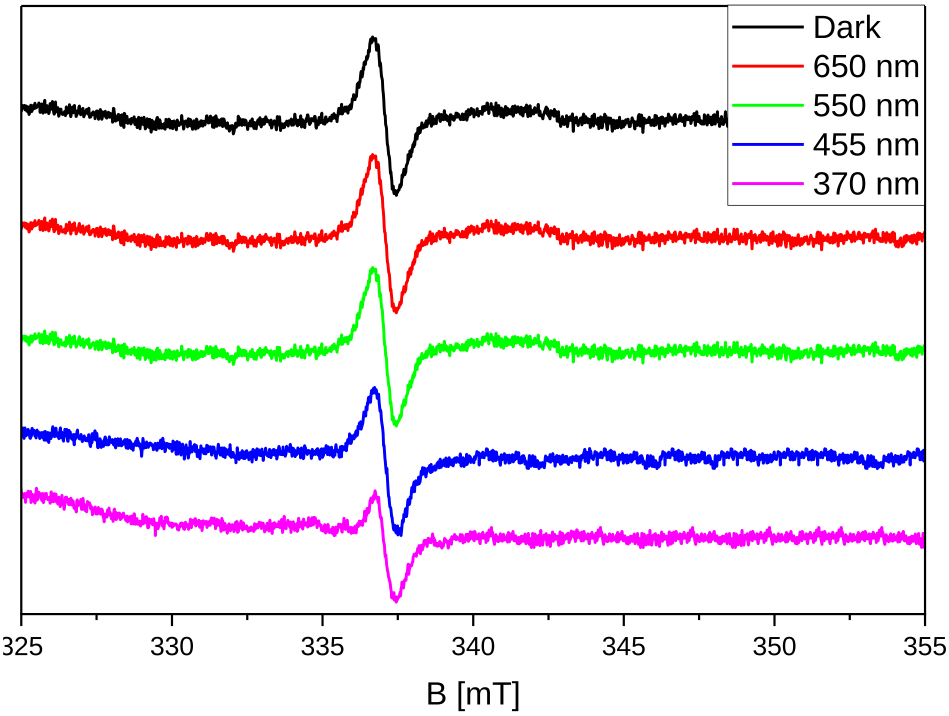

Figure 6.33: EPR spectra in the dark (a) and under in situ irradiation with 625 nm wavelength visible light (b), 530 nm wavelength visible light (c), 455 nm wavelength visible light (d) and 365 nm wavelength visible light (e) for the MW-R-WN-TiO_2 sample.

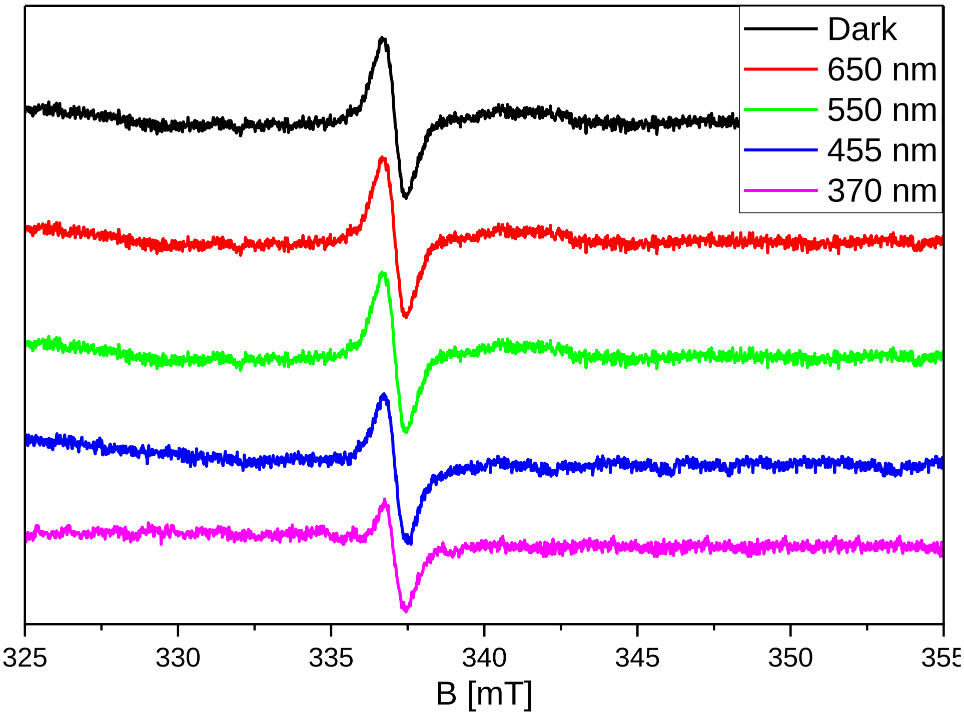

Figure 6.34: EPR spectra in the dark (a) and under in situ irradiation with 625 nm wavelength visible light (b), 530 nm wavelength visible light (c), 455 nm wavelength visible light (d) and 365 nm wavelength visible light (e) for the MW-R-TaN-TiO_2 sample.

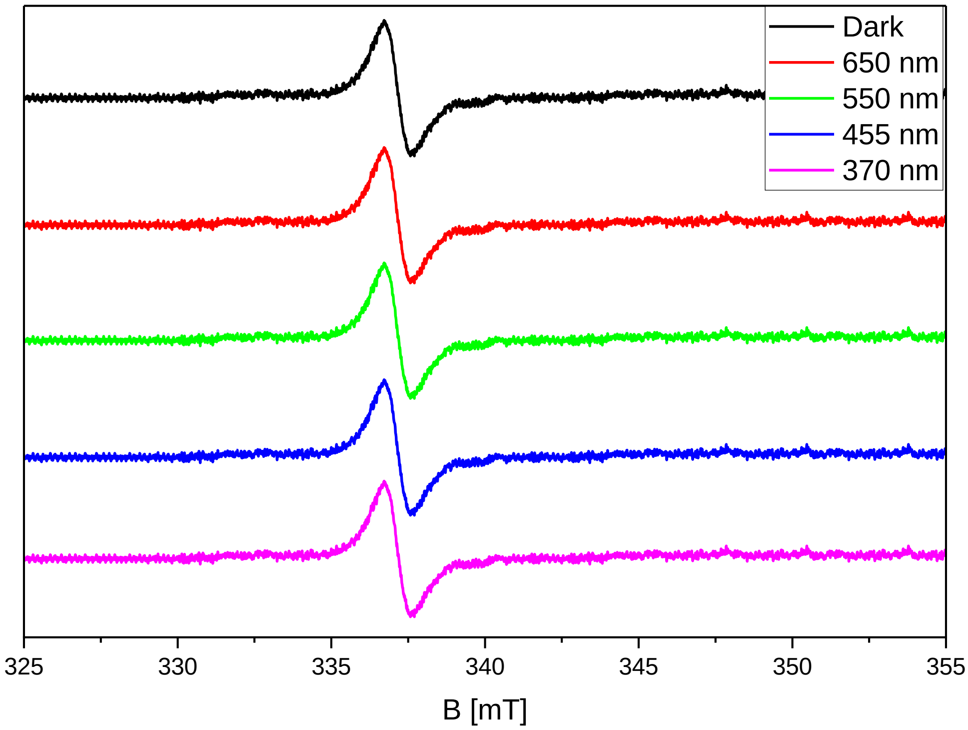

Figure 6.35: EPR spectra in the dark (a) and under in situ irradiation with 625 nm wavelength visible light (b), 530 nm wavelength visible light (c), 455 nm wavelength visible light (d) and 365 nm wavelength visible light (e) for the MW-R-TaN-TiO_2 sample.

It was observed that only three samples presented an EPR profile of interest. The microwave pathway has affected the type and weight contribution of the paramagnetic centres formed. The majority of the microwave calcined samples demonstrated no change in their profile as the wavelength was decreased, which aligns with the furnace samples, apart from the MW-A-WN-TIO_2, MW-A-TaN-TiO_2 and MW-R-WN(U)-TiO_2 co-doped materials. However, one of the more noticeable differences between the two calcination paths is the fact that anatase samples using urea as a source demonstrated a change in their spectra when calcination occurred via a furnace as the EPR profile presents a change during irradiation. Whereas there was no change in the spectra when the microwave calcination process was followed. Additionally, for the MW-A-WN-TiO_2 and MW-R-WN(U)-TiO_2 co-doped samples, the formation of superoxide was only observed under UV light (365 nm) irradiation compared to samples calcined through furnace where, the superoxide presence was observed even from green light.

6.4 Discussion

Substitutional doping of non-metals (such as nitrogen) and metals (such as tungsten and tantalum) into TiO_2 can drastically alter its electronic, optical, and photocatalytic properties. These dopants introduce new defect states, alter the band gap, and in some cases, create paramagnetic centres that can be studied using EPR spectroscopy. By analysing the EPR spectra, the nature of the dopant species, their electronic environment, and the impact of doping on the material's properties can determined.

For all the co-doped samples the nitrogen doping modifies the band gap of TiO_2 and improve its optical absorption in the visible range, increasing the p-type character. Nitrogen typically substitutes for oxygen atoms in the TiO_2 lattice, and the substitutional N species can give rise to paramagnetic centres that are detectable by EPR and have been present in the synthesised co-doped samples. When nitrogen replaces oxygen in the lattice (substitutional doping), N atoms introduce localised states near the valence band of TiO_2. The EPR signal is associated with the interaction of the unpaired electron on the nitrogen site interacting with the surrounding TiO_2 lattice. The *g*-value is close to that of free electrons, as nitrogen introduces shallow defect levels near the valence band. In addition to substitutional nitrogen, N can also be present in interstitial sites. These interstitial sites may also generate paramagnetic centres depending on the surrounding lattice structure. The signal intensity for interstitial nitrogen is typically weaker than substitutional nitrogen and can vary resulting in changes in the spectral width due to differences in the local symmetry and bonding. Both of these signals have a more dominant presence in the majority of the anatase samples, Chapter 5 provides further proof through the decrease in the band gap along with the change in the lattice structure parameters.

Tungsten doping was chosen as the metal dopant, in order to modify the electronic and catalytic properties of TiO_2, particularly for enhancing photocatalytic activity under visible light. Tungsten can be incorporated into TiO_2 in several oxidation states, with W^{6+} and W^{5+} being the most common. W^{6+} is non-paramagnetic (d^0), whereas W^{5+} is paramagnetic and detectable by EPR. W^{5+} often forms when TiO_2 is annealed under reducing conditions (e.g., vacuum), where W^{6+} can capture an electron, resulting in a W^{5+} ion. Measuring the EPR at temperatures around 50 K the signal for W^{5+} is typically observed at $g \approx 1.90–1.94$. This g-value reflects the d^1

configuration of the W^{5+} ion in a distorted octahedral coordination environment. The distortion can cause slight shifts in the g-value depending on the local geometry and interactions with neighbouring ions or defects. Despite the fact that no tungsten signal was observed during these experiments the co-doped materials demonstrated an interesting difference between the two metal dopants. Materials that tungsten was added a signal was observed that was assigned to an interaction between nitrogen and tungsten.

Tantalum is another transition metal dopant used to modify the electronic properties of TiO_2, particularly in enhancing catalytic activity. Tantalum typically substitutes for Ti^{4+} in the TiO_2 lattice, and Ta can exist in different oxidation states. The most common state in TiO_2 is Ta^{5+}, but Ta^{4+} can also exist under reducing conditions. Ta^{5+} ($5d^0$ configuration) is the most common oxidation state when tantalum substitutes for titanium. Since Ta^{5+} does not have unpaired electrons, it is not paramagnetic and, thus, does not produce an EPR signal. Similarly to tungsten, in reducing conditions, Ta^{5+} can be reduced to Ta^{4+} ($5d^1$ configuration) and shows similar behaviour to other d^1 ions like W^{5+}. And it is estimated that the Ta^{4+} signal would be appearing at $g \approx 1.90–1.94$ when measured at 50 K. The signal reflects the d^1 electron localised in a distorted octahedral environment in the TiO_2 lattice. In some cases, hyperfine interactions can be observed in the EPR spectrum due to the coupling of the unpaired electron with the tantalum nucleus ($I = 7/2$), providing further insights into the local environment of the Ta^{4+} ion. These interactions were not observed in these spectra, but further investigation at lower temperatures could resolve and provide a deeper understanding the hyperfine interactions. Compared to the tungsten counterparts none of the tantalum co-doped materials presented signals associated with the metal's interaction with nitrogen.

The results indicate that the species generated are influenced by more than just the TiO_2 polymorph. The data exhibit consistent reduction patterns across all TiO_2-based materials, with nearly all samples producing the Ti^{3+} or free electron signals. These signals arise from oxygen abstraction from the lattice during annealing, suggesting that both conduction band electrons and trapped electrons are stable at room temperature, as evidenced by their prolonged presence. The two species are unrelated between them, as the relative intensities of the signals vary inconsistently between samples.

It is well established that higher reduction temperatures under vacuum lead to an increased generation of Ti^{3+} ions. Additionally, higher temperatures are necessary for the emergence of the isotropic signal associated with free electrons. Conduction band free electrons do not interact with surface adsorbates, with Ti^{3+} species being the only ones involved in such interactions. For these novel synthesised materials, the inclusion of the dopants indicates that the temperature required to generate free electrons decreases compared to undoped TiO_2. This implies that reduction profiles are influenced not only by the material's phase but also by additional factors such as a shift in the particle size caused by the introduction of dopants (Chapter 5). When comparing the materials that were calcined through the microwave there is an evident difference between the pairs of samples. The calcination method is, therefore, indicative of the paramagnetic species formed during the experimental procedures.

Not all materials produce surface-stabilized superoxide, as shown in the results. Anatase samples, such as F-A-WN-TiO_2 and MW-A-WN-TiO_2, consistently produced superoxide, accompanied by reduction profiles dominated by Ti^{3+} signals. These anatase materials also exhibited multiple surface stabilization sites for superoxide (sites I, II, and III), distributed in typical patterns. In contrast, rutile samples containing tantalum dopants did not produce surface-stabilized superoxide. For the co-doped samples tungsten, various nitrogen species were detected within the material, and substitutional nitrogen requires a high concentration of Ti^{3+} ions to facilitate the necessary charge transfer for superoxide formation.

As indicated by the formation of Ti^{3+} another important factor to consider is the predominant crystallographic surface facet of the material. Each TiO_2 polymorph exhibits preferred facets: anatase favours the [101] surface, while rutile prefers the [110] facet. The MW-A-WN(U)-TiO_2, MW-A-TaN(U)-TiO_2, MW-R-WN-TiO_2, MW-R-TaN-TiO_2 and MW-R-TaN(U)-TiO_2 samples produced Ti^{3+} but did not generate any nitrogen centres, or superoxide, suggesting that while defective sites were abundant, they were not all accessible for superoxide formation. The favoured surface facets of different polymorphs promote distinct surface reactions. For anatase, the most stable surface is the [101] facet, though oxygen adsorption is preferred on the [110] surface, with oxidation occurring on the [001] surface. In contrast, for rutile, the most stable facet is the [110], but oxygen adsorbs preferentially on the [101], with oxidation occurring on the [111] facet. These variations in surface chemistry likely contribute to differences in superoxide formation between materials of the same phase. (1)

Superoxide formation is facilitated by a one-electron transfer from the surface. However, the second electron transfer, necessary for further oxygen reduction, encounters an energy barrier. Thus, the absence of an energy barrier for the first electron transfer in anatase supports the material's ability to form superoxide, which was demonstrated by the F-A-WN-TiO_2 and MW-A-WN-TiO_2 samples and their direct comparison with their counter rutile samples. The material's ability to adsorb oxygen prior to electron transfer is a critical factor in superoxide formation. However, the absence of superoxide in the majority rutile samples suggests that oxygen may saturate the surface, potentially reducing the energy barrier for the second electron transfer. This could promote dissociation of diatomic oxygen, leading to re-oxidation of the oxygen vacancies created during reduction. Literature demonstrated that there are up to four observable stabilisation sites in P25. (11)

This works demonstrates that since the incorporation of dopants and the calcination pathways affect the structure of the material and thus the availability of stabilisation sites for superoxide. For the detection of the superoxide with EPR, the g_{zz} for superoxide can vary based on the synthesis. (11) For the F-A-WN-TiO_2, MW-A-WN-TiO_2 and MW-R-WN(U)-TiO_2 samples the g_{zz} average at 2.023 demonstrates that there is only one site for O_2^{-} stabilisation which can be explained and attributed as a result to the different synthetic pathways. These synthetic routes demonstrated an influence in several factors, including the chemical environment around the active centres and the degree of doping or defects introduced during synthesis. Consequently, deviations in the synthesis can result in measurable differences in the EPR signals, highlighting the sensitivity of the method to subtle structural and electronic variations in the materials. These materials demonstrated slight structural changes in the samples, reported in Chapter 5 (through XRD and XPS) as a result of variations in temperature (in this study 500 ^{o}C for anatase and 900 ^{o}C for rutile), calcination technique (furnace or microwave oven), precursor materials (ammonia and urea), and dopant (metals and non-metals) incorporation during the synthesis. Which, in turn, affect the electronic distribution and local symmetry of the superoxide species.

The three most promising photocatalysts in this chapter were demonstrated to be F-A-WN-TiO_2, MW-A-WN-TiO_2 and MW-R-WN(U)-TiO_2, based on the presence of superoxide formed under irradiation. Chapter 5 demonstrated that F-A-WN-TiO_2 as the most promising photocatalyst, as it was calculated to have the most improved optimised band gap. The EPR solid state aligned with the improvement in the catalyst by demonstrating the formation of superoxide signal from 530 nm irradiation. However, in Chapter 7 it was demonstrated that the samples with most improved performance are F-A-WN(U)-TiO_2 and MW-R-WN(U)-TiO_2. Thus, indicating that the recombination rate is too fast in the F-A-WN-TiO_2 and MW-A-WN-TiO_2 and catalytic processes are hindered. An interesting behaviour was demonstrated by the MW-R-WN(U)-TiO_2 with E_{gap} = 2.90 eV (Chapter 5) as superoxide was detected under UV irradiation along with the increase of N_iO^{2-} signal.

There was no superoxide formation observed in the rest materials, yet Chapter 7 demonstrated that the F-A-WN(U)-TiO_2 and F-A-TaN(U)-TiO_2 materials still hold promising catalytic capabilities, with the EPR in this chapter providing an insight to the reason behind it. The N_iO^{2-} signal could be the result of two pathways. The encapsulated molecular NO that is adsorbed onto a subsurface oxygen vacancy, and this vacancy serves as an electron trapping site for conduction-band electrons generated by light irradiation. The reduction of NO may take place, where $NO + V_o + 2e^- \rightarrow N_iO^{2-}$, thus explaining the decrease in the NO signal during the simultaneous increase of the N_iO^{2-} signal. A different origin for the N_iO^{2-} could be attributed to electron transition CB $\leftarrow$ NO^{3-} during irradiation, causing the appearance of the signal. Thus, the F-A-WN(U)-TiO_2 and F-A-TaN(U)-TiO_2 samples demonstrating a correlation between the NO and N_iO^{2-}, with the NO decreasing as the N_iO^{2-} were also the samples that presented good catalytic capabilities.

The broadening of the Ti^{3+} signal in doped TiO_2 can be attributed to several factors. Doping TiO_2 introduces additional defects and disrupts the regular crystal lattice, as seen in Chapter 5, creating oxygen vacancies or interstitial dopants that generate localised electronic states, leading to inhomogeneous broadening of the Ti^{3+} signal. Additionally, dipole-dipole interactions between Ti^{3+} centres in the lattice contribute to signal broadening by causing variations in the local magnetic field experienced by the Ti^{3+} ions. In materials with a high concentration of Ti^{3+} ions or other paramagnetic centres, exchange interactions between these centres can further broaden the signal, as closer distances between Ti^{3+} centres lead to collective behaviour. An uneven distribution of Ti^{3+} centres due to doping could also lead to localised regions of high defect density, where variations in local strain, coordination, or oxygen vacancy concentration further contribute to broadening. Finally, magnetic interactions between Ti^{3+} centres and other paramagnetic defects, such as oxygen vacancies or dopant ions, can introduce additional magnetic field fluctuations, further widening the signal. Thus, the broad Ti^{3+} signal arises from a combination of lattice disorder, magnetic interactions, and electron-lattice coupling, all of which create variations in the local environments and energy levels of the Ti^{3+} ions.

In summary, superoxide formation, Ti^{3+} production, and electron dynamics in TiO_2 are influenced by a complex interplay of factors, including polymorph phase, particle size, surface facets, and oxygen adsorption behaviour. Understanding these variables is crucial for tailoring TiO_2 materials for specific catalytic or photocatalytic applications.

6.5 Conclusions

Within this chapter two metal dopants have been successfully incorporated into the TiO_2 matrix, via sol – gel synthesis, using two different sources for the non – metal dopant. Upon introduction of all the dopants N based species were presented and detected via EPR. EPR identified, via the variation in **g** and **A** tensors the influence each dopant had on each other and the overall profile of each material. This was due to its ability to recognise and characterise the close-range interactions between the nitrogen and the metal, predominantly tungsten, atoms. The calcination effect of a microwave oven was also studied, as in general, a calcination pathway that uses a microwave oven is faster than a conventional oven, than more cost effective and environmentally friendly. EPR demonstrated the key differences between the two calcinations and identified the key aspects of each contribution to the overall profile. Future experiments should aim to target the repetition of these dataset at lower temperatures, e.g. 50 K. Thus, allowing for a better understanding and resolution of the hyperfine splitting and an improvement of on the signal-to-noise ratio.

6.6 References

(1) C. Di Valentin, E. Finazzi, G. Pacchioni, A. Selloni, S. Livraghi, M. C. Paganini, E. Giamello, *Chem. Phys*. 2007, **339**, 1−3, 44−56.

(2) S. Livraghi, M. R. Chierotti, E. Giamello, G. Magnacca, M. C. Paganini, G. Cappelletti, C. L. Bianchi, *J. Phys. Chem. C* 2008, **112**, 44, 17244−17252

(3) C. D. Di Valentin, G. Pacchioni, M. Chiesa, E. Giamello, U. Heiz, S. Abbet, *J. Phys. Chem. B* 2002, **106**, 1637−1645

(4) S. Livraghi, M. C. Paganini, E. Giamello, A. Selloni, C. DiValentin, G. Pacchioni, *J. Am. Chem. Soc.* 2006, **128**, 49, 15666−15671.

(5) G. Barolo, S. Livraghi, M. Chiesa, M. C. Paganini, E. Giamello, *J. Phys. Chem. C*2012, **116**, 39, 20887−20894

(6) X. Chen, C. Burda, *J.Am. Chem. Soc*. 2008, **130**, 15, 5018−5019

(7) F. Napoli, M. Chiesa, S. Livraghi, E. Giamello, S. Agnoli, G. Granozzi, G. Pacchioni, C. Di Valentin, *Chem.Phys. Lett.* 2009, **477**, 1−3, 135−138.

(8) A. Folli, *et al., The Journal of Physical Chemistry C*, 2013, **117**, 42, pp. 22149–22155.

(9) A. Folli, J.Z. Bloh, D.E. Macphee, *Journal of Electroanalytical Chemistry*, 2016, **780**, pp. 367–372.

(10) A. Folli, J.Z. Bloh, K. Armstrong, E. Richards, D.M. Murphy, L. Lu, C.J. Kiely, D.J. Morgan, R.I. Smith, A.C. Mclaughlin, D.E.Macphee, *ACS Catalysis*, 2018, **8**, 8, 6927–6938.

(11) E. Carter, A.F. Carley, D.M. Murphy*, The Journal of Physical Chemistry C* 2007, **111**, 28, 10630-10638

Chapter 7: Targeting the decomposition of VOCs and the transformation of glycerol

7.1 An introduction to the targeted photocatalytic processes

7.1.1 Decomposition of toluene.

Volatile organic compounds (VOCs) are a group of organic compounds that easily change from a liquid to a vapour at typical ambient air temperatures (1) e.g. for toluene at 25ºC the vapour pressure is 26.9 Torr (2) and for DMSO is 0.6 Torr. (3) VOCs are found in air streams as a result of biogenic activities (animal and plant decomposition) and human processes (solvent, paint, and glue manufacture). (4–7) Due to their toxicity, many VOCs have a severe influence on human health and the environment, these effects include ground level pollution, ozone depletion, and global warming. Since high concentrations of VOCs are frequently found in both urban and industrial locations, it is crucial and pertinent to conduct research to find a solution for VOC pollution. The goal of many chemical industries has been to minimise the quantity of VOCs discharged into the atmosphere. Since physical application of conventional air filtration technologies for VOCs removal in chemical facilities is frequently costly and impractical, alternative approaches have been investigated. (8-11) One method for degrading VOCs that has shown promise is heterogeneous photocatalytic oxidation (PCO) (Chapter 2). It has been demonstrated that VOCs can be transformed into CO_x by utilising PCO; this typically entails a charge transfer to or from the photocatalyst. (12)

Formaldehyde and toluene are the most important and representative hazardous chemicals among these VOCs, and they have been extensively studied as single model reactants to assess the effectiveness of photocatalysts. (13-16) According to mechanistic research, formaldehyde photo-dissociation either directly oxidises to CO_2 or takes an indirect pathway that involves formic acid as an intermediary. (13,17) The predominant oxidative species in both situations has been found to be the noticeable abundance of hydroxyl radicals ($^{\bullet}OH$). (18,19) Benzaldehyde is seen as an intermediary in the photodecomposition of toluene, occurring before the aromatic ring is broken by $O_2^{\bullet—}$ (superoxide radicals). (20,21)

Molecular oxygen facilitates an efficient separation of charge carriers, which is another important aspect of the photoinduced processes on irradiated TiO_2 surfaces. Reactions between the adsorbed oxygen molecules and the momentarily trapped electrons on the surface or in adjacent surface defects are, therefore, possible. Thus, generating $O_2^{\bullet-}$, with the properties of the solvent have an impact on the subsequent reactions of the $O_2^{\bullet-}$ that is created. While the superoxide radical anion is rather stable in aprotic solvents, it reacts favourably with protons in aqueous solutions to create hydrogen peroxide, which is then used in additional photocatalytic processes (Equations 7.1 – 7.6). (22) Examining reactive radicals generated in the irradiated TiO_2 dispersions in DMSO via EPR spin trapping was the subject of investigations by Dvoranová et al. (22), who generated the chemical strategy (Equations 7.7 – 7.13) for the formation and subsequent use of superoxide radicals.

$$O_2^{\bullet-} + H^+ \rightarrow {}^{\bullet}OOH \qquad (7.1)$$

$$2{}^{\bullet}OOH \rightarrow H_2O_2 + O_2 \qquad (7.2)$$

$$H_2O_2 + O_2^{\bullet-} \rightarrow {}^{\bullet}OH + O_2 + OH^- \qquad (7.3)$$

$$H_2O_2 \overset{hv}{\rightarrow} 2\,{}^{\bullet}OH \qquad (7.4)$$

$$H_2O_2 + e^- \rightarrow {}^{\bullet}OH + OH^- \qquad (7.5)$$

$$H_2O_2 + h^+ + OH^- \rightarrow H_2O + {}^{\bullet}OOH \qquad (7.6)$$

$$(CH_3)_2SO + {}^{\bullet}OH \rightarrow CH_3(OH)SO + {}^{\bullet}CH_3 \qquad (7.7)$$

$${}^{\bullet}CH_3 + DMPO \rightarrow {}^{\bullet}DMPO\text{-}CH_3 \qquad (7.8)$$

$${}^{\bullet}CH_3 + O_2 \rightarrow CH_3OO^{\bullet} \qquad (7.9)$$

$$DMPO + CH_3OO^{\bullet} \rightarrow {}^{\bullet}DMPO\text{–}OOCH_3 \qquad (7.10)$$

$$2\,{}^{\bullet}DMPO\text{–}OOCH_3 \rightarrow O_2 + 2\,{}^{\bullet}DMPO\text{–}OCH_3 \qquad (7.11)$$

$$2\,CH_3OO^{\bullet} \rightarrow 2\,CH_3O^{\bullet} + O_2 \qquad (7.12)$$

$$DMPO + CH_3O^{\bullet} \rightarrow {}^{\bullet}DMPO\text{–}OCH_3 \qquad (7.13)$$

Toluene is one of the most common VOCs in air pollution, and therefore a section of work is focused on the photocatalytic decomposition of toluene using the newly prepared and characterized TiO_2 catalysts. (23-38) Experimental infrared spectroscopy (24, 25, 32) (IR) data showed that toluene bounds strongly to TiO_2 due to electron donation from the methyl group, which increases the electron density on the aromatic ring resulting in an increased strength of interaction between the adsorbate (π electrons) and the catalyst surface. To achieve full decomposition, four attacking pathways are plausible (Figure 7.1):

i) Photogenerated hole trapped by the hydroxyl group producing the $^{\bullet}$OH radical, which then attacks the aromatic ring.

ii) Photogenerated hole trapped by the hydroxyl group producing the $^{\bullet}$OH radical which attacks the methyl group.

iii) Direct attack of the aromatic group via the photogenerated hole.

iv) Direct attack of the methyl group hydrogen via the photogenerated hole.

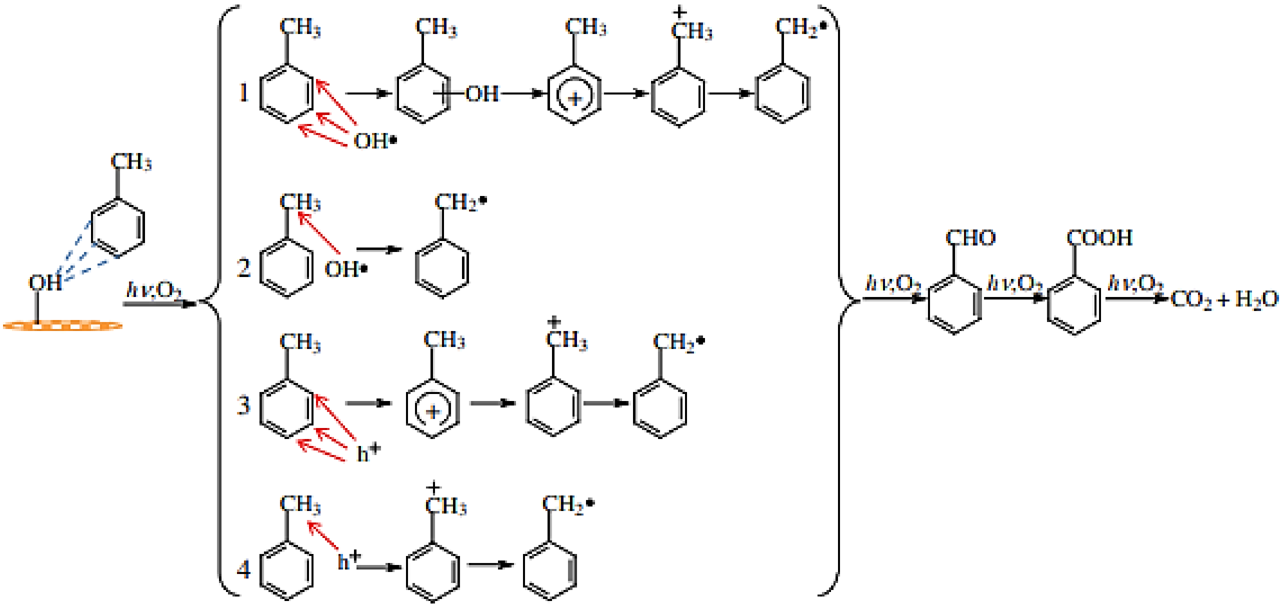

Figure 7.1: Photocatalytic degradation of toluene on TiO_2 reaction pathway.(24)

It is due to the reasons that have been described that the interest around the VOC degradation have been kept at a high demand and that is where these catalysts prove to be beneficial. Up to this point literature has studied plated TiO_2 materials for VOC degradation, leaving a gap in research surrounding doped materials. In the collaborative work presented in the Ren et. al. similar reactions took place to explain the Pd cocatalyst's role in influencing the degradation pathways of a formaldehyde-toluene mixture through EPR analysis. Thus, revealing differences in surface characteristics between pristine TiO_2 and Pd/TiO_2 under dark conditions. The EPR spectra showed that pristine TiO_2 is dominated by $^{\bullet}OH$ radicals, originating from its hydroxylated surface, while Pd/TiO_2 exhibits weaker $^{\bullet}OH$ signals, indicating the removal of surface —OH groups after Pd modification. This suggests that the —OH groups on pristine TiO_2 contribute to the formation of methyl-phenolics during toluene photodegradation. (39) Further collaborations took place with Prof. Su Ren’s group where EPR experiments, and their simulations were performed in Cardiff. (40-42) These studies utilised bare or plated TiO_2 as it has been proven to be one of the better catalysts under UV irradiation. These results can further demonstrate the interest to study similar reactions with the use of the co-doped TiO_2 materials as catalysts. The work presented in this thesis will aim to give a novel insight to the reactions described in i) - iv) and bring an insight into the reaction’s mechanism through the radical formation for these co-doped materials. Additionally, this work will aim to present links between mechanisms and synthetic procedures.

7.1.2 Glycerol transformation

Another reaction of interest that these photocatalyst could be used for is the photoinduced transformation of glycerol. Section 7.4 hence investigates the photo reforming of glycerol to produce H_2 and CO_2 using the most promising co-doped photocatalysts synthesised during this work and characterised in Chapters 5 and 6. Glycerol (hereafter abbreviated as GLY) is a material with physical and chemical properties that are used in many different commercial applications, such as uses in the food, pharmaceutical, and cosmetics industries, where it is used as a thickener, sweetener, humectant, and anti-freezer. (43, 44) The production of biodiesel has increased exponentially in recent years, resulting in a considerable amount of glycerol as a byproduct that accounts for around 10% of the overall output. This has caused a drastic change in the worldwide glycerol market. (44) As a result, an extensive effort has been made to find alternate applications or transformations of glycerol into useful chemicals or hydrogen using various processes, including photocatalysis. (45-50) A thorough study was performed to differentiate between the radical $^{\bullet}OH$ mediated process and direct electron transfer intermediates generated during glycerol photooxidation in P25 suspensions. (51)

The hydroxyl radicals react non-selectively with high reaction rates with most organic compounds. (52) Carbon-bond hydrogen atoms are abstracted from two distinct locations in the glycerol molecule as a result of the interaction of hydroxyl radicals with the molecule. It is worth noting that in the presence of molecular oxygen in the system the hydroxyalkyl radicals produce hydroperoxyl radicals. It is possible to interpret the creation of products from glycerol by taking into account various reaction pathways because of the intricate parallel reactions between hydroxyalkyl and hydroperoxyl radicals in the aerated aqueous solutions. (53-56) Since free glycerol reacts most likely simultaneously with hydroxyl radicals in the solution and chemi- and physiosorbed glycerol reacts promptly with photogenerated holes, (57,58) the photocatalytic reactions of glycerol in the TiO_2 suspensions are even more complex. The behaviour of the photogenerated light-absorbing holes in the aqueous TiO_2 suspensions is dramatically altered once the addition of glycerol takes place, as it is added as a selective hole scavenger. The titanium atom at the nanoparticle surface is chelated by the chemisorbed glycerol molecules, which quickly scavenge the holes. This ultrafast reaction, occurring in less than 100 femtoseconds (57), can compete with charge recombination and hole trapping caused by other surface defects, (57, 59) natural occurring or doping induced. The remaining holes subsequently react with the physiosorbed glycerol at a slower pace, within the first 200 ns, via charge transfer or H-abstraction. The remaining holes are unable to react with chemi- or physiosorbed glycerol because they are confined by lattice defects in the subsurface or bulk. (57)

When considering the diffusion of mobile radical $^{\bullet}OH$ into the bulk of the solution, as was directly confirmed for the irradiated anatase using single-molecule detection system, (60) the DMPO spin-adducts of hydroxyalkyl radicals radical $^{\bullet}R_1$ ($^{\bullet}CHOH-CHOH-CH_2OH$) and radical $^{\bullet}R_2$ ($CH_2OH-^{\bullet}COH-CH_2OH$) are well compatible with the processes attributed to the interaction of physiosorbed glycerol molecules with the trapped holes resulting in the formation of unbound radicals (57, 58) or to the reaction of free hydroxyl radicals with glycerol in solution in the close vicinity of TiO_2 surface.

7.1.3 Spin trap agents characteristics

As explained in Chapter 2, TiO_2 based semiconductors have characteristic band gaps, which through doping was demonstrated to have been decreased (Chapter 5) . Many radicals have short lifetimes, which makes it very challenging to isolate and characterise them. Spin-trapping, a process that involves reacting a transitory radical with a trap to create a persistent, stable radical, is a way to get around this. A long-lived spin trapped adduct is created when a short-lived radical molecule attacks the double bond present in the spin trap, to make another radical molecule. The R group, Figure 7.2, in spin trap agents plays a crucial role in determining the reactivity, stability, and specificity of the spin adducts formed. The arising hyperfine couplings attributed to the adduct provide structural details about the trapped radical. Introducing bulky R groups can shield the radical centre from secondary reactions, thus increasing the half-life of the spin adduct, providing a better insight to the radicals produced.

There are two different spin trap categories, known as nitrone and nitroso, Figure 7.2 demonstrates the two nitrones used through this work. Linear nitrones, such as PBN are preferred when detecting C-based radicals, while cyclic nitrones, such as DMPO, are better suited for the detection of O-based radicals.

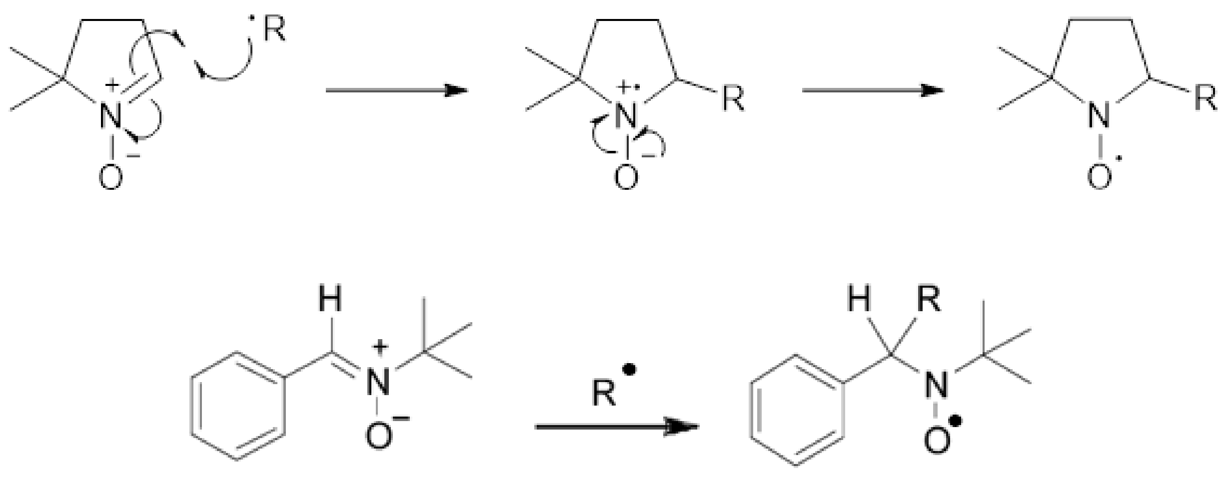

Figure 7.2: Nitrone spin trap agents, DMPO (top) and PBN (bottom).

DMPO is the most commonly used spin trap in the literature, as it holds many advantages over other nitrone and nitroso spin traps. Firstly, nitrone spin traps are reactive towards a broader radical scope than nitroso traps. DMPO has a much broader redox potential window than other nitrones, meaning it is the least redox active. (61) This is important when the trap is employed in reactions involving a redox process, as the likelihood of degradation of the trap and adduct is significantly reduced. The lower redox activity leads to clearer and more reliable signals for the identification and quantification of radicals, which in the case of the co-doped catalysts is important as the different oxygen-based type radicals can be involved in or initiate different catalytic pathways.

During the experiments presented in this chapter the presence of degraded DMPO is attributed to superoxide radicals, as the DMPO was tested prior to use and there was a lack of degraded signals. Due to the short lifetime of hydroperoxyl adducts DMPO-OOH, they can decompose to produce DMPOX adduct signals, thus the signal arising from degraded DMPO during experiments can be traced back superoxide formation. (62)

7.2 Spin trap of VOC suspensions

Suspension systems using mixtures of liquid toluene, DMSO and dissolved paraformaldehyde were studied herein using EPR spin trapping. In order to have high confidence during the radical assignment stage the spin trap experiments were performed using two different spin trap agents, PBN and DMPO. The benefits of using PBN is that it produces longer lived spin adducts that could give an insight on the quantity of the generated radicals. For example, at room temperature the half-life of the $^{\bullet}$OOH radical is 10^{-6} seconds, whereas the DMPO-OOH has a half-life of 1 minute. (63) However, differentiating between different oxygen-based radicals can be challenging with PBN due to similar hyperfine splitting constants (a_N and a_H), as Table 7.1 demonstrates.

Table 7.1: Hyperfine values of oxygen based adducts with PBN and DMPO agent.

Radical Adduct	**a_N / G**	**a_H / G**	**Reference**
PBN-OH	15.7	2.7	(64)
PBN-OOH	15.6	2.4	(65)
PBN-OOR	15.5	3.2	(66)
DMPO-OH	14.9	14.9	(67)
DMPO-OOH	13.2	11.2	(68)
DMPO-OOR	14.0	9.7	(69)

These hyperfine values highlight the difficulty in distinguishing between different oxygen-based radicals using PBN, as the nitrogen hyperfine splitting constants (a_N) are near identical. The slight variations in the hydrogen hyperfine splitting constants (a_H) can sometimes aid in differentiation, but the overlap is significant, hence the importance and need to use DMPO becomes evident. DMPO oxygen-based spin adducts present differences in their hyperfine splitting values, Table 7.1.

To better understand the radical origins each catalyst produces, different experimental conditions were taken into account, Table 7.2. Maintaining the concentrations of the catalysts, solvents and spin trap agents along with the physical experimental parameters, the change of the solvent environment was varied.

Table 7.2: Conditions of the experimental procedures for each catalyst and each spin trap agent.

Code	**Sample Condition**
DMSO	Each suspension had one solvent, DMSO, one catalyst and one spin trap agent.
DMSO + PF	Each suspension had DMSO that included dissolved paraformaldehyde as solvent, one catalyst and one spin trap agent.
DMSO + T	Each suspension had a mixture of solvents, DMSO and toluene, one catalyst and one spin trap agent.
T	Each suspension had one solvent, toluene, one catalyst and one spin trap agent.
PF + T	Each suspension had toluene that included dissolved paraformaldehyde as solvent, one catalyst and one spin trap agent.
DMSO + PF + T	Each suspension had DMSO and toluene, that included dissolved paraformaldehyde, one catalyst and one spin trap agent.

In order to understand the radicals produced during the reaction, suspensions were measured under no irradiation (dark) conditions and under UV irradiation. A 1 ml suspension of DMSO, toluene and paraformaldehyde were prepared, in which 10mg of each catalyst was measured in the presence of 30 mM from one of the two spin trap agents but without any irradiation source. The dark suspensions that were studied did not indicate the presence of any radicals. Figure 7.3 presents the seven different experimental conditions each catalyst was subjected to; all catalysts presented the same trend.

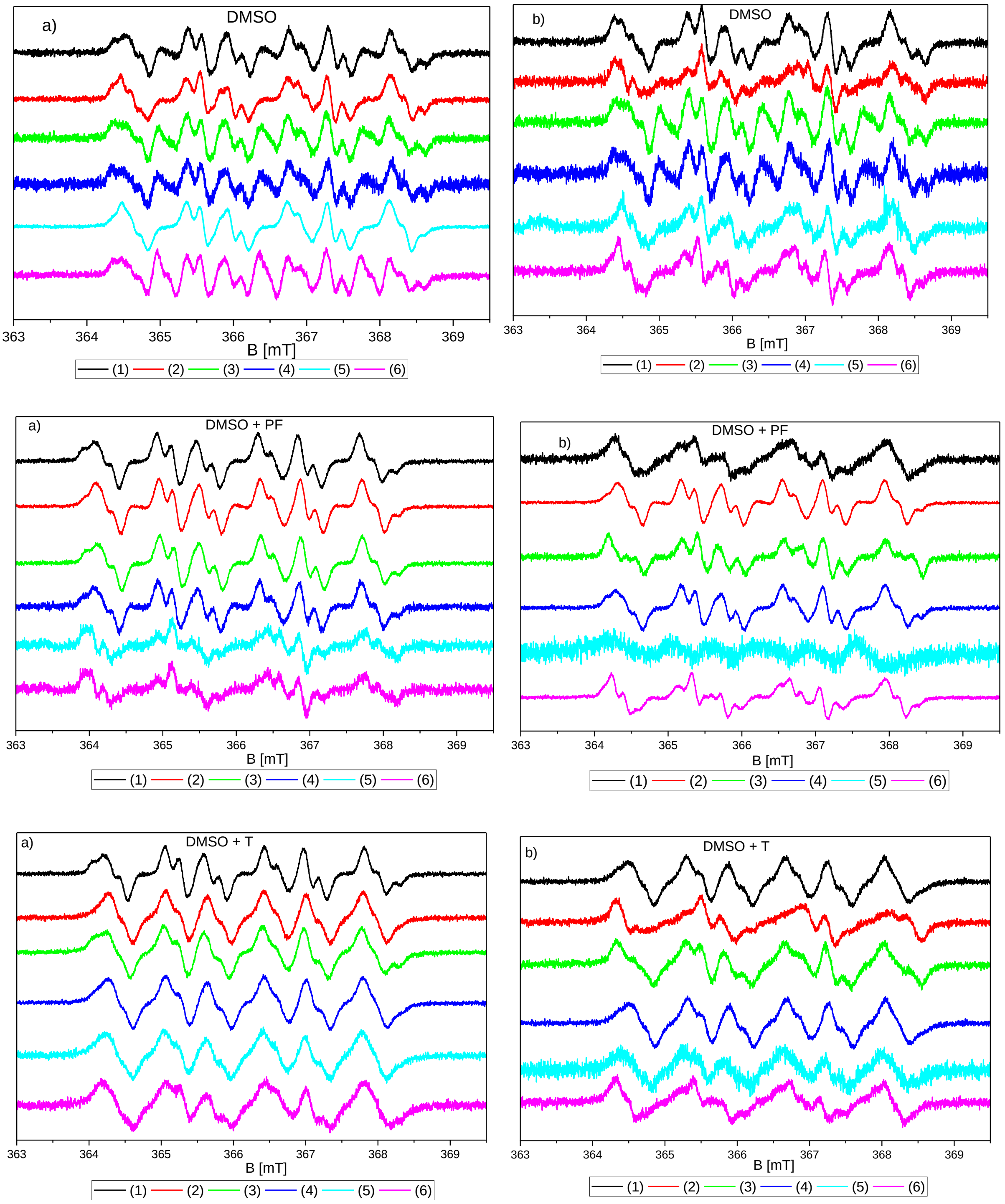

Figure 7.3(i): Spectra for all the catalysts under all the different experimental conditions, (1) F-WN, (2) F-WN(U), (3) F-TaN, (4) F-TaN(U), (5) MW-WN, (6) MW-WN(U) and a) anatase and b) rutile. The suspensions were all irradiated for 5 min and the spin trap agent used for these experimental data set was DMPO. The microwave power was 2 mW, and the catalyst was filtered from the suspensions prior to measuring.

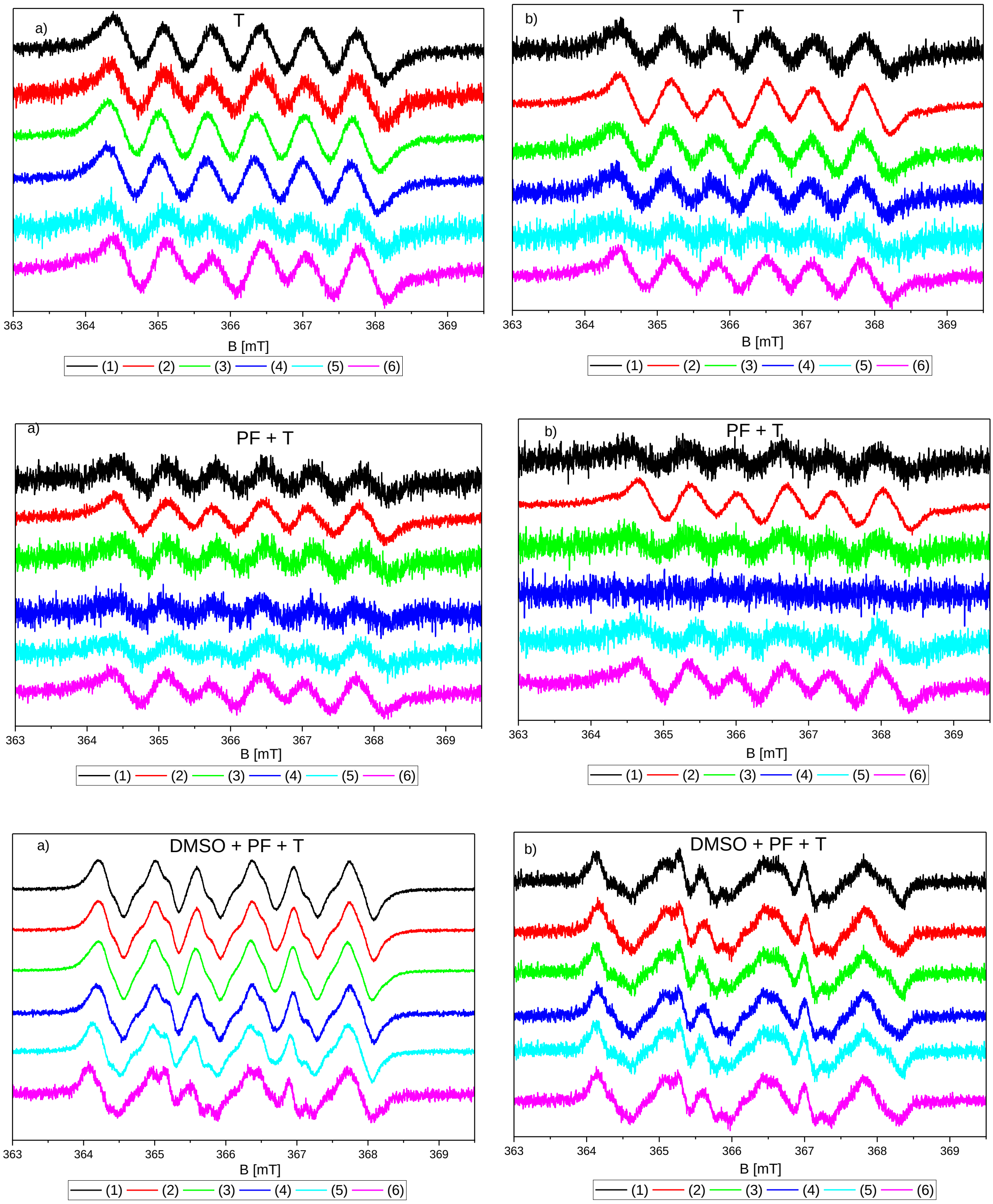

Figure 7.3(ii): Spectra for all the catalysts under all the different experimental conditions, (1) F-WN, (2) F-WN(U), (3) F-TaN, (4) F-TaN(U), (5) MW-WN, (6) MW-WN(U) and a) anatase and b) rutile. The suspensions were all irradiated for 5 min and the spin trap agent used for these experimental data set was DMPO. The microwave power was 2 mW, and the catalyst was filtered from the suspensions prior to measuring.

It is evident that the presence of DMSO highly affects the different adducts that are formed. As those EPR spectra demonstrated the presence of multiple radicals formed including the methyl radical ($CH_3^{\bullet}$). While the spectra from toluene and toluene with paraformaldehyde demonstrated boarder signals. For the DMPO in DMSO, Figure 7.3(i) experiments the contributing adducts that were identified after simulating the spectra as DMPO-OOH, DMPO-OCH_3, DMPO-OR, where OR = $OCH_2S(O)CH_3^{-}$, degraded DMPO (Deg), DMPO-OH and DMPO-CH_3 and their hyperfine values are presented in Table 7.3. The weighted contribution of each radical adduct is listed in Table 7.4 for the different photocatalysts tested herein. The weight percentages were derived from the simulations. A representative simulation for sample F-A-WN-TiO_2 is shown in Figure 7.4, as this catalyst presented the smallest band gap in Chapter 5, indicating the individual components of the contributing radical adducts (the results for all other catalysts are presented in Figure 7.3). The results from ammonia doped anatase catalysts for each calcination method demonstrate that the peroxomethyl to superoxide ratio does not significantly change; however, the rutile catalyst that were calcined via the microwave exhibits nearly half the amount of peroxomethyl as compared to furnace catalyst. However, the trend that appears in the urea- based co-doped samples demonstrates that samples calcined via the conventional way had a higher peroxomethyl weight contribution than the microwave calcined. Therefore, the superoxide contribution was significantly bigger for in the microwave-based catalysts. While the change of the metal dopant was of insignificant effect towards the species produced using DMSO as a solvent, as the tantalum-based catalyst followed the same trend with the tungsten catalysts.

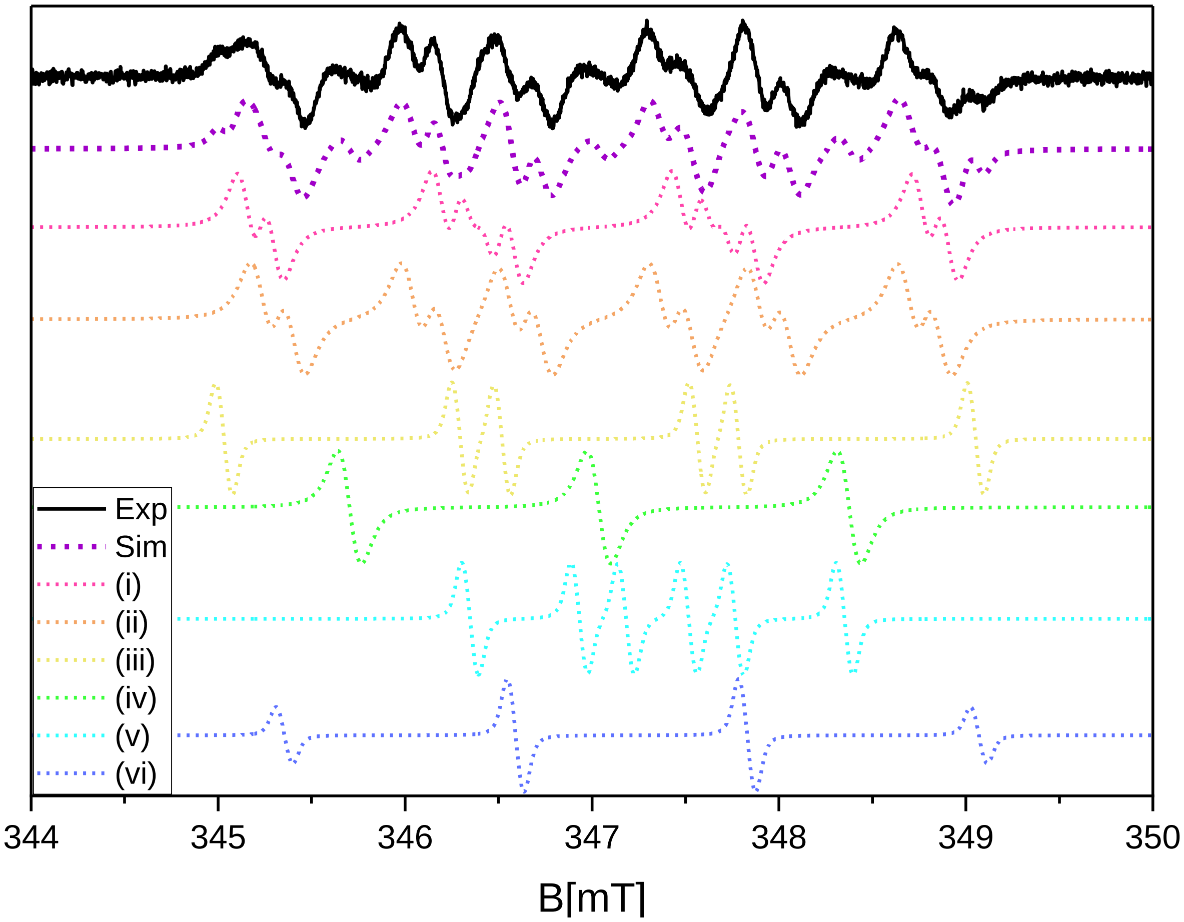

Figure 7.4: Spectra for the F-A-WN (solid) sample along with the overall simulation (dot) and each contributing specie in DMSO, (i) DMPO-OOH, (ii) DMPO-OCH$_3$, (iii) DMPO-OR, (iv) degraded DMPO, (v) DMPO-CH$_3$ and (vi) DMPO-OH.

Table 7.3: Hamiltonian parameters, g_{iso} and A_{iso}, for the suspensions in DMSO, DMSO + PF and T, using DMPO and PBN.

Species	***g***	**$^{1}H_{\beta}$ [MHz]**	**$^{1}H_{\gamma}$ [MHz]**	**^{14}N [MHz]**	**Solvent**	***Ref***
			DMPO			
$^{\bullet}$OH	2.0055	40.2		40.2	DMSO	i
		40.2		40.2	DMSO	(22)
$^{\bullet}$OOH	2.0060	29.2	3.9	36.0	DMSO	i
	2.0061	28.9	3.6	35.7	DMSO + PF	i
	2.0060	19.4	5.3	35.4	Toluene	i
		28.9	3.9	35.6	DMSO	(22)
		19.3	5.3	35.9	Benzene	(71)
$^{\bullet}$OR	2.0061	41.8		35.5	DMSO	i
	2.0058	41.3		33.9	DMSO + PF	i
		41.5		35.6	DMSO	(22)
$^{\bullet}$OCH$_3$	2.0055	22.6	4.6	37.2	DMSO	i
	2.0059	23.5	4.3	37.5	DMSO + PF	i
	2.0057	21.1		38.3	Toluene	i
		22.4	4.5	37.0	DMSO	(22)
		21.3	5	38.1	Benzene	(71)
$^{\bullet}$CH$_3$	2.0056	46.0		65.3	DMSO	i
		45.9		65.3	DMSO	(22)
Deg.	2.0058			41.0	DMSO	i
				40.9	DMSO	(70)
			PBN			
$^{\bullet}$CH$_3$	2.0064	8.41		43.16	DMSO	i
		9.08		43.72	DMSO	(64)
Oxygen-based	2.0064	6.73		39.24	DMSO	i
		7.88		40.43	DMSO	(64)

i. This work

Table 7.4: Percentage contribution of radical adducts in DMSO, for furnace and microwave calcined samples

Sample	**$^{\bullet}$OH**	**$^{\bullet}$OOH**	**$^{\bullet}$OR**	**$^{\bullet}$OCH$_3$**	**$^{\bullet}$CH$_3$**	**Deg**	**$^{\bullet}$OOH**	**$^{\bullet}$OR**	**$^{\bullet}$OCH$_3$**	**Deg**
	Furnace Anatase						Microwave Anatase			
Bare	3	18	2	60	2	15	30	0	65	5
WN	2	35	3	51	1	8	22	3	75	0
WN(U)	2	25	0	61	2	1	39	0	59	2
TaN	0	19	0	81	0	0				
TaN(U)	0	12	0	88	0	0				
	Furnace Rutile						Microwave Rutile			
Bare	0	20	1	79	0	0	55	0	43	2
WN	0	29	1	60	0	10	58	0	40	2
WN(U)	0	37	38	7	0	18	51	0	45	4
TaN	0	36	0	64	0	0				
TaN(U)	0	41	0	59	0	0				

The spectra acquired demonstrated the presence of an oxygen based radical along with the carbon based radical. The presence of the $^{\bullet}$CH$_3$ adduct was more clearly resolved using PBN as the spin trap, Figures 7.5, as the hyperfine values are similar between oxygen-based radicals but differ compared to carbon-based radicals. The hyperfine values and weight contributions are presented in Tables 7.3 and 7.5 respectively. The importance of utilizing different spin traps is clearly identified during these experiments. However, no significant differences in the weight contributions are observed between the different catalysts. Reproducibility was achieved via three repetitions of the spin trap experiments for each catalyst, which all spectra demonstrating the same radicals present and with weight contributions in agreement with Table 7.4.

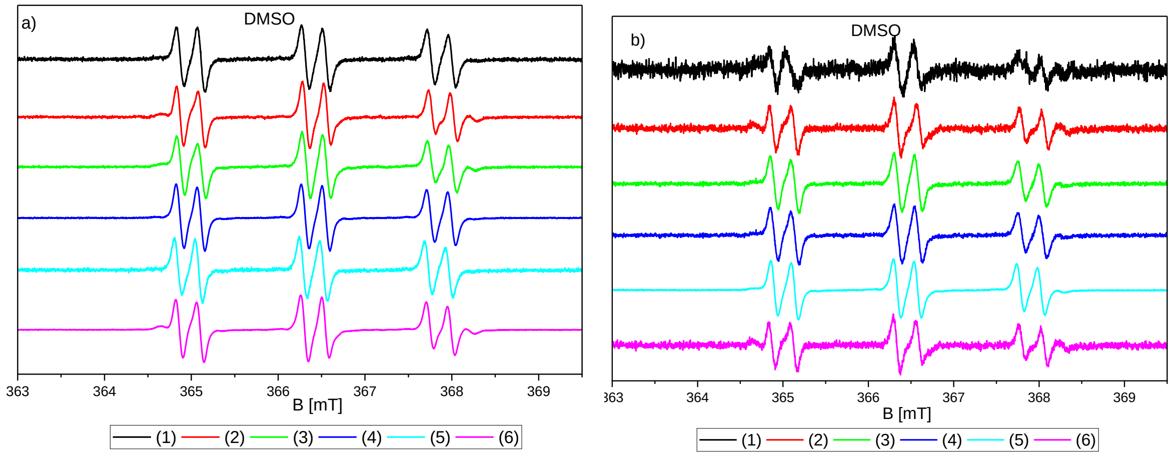

Figure 7.5: Spectra for all the catalysts under all the different experimental conditions, (1) F-WN, (2) F-WN(U), (3) F-TaN, (4) F-TaN(U), (5) MW-WN, (6) MW-WN(U) and a) anatase and b) rutile. The suspensions were all irradiated for 5 min and the spin trap agent used for these experimental data set was PBN. The microwave power was 2 mW, and the catalyst was filtered from the suspensions prior to measuring.

Table 7.5: Percentage contribution of radical adducts in DMSO, for furnace and microwave calcined samples using PBN.

Samples	**$^{\bullet}CH_3$**	**Oxygen-based**	**$^{\bullet}CH_3$**	**Oxygen-based**
	Furnace Anatase		Microwave Anatase	
Bare	14	86	15	85
WN	11	89	13	87
WN(U)	20	80	16	84
TaN	17	83		
TaN(U)	12	88		
	Furnace Rutile		Microwave Rutile	
Bare	15	85	16	84
WN	20	80	12	88
WN(U)	17	83	18	82
TaN	13	87		
TaN(U)	14	86		

For the DMPO in toluene experiments the contributing adduct identified after simulating the spectra were DMPO-OOH and DMPO-OCH_3, Table 7.3 presents the g_{iso} and a_{iso} for these radicals. The detection of DMPO-OOH and DMPO-OCH_3 suggests that oxidation is initiated but may not be complete and the reaction may stall at intermediate stages. To fully convert to CO_2, stronger oxidation steps are required, particularly through $^{\bullet}$OH radicals. All of the samples demonstrated a broadening of the signal; however, their hyperfine values were within agreement from literature. The spectra for the F-A-WN sample along with the simulation can be found in Figure 7.6 as a representative example of all catalysts tested (remaining data presented in Figure 7.3), The results from ammonia doped anatase catalysts for each calcination method demonstrate that the peroxomethyl to superoxide ratio does not significantly change; however, for the majority of the rutile catalyst that were calcined via the microwave exhibits a smaller amount of peroxomethyl as compared to furnace catalyst. An interesting observation can be made for the F-A-WN catalyst, as it presents the smallest amount of $^{\bullet}$OOH. In Chapter 6.1, this catalyst demonstrated the presence of superoxide, which further strengths the explanation of the consumption of superoxide for the peroxomethyl production. Table 7.7 presents the weight contribution for each species involved in the suspension that had only toluene as a solvent.

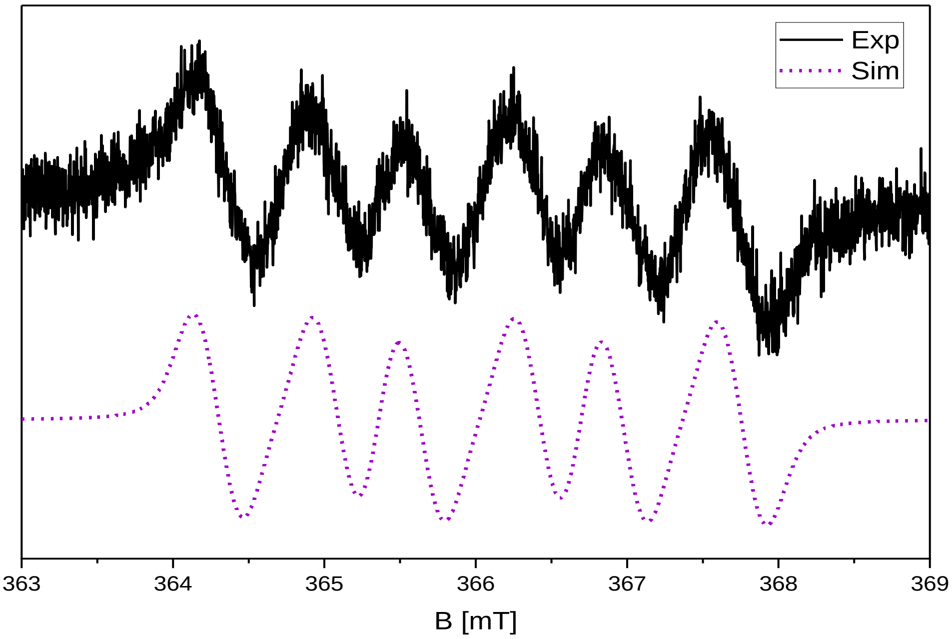

Figure 7.6: Spectra for the F-A-WN (solid) sample along with the overall simulation (dot) which only contains one contributing specie in toluene, DMPO-OOH.

Table 7.6: Percentage contribution of radical adducts in toluene, for furnace and microwave calcined samples.

Samples	**$^{\bullet}OOH$**	**$^{\bullet}OR$**	**$^{\bullet}OCH_3$**	**$^{\bullet}OOH$**	**$^{\bullet}OCH_3$**
	Furnace Anatase			Microwave Anatase	
Bare	75	0	25	84	16
WN	74	0	26	81	19
WN(U)	91	1	8	76	24
TaN	93	0	7		
TaN(U)	94	0	6		
	Furnace Rutile			Microwave Rutile	
Bare	58	0	42	83	17
WN	34	0	66	78	22
WN(U)	23	39	38	92	8
TaN	64	0	36		
TaN(U)	59	0	41		

It is worth mentioning that when toluene was added to DMSO the formation of peroxomethyl radicals was observed across every catalyst at an approximate 80:20 ratio of peroxomethyl to superoxide. Indicating two possible explanations, that the formation and detection of superoxide is hindered by environment or that the consumption of the superoxide produces an increased amount of peroxomethyl. These results align with findings from Chapter 6 that have highlighted the presence of superoxide radicals and trapped holes during the UV irradiation of the catalysts under oxygen atmosphere. The detection of the NiO^{2-} that was successfully produced, effectively demonstrates the presence of the intra-band gap NO^{2-} state which could track the presence desired oxygen and hole species: $h^+ + O^{2-} \rightarrow O^-$, thus, $NO + O^- \rightarrow NO^{2-}$.

When paraformaldehyde what added in DMSO the experiments demonstrated a shift in the radicals that are produced in the suspension. The spin Hamiltonian parameters for the experiments that included paraformaldehyde in the suspension mixture are presented in Table 7.1. The addition of paraformaldehyde increases the amount of peroxomethyl radicals present in experiments involving both furnace-calcined co-doped anatase catalysts Table 7.7 ; in contrast, paraformaldehyde decreases the peroxomethyl weighting in experiments involving microwave-calcined co-doped anatase catalysts. When paraformaldehyde was added to the ammonia tungsten co-doped furnace calcined rutile experiment, the amount of peroxomethyl significantly decreased. Rutile catalysts typically have substantially lower peroxomethyl loading than anatase catalysts. On the other hand, the peroxomethyl weighing increases for both the ammonia microwave catalyst and the urea furnace catalyst.

Once the paraformaldehyde was added to toluene only no observed difference was feasible to be detected, as the signal was too broad.

A formaldehyde formation via hydroxyl radical scavenging needs to be considered as the mechanism demonstrated in Equations (7.14) – (7.16) demonstrates that the radicals present in these samples could be utilized for those reactions. (72, 73)

$$\mathrm{DMSO{+}OH^{\bullet} \rightarrow CH_3SOOH + CH_3^{\bullet}} \qquad (7.14)$$

$$\mathrm{CH_3^{\bullet}{+}O_2 \rightarrow CH_3OO^{\bullet}} \qquad (7.15)$$

$$\mathrm{2CH_3OO^{\bullet} \rightarrow HCOH{+}CH_3OH + O_2} \qquad (7.16)$$

The variation of the weight contribution between the radicals formed under the different conditions could be attributed to the variance in the surface area (demonstrated in Chapter 5) of the materials, as it could allow the adsorption and degradation of paraformaldehyde to occur. As samples such as F-A-WN(U) with the highest calculated BET specific surface area of 197.13 m^2g^{-1} produces an approximate 50/50 between •OCH3 and •OOH. Whereas for the remaining anatase catalysts demonstrated the same radical ratios with specific areas relative similar to each other, averaging at 119 m^2g^{-1}.

Table 7.7: Percentage contribution of radical adducts in DMSO + PF, for furnace and microwave calcined samples using DMPO.

Samples	$^{\bullet}\mathrm{OCH_3}$	$^{\bullet}\mathrm{OR}$	$^{\bullet}\mathrm{OOH}$	$^{\bullet}\mathrm{OCH_3}$	$^{\bullet}\mathrm{OOH}$	Degraded DMPO
	Furnace Anatase			Microwave Anatase		
Bare	68	3	26	47	53	0
WN	74	4	22	21	75	4
WN(U)	59	0	41	49	43	8
TaN	78	0	22			
TaN(U)	89	0	11			
	Furnace Rutile			Microwave Rutile		
Bare	58	0	42	44	52	4
WN	34	0	66	94	6	0
WN(U)	23	39	38	40	57	3
TaN	64	0	36			
TaN(U)	59	0	41			

7.3 Toluene conversion and gas VOC pressure contact

The conversion of toluene was studied externally from collaborators in China (Professor Su Ren), 0.3 μL of toluene dosed on photocatalyst film that contains 4 mg photocatalysts were irradiated using a 365 nm LED for 1 h at RT and ambient air pressure. The film deposited on the vessel is shown in Figure 7.7. The results are demonstrated in Figure 7.8 and the conversion, that is equivalent to the decomposition of toluene was measured via *in-situ* MS for the catalysts. The decomposition of toluene was followed through to the complete conversion to CO_2. The A-WN(U) demonstrated better performance than the rest of the samples. However, P25 still presents the best performance, reaching 91% of conversion. Full decomposition of toluene using the synthesised co-doped catalysts could be achieved by prolonging the irradiation time (i.e., 2 h), as plateau was not reached during measurements. The anatase catalysts that utilised urea as the nitrogen source demonstrated a higher toluene decomposition compared to the ammonia-based catalysts. This trend is, also, observed for the tungsten rutile catalysts, however, the materials with tantalum as the metal dopant demonstrated the opposite trend, where the TaN had a higher conversion percentage than TaN(U). Additionally, for 3 out of the 4 sets the anatase provided a higher conversion percentage, except for the R-TaN catalyst reaching one of the highest decomposition amounts.

Furthermore, the tungsten-nitrogen catalysts that were calcined via the microwave oven were tested to determine the photocatalytic activity for toluene decomposition. Figure 7.9 presents the percentage of the conversion from these catalysts under the same conditions. The microwave samples demonstrated a significant change in the results, with the rutile WN(U) reaching one of the highest conversions at 60%, while the anatase WN(U) demonstrated a significant decrease of 50% in its photocatalytic capabilities. An increase in the decomposition of toluene was observed for the catalysts originated from ammonia. This agrees with spin trap experiments, as the anatase and the one rutile samples produced a higher quantity of the $O_2^{\bullet -}$ compared to the $^{\bullet}OCH_3$. With the increased amount of superoxide produced the photocatalyst can break down a higher quantity of toluene. When the photocatalyst is doped the generation of these radicals is enhanced and it initiates more efficient oxidation processes, leading to the cleavage of toluene's aromatic ring and its subsequent conversion into smaller, less harmful molecules such as carbon dioxide and water. This increase in superoxide radical production not only accelerates the degradation rate of toluene but also improves the overall photocatalytic efficiency, making the process more viable for large-scale applications in environmental remediation.

Figure 7.7: Photocatalyst film deposited on the bottom of the vessel.

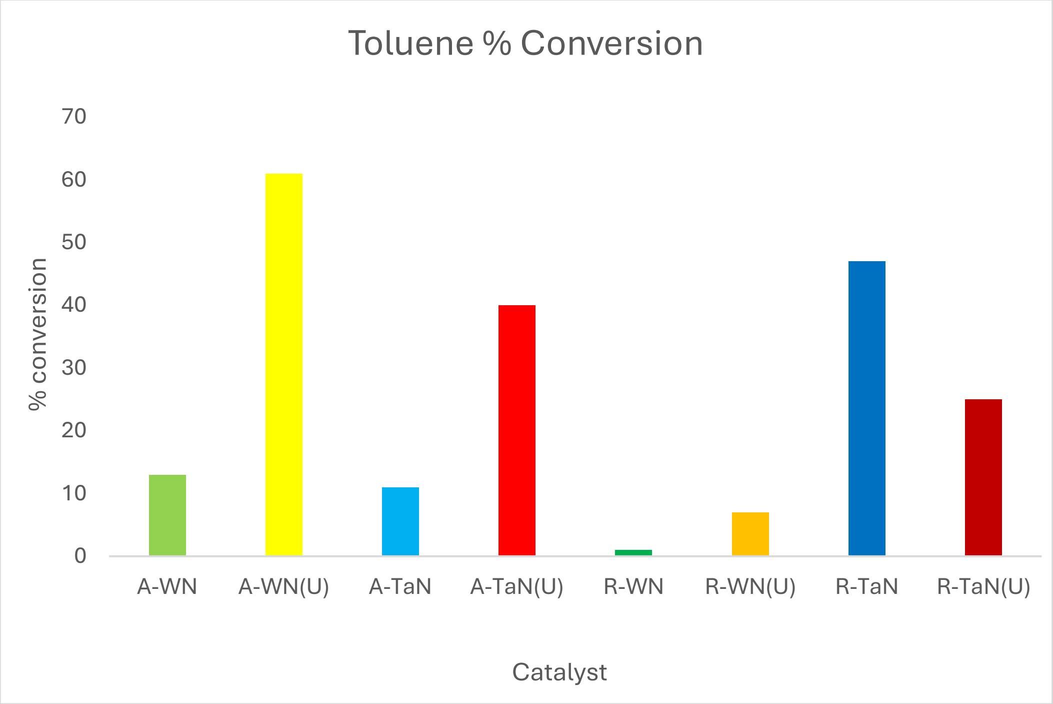

Figure 7.8: Photocatalytic decomposition of toluene by different photocatalyst calcined utilizing a conventional heating furnace under UV irradiation.

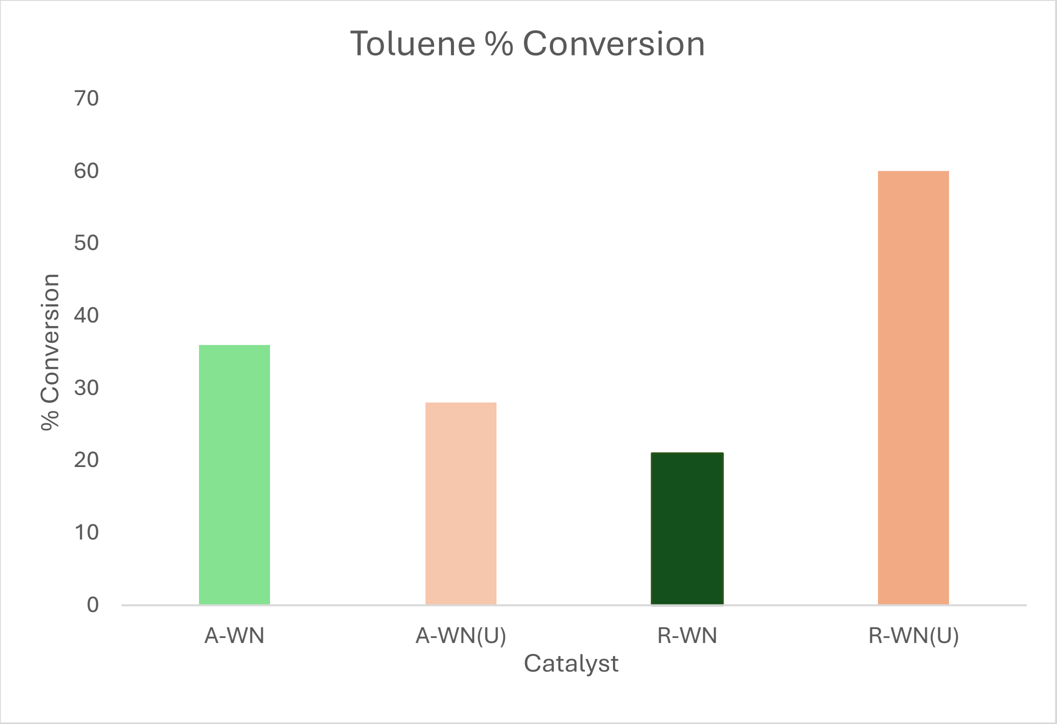

Figure 7.9: Photocatalytic decomposition of toluene by W,N photocatalyst calcined via the microwave pathway under UV irradiation.

In order to better understand the role of the radicals that are formed during the photocatalytic degradation of toluene solid-state EPR was employed. The presence of molecular oxygen has a significant effect on the mechanism of the toluene decomposition, as it allows for the formation of superoxide radicals, rather than hydroxyl, thus, creating a favourable ROS environment. Based on the different photocatalytic experiments performed and examined in this chapter (7.2 and 7.3), the F-A-W,N(U) demonstrated the most effective photocatalytic responses. Thus, vapour pressures of toluene and oxygen (T + O) and DMSO and oxygen (DMSO + O) were added after the freeze – pump – thaw cycles (described in Chapter 4) with a ratio of 1:10 organic to oxygen.

Figures 7.10 presents the contact of the mixture of gasses (T+ O) with the catalyst under different irradiated conditions, dark and UV. It is observed that under UV irradiation the formation of superoxide can be identified, with g-tensor of g_1 = 2.019-2.026, g_2 = 2.010 and g_3 = 2.004 , after the spectra were simulated. The Spin Hamiltonian parameters for the species present (which have been characterised in Chapter 6) along with the corresponding weight contribution are listed in Table 7.8. It is important to note that the mixture of gasses took place prior to exposure to the catalyst, as literature has demonstrated that if a secondary gas, such as oxygen, is exposed the adsorption sites are not accessible for superoxide formation. (74) According to literature when toluene decomposes it goes through the pathway that forms a benzyl radical. However, during these experiments no benzyl radicals (g_1 = 2.0315, g_2 = 2.010 and g_3 = 2.002 (75) were observed, indicating that the presence of oxygen hinders the abstraction of hydrogen, thus the benzyl formation. The observation of the superoxide signal indicates that the Ti^{3+} centre, used for oxygen adsorption, remains free, thus indicating that toluene interacts and binds to the Ti^{4+}. The presence of the superoxide and the trapped hole have been identified and described in Chapter 6 along with their importance for photocatalytic reactions.

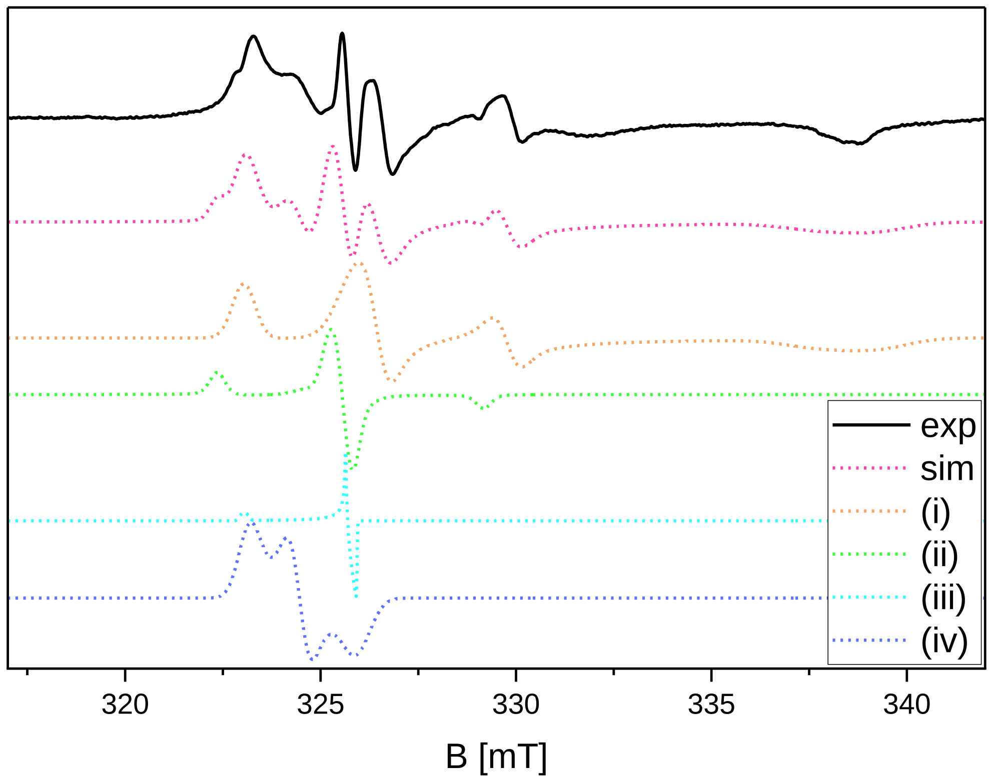

Figure 7.10: Spectra for the experimental F-A-WN(U) (solid) sample under toluene and oxygen atmosphere along with the overall simulation (dot) and each contributing specie in (i) NO, (ii) N_iO^{2-}, (iii) trapped hole and (iv) O_2^-.

Table 7.8: Hamiltonian parameters, **g** and **A** tensors, and individual weight contributions of each species for the two gas mixtures.

Gas mix	**Species**	g_{xx}	g_{yy}	g_{zz}	A_1 [MHz]	A_2 [MHz]	A_3 [MHz]	**weight**
T + O	**NO**	2.002	1.998	1.927	2.8	92.5	26.9	76
	N_iO^{2-}	2.005	2.004	2.002	6.5	15.7	89.7	10
	O_2^-	2.019	2.010	2.001				5
	h^+	2.019	2.002	2.002				9
DMSO + O	**NO**	2.002	1.998	1.927	2.8	92.5	26.9	79
	N_iO^{2-}	2.005	2.004	2.002	6.5	15.7	89.7	5
	O_2^-	2.019	2.010	2.001				11
	h^+	2.019	2.002	2.002				5

Figure 7.11 presents the contact of the mixture of gasses (DMSO + O) with the catalyst under different irradiated conditions, dark and UV. Under UV irradiation the formation of superoxide can be identified, with **g**-tensor of g_1 = 2.019-2.026, g_2 = 2.010 and g_3 = 2.004. The spin Hamiltonian parameters for the species (which have been characterised in Chapter 6) present along with the corresponding weight contribution can be seen in Table 7.8. Similarly to the toluene the mixture of gasses took place prior to exposure to the catalyst to avoid site blockage. (76) According to literature during DMSO decomposition through irradiation, it generates $^{\bullet}CH_3O$, $HCOO^{\bullet}$ and $^{\bullet}CH_3S$. However, once oxygen is present the CH_3S is further oxidised to CH_3SO_3 . (77) The presence of the superoxide and the trapped hole have been identified and described in Chapter 6 along with their importance for photocatalytic reactions, however, no further different signals were observed in the spectra under these conditions.

These results indicate that the F-A-WN(U) catalyst presents a great potential to be used for VOC photodegradation as it produces superoxide and trapped hole signals, both of great significance during catalytic processes. The presence of these species along with the decrease of the band gap (Chapter 5) indicate the presence of a pathway for the photodegradation to occur under visible light. Whereas undoped titania of the single polymorph or a mixture, such as P25, can only reach their photocatalytic potentials under UV light only.

Literature has demonstrated the capability of co-doped catalysts for photodegradation of gaseous toluene. However, this work has provided an important novel insight into the mechanism taking place in the presence of gaseous toluene with oxygen and in the presence of gaseous DMSO with oxygen. These reactions were monitored via EPR and demonstrated that mixing of the gases prior to their addition on the catalyst surface produced signals attributable to superoxide and trapped holes, both species of importance during photocatalytic reactions.

The formation of superoxide radicals is particularly significant, as these species are known to participate in a variety of photocatalytic pathways, including the oxidation of organic pollutants and the generation of hydroxyl radicals ($^{\bullet}OH$), which further enhance the photocatalytic activity.

Trapped holes, on the other hand, contribute to the oxidation of adsorbed species on the catalyst surface, facilitating the breakdown of complex molecules into simpler compounds such as CO_2 and H_2O.

The presence of these reactive species, as identified through EPR, underscores the importance of optimizing gas-phase conditions to maximize the efficiency of photocatalytic reactions for future understanding of these co-doped catalysts.

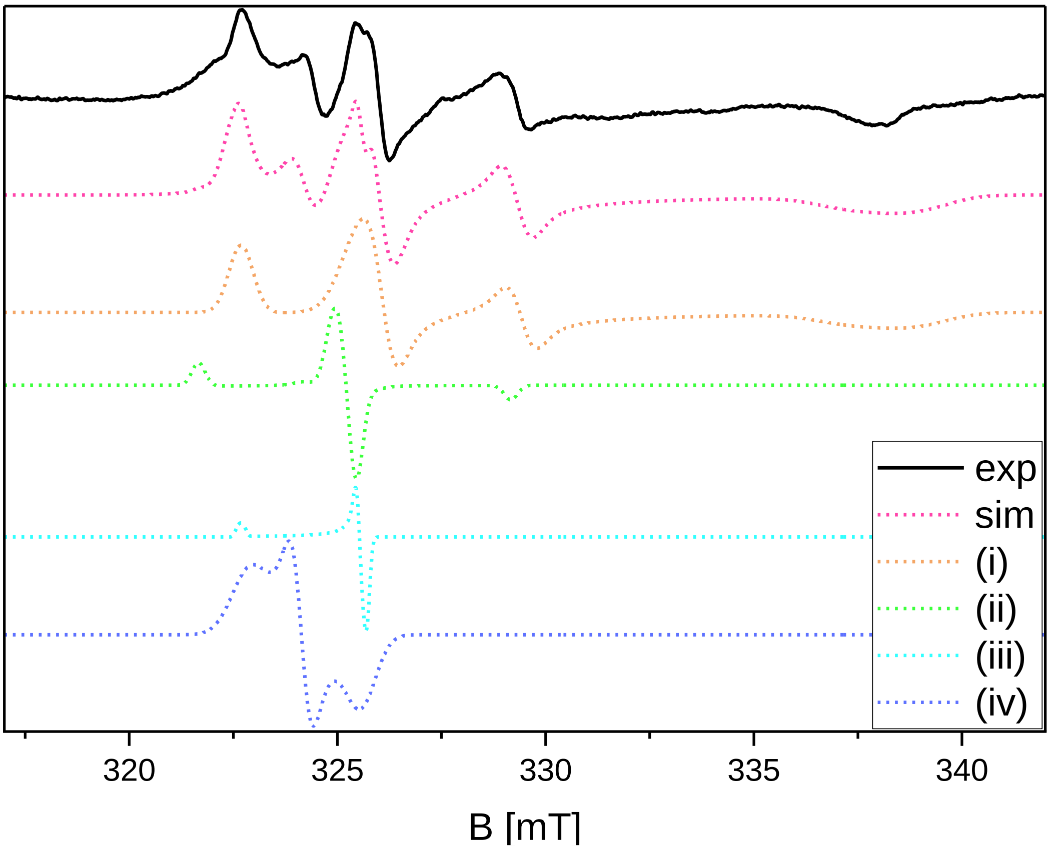

Figure 7.11: Spectra for the experimental F-A-WN(U) (solid) sample under DMSO and oxygen atmosphere, along with the overall simulation (dot) and each contributing specie in (i) NO, (ii) N_iO^{2-}, (iii) trapped hole and (iv) and O_2^{-}.

7.4 Spin trap and Hydrogen production results

Another potential application for these photocatalysts is the photoinduced transformation of glycerol to produce H_2 and CO_2 using the most promising co-doped photocatalysts developed. Glycerol oxidation helps in understanding radical-driven reaction mechanisms, especially in photocatalysis on TiO_2 surfaces. This has implications in environmental remediation and energy storage, where glycerol serves as a model compound for biomass-derived molecules. Its selective transformation allows for efficient carbon utilisation, reducing waste and promoting a circular economy. Glycerol free solutions were measured in order to be able to understand the differences presented in the spectra that contained glycerol. The glycerol free suspensions were only characterised by the well-established DMPO-OH spin adduct with Hamiltonian parameters of a_N = 14.97 G, a_H = 14.77 G and g = 2.005 (78), the bare anatase spectrum of the suspension can be seen as an example in Figure 7.12.

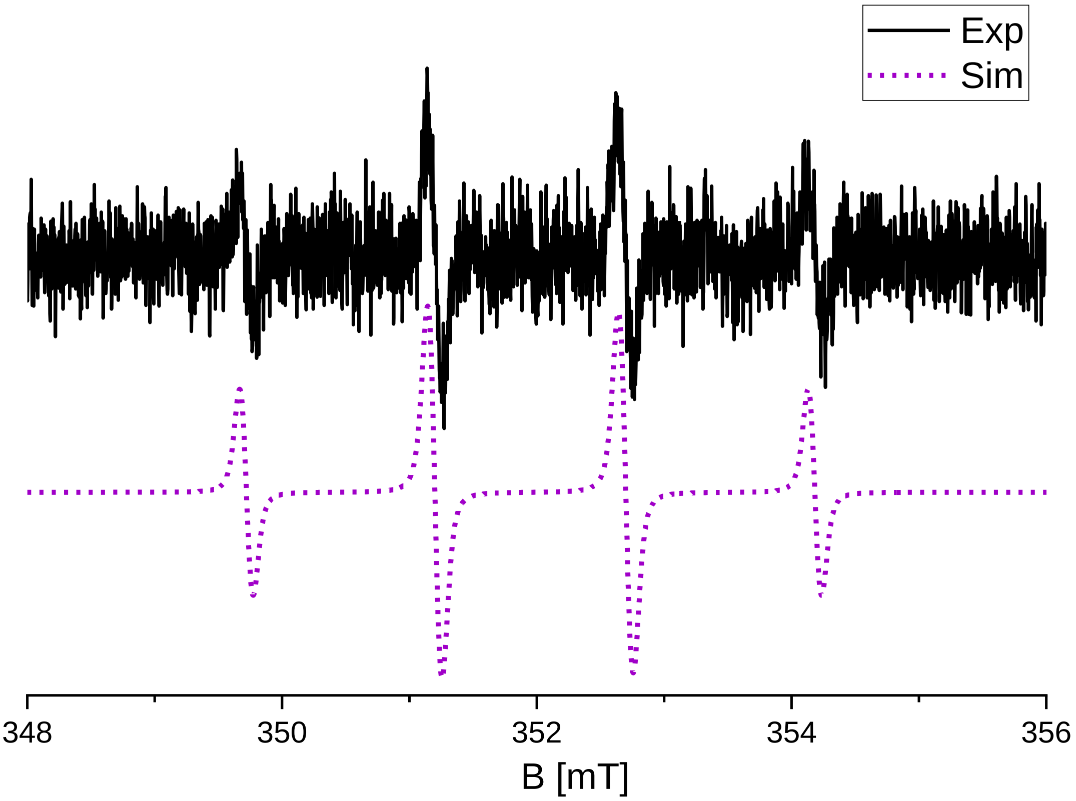

Figure 7.12: Spectra for the bare TiO_2 (solid) sample along with the overall simulation (dot) which only contains one contributing specie in water, DMPO-OH.

Once the glycerol was added as part of the suspension mixtures the presence of different signals, ${}^{\bullet}R_1$ (${}^{\bullet}CHOH\text{-}CHOH\text{-}CH_2OH$) and ${}^{\bullet}R_2$ ($CH_2OH\text{-}{}^{\bullet}COH\text{-}CH_2OH$), were detected, Figure 7.13. The hyperfine and g tensors of the ${}^{\bullet}R_1$ and ${}^{\bullet}R_2$ are $a_N = 15.96$ G, $a_{H\beta} = 22.25$ G, $g = 2.005$ and $a_N = 16.04$ G, $a_{H\beta} = 23.20$ G, $g = 2.005$, respectively. (53, 78, 79) The profile of the carbon based DMPO radicals based on the literature matches the six-line profile of the hydroxyalkyl radicals produced from the glycerol addition, as it causes hydrogen abstraction. (80, 81)

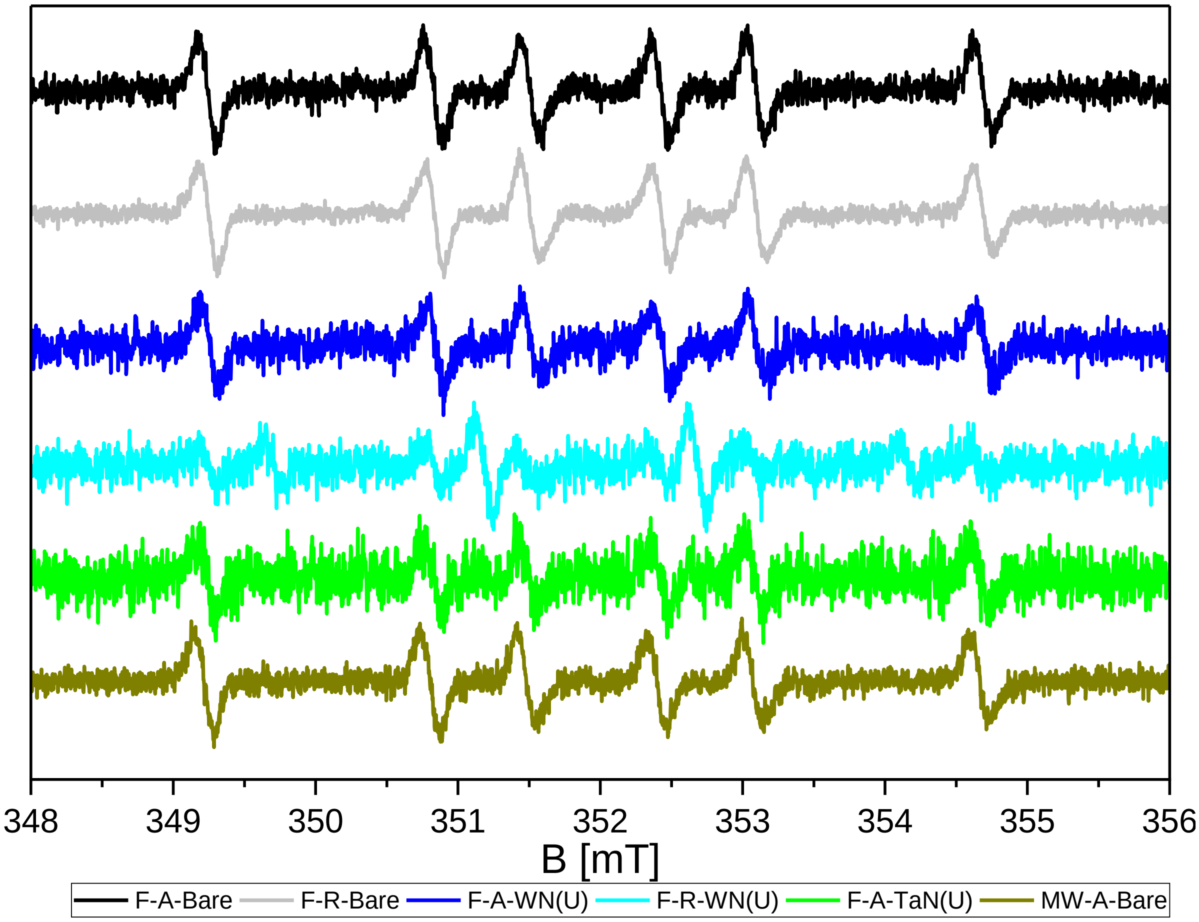

Figure 7.13: Spectra for different catalysts in water with glycerol. The suspensions were all irradiated for 5 min and the spin trap agent used for these experimental data set was DMPO. The microwave power was 2 mW, and the catalyst was filtered from the suspensions prior to measuring.

Table 7.9 presents the relative weights present in the spectra for each catalyst. The lack of the DMPO-OH adduct is explained as this is the species responsible for the formation of $^{\bullet}R_1$ and $^{\bullet}R_2$ during the irradiation of the suspension. However, the rutile WN(U) catalyst demonstrated an interesting exception as a large portion of the $^{\bullet}OH$ was able to be detected, indicating that it did not react with the glycerol or that the concentration of glycerol was not high enough for all of the $^{\bullet}OH$ generated radical to react with.

The microwave undoped catalyst demonstrates a 1:1 ratio between the $^{\bullet}R_1$ and $^{\bullet}R_2$ formation, something that is not observed in the corresponding furnace sample. This could be attributed to the fact that the two different calcination processes have an effect on the surface of the catalyst. Dvoranová (22) has demonstrated that the surface defects of the catalysts have a significant role in pathway taken, thus the radicals formed. The difference of the radical contributions between the furnace and the microwave samples was further proven through the distinctions in the samples presented in Chapters 5 and 6. The most distinct difference is described in Chapter 6.1, that demonstrates that R-NW(U) presented no change during irradiation under O_2 atmosphere and there were only two contributing paramagnetic species, NO and Ti^{3+}. The detection of such a high $^{\bullet}OH$ percentage indicates that upon UV exposure glycerol undergoes incomplete oxidative transformation. For the MW-A-undoped-TiO_2 the detection of the 50/50 of the organic radicals indicates that multiple oxidation pathways are occurring simultaneously, leading to complete glycerol degradation through a diverse and efficient radical-driven oxidation process. For the remaining catalysts the presence of one radical suggests a more selective and limited oxidation pathway.

Table 7.9: Percentage contribution of each radical species in the overall profile of the signals in the water and glycerol mixture.

Samples	$^{\bullet}OH$	$^{\bullet}R_1$	$^{\bullet}R_2$
Furnace			
A-Bare	0	0	100
R-Bare	0	5	95
A-WN(U)	0	0	100
R-WN(U)	45	0	55
A-TaN(U)	0	0	100
Microwave			
A-Bare	0	49	51

The doping of the catalysts demonstrated a significant impact on the photocatalytic activity of these newly synthesised materials, offering an insight into the capabilities of these catalysts. It is well known and explained in Chapter 2 that doping decreases the photocatalytic reactivity of TiO_2 as the recombination accelerates due to band gap shortening, it is however, the same shortening that is of greatest importance as it becomes photoactive under solar light. During these photocatalytic experiments the doped materials' photo reactivity were significantly reduced, which is within agreement of the toluene decomposition experiments. Figure 7.14 presents the H_2 evolution for the tested catalysts, where once again the F-A-WN(U) is demonstrating the highest production of hydrogen, with only bare catalysts outperforming it. The data presented by the photocatalytic experiments are within agreement of those obtained via the spin trap, as the least efficient catalyst was proven to be the F-R-WN(U), and it is also the catalyst that presented an almost 50-50% profile between the $^{\bullet}OH$ and $^{\bullet}R_2$ radicals. The data, presented in Figure 7.14, suggests that despite some doped TiO_2 samples having a significantly higher BET surface area, reaching 197.13 m^2g^{-1} (Chapter 5), their photocatalytic hydrogen evolution remains low. A-TiO_2, which has a lower surface area, exhibits the highest H_2 evolution rate, indicating that increased surface area alone does not guarantee improved photocatalytic activity. This discrepancy could be due to several factors, such as doping-induced recombination centres that reduce electron-hole separation efficiency, shifts in the conduction band edge that make H_2 evolution less favourable, or changes in surface chemistry that hinder the adsorption of reactants. Additionally, the active sites responsible for hydrogen evolution may not scale directly with BET surface area, as some doped sites might be catalytically inactive. This suggests that intrinsic electronic properties and defect structures introduced by doping play a more significant role in photocatalytic performance than surface area alone.

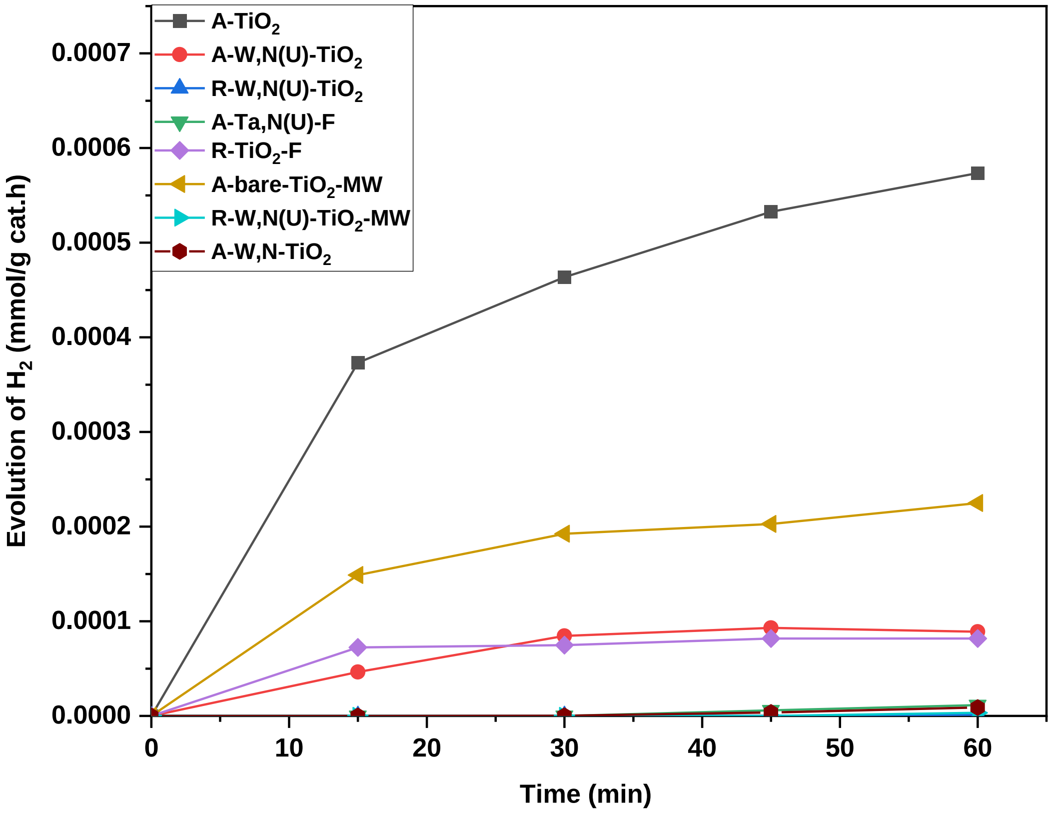

Figure 7.14: Comparison of H_2 production rates using different photocatalysts. Lines are drawn as guidance and the experimental conditions were: 0.1 g of catalysts, 40 ml of water, 100 µl of glycerol and a Xe lamp for UV irradiation only.

7.5 Conclusion

The results observed throughout this chapter clearly identify that different precursors and calcination method have a different spatial arrangement, thus, they present variations on the surface activity during photocatalytic processes. This is proven through the different in species and weight contribution during the spin trap and decomposition experiments. From the experiments performed the most promising catalyst was shown to be the W,N(U) and was calcined via a conventional furnace. However, high promise was also indicated from the microwave samples, but due to the limited quantity of samples synthesised via a microwave the experiments performed where limited. Additionally, the experiments demonstrated the capabilities these catalysts have based on the radicals formed under different conditions.

Despite the fact that these materials underperformed when compared to commercial P25, their true photocatalytic advantages and benefits can only be assessed after these photocatalytic experiments take place under visible light irradiation, for example using a blue lamp with a wavelength around 455 nm and under. This would offer a more complete profile of the catalysts which could indicate that these materials can be used under visible light for VOC decomposition and glycerol transformation, something that is out of reach for the conventional P25. Chapter 5, demonstrated that these materials have a red shift in their light absorption, thus, bringing the band gap into the visible region. Therefore, making them suitable for these reactions to take place at the surface of the materials under sun light irradiation. The materials would be expected to perform following the trends observed under UV light, as the radical species that are produced are related to the surface availability of the materials rather than the wavelength of irradiation. However, due to time constraints and equipment limitations, the visible light experiments were not able to be performed.

7.6 References

(1) Directive 2004/42/CE of the European parliament and the council, EUR-Lex. European Union Publications Office.

(2) N. W. Krase, J. B. Goodman, *Industrial Engineering Chemistry*, 1930, **22**, 13

(3) G. A. Kapralova, A. M. Chaikin, *Chemical Physics Reports*, 2000, **18**, 12, 2359-2362

(4) R. Atkinson, J. Arey, *Chemical reviews* 2003, **103**, 4605

(5) *Scientific Assessment of Ozone Depletion*: World Meteorological Organization Global Ozone Research and Monitoring Project; Report No **37**; Geneva, Switzerland 1994

(6) A. Guenther, C. Geron, T. Pierce, B. Lamb, P. Harley, R. Fall, *Atmos. Environ*. 2000, **34**, 2205

(7) M. Placet, C. O. Mann, R. O. Gilbert, M. Niefer, *J. Atmos, Environ*. 2000, **34**, 2183

(8) F. I. Khan, A. K. Ghoshal, *Journal of loss prevention in the process industries* 2000, **13**, 527

(9) K. Urashima, J. S. Chang, I*EEE Transactions on Dielectrics and Electrical Insulation* 2000, **13**, 527

(10) D. Das, V. Gaur, N. Verma, *Carbon* 2004, **42**, 2949

(11) Y. Zhang, R. Yang, R. Zhao *Atmospheric Environment* 2003, **37**, 3395

(12) U. I. Gaya, A. H. Abdullah, *Journal of Photochemistry and Photobiology C: Photochemistry Reviews* 2008, **9**, 1

(13) J. Y. Li, W. Cui, P. Chen, X. A. Dong, Y. H. Chu, J.P. Sheng, Y. X. Zhang, Z. M. Wang, F. Dong, *Appl. Catal. B: Environ*., 2020, **260**, Article 118130

(14) S. Ardizzone, C.L. Bianchi, G. Cappelletti, A. Naldoni, C. Pirola, *Environ. Sci. Technol*., 2008, **42**, 6671-6676

(15) J. Y. Li, X. A. Dong, G. Zhang, W. Cui, W. L. Cen, Z. B. Wu, S. C. Lee, F. Dong, *J. Mater. Catal. A*, 2019, **7**, 3366-3374

(16) J. H. Mo, Y. P. Zhang, Q. J. Xu, Y. F. Zhu, J. J. Lamson, R. Y. Zhao, *Appl. Catal. B: Environ.*, 2009, **89**, 570-576

(17) G. X. Zhang, Z. M. Sun, Y. W. Duan, R. X. Ma, S. L. Zheng, *Appl. Surf. Sci*., 2017, **412**, 105-112

(18) N. He, Z.H. Li, *Phys. Chem. Chem*. Phys., 2016, **18**, 10005-10017

(19) C. S. Huang, C. M. Zhang, X. M. Yang, *J. Chem. Phys*., 2010, **132**, Article 154306

(20) Z. Y. Sheng, D. R. Ma, Q. He, K. Wu, L. Yang, *Catal. Sci. Technol*., 2019, **9**, 5692-5697

(21) S. M. Liang, Y. J. Shu, K. Li, J. Jian, H. B. Huang, J. G. Deng, D. Y. C. Leungd, M. Y. Wu, Y. G. Zhang *J. Hazard. Mater*., 2020, **399**, Article 122967

(22) D. Dvoranová, Z. Barbieriková and V. Brezová, *Molecules*, 2014, **19**, 17279.

(23) X. Duan, D. Sun, Z. Zhu, X. Chen, P. Shi, *Journal of Environmental Science and Health* 2002, Part A, **37**, 4, 679

(24) F. Zhang, X. Zhu, J. Ding, Z. Qi, M. Wang, S. Sun, J. Bao, C. Gao, *Catalysis Letters* 2014, **144**, 6, 995

(25) M. Nagao, Y. Suda, *Langmuir*, 1989, **5**, 42

(26) T. Ibusuki, K. Takeuchi, *Atmospheric Environment* 1986, **20**, 1711

(27) F. A. Momani, N. Jarrah, *Environmental Technology* 2009, **30**, 1085

(28) Y. Luo, W. S. Tai, H. O. Seo, K. D. Kim, M. J. Kim, N. K. Dey, Y. D. Kim, K. H> Choi, D. C. Lim, *A Catalysis letters*, 2010, **138**, 76

(29) H. Einaga, S. Futamura, T. Ibusuki, *Physical Chemistry Chemical Physics*, 1999, **20**, 4903

(30) T. Ibusuki, K. Takeuchi, *Atmospheric Environment* 1967, **20**, 1711

(31) V. Augugliaro, S. Coluccia, V. Loddo, L. Marchese, G. Martha, L. Palmisano, M. Schiavello, *Applied Catalysis B: Environmental*, 1999, **20**, 15

(32) T. N. Obee, R. T. Brown, *Environmental Science Technology* 1995, **29**, 1223

(33) A. J. Maira, K. L. Yeung, J. Soria, J. M. Coronado, C. Belver, C. Y. Lee, V. Augugliaro, *Applied Catalysis B: Environmental* 2001, **29**, 327

(34) J. M. Coronado, J. Soria, *Catalysis Today*: 2007, **30**, 123, 37

(35) M. Wang, F. Zhang, X. Zhu, Z. Qi, B. Hong, J. Ding, J. Bao, S. Sun, C. Gao, *Langmuir* 2015, **31**, 1730

(36) H. Einaga, S. Futamura, T. Ibusuki, *Applied Catalysis B: Environmental* 2002, **38**, 215

(37) H. Einaga, K. Mochiduki, Y. Teraoka, *Catalysis* 2013, **3**, 219

(38) A. J. Maira, J. M. Coronado, V. Augugliaro, K. L. Yeung, J. C. Conesa, J. Soria, *Journal of Catalysis* 2001, **202**, 413

(39) Q. Wu, J. Ye, W. Qiao, Y. Li, J. W. Niemantsverdriet, E. Richards, F. Pan, R. Su, *Applied Catalysis B: Environmental,* 2021, **291**, 120118

(40) D. Zhang, P. Ren, W. Liu, Y. Li, S. Salli, F. Han, W. Qiao, Y. Liu, Y. Fan, Y. Cui, Y. Shen, E. Richards, X. Wen, M. H. Rummeli, Y. Li, F. Besenbacher, H. Niemantsverdriet, T. Lim, R. Su, *Angew. Chem. Int. Ed.*, 2022, **61**, 24, e202204256

(41) F. Han, D. Zhang, S. Salli, J. Ye, Y. Li, F. Rosei, X.-D. Wen, H. Niemantsverdriet, E. Richards, R. Su, *ACS Catalysis*, 2023, **13**, 1, 248-255

(42) J. Ye, D. Zhang, S. Salli, Y. Li, F. Han, Y. Mai, F. Rosei, Y. Li, Y. Yang, F. Besenbacher, H. Niemantsverdriet, E. Richards, R. Su, *Angew. Chem. Int. Ed.,* 2023, **62**, e202302994.

(43) M. Ayoub, A. Z. Abdullah, *Renew. Sustainable Energy Rev*., 2012, **16**, 2671-2686

(44) R. Ciriminna, C.D. Pina, M. Rossi, M. Pagliaro *Eur. J. Lipid Sci. Technol*., 2014, **116**, 1432-1439

(45) Z. Y. Zakaria, N. A. S. Amin, J. Linnekoski *Biomass Bioenergy*, 2013, **55**, 370-385

(46) M. Pagliaro, R. Ciriminna, H. Kimura, M. Rossi, C. Della Pina *Angew. Chem. Int. Ed*., 2007, **46**, 4434-4440

(47) V. M. Daskalaki, D. I. Kondarides *Catal. Today*, 2009, **144**, 75-80

(48) V. Maurino, A. Bedini, M. Minella, F. Rubertelli, E. Pelizzetti, C. Minero *J. Adv. Oxid. Technol*., 2008, **11**, 184-192

(49) R. Liu, H. Yoshida, S. I. Fujita, M. Arai *Appl. Catal. B*, 2014, **144**

(50) F. J. López – Tenllado, J. Hidalgo – Carrillo, V. Montes, F. J. Urbano, J. M. Marinas, L. Ilieva, T. Tabakova, F. Rei, *Catal. Today,* 2017, **280**, 58-64

(51) C. Minero, A. Bedini, V. Maurino *Appl. Catal. B*, 2012 **128**, 135-143

(52) G. Buxton, C. Greenstock, W. Helman, A. Ross *J. Phys. Chem. Ref. Data*, 1988, **17**, 513-886

(53) J. Rashba-Step, E. Step, N.J. Turro, A.I. *Cederbaum Biochemistry*, 1994, **33**, 9504-9510

(54) M. Kuwabara, Z.Y. Zhang, G. Yoshii Radiat. *Phys. Chem*., 1983, **21**, 451-457

(55) M. Kuwabara, Z.Y. Zhang, O. Inanami, G. Yoshii Radiat. *Phys. Chem*., 1984, **24**, 217-227

(56) P.J. Baugh, J.S. Moore, A.F. Norris, C. von Sonntag Radiat. *Phys. Chem.*, 1982, **20**, 215-222

(57) I. A. Shkrob, M. C. Sauer Jr. *J. Phys. Chem. B,* 2004, **108**, 12497-12511

(58) I. A. Shkrob, M.C. Sauer Jr., D. Gosztola *J. Phys. Chem. B*, 2004, **108**, 12512-12517

(59) J. Schneider, M. Matsuoka, M. Takeuchi, J. Zhang, Y. Horiuchi, M. Anpo, D.W. Bahnemann *Chem. Rev*., 2014, **114**, 9919-9986

(60) W. Kim, T. Tachikawa, G.H. Moon, T. Majima, W. Choi *Angew. Chem. Int. Ed*., 2014, **53**,14036-14041

(61) N. Kornblum and H. E. DeLaMare, *J. Am. Chem. Soc.*, 1951, **73**, 880–881

(62) G. M. Rosen and E. J. Rauckman, *Mol. Pharmacol.*, 1980, **17**, 233–238

(63) I. Yamazaki, L. H. Piette, T. A. Grover, *J Biol Chem.*, 1990, **265**, 2, 652-689.

(64) G. R. Buettner, L. W. Oberley, *Biochemical and Biophysical Research Communications,* 1978, **83**, 1, 69-74

(65) E. Finkelstein, G. M. Rosen, E. J. Rauckman, *Archives of Biochemistry and Biophysics,* 1980, **200***,* 1, 1-16.

(66) E. G. Janzen, B. J. Blackburn, *Journal of the American Chemical Society,* 1968, **90**, 22, 5909-5910.

(67) E. G. Janzen, B. J. Blackburn, *Canadian Journal of Chemistry,* 1969, **47**, 20, 3771-3773.

(68) E. G. Janzen, J. I Liu, *Journal of the American Chemical Society,* 1985, **107,** 11, 3599-3605.

(69) K. Hideg, E. A. Nyitrai, *Journal of the Chemical Society, Perkin Transactions 2*, 1981, 1372-1375

(70) L. Ghassemzadeh, T. J. Peckham, T. Weissbach, X. Luo, S. Holdcroft, *J. Am. Chem. Soc*., 2013, **135,** 42, 15923-15932

(71) E. G. Janzen, J. I.-P. Liu, *J. Mar. Resonance* 1973, **9**, 510-512

(72) S. M. Klein, G. Cohen and A. I. Cederbaum, *Biochemistry*, 1981, **20**, 6006–6012

(73) M. G. Steiner and C. F. Babbs, *Arch. Biochem. Biophys.*, 1990, **278**, 478–481

(74) Z. Wang, Y. Wang, R. Mu, Y. Yoon, A. Dahal, G. K. Schenter, V. Glezakou, R. Rousseau, I. Lyubinetsk, Z. Dohnalek *PNAS* 2017, **114**, 8, 1801

(75) T. Ibusuki, K. Takeuchi, *Atmospheric Environment* 1967, **20**, 1711

(76) M. Wang, F. Zhang, X. Zhu, Z. Qi, B. Hong, J. Ding, J. Bao, S. Sun, C. Gao, *Langmuir* 2015, **31**, 1730

(77) S. J. Huang, Y. C. Lin, and J. L. Lin, *Chemical Physics Letters*, 2012, **549**, 17–21

(78) Z. Barbieriková, D. Dvoranová, V. Brezová, *Catalysis Today*, 2018, **313**, 106–113

(79) H. Taniguchi, K.P. Madden *Radiat. Res.*, 2000, **153**, 447-453

(80) P. J. Thornalley, S. Wolff, J. Crabbe, *A.* Stern BBA Gen. Subj., 1984, **797**, 276-287

(81) P. J. Thornalley, *A. Stern Carbohydr. Res.*, 1984, **134**,191-204

Chapter 8. Conclusion

This thesis utilizes EPR spectroscopy to investigate the generation and behaviour of paramagnetic states in various TiO_2 materials following exposure to oxygen, organic substrates of interest, and irradiation. Due to its high sensitivity, non-invasive nature, and the precision of spin Hamiltonian parameters, the findings presented highlight the unique value of EPR for studying heterogeneous photocatalytic and photodynamic processes. The sensitivity EPR offers surpasses that of many other spectroscopic methods, and its variable temperature capabilities enable the detection of thermally unstable radicals that may otherwise go undetected at room temperature.

EPR experiments have shown that the nature, stability, and lifetimes of radicals stabilized on the TiO_2 surface are influenced by several key factors, including the type of TiO_2 sample (anatase vs. rutile), pre-treatment conditions (hydrated vs. dehydrated surfaces), and the method of adsorbate exposure (co-adsorption vs. sequential adsorption). Additionally, the photodynamic of the paramagnetic species were found to depend on various factors such as temperature, dopant level, the location of the paramagnetic species (surface vs. bulk), and the specific type of TiO_2 sample used.

It has been shown that the surface properties of a polycrystalline oxide undergo varying degrees of alteration depending on the physical and/or chemical pre-treatment conditions. Consequently, the defect density and the extent of the surface planes are affected, leading to changes in the reactivity of the samples and ultimately influencing the rate of generation and the lifetimes of the trapped charge carriers.

Material modifications

Different morphologies were achieved through calcination, however, the two different calcination pathways demonstrated variations in the unit cell and the contributing percentage of each morphology within each material. The variation in unit cell parameters of the various polymorphs gave rise to differences in stabilised surfaces and hence surface activities. Despite thermal reductions, demonstrating that oxygen abstraction is equally probable for anatase and rutile materials.

A number of doped TiO_2 samples were successfully synthesised via aliovalent doping. Anatase remained the predominant phase of the material indicating the introduction of dopants (W, Ta and N) despite the small amount of strain on the unit cell did not initiate a phase transition. Whereas, for rutile the incorporation of the sae dopants results in the hindrance of rutilisation. However, once the microwave oven was utilised the rutilisation seemed to be achieved at a better percentage. The furnace anatase and microwave anatase and rutile calcined tungsten materials demonstrated a narrowing of the extrinsic optical band gap. The alteration to the optical band gaps allowed exploitation of the materials for specific surface reactions including the use of visible light to induce photocatalysis. Along with the unit cell and optical band gaps studies, surface studies of the materials were performed and from those studies the accurate dopant level was calculated for each material. As a result of this more focussed catalytic design can be employed to design more efficient photocatalysts. This will allow for industrial catalysts to move away from PGM metals.

EPR Solid State

Low temperature UV irradiation of the clean dehydrated TiO_2 samples under an oxygen atmosphere, followed by removal of the excess oxygen revealed the formation of signals for the trapped holes on F-A-WN-TiO_2 and MW-R-WN(U)-TiO_2 samples and detection of photo-generated superoxide anion on the F-A-WN-TiO_2, MW-A-WN-TiO_2 and MW-R-WN(U)-TiO_2 samples. The formation of the Ti3+ centres were for all the samples, with the microwave calcined samples demonstrating a significant signal broadening. For the following materials: F-A-WN(U)-TIO_2, F-A-TaN(U)-TiO_2, F-R-TaN-TiO_2 and F-R-TaN(U)-TiO_2, which demonstrated a good photocatalytic performance, it could be conceivable that the lifetimes of the paramagnetic species of the trapped hole and the superoxide are too short to detect by EPR as no surface sites are available for stabilisation. The lack of stabilisation sites could be attributed to the materials modification through different dopants and calcination techniques.

The presence of surface defects in each sample are likely to act as additional traps, thus, altering the species formed under irradiation. The most significant alteration in photo-response due to the presence of defects was observed in the photo-response study of N_iO^{2-} centre. The addition of the dopants acts as additional traps for the photo excited electrons.

Photocatalysis

Different precursors and calcination methods lead to variations in the spatial arrangement and surface activity during photocatalytic processes. This is evidenced by differences in species and their contributions during spin trap and decomposition experiments. The most promising catalyst was F-A-WN(U)-TiO_2, though microwave calcined samples also showed potential.

The experiments highlighted the catalysts' capabilities based on the radicals formed under various conditions. Although these materials underperformed compared to commercial P25, their true advantages can only be assessed under visible light irradiation, such as using a blue lamp with a wavelength around 455 nm or lower. This could reveal their potential for VOC decomposition and glycerol transformation, areas beyond the reach of conventional P25.

In conclusion, this thesis has brought novel insights by demonstrating the value of EPR spectroscopy in investigating the generation and behaviour of paramagnetic states in TiO_2 materials, particularly in relation to their photocatalytic processes. Through variations in precursors, dopants, calcination methods, and treatment conditions, the stability and reactivity of the surface radicals were shown to be highly dependent on these factors. The study of optical band gaps further revealed the potential for these materials to be employed under visible light, expanding their applications beyond those of traditional P25. Though some of these materials underperformed compared to P25 under UV light, their true potential lies in their use under visible light, offering opportunities for advanced photocatalytic reactions, such as VOC decomposition and glycerol transformation. The results point to promising future directions for the design of more efficient photocatalysts for industrial applications.

Appendix

A1)

In the following section the spectral output for the xenon arc lamp (LOT Quantum Design MODEL: LSB520) is presented in Figure A.1. The distance between the lamp and the Pyrex flask was 20 cm.

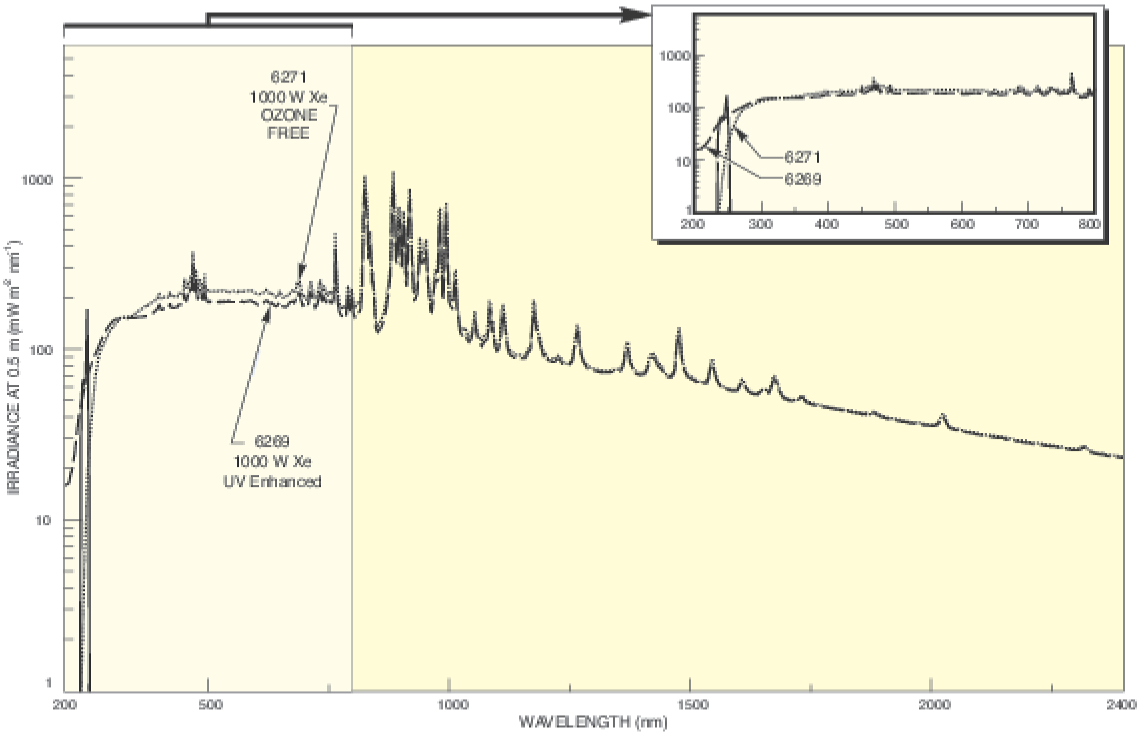

Figure A.1: Spectral output for the xenon arc lamp utilised for the glycerol photocatalytic experiments.

A2)

In the following section the spectral output of the XPS for the furnace anatase and rutile materials for the 4f region are presented in Figures A.2.1 and A.2.2.

The core levels presented in Figure A.2.1 can be utilised to give supplementary information for the Ta (4f), W (4f) and Ti (3p) core-levels. The Ti $3p_{3/2}$ peak appears at 37.2. There are two peaks arising from tungsten appearing at 35.6 and 37.8 and are attributed to W $4f_{7/2}$ and $4f_{5/2}$ respectively, all indicating the presence of W^{6+} state. The peaks at 26.0 and 27.9 eV are identified contributions from the Ta $4f_{7/2}$ and $4f_{5/2}$ electronic states, respectively. The overlapping 22.2 eV is a contribution from O 2s.

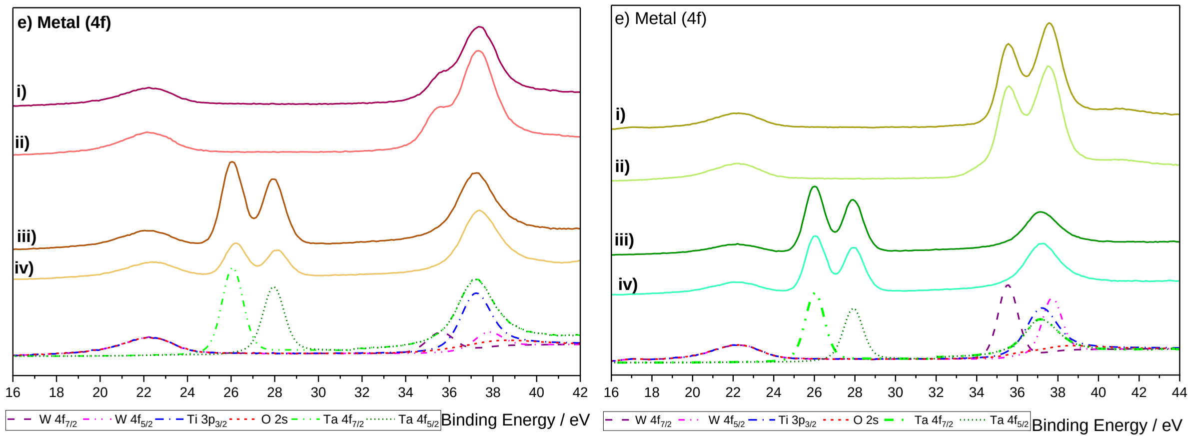

Figure A.2.1: XPS spectra for e) W (4f) and Ta (4f) region for the anatase co-doped TiO_2 (left) and rutile co-doped TiO_2 (right).

The core level spectra for both the rutile and the microwave samples O (1s), Ti (2p), metal (4d) and metal (4f) present the very similar peaks as the furnace samples. The following binding energies 529.9 eV (Ti— O), 530.5 eV (surface hydroxide), 532.1 eV (surface carbonate), 458.4 eV (Ti $2p_{3/2}$), 464.2 eV (Ti $2p_{1/2}$), 472.1 eV (Ti satellite), 229.9 eV (Ta $4d_{5/2}$), 242.4 eV (Ta $4d_{3/2}$), 247.2 eV (W $4d_{5/2}$) and 260.3 eV ($4d_{3/2}$).

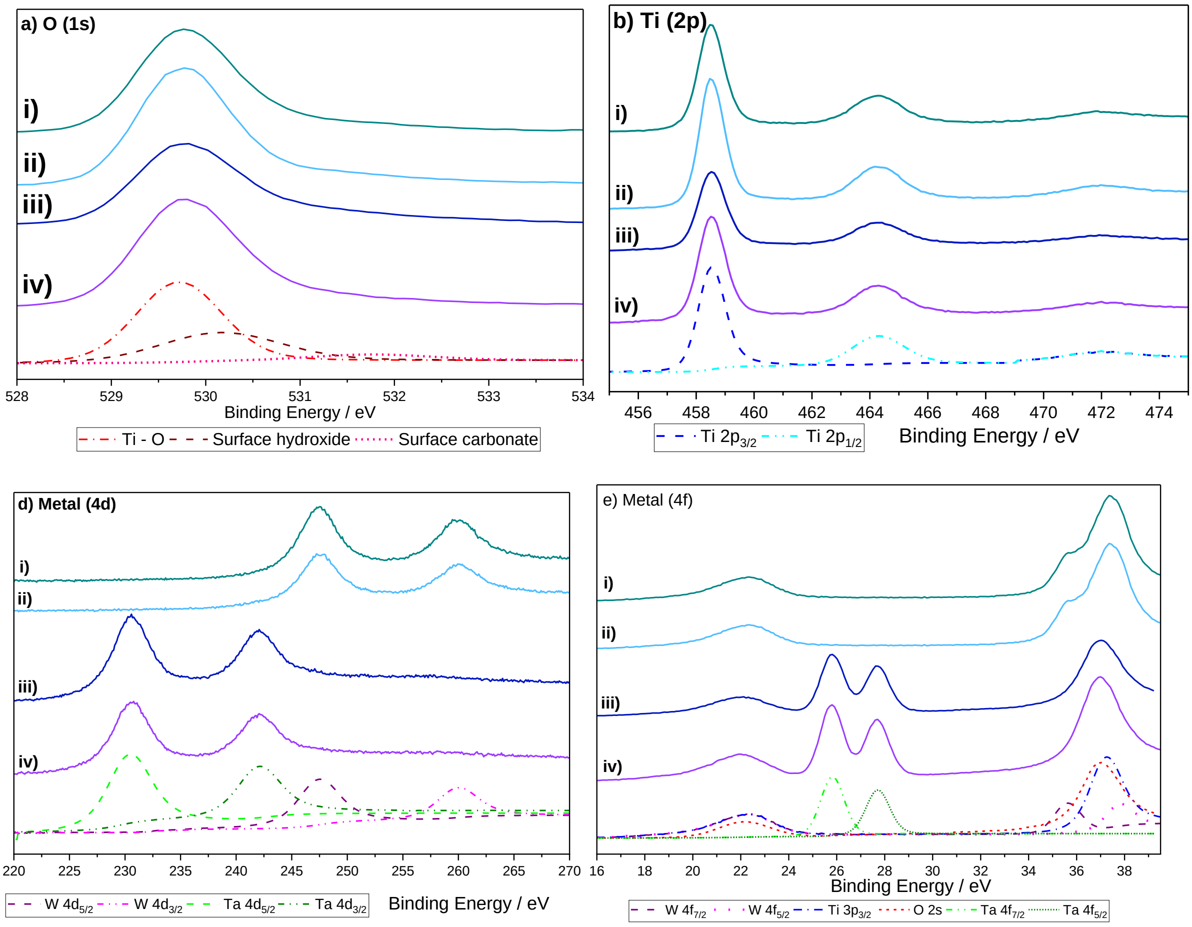

Figure A.2.2: XPS spectra for the anatase co-doped TiO_2 i) MW-A-WN-TiO_2, ii) MW-A-WN(U)-TiO_2, iii) MW-A-TaN-TiO_2 and iv) MW-A-TaN(U)-TiO_2.

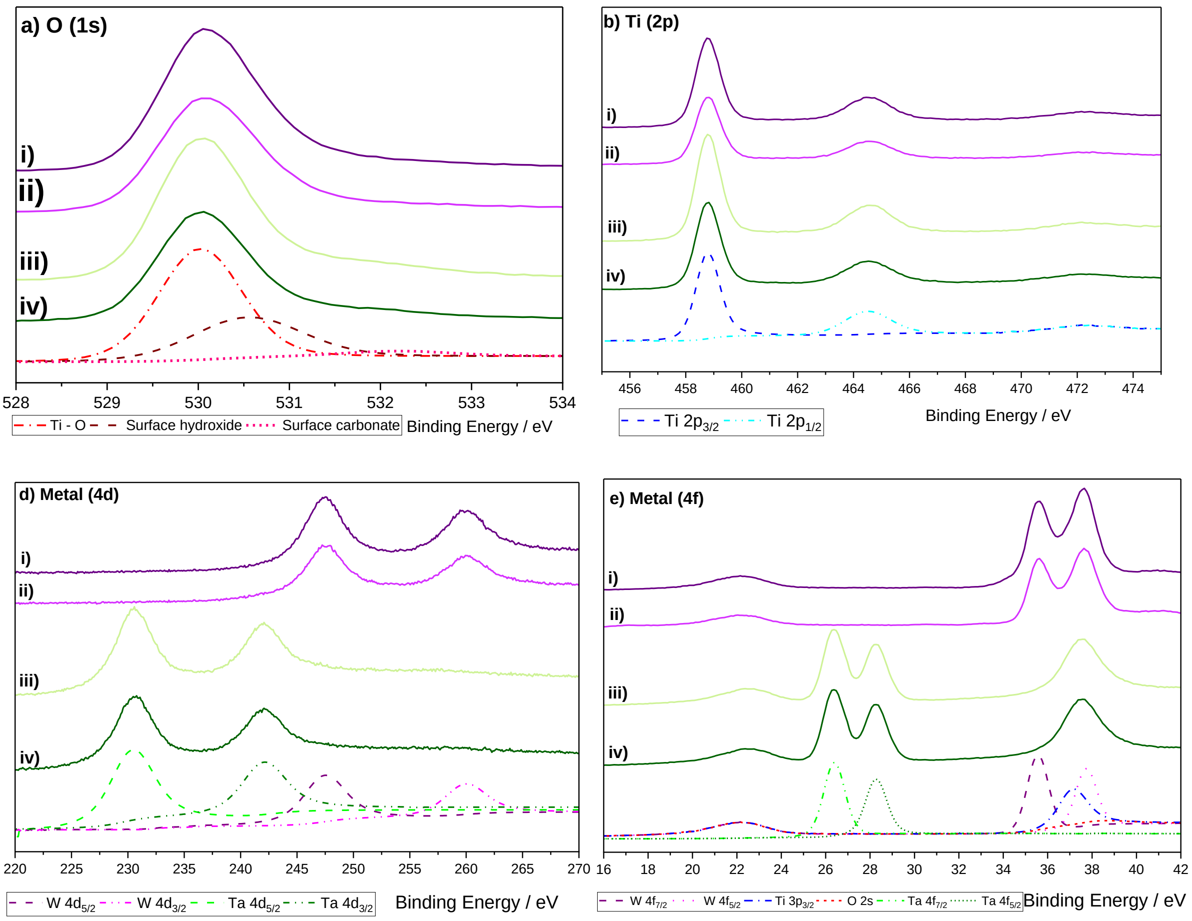

Figure A.2.3: XPS spectra for the rutile co-doped TiO_2 i) MW-R-WN-TiO_2, ii) MW-R-WN(U)-TiO_2, iii) MW-R-TaN-TiO_2 and iv) MW-R-TaN(U)-TiO_2.